Experimental Methods for the Constitutive Characterization of Sheet Materials in Generalized Plane Strain

by

Johnathon Cole Fast-Irvine

A thesis

presented to the University of Waterloo

in fulfilment of the

thesis requirement for the degree of

Master of Applied Science

in

Mechanical and Mechatronics Engineering

Waterloo, Ontario, Canada, 2022

Author's Declaration

This thesis consists of material all of which I authored or co-authored: see Statement of Contributions included in the thesis. This is a true copy of the thesis, including any required final revisions, as accepted by my examiners.

I understand that my thesis may be made electronically available to the public.

Statement of Contributions

Chapter 3 of this thesis includes portions of a post-print of a published journal article, revised for additional content and to reflect the format of this thesis. As the primary author, the candidate was responsible for the Matlab® coding, analysis of the experimental results, preparing the manuscript and generating many of the figures. Dr. Armin Abedini and Ms. Jacqueline Noder reviewed the manuscript and completed the experimental characterization and testing for the DP1180 and AA5182 materials, respectively. Professor Cliff Butcher provided technical advice, feedback and reviewed the manuscript.

Abstract

Decreasing vehicle weight by substituting traditional steel for high-strength steel or aluminum is an effective way to improve fuel economy and decrease greenhouse gas emissions in the transportation sector. The optimization of a lightweight vehicle structure and subsequent prediction of forming operations and crash performance of its components requires accurate material models that capture the anisotropic response of sheet metals in a diversity of loading conditions, particularly in generalized plane strain. The objective of this work is to develop and validate two novel experimental methodologies to extract the constitutive response from sheet materials under two generalized plane strain stress states: plane strain tension and through-thickness shear.

Plane strain tension is one of the most prominent failure conditions in formed parts, but determination of the plane strain yield strength is complicated. Although plane strain notch experiments are simple to perform, their analysis is not straightforward since the load distribution along the sample gauge width transitions from plane strain tension in the middle to uniaxial tension at each edge. Existing analysis techniques are unreliable due to the assumption of a yield function in the inverse-identification of correction factors or the use of empirical techniques that lack a theoretical foundation. A review of the experimental literature on cruciform tests suggests that a principal in-plane stress ratio of 0.5 applies at plane strain tension for aluminum and steel, independent of isotropy and consistent with the theory of pressure-independent plasticity. With the stress ratio at plane strain tension known along with the tensile R-value, the uniaxial-to-plane strain arc of an isotropic yield surface can be controlled by a single parameter – the yield exponent. The optimal value of the exponent occurs when the modelled stress response, from the integration of optical strain measurements across the gauge region of a plane strain notch specimen, agrees with the experimentally measured stress-strain curve. Multivariable optimization may be used to model differential hardening, by assuming a distribution of the exponent with plastic strain, or non-associated flow, by calibrating two independent exponents for the yield function and plastic potential. Four disparate automotive materials were selected to demonstrate the plane strain notch test integration methodology: AA6xxx-T4 (1.5 mm thick), AA6xxx-T81 (2.7 mm thick), AA5182-O (1.5 mm thick) and DP1180 (1 mm thick).

Dual phase steels and high strength aluminum alloys tend to exhibit so-called shear fracture, evidenced by through-thickness cracking at an approximate angle of 45°. Due to the difficulty in obtaining reliable experimental data for sheet metals, the through-thickness shear stress is often left uncalibrated in yield surfaces leading to the inability of the analyst to accurately predict and avoid shear fracture in forming operations. A through-thickness shear test was developed by machining two shear-promoting notches

through the sheet thickness of each test specimen and designing a test fixture to minimize gauge region rotation as each specimen was pulled by a standard uniaxial test frame. Experimental tests were completed using AA6xxx-T81 and DP1180 steel to analyze a representative steel and aluminum in different sheet thicknesses. The measured load was corrected for the friction introduced by the test fixture, using a modified strip draw test conducted under analogous conditions as the through-thickness shear test. Normalized shear stress ratios of 0.50 for the AA6xxx-T81 and 0.68 for the DP1180, were identified for input into three-dimensional yield criteria.

To describe yielding of a material under all stress states and orientations, a so-called master yield surface was calibrated to the experimental data. Despite the prevalence of plane strain and through-thickness shear induced failures in industry, conventional yield surfaces used for formability models are usually calibrated with the uniaxial tensile stresses, uniaxial tensile R-values (representing the strain directions) and the equal-biaxial stress and R-value. In this analysis, Yld2000, Yld2004 and Vegter master yield surfaces were calibrated to capture the complete material response in all tested loading conditions for each of the four studied materials. The addition of the plane strain tensile and through-thickness shear yield stresses improved the accuracy of the models compared to the conventional calibration. Optimal agreement with the experimental data was obtained by adopting a variable yield function exponent, rather than relying on conventional values of 6 for BCC and 8 for FCC materials.

Each of the master yield surface models was evaluated by comparing the simulated responses of plane strain and through-thickness shear tests to experimental data. By leveraging knowledge of the yield surface and the hardening behavior to large strains obtained from shear tests, the stress-strain response of a plane strain notch geometry was accurately simulated beyond necking up to fracture for AA5182 and DP1180. The plane strain notch geometry was different than the geometry used for experimental evaluation of the plane strain yield strength. Small differences between the simulated and experimental stress-strain and localized major strain evolution for AA6xxx-T4 and AA6xxx-T81 were attributed to post-uniform differential hardening. Simulating the AA6xxx-T81 through-thickness shear test using the calibrated Yld2004 model confirmed excellent agreement with the experimental load displacement response.

Acknowledgements

This work would not have been possible without the assistance of many people and organizations who generously provided time and resources. I must begin by thanking my supervisor Dr. Clifford Butcher for encouraging me to pursue a master's degree. His willingness to teach, explain and advise piqued my interest in the field and accelerated my understanding of this research topic. My work benefitted from the technical assistance, ideas, and training provided by Dr. Armin Abedini, Jacqueline Noder, Eckhard Budziarek, Amir Zhumagulov, Dr. Jose Imbert-Boyd, Kenneth Cheong, Farinaz Jeyranpourkhameneh, Brock Watson and Tom Gawel.

I owe a special thanks to all those who made my time in Waterloo so enjoyable, especially Enrico Lai, Reza Tangestani, Ben Harvey, and Claire Bourque. I enjoyed our spirited coffee breaks. Thank you to Evan Sauve, for not only joining me on many spaghetti dinners, but also meticulously proofreading an early version of this thesis. To all the students and staff in the Forming and Crash Lab: you motivated me to work hard, have fun, and do my best.

Thank you to my family for your support. My mother, Carolyn Fast, not only instilled in me the value of education at a young age but has been a guiding example of hard work, perseverance, and academic achievement. I am proud to follow in her footsteps.

Finally, I would like to gratefully acknowledge the University of Waterloo, the Natural Sciences and Engineering Research Council of Canada (NSERC) and the Auto/Steel Partnership Project on Fracture Prediction in Non-Linear Strain Paths for their financial support of the projects in this thesis and providing the materials for characterization.

Table of Contents

List of Figures

List of Tables

Chapter 1 Introduction

The fabrication of the modern vehicle requires the use of advanced high strength steels and aluminums to reduce curb weight, improve fuel efficiency, and meet emissions standards (Davies, 2012; Froes, 1994). The process of weight reduction, or so-called lightweighting, is one of the most efficient ways to decrease emissions since reducing the curb weight by 10% increases the fuel efficiency by 6.9-7.6% (MIT, 2008). By substituting a higher strength steel in place of a standard plain carbon steel, components can be downgauged to minimize weight while maintaining strength. Today, the average vehicle consists of 17.6% high strength steel by weight compared to only 8.8% in 1995 (Oak Ridge National Laboratory, 2017). Advanced aluminum alloys are also central to vehicle lightweighting having one third the density of steel (Davies, 2012). As evidence of industrial adoption, the percentage of a vehicle constructed from aluminum has increased from 6.3% in 1995 to 9.9% in 2015 (Oak Ridge National Laboratory, 2017).

Unfortunately, these advanced materials come with their own set of challenges that underline the importance of accurate characterization techniques. Dual phase steels are a mixture of ferrite and martensite, the latter of which increases the strength at the expense of ductility, making forming more difficult (Billur and Altan, 2013). While AA5xxx aluminum alloys (Al-Mg) generally have good formability, they are not well suited for structural applications due to their lower strength and are limited to inner closure panels due to Portevin-Le Châtelier (PLC) effect that cause stretch marks on the surface. The stronger, heat-treatable, and increasingly popular AA6xxx alloys (Al-Mg-Si) can be used for outer panels with a Class A finish and some structural components but generally have lower ductility than the AA5xxx series due to the formation of Mg-Si precipitates (Zheng *et al.*, 2018). Regardless of the material, the cold rolling process used to produce sheet metal induces anisotropy – or directionally dependent properties – that require multiple experimental characterization tests to full define a material model.

An accurate material model is necessary to avoid costly defects by simulating sheet metal forming processes prior to production. Necking, defined as localized sheet thinning, is one of the dominant failure modes in formed parts (Mahmudi, 1999). Other failures include wrinkling and fracture, depending on the loading state. Experimental testing is required to produce accurate material models for crashworthiness and formability computer models to aid in the engineering, design, and manufacturing of automotive components.

Progress in the characterization of sheet metals has been marked by advancements in anisotropy modelling, experimental measurement techniques, and new specimen geometries that permit obtaining material properties in a wide array of stress states. Sections 1.1 – 1.3 introduce the underlying fundamentals of this field. Section 1.4 then considers the relevance and contribution of the work in this thesis.

1.1 Anisotropy in Rolled Sheet Metals

An anisotropic material has different properties depending on its orientation. The preferred orientation of grains, grain boundaries, and dislocations within a material is known as texture. In an isotropic metal, the properties are macroscopically the same in all directions because the grains are randomly orientated. Cold rolling of billets to produce sheet metal compresses the grains causing them to elongate along the rolling direction and resulting in a non-random structure. The strength, defined by the yield stress, and ratio of width-to-thickness strain under uniaxial tension, defined by the R-value, are therefore directionally dependent. Crystallographic slip will be easier along loading directions with favorable crystal orientations, that promote a higher resolved shear stress on slip systems, and along directions with lower grain and dislocation densities (Cui *et al.*, 2013).

Perhaps the easiest visualization of sheet anisotropy is in the formation of a deep drawn cup, a typical example of which is shown in Figure 1. Due to texture, so-called "ears" will form along the circumference of the cup formed from an anisotropic sheet material as greater circumferential compression is promoted along particular axes. The number of ears is directly proportional to the number of "peaks" observed in the directional variation of the R-values (Yoon *et al.*, 2006). Consequently, experimental tests along 15-degree or 45-degree increments with respect to the rolling direction are necessary to obtain the yield strength and R-values in each orientation to fully define the expected behavior in forming operations. Adopting an anisotropic yield function permits interpolation between known experimental values.

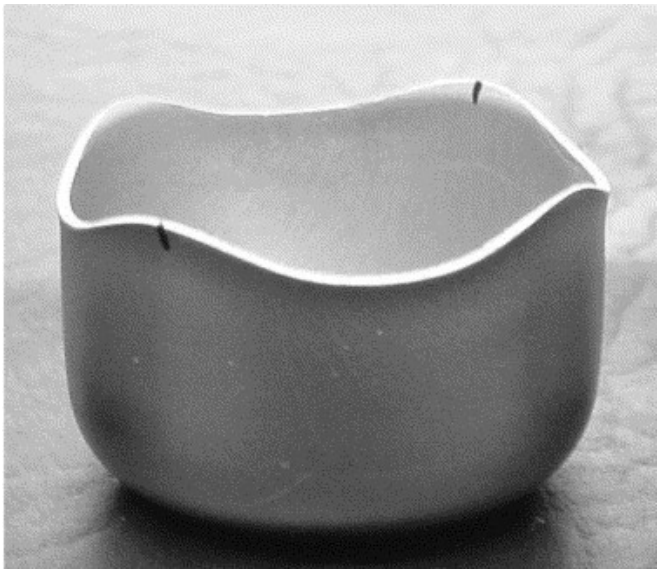

Figure 1: Typical earring profile of an AA1200-O deep drawn cup, with the rolling direction indicated by the black lines (Engler and Hirsch, 2007). Used with permission.

1.2 Stress and Strain

Stress is a measure of the intensity of a load, or force F acting over an area. The true (Cauchy) stress σ_{true} is computed using the instantaneous area A_i (Eq. 1.1a) while using the initial, undeformed area A_o defines the engineering stress σ_{eng} (Eq. 1.1b).

$$\sigma_{true} = \frac{F}{A_i}, \sigma_{eng} = \frac{F}{A_o} \tag{1.1a, b}$$

The Cauchy stress tensor of Eq. (1.2) represents the full three-dimensional state of the true stress at a material point.

$$\boldsymbol{\sigma} = \sigma_{ij} = \begin{bmatrix} \sigma_{11} & \sigma_{12} & \sigma_{13} \\ \sigma_{21} & \sigma_{22} & \sigma_{23} \\ \sigma_{31} & \sigma_{32} & \sigma_{33} \end{bmatrix} \tag{1.2}$$

The diagonal components (11, 22, 33) correspond to normal stresses, and the off-diagonal components correspond to shear stresses. The principle of complementary shear requires that $\sigma_{21} = \sigma_{12}$, $\sigma_{31} = \sigma_{13}$ and $\sigma_{23} = \sigma_{32}$ such that the tensor is fully defined by six unique stress components. When the shear terms in a coordinate system are all zero, the stress is called "principal". The material coordinate system is often aligned with the axes of orthotropic symmetry (rolling, transverse, and normal direction) where, the 11-component refers to the stress along the rolling direction, the 22-component along the transverse direction, and the 33-component along the normal (thickness) direction. For thin sheet metal, the simplifying case of plane stress is often valid since the through-thickness stresses are negligible relative to the in-plane stresses such that $\sigma_{31} \cong \sigma_{32} \cong \sigma_{13} \cong \sigma_{23} \cong \sigma_{33} \cong 0$.

While stress is a measure of the resistance of a material to deformation, strain is the metric used to define the applied deformation. There are many definitions of the strain tensor that can be employed but in the mechanics of ductile metals, the true (ε_{true}) and engineering (ε_{eng}) strain are most common. Eq. (1.3) defines a normal strain, where l is the length of the deformed element and l_o is the initial length in both true and engineering forms.

$$\varepsilon_{true} = \ln\frac{l}{l_o}, \varepsilon_{eng} = \frac{l}{l_o} \tag{1.3a, b}$$

Shear strains do not produce any change in length or volume but instead a change in angle. The engineering strain for a simple shear deformation in the 12-plane is defined as γ_{12}, where α is the angle between the

deformed and undeformed element. In the tensorial component representation of Eq. (1.4), ε_{12} is defined as half of the engineering strain and the shear angle.

$$\varepsilon_{12} = \frac{\gamma_{12}}{2} = \tan\alpha \tag{1.4}$$

In the absence of shear strains, the principal strains are aligned with the 11, 22 and 33 directions. A state of plane strain occurs if the normal strain along one direction is equal to zero, as is often the case in a wide sheet where the amount of material restrains elongation or contraction along the corresponding axis. Plane strain also occurs in shear tests where there is no thinning strain.

The uniaxial (R^{UT}) and equal-biaxial (R^{EB}) instantaneous R-values quantify the direction of the plastic strain increments, as shown in Eq. (1.5). It is common to calculate the average R-value by applying a linear fit over a representative range of strain.

$$R^{UT}(\theta) = \frac{d\varepsilon_w^P}{d\varepsilon_t^P}, \qquad R^{EB} = \frac{d\varepsilon_2^P}{d\varepsilon_1^P} \tag{1.5}$$

The R-value in uniaxial tension is the ratio of the width to the thickness strain, whereas in equal-biaxial tension it is the ratio of the in-plane major and minor strains. Metals with relatively high formability tend to have high uniaxial R-values such as mild steels where R > 2 because they are more resistant to thinning and necking. An isotropic material has an R-value equal to one.

The stress triaxiality and Lode parameters are common metrics that define the type of loading as a function of the three invariants of the stress tensor, based on the proportions of hydrostatic to deviatoric stress. The deviatoric stress $\boldsymbol{\sigma}'$ is defined by subtracting the hydrostatic stress σ_m from the Cauchy stress tensor. The three invariants of the Cauchy and deviatoric stress tensors are defined by I_{1-3} and J_{1-3}, respectively. As will be discussed further in Chapter 3, only deviatoric loading is responsible for slip and plastic deformation under pressure independent plasticity theory[1].

---

[1] The stress invariants are intrinsically linked with the definition of a yield surface. A pressure independent yield surface is modelled as a cylinder of some cross-sectional shape orientated along the $\hat{n} = \frac{1}{\sqrt{3}}\hat{e}_1 + \frac{1}{\sqrt{3}}\hat{e}_2 + \frac{1}{\sqrt{3}}\hat{e}_3$ in principal stress space, where movement parallel to $\hat{n}$ represents an increase in only hydrostatic stress ($\sigma_1 = \sigma_2 = \sigma_3$) proportional to the first invariant. The second invariant describes movement perpendicular to $\hat{n}$ causing a stress component to develop on the so-called octahedral or π-plane. The third invariant is related to the angle that the stress point makes, rotated about $\hat{n}$. The von Mises stress is $\sigma_{eq} = \sqrt{3J_2}$, a function of the magnitude of the deviatoric stress acting on the octahedral plane. With no reliance on the third invariant, the von Mises yield surface appears as a circle on the octahedral plane. The Tresca criterion is a function of the second and third invariants, which explains its non-circular hexagonal shape on the octahedral plane (Kelly, n.d.).

The stress triaxiality T quantifies the ratio of hydrostatic loading, defined by the first invariant of the Cauchy stress tensor I_1, to the deviatoric loading, defined by the second invariant of the deviatoric stress tensor J_2, as shown in Eq. (1.6).

$$T = \frac{I_1}{3\sqrt{3J_2}}$$

$$I_1 = tr(\boldsymbol{\sigma}),\ J_2 = \sqrt{\frac{\boldsymbol{\sigma}' : \boldsymbol{\sigma}'}{2}},\ \boldsymbol{\sigma}' = \boldsymbol{\sigma} - \sigma_m \boldsymbol{I},\ \sigma_m = \frac{\mathrm{tr}(\boldsymbol{\sigma})}{3} \tag{1.6a-e}$$

For plane stress loading, $T = 0$ in shear and $T \approx 0.578$ in plane strain tension. In uniaxial compression, uniaxial tension, and equal-biaxial tension, the triaxiality obtains a value of -1/3, 1/3 and 2/3, respectively.

Quantifying the type of deviatoric (shear) loading, the Lode parameter (L) is defined in stress form as (Danas and Castaneda, 2012)

$$L = -\frac{3\sqrt{3}J_3}{2J_2^{3/2}},\ J_3 = \det(\boldsymbol{\sigma}') \tag{1.7a, b}$$

where J_3 is the third invariant of the deviatoric stress tensor. The stress-based Lode parameter is bounded between -1 and 1, where a value of -1 signifies uniaxial tension and a value of 1 signifies equal-biaxial tension.

The strain-based Lode parameter (v_L) is defined as (Lode, 1926):

$$v_L = \frac{3d\varepsilon_2}{d\varepsilon_1 - d\varepsilon_3} \tag{1.8}$$

The strain-based Lode parameters are influenced by plastic anisotropy unlike the stress-based Lode parameter. The value of v_L in uniaxial and biaxial tension depends upon the R-values. However, both the stress and strain-based Lode parameters are equal to zero in states of shear and plane strain tension as shown by Butcher and Abedini (2019) and briefly summarized in Chapter 3 of this thesis.

1.2.1 Measurement of Strain

Unlike stress, which is calculated from the measured load and area, the strain can be directly measured in the lab from the applied deformation. Modern strain measurement technology, like Digital Image Correlation (DIC) used in this work, allows for contact-free, accurate measurement of the in-plane components of the strain tensor. A camera system tracks the movement of unique pixel regions known as

subsets based on the pixel gray values of a stochastic speckle pattern. The pattern is commonly generated using spray paint to apply a white base coat followed by black speckles to the surface of the test specimen. Subsets can consist of a unique pixel region or overlap with neighboring subsets by adjusting the so-called step size. Applying a decay type filter reduces noise by smoothing the data over neighboring subsets where the subset of interest holds the most weight in the filtering scheme (Byrne and Simonsen, 2016; Correlated Solutions, n.d.). The number of neighboring subsets included in the filter is adjustable such that an overall measurement length scale, known as the Virtual Strain Gauge Length (VSGL), is defined by:

$$VSGL = \text{Camera Resolution } \left[\frac{\text{mm}}{\text{px}}\right] * \text{Step Size [px]} * \text{Filter Size} \tag{1.9}$$

The size of the VSGL can strongly affect the measured strain as demonstrated by Khameneh *et al.* (2021). Adopting a smaller VSGL, particularly during fracture where strain concentrates into a narrow band, captures the localized strain with less averaging over subsets that are outside the zone of interest. In general, the VSGL should be as small as possible for measuring fracture strains or alternatively rotation-based methods can be used for greater resolution (Khameneh *et al.*, 2021). For constitutive characterization of macroscopic plastic yielding before the onset of localization or fracture and when deformation is approximately homogeneous, the selection of the VSGL is of less importance.

1.3 Phenomenological Plasticity

Plasticity refers to irreversible deformation caused by the application of a sufficient force to initiate the gliding of atoms across slip planes within a material's crystal lattice structure. Plasticity modelling approaches fall into two categories. The first category is crystal plasticity, which attempts to model the physics at the crystallographic level by accounting for the critical shear stress required to induce slip. The second category is phenomenological plasticity based on continuum mechanics, which attempts to fit constitutive equations to experimental data (Hosford, 2013). Since the phenomenological approach is much more common in practice due to its simplicity and computational efficiency, it forms the basis of this work. Phenomenological plasticity theory is composed of three constitutive equations: a flow rule, hardening model, and yield function.

1.3.1 Hardening Model

The hardening curve of a material quantifies the increase in flow stress as a function of the accumulated plastic strain. Common sheet materials, like steel and aluminum, exhibit a high hardening rate after initial yielding as dislocations are introduced into the crystal lattice that resist further slip (Hosford, 2013). Gradually as the dislocation density increases, annihilation dominates the formation of new dislocations,

and the hardening rate begins to decrease. While complicated on a microstructural level, the tensile test is macroscopically described by so-called uniform elongation between the yield strength and ultimate tensile strength and so-called necking between the ultimate tensile strength and fracture strength.

A typical hardening curve, generated from a uniaxial tension test under quasi-static conditions, takes the shape of Figure 2 and is defined by two distinct regions. The first region is between the onset of yielding σ_y and the ultimate tensile strength σ_{UTS} taken at the point of peak load. In this region, the equivalent plastic strain ε_{eq}^{p} is relatively uniform along the gauge region of the specimen and the flow stress $\bar{\sigma}$ increases due to work hardening. As defined by the Considère criterion, shown in Eq. (1.10), diffuse necking begins at the ultimate tensile strength, where the flow stress equals the instantaneous hardening rate.

$$\bar{\sigma} = \frac{d\bar{\sigma}}{d\varepsilon_{eq}^{P}} \tag{1.10}$$

As the test loses uniformity due to developing gradients of stress and strain, the stress state in the neck transitions from uniaxial tension to triaxial loading. The engineering stress begins to decrease because the increase in strength made possible by work hardening is insufficient to counteract the decrease in area due to thinning of the sheet. The true stress in the material continues to increase. Finally, the strain concentrates into a localized neck which ultimately leads to fracture (Hosford, 2013). Although the advent of DIC technology permits measurement of the instantaneous cross-sectional area until fracture (Omer *et al.*, 2020), the equivalent stress is no longer simply equal to the true stress obtained from the cross-sectional area and force, due to the departure from uniform uniaxial loading.

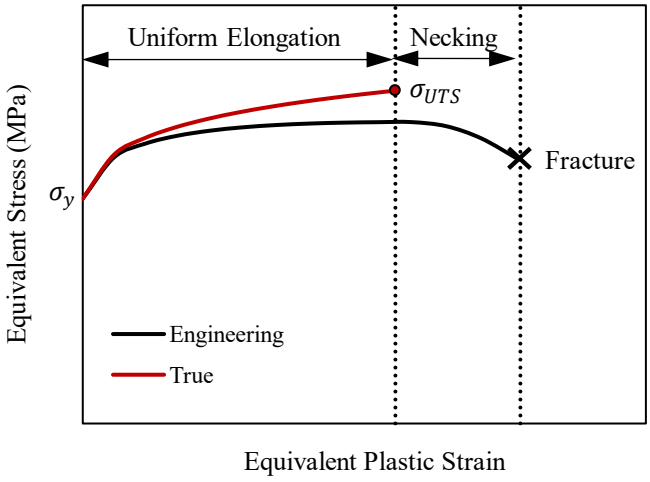

Figure 2: True and engineering stress-strain curves showing the yield strength and ultimate tensile strength. Uniform elongation occurs between the yield point and the ultimate tensile point, after which diffuse then localized necking develop.

Although a uniaxial tensile test only provides data on the stress-strain response until the onset of diffuse necking, strains in typical forming operations are well above the ultimate tensile point. Other stress states, including shear and equal-biaxial tension, suppress necking, allowing for greater forming strains than typically seen in a uniaxial tension test. As a result, various methods exist for determining the equivalent stress-strain response during necking. For uniaxial tension tests of cylindrical specimens, the well-known analytical Bridgman correction (Bridgman, 1952) may be used. In the case of rectangular sheet or so-called "dogbone" specimens, no analytical correction factor exists, but empirical corrections have been proposed by Zhang *et al.* (1999), Scheider *et al.* (2004) and Choung and Cho (2008). Unfortunately, these methods are heavily dependent on the specimen aspect ratio and may not work for standard ASTM or JIS specimens.

Simple shear or equal-biaxial bulge tests may be used in place of a uniaxial tension test to determine the equivalent stress-strain response to larger strains. Shear specimens consist of two notches machined through the sheet, which encourage a state of shear in the gauge region when pulled using a standard uniaxial tensile frame. The principal of equivalent plastic work is then used to equate the measured shear stress and strain in the gauge region of the specimen to an equivalent stress and strain experienced in a uniaxial tension test. In a bulge test, a sheet is clamped to a hydraulic reservoir using a circular die. As the hydraulic fluid is pressurized, the sheet expands until rupture. The equivalent stress in a bulge test is obtained using membrane theory, given a known pressure of the hydraulic fluid and measured radius of curvature and thickness of the expanding sheet (Min *et al.*, 2017). The onset of diffuse necking occurs at $\varepsilon_{eq}^{p} = n$ in a uniaxial tension test and $\varepsilon_{eq}^{p} = \frac{4}{11}(2n+1)$ in a bulge test, where n is the power law hardening exponent (Hill, 1950). Theoretically, fracture occurs without any necking or localization in a shear test since the mechanics enforce a through-thickness strain of zero, making the test ideal for characterization to large strains.

The hardening behavior of sheet metals is often idealized as isotropic in which hardening is independent of the stress state, such as uniaxial or biaxial tension, and material direction. Anisotropic hardening is observed in materials with evolving microstructures, such as in the transformation of austenite to martensite in TRIP steels, or in HCP materials such as magnesium where a combination of slip and twinning deformation modes are activated in different stress states. An empirical relationship called the hardening model is often fit to the experimental data up to uniform elongation unless extended with corrections or shear/bulge tests. Common forms include the Swift power law hardening model (Swift, 1952) shown in Eq. (1.11) or the Modified Hockett Sherby proposed by Noder and Butcher (2019) shown in Eq. (1.12). The parameters K, n and ε_0 in the Swift model and C_1-C_5 in the Modified Hockett Sherby model must be obtained from experimental tests. While closed form models are convenient for analysis, the flow stress can also be fit with shape-preserving cubic splines and sampled at discrete points for entry into finite-

element software input decks. The choice of closed form hardening model will dictate the value of the extrapolated flow stress outside the domain of equivalent plastic strain used for calibration.

$$\bar{\sigma}^{Swift} = K\left(\varepsilon_0 + \varepsilon_{eq}^p\right)^n \tag{1.11}$$

$$\bar{\sigma}^{MHS} = C_2 - (C_2 - C_1)\exp\left(-C_3(\varepsilon_{eq}^p)^{C_4}\right) + C_5\sqrt{\varepsilon_{eq}^p} \tag{1.12}$$

The extrapolation can be adjusted using a scaled exponential decay function and midpoint integration of the hardening rate, $H = d\bar{\sigma}/d\varepsilon_{eq}^p$, as shown in Eq. (1.13).

$$\begin{aligned} \overline{\sigma_i^{adj}} &= \left(\frac{H_{i-1}^{adj} + H_i^{adj}}{2}\right)\Delta\varepsilon_{eq}^p + \overline{\sigma_{i-1}^{adj}} && \left(\varepsilon_{eq}^p\right)_i > \varepsilon_{UTS}^p \\ \overline{\sigma_i^{adj}} &= \overline{\sigma_i} && \left(\varepsilon_{eq}^p\right)_i \le \varepsilon_{UTS}^p \end{aligned} \tag{1.13}$$

The initial extrapolation may be obtained assuming Swift power law hardening (with $\varepsilon_0 = 0$), fit to the last (terminal) point in the pre-necking hardening model. At the terminal point, the instantaneous hardening exponent used for extrapolation is calculated as:

$$n_{extrap} = \frac{H_{term}\left(\varepsilon_{eq}^p\right)_{term}}{\bar{\sigma}_{term}} \tag{1.14}$$

Note that if the last point in the calibrated, pre-extrapolation model is the point of uniform elongation, then the hardening exponent used for extrapolation is simply the equivalent plastic strain at uniform elongation as a result of the Considère Criterion. The post-uniform hardening rate can then be easily adjusted by the variable a to model high, low, and saturated hardening materials using a single model as:

$$\begin{aligned} H_i^{adj} &= H_i e^{-a\left(\left(\varepsilon_{eq}^p\right)_i - \varepsilon_{UTS}^p\right)^b} && \left(\varepsilon_{eq}^p\right)_i > \varepsilon_{UTS}^p \\ H_i^{adj} &= H_i && \left(\varepsilon_{eq}^p\right)_i \le \varepsilon_{UTS}^p \end{aligned} \tag{1.15}$$

The value of b is material dependent and controls the amount of decay, with $b = 0.25$ suggested for aluminums. As shown in Figure 3 for a generic power law hardening material ($K = 1000$ MPa, $n = 0.1$), a value of $a = 0$ maintains the initial power law extrapolation and a value of $a \to \infty$ promotes saturation.

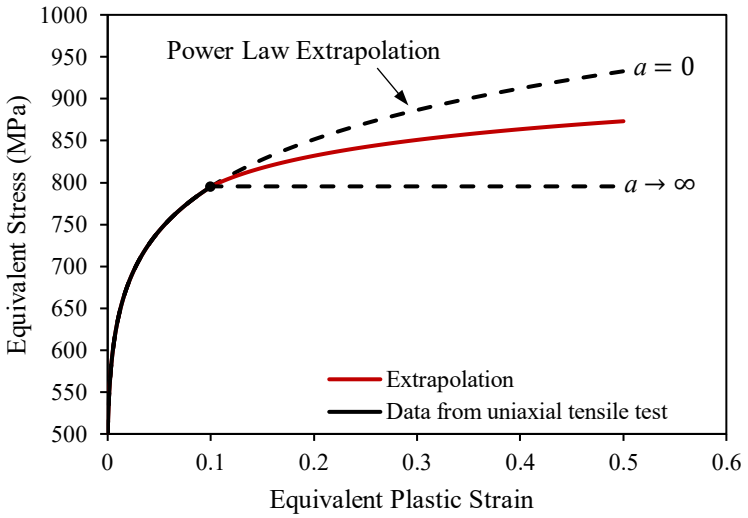

Figure 3: Illustration of adjusted spline hardening model extrapolation using an exponential decay function to model the post-necking response. A value of $a = 0$ results in power law extrapolation. Saturation occurs by increasing the value of a.

The value of a may be calibrated using inverse analysis or fit to converted shear or bulge tests to extend an initial hardening curve generated from a uniaxial tensile test to higher strains.

1.3.2 Yield Function

The yield function shown in Eq. (1.16) equates any multiaxial loading state to an equivalent stress, for instance from a uniaxial tensile test, that would cause yielding. Yielding occurs when $f = 0$, meaning that the equivalent stress from the yield function σ_{eq} equals the flow stress from the hardening curve at the current level of equivalent plastic strain $\bar{\sigma}\left(\varepsilon_{eq}^{P}\right)$.

$$f = \sigma_{eq} - \bar{\sigma}\left(\varepsilon_{eq}^{P}\right) \tag{1.16}$$

If $f < 0$, then the deformation is elastic and completely described by Hooke's Law as

$$\boldsymbol{\varepsilon} = \frac{1+\nu}{E}\boldsymbol{\sigma} - \frac{\nu}{E}\mathrm{tr}(\boldsymbol{\sigma})\boldsymbol{I} \tag{1.17}$$

where ν is Poisson's ratio, E is Young's modulus, and $\boldsymbol{I}$ is the identity matrix. One way to determine the equivalent plastic strain is through an incremental plastic work balance, which is expressed using principal stresses and strains as:

$$\sigma_{eq} d\varepsilon_{eq}^{P} = \boldsymbol{\sigma} : \boldsymbol{d\varepsilon^{P}} = \sigma_1 d\varepsilon_1^{P} + \sigma_2 d\varepsilon_2^{P} + \sigma_3 d\varepsilon_3^{P} \tag{1.18}$$

Two of the earliest and most used yield functions include those of von Mises and of Tresca, both designed for isotropic materials. Each function may be conveniently obtained as a special case of Hosford's 1972 generalized isotropic yield function shown in Eq. (1.19) (Hosford, 1972). An exponent of $m = 2$ reproduces the von Mises yield surface, an exponent of $m \to \infty$ reproduces the Tresca yield surface and intermediary exponents interpolate between the two functions. The isotropic von Mises and Tresca are perhaps the only yield criteria used for metals that can be directly derived from mechanics with the remainder being phenomenological variants of these models.

$$|\sigma_1 - \sigma_2|^m + |\sigma_2 - \sigma_3|^m + |\sigma_3 - \sigma_1|^m = 2\sigma_{eq}^m \tag{1.19}$$

As reviewed by Banabic (2010) and Hosford (2013), numerous anisotropic yield functions have been proposed over the last 40 years. Particularly relevant to this work are the anisotropic Drucker (Lou and Yoon, 2018), Yld2000 (Barlat *et al.*, 2003), Yld2004 (Barlat *et al.*, 2005), Vegter (Vegter and van den Boogaard, 2006) and Hosford's 1985 "HF85" function (Hosford, 1985). With the exception of Vegter and HF85, the aforementioned yield functions extend anisotropy into existing isotropic yield functions using linear transformations. Vegter instead adopts a Bezier curve formulation while HF85 is calibrated using two uniaxial R-values R_θ and $R_{\theta+90}$ along the principal axes, where θ represents the angle from the rolling direction to the principal frame as shown in Eq. (1.20).

$$\sigma_{eq}^{HF85} = \left(\frac{R_{\theta+90}|\sigma_1|^m + R_\theta|\sigma_2|^m + R_\theta R_{\theta+90}|\sigma_1 - \sigma_2|^m}{R_{\theta+90}(1 + R_\theta)} \right)^{\frac{1}{m}} \tag{1.20}$$

Recent work shows that many engineering materials experience anisotropic hardening that can be separated into differential and distortional hardening where the yield surface expands and changes shape with plastic flow even in proportional loading. In the present work, differential hardening refers to the evolving differential in the hardening behavior between stress states such as between uniaxial and equal-biaxial tension. Distortional hardening refers to the change in the plastic potential, or yield function in associated flow, due to evolving R-values. Notable experiments by Kuwabara and collaborators have documented these hardening mechanisms in steel (Kuwabara and Ichikawa, 2015; Kuwabara and Sugawara, 2013), aluminum (Kuwabara *et al.*, 2017; Kawaguchi *et al.*, 2015) and titanium (Nagano *et al.*, 2018) using stress-controlled biaxial cruciform and tube expansion tests.

1.3.2.1 Barlat family of yield criteria

The Barlat family of yield functions applies fourth-order linear transformations upon the deviatoric stress tensor to account for anisotropy. The linear transformations scale and stretch Hosford's 1972

generalized isotropic yield function to change the yield stress and plastic normal vectors related to the yield surface curvature in associated flow. Karafillis and Boyce (1993) described these models as creating an "isotropic plasticity equivalent stress". Barlat's plane stress Yld2000 model (Barlat *et al.*, 2003) represents the equivalent yield stress based on the in-plane principal values S_1 and S_2 of two second-order tensors $\boldsymbol{S}'$ and $\boldsymbol{S}''$ as shown in Eq. (1.21).

$$\sigma_{eq}^{Yld2000} = \left(\frac{|S_1' - S_2'|^m + |2S_2'' + S_1''|^m + |2S_1'' + S_2''|^m}{2} \right)^{\frac{1}{m}} \tag{1.21}$$

Generating each of the tensors $\boldsymbol{S}'$ and $\boldsymbol{S}''$ requires a linear transformation of the Cauchy stress tensor $\boldsymbol{\sigma}$ or deviatoric stress tensor $\boldsymbol{\sigma}'$ as shown in Eq. (1.22).

$$\boldsymbol{S}' = \boldsymbol{C}' : \boldsymbol{\sigma}' = \boldsymbol{L}' : \boldsymbol{\sigma}, \qquad \boldsymbol{S}'' = \boldsymbol{C}' : \boldsymbol{\sigma}' = \boldsymbol{L}'' : \boldsymbol{\sigma} \tag{1.22}$$

The components of the transformation tensors $\boldsymbol{L}'$ and $\boldsymbol{L}''$ are obtained by calibrating eight anisotropy parameters α_{1-8} to experimental data.

$$\boldsymbol{L}' = f(\alpha_1, \alpha_2, \alpha_7), \qquad \boldsymbol{L}'' = f(\alpha_3, \alpha_4, \alpha_5, \alpha_6, \alpha_8) \tag{1.23}$$

Barlat's Yld2004 (Barlat *et al.*, 2005) function, shown in Eq. (1.24), provides greater calibration flexibility, as well as the ability to describe a three-dimensional state of stress. Like Yld2000, S_{1-3}' and S_{1-3}'' represent the principal values of two tensors $\boldsymbol{S}'$ and $\boldsymbol{S}''$obtained by applying linear transformations to the deviatoric stress as shown in Eq. (1.22).

$$\sigma_{eq}^{Yld2004} = \left(\frac{1}{4} (|S_1' - S_1''|^m + |S_1' - S_2''|^m + |S_1' - S_3''|^m + |S_2' - S_1''|^m + |S_2' - S_2''|^m + |S_2' - S_3''|^m + |S_3' - S_1''| + |S_3' - S_2''|^m + |S_3' - S_3''|^m) \right)^{\frac{1}{m}} \tag{1.24}$$

In this case, the components of the linear transformation tensors $\boldsymbol{C}'$ and $\boldsymbol{C}''$ are described by the 18 parameters in Eq. (1.25).

$$\boldsymbol{C'} = \begin{bmatrix} 0 & -C'_{12} & -C'_{13} & 0 & 0 & 0 \\ -C'_{21} & 0 & -C'_{23} & 0 & 0 & 0 \\ -C'_{31} & -C'_{32} & 0 & 0 & 0 & 0 \\ 0 & 0 & 0 & C'_{44} & 0 & 0 \\ 0 & 0 & 0 & 0 & C'_{55} & 0 \\ 0 & 0 & 0 & 0 & 0 & C'_{66} \end{bmatrix}, \boldsymbol{C''} = \begin{bmatrix} 0 & -C''_{12} & -C''_{13} & 0 & 0 & 0 \\ -C''_{21} & 0 & -C''_{23} & 0 & 0 & 0 \\ -C''_{31} & -C''_{32} & 0 & 0 & 0 & 0 \\ 0 & 0 & 0 & C''_{44} & 0 & 0 \\ 0 & 0 & 0 & 0 & C''_{55} & 0 \\ 0 & 0 & 0 & 0 & 0 & C''_{66} \end{bmatrix} \quad (1.25)$$

If the two transformation tensors are equivalent ($\boldsymbol{C'} = \boldsymbol{C''} = \boldsymbol{L^{Yld91}}$), then Barlat's Yld91 model (Barlat *et al.*, 1991) is recovered where the components of the single linear transformation tensor are functions of the six parameters shown in Eq. (1.26).

$$\boldsymbol{L^{Yld91}} = f(a, b, c, f, g, h) \quad (1.26)$$

Regardless of the choice of yield function, calibration of the anisotropy parameters typically requires numerical optimization to minimize the least squared error between the function's prediction and the experimental results obtained at a consistent amount of plastic work. The experimental data points may include yield strengths in plane strain tension (σ_1^{PST}), uniaxial tension (σ_1^{UT}), equal-biaxial tension (σ_1^{EB}) and shear $\left(\sigma_1^{SH}\right)$, theoretical constraints on the plastic flow and R-values in uniaxial (R^{UT}) and equal-biaxial tension (R^{EB}).

If a material is in a state of plane stress where $\sigma_3 = 0$, then a two-dimensional yield function like Yld2000 is suitable and thus requires only experimental data for the in-plane loading conditions. In addition to in-plane data, three-dimensional yield functions also require through-thickness data which can be difficult to acquire from a thin sheet. For instance, the linear transformation tensors of the Yld2004 yield criterion include variables C'_{55}, C'_{66}, C''_{55} and C''_{66} that require out-of-plane σ_{yz} and σ_{zx} shear stresses for calibration. In the absence of experimental data, a common recommendation is to assume isotropy in the unknown conditions and set these components equal to one. An alternative is to calibrate the out-of-plane variables to crystal plasticity "pseudo experiments" (Barlat *et al.*, 2005; Yoon *et al.*, 2006).

The yield function exponent must also be either assumed or calibrated. Commonly recommended values of the exponent are $m = 6$ for Body Centered Cubic (BCC) materials like steel and $m = 8$ for Face Centered Cubic (FCC) materials like aluminum based on the crystallographic calculations of Logan and Hosford (1980). It has since been shown that due to existing texture from sheet rolling processes, evolving texture during deformation, and microstructural interactions between phases and precipitates, the yield exponent may differ from the recommended values (Cai *et al.*, 2020; Cai *et al.*, 2016; Kuwabara *et al.*, 2017; Yanaga *et al.*, 2013). Perhaps the most immediate uncertainty in applying these recommendations is the observation that modern materials are predominantly multiphase (Aretz *et al.*, 2007), such as a dual

phase steel consisting of BCC ferrite and Body Centered Tetragonal (BCT) martensite. Therefore, treating the yield function exponent as a free variable and calibrating it to match the experimental data has been gaining acceptance within the literature.

It is worth emphasizing that the stress components in the Barlat family of yield criteria are expressed in the material frame (xx, yy, xy, etc.), although experimental tests generally align the loading direction with a principal stress direction. Therefore, before running the numerical optimization solver, it is important to rotate the stress to the material frame. For an in-plane principal, plane stress state, $\boldsymbol{\sigma}^{P,ip}$, this rotation to the material axes is:

$$\boldsymbol{\sigma}^{Material} = \boldsymbol{R}\boldsymbol{\sigma}^{P,ip}\boldsymbol{R}^{T}, \qquad \boldsymbol{R} = \begin{bmatrix} \cos\theta & -\sin\theta & 0 \\ \sin\theta & \cos\theta & 0 \\ 0 & 0 & 1 \end{bmatrix}, \qquad \boldsymbol{\sigma} = \begin{bmatrix} \sigma_{11} & \sigma_{12} & 0 \\ \sigma_{21} & \sigma_{21} & 0 \\ 0 & 0 & 0 \end{bmatrix} \tag{1.27}$$

where θ is the angle between the major principal axis and the rolling direction.

1.3.2.2 Anisotropic Drucker yield criterion

The anisotropic Drucker surface is a function of linearly transformed second ($J_2{}'$) and third ($J_3{}'$) invariants of the deviatoric stress as shown in Eq. (1.28). The resulting surface is uniquely suited for materials with larger plane strain yield strengths and high R-values.

$$\sigma_{eq}^{Anisotropic\ Drucker} = \left(J_2'^{\,3} - cJ_3'^{\,2}\right)^{\frac{1}{6}} \tag{1.28}$$

The invariants $J_2' = (\boldsymbol{S}' : \boldsymbol{S}')/2$ and $J_3' = \det \boldsymbol{S}'$ are calculated using the linearly transformed deviatoric stress $\boldsymbol{S}' = \boldsymbol{L}'\boldsymbol{\sigma}$ where $\boldsymbol{L}'$ is shown by Eq. (1.29) and c_1' to c_6' are calibrated to the experimental data.

$$\boldsymbol{L}' = \begin{bmatrix} \frac{c_2' + c_3'}{3} & -\frac{c_3'}{3} & -\frac{c_2'}{3} & 0 & 0 & 0 \\ -\frac{c_3'}{3} & \frac{c_3' + c_1'}{3} & -\frac{c_1'}{3} & 0 & 0 & 0 \\ -\frac{c_2'}{3} & -\frac{c_1'}{3} & \frac{c_1' + c_2'}{3} & 0 & 0 & 0 \\ 0 & 0 & 0 & c_4' & 0 & 0 \\ 0 & 0 & 0 & 0 & c_5' & 0 \\ 0 & 0 & 0 & 0 & 0 & c_6' \end{bmatrix} \tag{1.29}$$

The von Mises function $\sigma_{eq} = \sqrt{3J_2}$ is recovered with c = 0 and $c_1' - c_6' = \sqrt{3}$. Isotropic FCC and BCC materials are modelled using c = 2.0 and $c'_{1-6} = 1.8365$, and c = 1.226 and $c'_{1-6} = 1.7909$, respectively (Lou and Yoon, 2018).

1.3.2.3 Vegter yield criterion

In a stark contrast to linear transformation-based yield functions, the Bezier-interpolation based Vegter yield criterion (Vegter and van den Boogaard, 2006) is perhaps the most suitable plane stress yield surface if sufficient test data is available. The Vegter criterion consists of Bezier curve interpolation between reference "hinge" points located at simple shear, uniaxial tension, plane strain tension and equal-biaxial tension at multiple sheet orientations. For a particular sheet orientation, normalized principal stresses f_1 and f_2 between each of the reference points ***A*** and ***C*** are given by:

$$\begin{Bmatrix} f_1 \\ f_2 \end{Bmatrix} = \begin{Bmatrix} A_1 \\ A_2 \end{Bmatrix} + 2\mu \left[\begin{Bmatrix} B_1 \\ B_2 \end{Bmatrix} - \begin{Bmatrix} A_1 \\ A_2 \end{Bmatrix} \right] + \mu^2 \left[\begin{Bmatrix} A_1 \\ A_2 \end{Bmatrix} + \begin{Bmatrix} C_1 \\ C_2 \end{Bmatrix} - 2 \begin{Bmatrix} B_1 \\ B_2 \end{Bmatrix} \right], \qquad \mu \in [0,1] \tag{1.30}$$

Sweeping μ from 0 to 1 describes the arc of the yield surface between the reference stresses. Stitching together the curves between each pair of reference stresses defines the complete surface. Obtaining the components of the hinge point ***B*** requires the normal vectors at the reference stresses, given by $\boldsymbol{n}$ and $\boldsymbol{m}$ at stress points ***A*** and ***C***, respectively.

$$\begin{Bmatrix} B_1 \\ B_2 \end{Bmatrix} = \frac{1}{n_1 m_2 - m_1 n_2} \begin{Bmatrix} m_2(n_1 A_1 + n_2 A_2) - n_2(m_1 C_1 + m_2 C_2) \\ n_1(m_1 C_1 + m_2 C_2) - m_1(n_1 A_1 + n_2 A_2) \end{Bmatrix} \tag{1.31}$$

Interpolation of the reference points between sheet orientations is provided through a Fourier series written as:

$$f^k(\theta) = \sum_{m=0}^{n} \phi_m^k \cos 2m\theta \,, k \in \{PST, UT, Sh\} \tag{1.32}$$

where n is equal to the number of orientations tested in a particular stress state. The strain ratio (ρ) in uniaxial tension and each direction are similarly interpolated as:

$$\rho_{UT} = \sum_{m=0}^{n} \gamma_m \cos 2m\theta \tag{1.33}$$

The coefficients of the Fourier series ϕ_m and γ_m are obtained by simultaneously solving the system of equations represented by the series. For instance, for plane strain tension (PST) in three directions, the Fourier coefficients are obtained from:

$$\begin{Bmatrix} \phi_0^{PST} \\ \phi_1^{PST} \\ \phi_2^{PST} \end{Bmatrix} = \begin{bmatrix} 1 & 1 & 1 \\ 1 & 0 & -1 \\ 1 & -1 & 1 \end{bmatrix}^{-1} \begin{Bmatrix} f_0^{PST}(0°) \\ f_1^{PST}(45°) \\ f_2^{PST}(90°) \end{Bmatrix} \tag{1.34}$$

1.3.3 Flow Rule

The flow rule relates the incremental plastic strain components to a plastic potential function ψ shown in Eq (1.35) through a scalar multiplier $d\lambda$.

$$d\varepsilon_{ij}^{P} = d\lambda \frac{\partial \psi}{\partial \sigma_{ij}} \tag{1.35}$$

The use of the gradient operator enforces coincidence of the yield surface outward normal vectors and the direction of the plastic strain increment (the so-called Normality Principle). In three-dimensional stress space, the result is a second-order tensor, but in principal stress space, the result is a vector easily visualized in Figure 4.

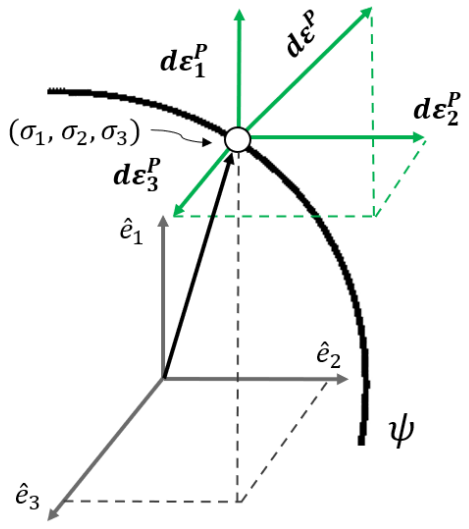

Figure 4: Physical meaning of the Normality Principle.

The plastic potential function may be set equal to the yield function ($\psi = \sigma_{eq}$), called the associated flow rule (AFR), or equal to a different function altogether ($\psi \neq \sigma_{eq}$), called the non-associated flow rule (NAFR). It is common to adopt the same functional form for the plastic potential as the yield function but

calibrate each to separate experimental data in the NAFR case (Lademo *et al.*, 1999). The yield function is responsible only for predicting the magnitude of the stress at each loading state that will cause yielding and thus calibrated to only the stress-based experimental data (i.e., tensile stresses, plane strain stress, shear stress, equal-biaxial stress, etc.). The plastic potential predicts the direction of the strain increments and is calibrated to the strain-based experimental data (i.e., tensile R-values, equal-biaxial R-values and physical constraints that apply at each state of generalized plane strain) as discussed in Section 1.3. Despite the increasing popularity of non-associated models, Pucik *et al.* (2015) argue that numerous instabilities are inherent to non-associated formulations including artificial softening (Rudnicki and Rice, 1975) and dynamic stiffening of the plastic modulus in excess of the elastic modulus (Sandler and Rubin, 1987). In opposition, Stoughton and Yoon (2008) assert that these issues are resolved. Ultimately adopting the AFR simplifies the analysis by calibrating only one function to the entirety of the stress and strain experimental data, while ensuring numerical stability and uniqueness of the solution.

1.4 Objectives and Motivations of Current Work

Tremendous improvements to the characterization of anisotropic sheet metal have occurred to meet the demands of the automotive sector over the last century. Phenomenological plasticity has provided a mathematical framework to evaluate yielding, while advancements in experimental techniques like Digital Image Correlation have enabled the calibration of anisotropic yield functions under increasingly diverse experimental stress states.

However, characterization in states of generalized plane strain, defined by a state of shear or plane strain tension that results in zero strain along one principal direction, remains an open area of research. Figure 5 shows the three generalized plane strain stress states and the corresponding experimental tests that activate each state. In all cases, loading along the *x*-axis of the material generates a plane strain state where the second principal strain is zero, as shown in the three-dimensional Mohr's circle representation. In plane strain tension, the strain along the *y*-axis is negligible due to the relatively large width of the specimen in comparison to the thin sheet thickness. Shear tests produce a simple shear state in the gauge region between the two notches, with the principal directions orientated along $\pm 45°$ from the axis of loading. For in-plane shear, no strain occurs through the thickness while for through-thickness shear, no strain occurs through the width.

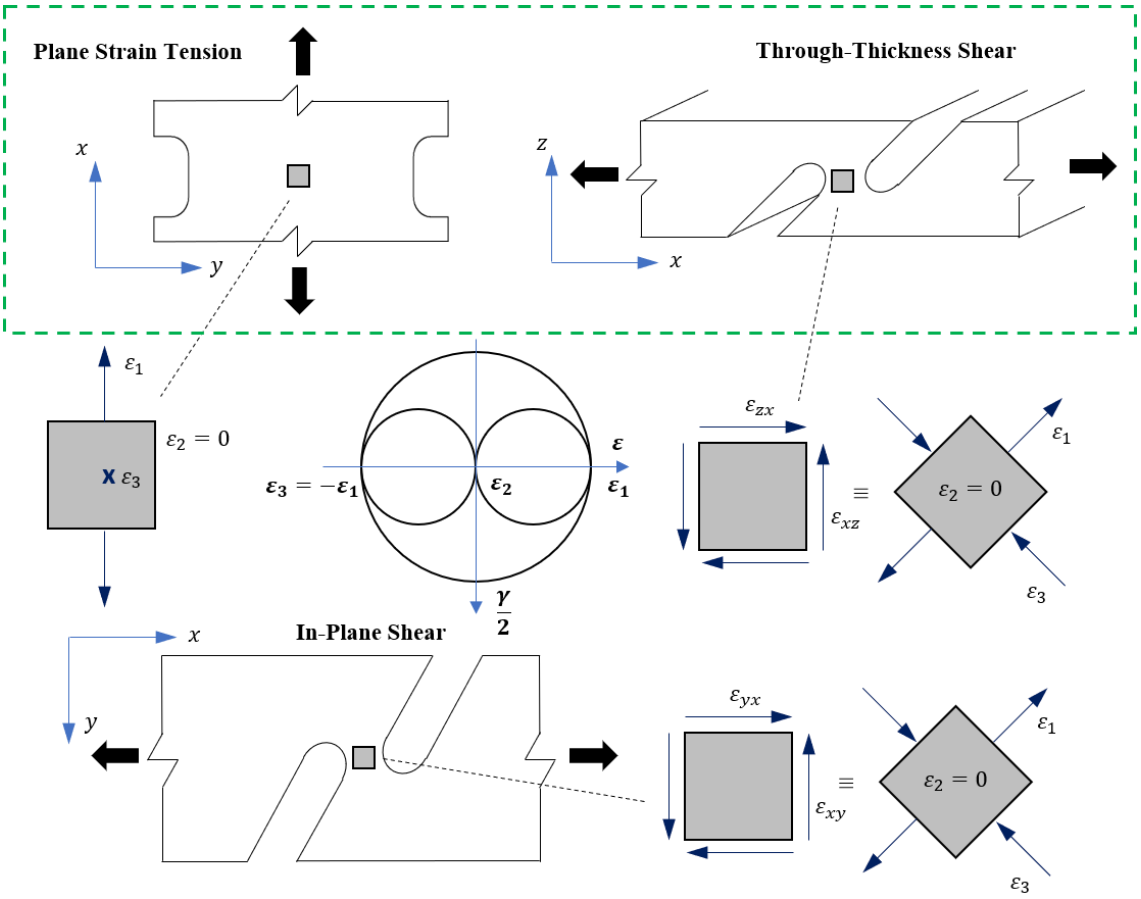

Figure 5: Mohr's circle visualization of states of generalized plane strain in terms of ordered principal strains $\varepsilon_1 > \varepsilon_2 > \varepsilon_3$. Consider two specimens tested in the loading direction along the x-axis; in plane strain tension, ε_1 is in the loading direction, ε_3 is in the through-thickness direction and ε_2 is in-plane and 90° to the loading direction. In through-thickness shear, ε_1 and ε_3 are in-plane and $\pm$45° to the loading axis, while ε_2 is out-of-plane along the specimen width. Plane strain tension and through-thickness shear are the focus of the investigation in this work.

A state of plane strain tension is not only common in industrial sheet metal forming operations but also the loading condition in which sheet metal failure generally occurs. A typical sheet metal blank is long relative to its thickness and width. The geometric constraint afforded by the larger planar dimension results in plane strain tension as the material can deform only along the other dimensions during stretching and bending operations. Plane strain shows the minimum strain on a forming limit diagram, making affected areas of a part most susceptible to failure. Plane strain is, in fact, central to necking itself as any uniaxial or biaxial stress state will gradually shift toward plane strain tension as deformation concentrates through the thickness (Berstad *et al.*, 2004).

Through-thickness shear (TTS) is also common to a variety of forming, and impact processes. Incremental forming, an advanced manufacturing process, can achieve higher forming strains than conventional operations by utilizing through-thickness shear and normal stresses to deform a part into its final shape by a series of small, successive indentations (Eyckens *et al.*, 2009; Esmaeilpour *et al.*, 2018). In

more conventional operations, sheet bending introduces TTS (Li *et al.*, 2018), whether it be at the folds of an automotive structural rail during axial crush or the draw beads of a stamping die. General friction between a die and a sheet during stamping is another source of TTS as noted by Fatemi and Dariani (2016).

Generating an accurate and complete model for stamping and incremental forming operations requires characterization of material behavior under through-thickness shear. Particularly for dual phase steel, Billur and Altan (2013), and Li *et al.* (2018) pointed to through-thickness shear as a possible explanation for fractures observed in bending operations. Even though three-dimensional yield functions like Yld2004 are available for solid element simulations, sheet metal forming processes are commonly simplified as plane stress, both for simplicity and due to the lack of accurate through-thickness experimental data. Simple methods for physical, experimental characterization of through-thickness shear are necessary for the improvement of industrial sheet metal forming processes.

Although in-plane shear tests are now commonplace (Peirs *et al.*, 2012; Yin *et al.*, 2014; Abedini *et al.*, 2020), experimental characterization of through-thickness shear yield strength has received comparatively little attention. In a notable exception, Herrmann *et al.* (2017) evaluated the through-thickness shear strength of a roll-bonded aluminum using a double notched shear specimen and a clamping fixture to prevent buckling under a compressive load. Other studies have been limited to only fracture and not constitutive characterization. For instance, Li *et al*. (2018) and Gu *et al*. (2020) evaluated the through-thickness shear fracture strain of dual phase sheets, with a novel test fixture bolted to the specimen that minimized friction while preventing rotation of the shear zone under tension.

To the author's knowledge, no study has attempted to calibrate the out-of-plane shear properties of a function like Yld2004 using physical experiments. Attempts to calibrate the out-of-plane properties of three-dimensional yield functions have mainly been through crystal plasticity pseudo experiments (Plunkett *et al.*, 2006; Grytten *et al.*, 2008; Barlat *et al.*, 2005; Zhang *et al.*, 2016; Esmaeilpour *et al.*, 2018). However, crystal plasticity models are either computationally demanding (Zhang *et al.*, 2016) or too simplistic to accurately describe a real material (Grytten *et al.*, 2008). Furthermore, crystal plasticity models rely on precise microstructural characterization using scanning electron microscopy (Zhang *et al.*, 2016) which is an expensive barrier to widespread industrial adoption.

In contrast to through-thickness shear, experimental testing in plane strain tension is more mature, albeit far from resolved. Plane strain conditions only exist in the center of the notched tensile specimen seen in Figure 5 because the loading transitions toward a state of uniaxial tension at each edge. Suggested methods to extract the constitutive plane strain tensile response generally encompass either correction factors assuming isotropy, inverse finite-element analysis, or empirical relationships. Due to the experimental

uncertainty, the plane strain yield strength is often omitted in the calibration of anisotropic yield functions despite its fundamental relationship with necking and the mechanics of thin sheet forming. Simply adopting the recommended exponent for the yield function, based on whether the material is FCC or BCC, does not guarantee accuracy of the interpolated plane strain yield strength (Lenzen and Merklein, 2018). Therefore, a need also exists for a more accurate, physically based experimental methodology to directly extract the constitutive response from plane strain tensile tests while including effects of anisotropy.

The objectives of this thesis are as follows:

1. Introduce, validate, and apply an experimental methodology to characterize the constitutive response along the arc of the yield surface from uniaxial to plane strain tension using plane strain tensile tests.
2. Design, test and evaluate an experimental setup to characterize the constitutive response of a sheet material in through-thickness shear.
3. Incorporate plane strain tensile and through-thickness shear yield strengths into the calibration of anisotropic yield functions.

The remaining eight chapters of this thesis attempt to achieve these objectives. Chapter 2 introduces the four materials selected for analysis, summarizes the basic constitutive characterization completed prior to this research and describes the experimental equipment used in this work. Chapter 3 is an adaptation of a journal article entitled “An Experimental Methodology to Characterize the Plasticity of Sheet Metals from Uniaxial to Plane Strain Tension” written by the author, Dr. Abedini, Ms. Noder and Dr. Butcher. In Chapter 3, further background on plane strain tension is presented as well as a combined experimental-analytical methodology to characterize the complete arc of a yield surface from uniaxial to plane strain tension. Chapter 4 investigates the effect of geometry and extends the plane strain tension methodology developed in Chapter 3 to differential hardening and non-associated flow. Chapter 5 describes the results of finite-element coupon level simulations used to evaluate the accuracy of the results of Chapter 3–4. Chapter 5 also demonstrates the improvement of the current process versus an existing empirical method found in the literature. Chapter 6 focuses on the characterization of yielding in through-thickness shear, encompassing specimen geometry selection, fixture design, DIC pattern generation, experimental testing, and results. Chapter 7 consolidates the work of the previous chapters into the generation of master yield surfaces to quantify the effect of the additional plane strain tension and through-thickness shear data points on the calibration. These master yield surfaces are validated using post-necking simulations of a different notch geometry in Chapter 8. Chapters 9 and 10 conclude with the main findings of this thesis and recommendations for future work.

Chapter 2 Material Selection, Mechanical Properties, Equipment and Test Geometries

The test geometries, materials and baseline mechanical properties are described in this chapter. Section 2.1 describes the seven geometries adopted to obtain the constitutive characterization in states of shear, plane strain tension, uniaxial tension, and equal-biaxial tension. Section 2.2 describes the four disparate automotive sheet alloys selected to illustrate the generalized plane strain characterization methods proposed in this thesis: AA5182-O, DP1180, AA6xxx-T4 and AA6xxx-T81.

2.1 Equipment and Test Geometries

In addition to the through-thickness shear and plane strain tests conducted in direct pursuit of this thesis, uniaxial tensile, shear and equal-biaxial tests were required to provide baseline mechanical properties to support further investigations into generalized plane strain. All uniaxial tensile, shear, through-thickness shear and plane strain experiments were conducted on either the *MTS E40 Criterion* 100 kN servo-electric testing machine with hydraulic grips or the *Shimadzu AG-X plus* 50 kN servo-electric uniaxial test frame with pneumatic grips available at the University of Waterloo. In all cases, the load cell data from the test frame was synchronized with a Digital Image Correlation (DIC) full-field optical strain measurement system. Post-processing was performed in the software Vic-3D 8® by Correlated Solutions Inc. for the uniaxial tensile and plane strain tensile tests. Due to the lack of through-thickness deformation in shear tests, Vic-2D 6® by Correlated Solutions Inc. was used for the post-processing of the in-plane and through-thickness shear tests. VSGL values of between 0.1 mm and 1 mm were selected, based on the specimen size, processing speed and degree of observed localization. A VSGL of 0.5 mm was selected for the entirety of the plane strain analysis to allow consistent comparison of different geometries. The test geometries are described in Figure 6 and explained further in this section.

(a) **Uniaxial tensile specimen (JIS No. 5)**

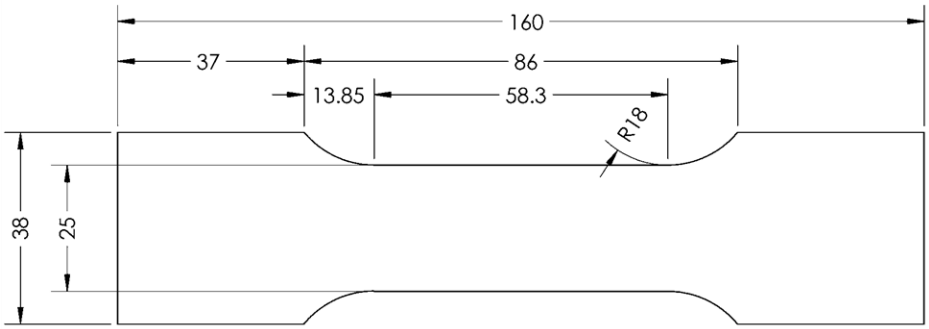

(b) **In-plane shear specimen (Mini Shear) from Piers *et al.*** (2012)

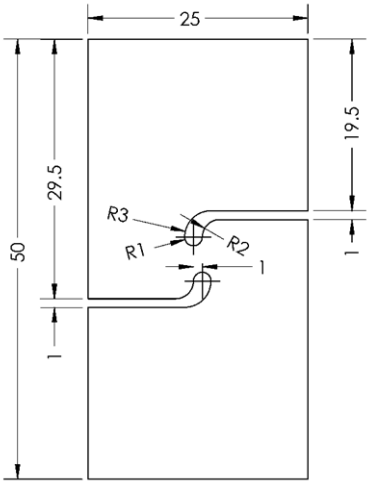

(c) **Through-thickness shear specimen adapted from Gu *et al.* (2020)**

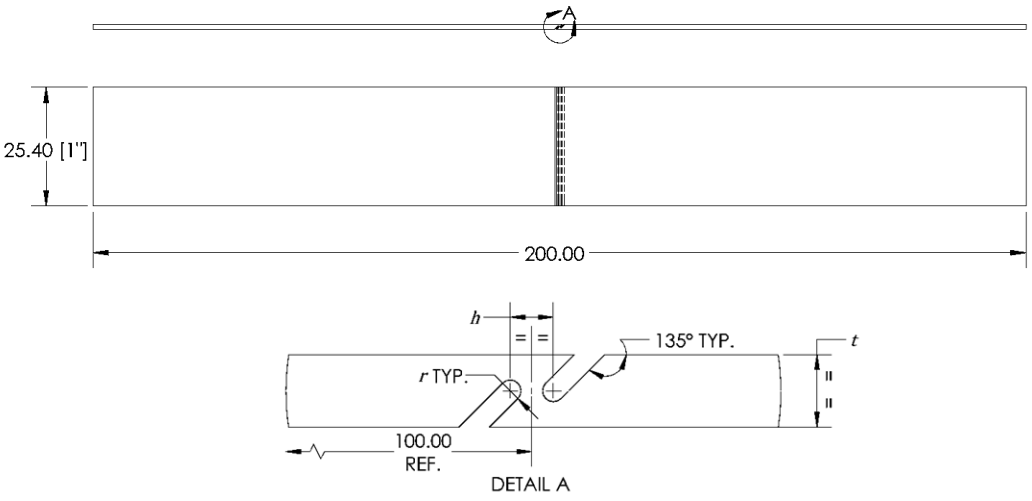

(d) **Plane strain tension specimen (Geometry A) adapted from Vegter and van den Boogaard** (2006)

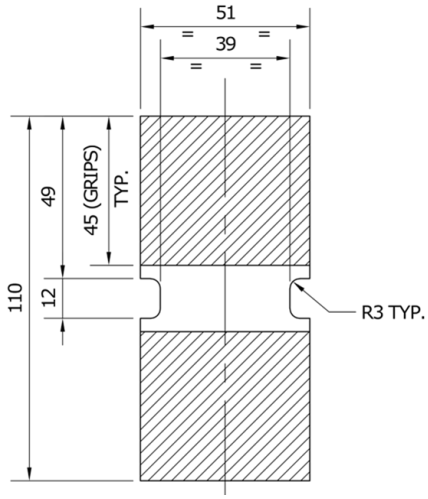

(e) **Plane strain tension specimen (Geometry B)**

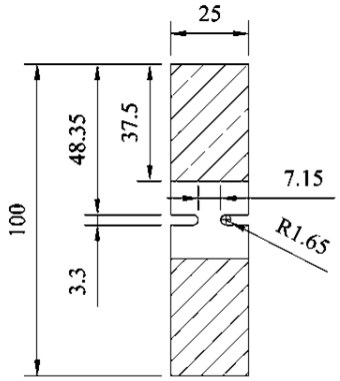

(f) **Plane strain tension specimen (Triple-Scaled Geometry B)**

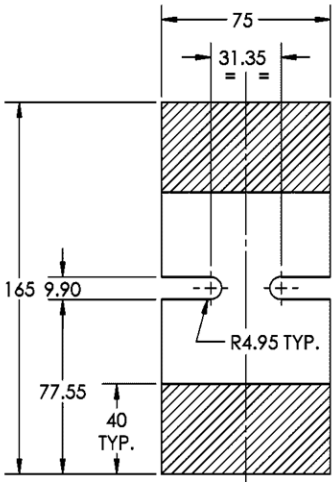

Figure 6: Specimen geometries adopted in this thesis. The loading conditions include (a) uniaxial tension, (b) in-plane shear, (c) through-thickness shear and (d, e, f) plane strain tension.

2.1.1 Disc Compression Tests

Disc compression tests were performed as part of the baseline characterization to establish the equal-biaxial R-value, as explained by Abedini *et al.* (2020). A 5-mm disc was compressed between two Teflon-lubricated dies, and the deformation along the rolling and transverse directions measured using an optical microscope at discrete load levels. The ratio of the true strain along the transverse direction to the true strain along the rolling direction was then calculated to determine the average R-value over the range of deformation.

2.1.2 Uniaxial Tensile Tests

Uniaxial tensile tests were used to determine the hardening curve, normalized yield strength and uniaxial R-value as well as the elastic parameters Young's Modulus and Poisson's ratio. JIS No. 5 specimens were adopted as shown in Figure 6(a). The longitudinal extension was measured using the average of three 50 mm long extensometers, while the transverse contraction was measured using the average of three 25 mm long extensometers. The R-value was obtained from the horizontal and vertical extensometers, considering volume conservation. All samples were pulled at a speed of 0.05 mm/s to maintain a quasi-static strain rate of 0.001 s^{-1} over the gauge region.

2.1.3 In-Plane Shear Tests

In-plane shear tests were conducted using the so-called "mini shear" geometry proposed by Piers *et al.* (2012) and shown in Figure 6(b). The use of eccentric notches promotes a state of simple shear in the gauge region, while the rounded notches and gauge region length are designed to improve accuracy and promote a more homogeneous state of strain across the gauge region. A test velocity of 0.003 mm/s ensured an equivalent von Mises quasi-static strain rate of 0.001 s^{-1} in the center of the gauge region. The shear stress was measured as the average load acting over the gauge region area, $\tau = F/A$.

2.1.4 Through-Thickness Shear Tests

The double-notched geometry proposed by Gu *et al*. (2020) was selected for through-thickness shear investigation since the use of two notches angled at 45° to the loading direction is analogous to the well-accepted ASTM B831-05 standard geometry for in-plane shear tests. It is also readily tested in a standard uniaxial test frame. The specimen width was increased from the originally proposed 10 mm to 25.4 mm to better promote plane strain conditions. The sample length was also extended to 200 mm to suit an existing clamping fixture under development at the University of Waterloo for tension-compression testing and modified in this work to provide the side clamping force required to minimize gauge region rotation. The

final specimen geometry is shown in Figure 6(c). Due to the novelty of the through-thickness shear tests, additional information on the experimental design is provided in Chapter 6.

2.1.5 Plain Strain Tensile Tests

A comprehensive investigation was performed into different plane strain notch geometries in the literature before selecting the specimens for analysis in this thesis. The profile of plane strain tension is controlled by two variables: the specimen width-to-thickness ratio and shape of the notches. As determined by An *et al.* (2004), specimens with a large aspect ratio (width-to-thickness ratio) promote more uniform plane-strain conditions across the sample width. Baral *et al.* (2018) propose through-thickness machining as a means of increasing the aspect ratio of notch specimens. Round notches combined with a small aspect ratio notch help promote a plane-strain fracture in the center of the specimen, although with only a small zone of plane strain that is difficult to measure. A larger aspect ratio and square-profile notches increase the size of the plane strain zone, but fracture instead occurs at the notches under uniaxial tension, rather than in the specimen gauge region under plane strain (Mahmudi, 1999).

Larger aspect ratio specimens are more conducive to DIC measurement. As explained by Byrne and Simonsen (2016), a minimum half-subset width of strain data at each edge cannot be calculated using DIC algorithms since strain data is always reported at the center point of each subset. The missing edge data may be minimized by adopting a smaller subset, although this approach is limited by the size of speckles required to maintain the recommended three-speckle density per subset. Therefore, as the sample width increases, the missing edge data makes up a smaller percentage of the overall gauge width and increases the completeness of the measured strain profile.

Three distinct specimen geometries were adopted to investigate the effect of specimen aspect ratio on the methodologies proposed in this thesis. Geometry A, shown in Figure 6(d), was adapted from the work of Vegter and van den Boogaard (2006), but with the gauge width reduced from 45 mm to 39 mm to match the grip width of the MTS E40 Criterion testing machine. In a stark contrast to the large aspect ratio of Geometry A, Geometry B was proposed by Honda R&D Americas and is uniquely suited to fracture characterization due its small aspect ratio and round notches. In a hybrid approach to develop a specimen for both fracture and constitutive characterization, a triple-scaled version of Geometry B was considered to incorporate both round notches and a large aspect ratio. The original and triple scaled Geometry B specimens are shown Figure 6(e) and Figure 6(f), respectively.

Each specimen geometry was CNC machined and tested to fracture in the rolling, diagonal, and transverse directions of each sheet. Crosshead velocities of 0.012 mm/s, 0.005 mm/s and 0.015 mm/s were selected to maintain a quasi-static strain rate for Geometry A, Geometry B, and the triple-scaled Geometry

B, respectively. Two 5 MP Point Grey® or two 12 MP Flir Systems® cameras with 180 mm or 85 mm Tamron® lenses were adopted for DIC measurement, depending on the size of the specimen.

2.2 Mechanical Properties of Selected Materials

To illustrate that the developed processes and methodologies are applicable to various materials, four different alloys were selected: AA6xxx-T4 (FCC), AA6xxx-T81 (FCC), DP1180 (BCC) and AA5182-O (FCC). The chemistry and microstructural information are intentionally withheld from this thesis, to instead focus on the mechanical performance and characterization. The two 6xxx series aluminum alloys were provided as part of the Numisheet 2022 benchmark activity at the University of Waterloo. Basic constitutive characterization results obtained from the slate of in-plane shear, uniaxial tension and disc compression tests are presented in this section and used in the development of the novel works presented in subsequent chapters. All properties are presented, at minimum, along the rolling (RD), diagonal (DD) and transverse (TD) directions.

2.2.1 Properties of AA6xxx-T4

Alloys of the wrought aluminum 6000 series contain magnesium and silicon as the dominant alloying elements. This series can be heat treated to form precipitates of magnesium silicide. In this case, the T4 temper designation signifies that the material has been naturally aged. A typical automotive application is an outer body panel requiring higher strength for structural integrity and dent resistance.

Amir Zhumagulov completed the tensile and mini shear experiments of the 1.5 mm thick sheet while Dr. Cliff Butcher analyzed the data to extract the stress ratios, R-values, elastic parameters, and hardening curve. Since the Modified Hockett Sherby hardening model of Eq. (1.11) could not capture the small-strain response of the materials, constrained cubic splines were employed to accurately model the equivalent stress up to uniform elongation. The equal-biaxial R-value and yield strength were estimated using the correlations developed by Abspoel *et al.* (2017) since no cruciform, bulge or disc compression data was available. The constitutive parameters and hardening curves are shown in Table 1 and Figure 7, respectively.

Table 1: Anisotropic constitutive characterization results for AA6xxx-T4 at a plastic work of 58 MJ/m^3. The equal-biaxial stress and R-value were estimated using the correlations identified by Abspoel *et al.* (2017). Standard deviations are shown in brackets.

	Angle with respect to the rolling direction (RD)							
	0°	15°	22.5°	30°	45°	60°	75°	90°
$\sigma_\theta^{UT}/\sigma_0$	1.000 (0.002)	0.996 (0.003)	-	0.986 (0.003)	0.975 (0.005)	0.992 (0.003)	0.986 (0.005)	0.980 (0.003)
R_θ^{UT}	0.600 (0.050)	0.690 (0.020)	-	0.760 (0.030)	0.730 (0.020)	0.720 (0.020)	0.650 (0.020)	0.610 (0.030)
$\sigma_\theta^{SH}/\sigma_0$	0.564 (0.007)	-	0.559 (0.009)	-	0.560 (0.006)	-	-	-
E (GPa)	70.4	-	-	-	69.7	-	-	71.4
ε_t^{UE}	0.199	-	-	-	0.215	-	-	0.207
ν	0.33							
σ_b/σ_0	0.975							
R_b	0.984							

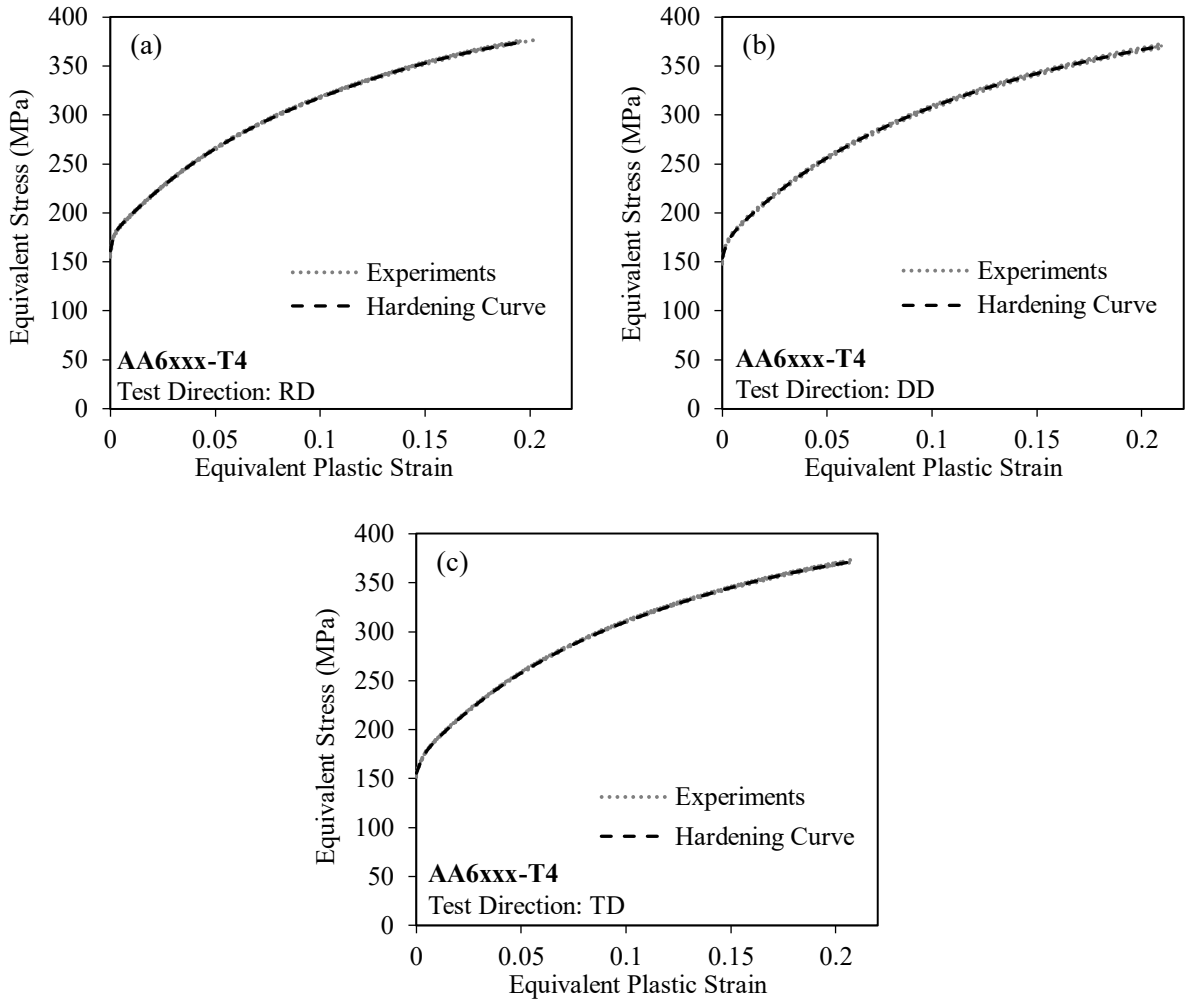

Figure 7: Spline hardening curves fit to the experimental uniaxial tensile data along the (a) RD (b) DD and (c) TD of the tested AA6xxx-T4. Experimental data is shown up to the onset of necking.

The average uniaxial R-value in Table 1 was obtained from the linear region of the plastic width versus thickness strain distribution in each tested direction. Figure 8 illustrates the strain path obtained by adopting the average R-value, in comparison to each of the experimental repeats along the RD, DD and TD. The average R-value is a reasonable assumption across the entire range of plastic deformation and in good agreement with the experimental data for the three material orientations considered in the plane strain integration methodology.

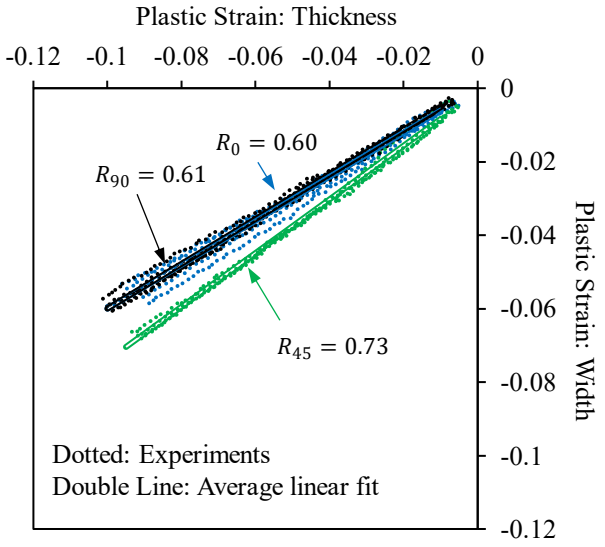

Figure 8: Average uniaxial R-value along the RD, DD and TD compared to the experimental data for each repeat of AA6xxx-T4.

2.2.2 Properties of AA6xxx-T81

The 2.7 mm thick sheet of 6000 series structural aluminum in the T81 temper has been solutionized, artificially aged to form precipitates and then cold worked. The presence of both precipitation hardening and work hardening gives this alloy additional strength over the T4 alloy. Although this alloy is in the 6000 series, it is compositionally different than the AA6xxx-T4 material and designed for structural applications such as rails and B-pillars.

As with the AA6xxx-T4 alloy, Amir Zhumagulov completed the experimental testing and Dr. Cliff Butcher performed the extraction of the stress ratios, R-values, elastic parameters, and hardening curve. The baseline constitutive characterization is presented in Table 2, with the calibrated hardening curves presented against the experimental uniaxial tensile test data in Figure 16.

Table 2: Anisotropic constitutive characterization results for AA6xxx-T81 at a plastic work of 59 MJ/m^3. The equal-biaxial stress and R-value were estimated using the correlations identified by Abspoel *et al.* (2017). Standard deviations are shown in brackets.

	Angle with respect to the rolling direction (RD)							
	0°	15°	22.5°	30°	45°	60°	75°	90°
$\sigma_\theta^{UT}/\sigma_0$	1.000 (0.006)	0.995 (0.006)	-	0.985 (0.007)	0.987 (0.007)	0.984 (0.007)	0.979 (0.006)	0.991 (0.006)
R_θ^{UT}	0.580 (0.020)	0.640 (0.030)	-	0.580 (0.020)	0.570 (0.040)	0.570 (0.020)	0.510 (0.020)	0.470 (0.040)
$\sigma_\theta^{SH}/\sigma_0$	0.589 (0.008)	-	0.569 (0.010)	-	0.578 (0.006)	-	-	-
E (GPa)	70.6	-	-	-	69.7	-	-	69.3
ε_t^{UE}	0.174	-	-	-	0.174	-	-	0.182
ν	0.33							
σ_b/σ_0	0.977							
R_b	1.234							

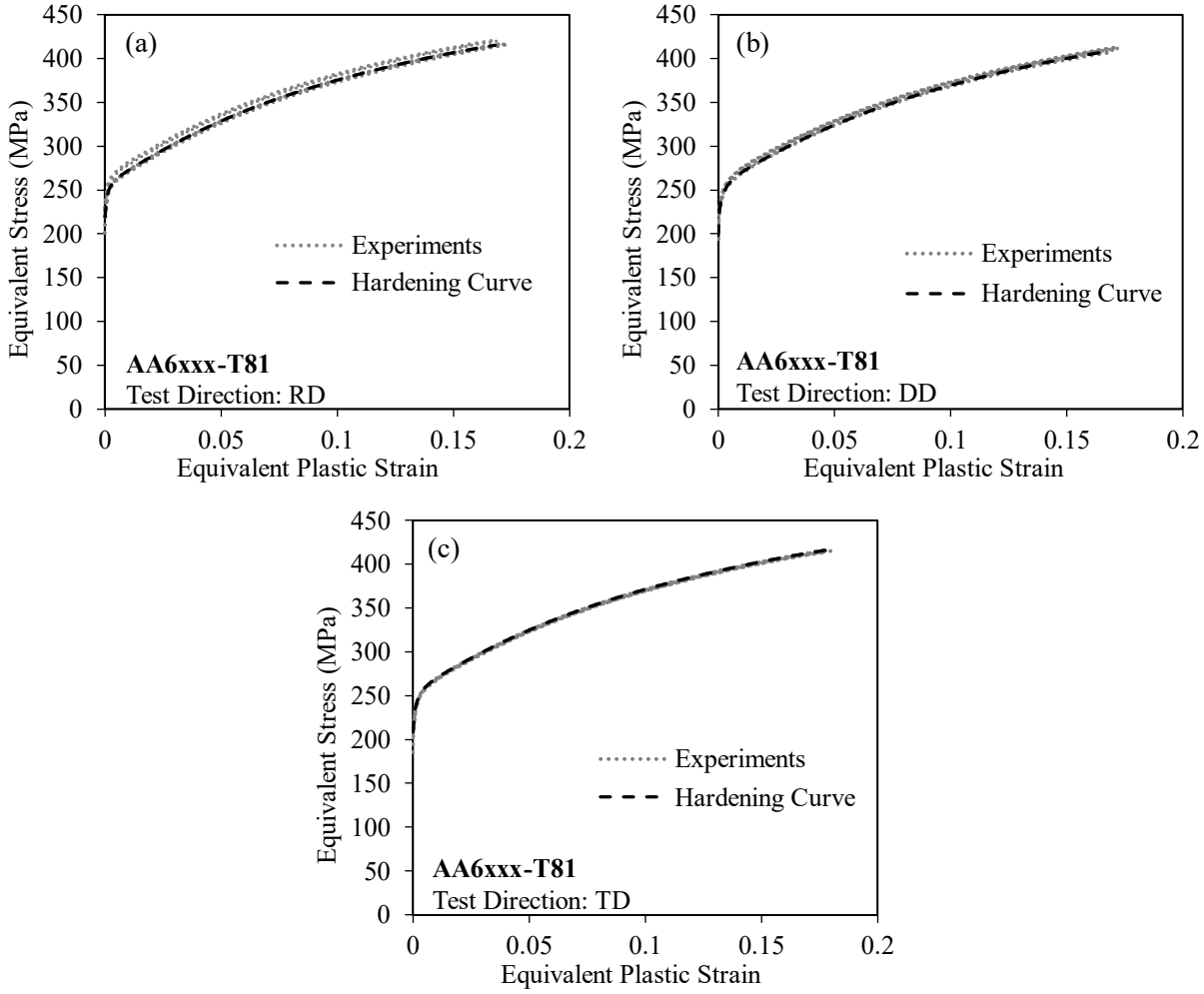

Figure 9: Comparison of spline hardening curves fit to the experimental uniaxial tensile data along the (a) RD (b) DD and (c) TD of the tested AA6xxx-T81. Experimental data is shown up to the onset of necking.

The average R-value is representative of the plastic width versus thickness strain response for AA6xxx-T81 as shown in Figure 10 along the RD, DD, and TD. The R-value is similar along the RD and DD, with a lower value occurring along the TD.

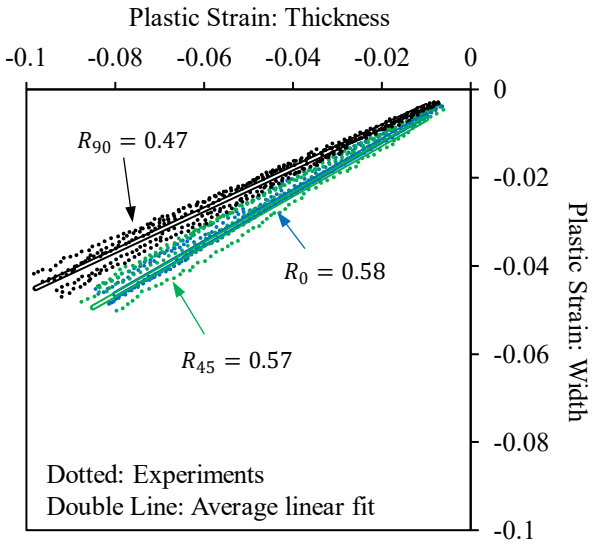

Figure 10: Average uniaxial R-value along the RD, DD and TD compared to the experimental data for each repeat of AA6xxx-T81.

2.2.3 Properties of DP1180

DP1180 is a structural dual-phase steel, with a microstructure of ferrite and martensite having an ultimate tensile strength of 1180 MPa and relatively low ductility. Common uses for DP1180 steels are in anti-intrusion applications such as sills, front side, and roof members (Davies, 2012). The 1.0 mm thick DP1180 sheet was provided by the Auto-Steel Partnership (A/SP) also as part of the Numisheet 2022 benchmark. Abedini *et al.* (2020) determined the basic mechanical properties and anisotropy. Uniaxial tension tests, simple shear tests, and disc compression tests were conducted to obtain the normalized stresses, tensile R-values and equal-biaxial R-values shown in Table 3.

Table 3: Anisotropic constitutive characterization results for DP1180 as presented by Abedini *et al*. (2020) for the same lot of material. The equal-biaxial stress was estimated as the in-plane average of the uniaxial tensile stresses. The equal-biaxial R-value was determined using a disc compression test. All values were calculated at a plastic work of 61.11 MJ/m^3. Sample standard deviations are shown in brackets.

	Angle with respect to the rolling direction (RD)							
	0°	15°	22.5°	30°	45°	60°	75°	90°
$\sigma_\theta^{UT}/\sigma_0$	1.000 (0.006)	0.995 (0.003)	-	0.996 (0.003)	1.004 (0.007)	1.008 (0.008)	1.013 (0.003)	1.025 (0.007)
R_θ^{UT}	0.82 (0.01)	0.84 (0.01)	-	0.90 (0.01)	0.95 (0.01)	0.98 (0.01)	1.00 (0.00)	0.98 (0.01)
$\sigma_\theta^{SH}/\sigma_0$	0.600 (0.005)	-	0.600 (0.008)	-	0.612 (0.005)	-	-	-
ε_t^{UE}	0.069	-	-	-	0.064	-	-	0.063
ν	0.30							
E (GPa)	210							
σ_b/σ_0	1.008							
R_b	0.94 (0.03)							

The hardening behavior for the rolling (RD), transverse (TD) and diagonal (DD) directions was described using the flexible modified Hockett-Sherby (MHS) model of Noder and Butcher (2019) previously presented in Eq. (1.11). Since the model well described the experimental data, the spline fit model adopted for the AA6xxx alloys was unnecessary. The coefficients C_1-C_5 were calibrated to the experimental data from standard uniaxial tension tests shown in Figure 11 up to the start of diffuse necking.

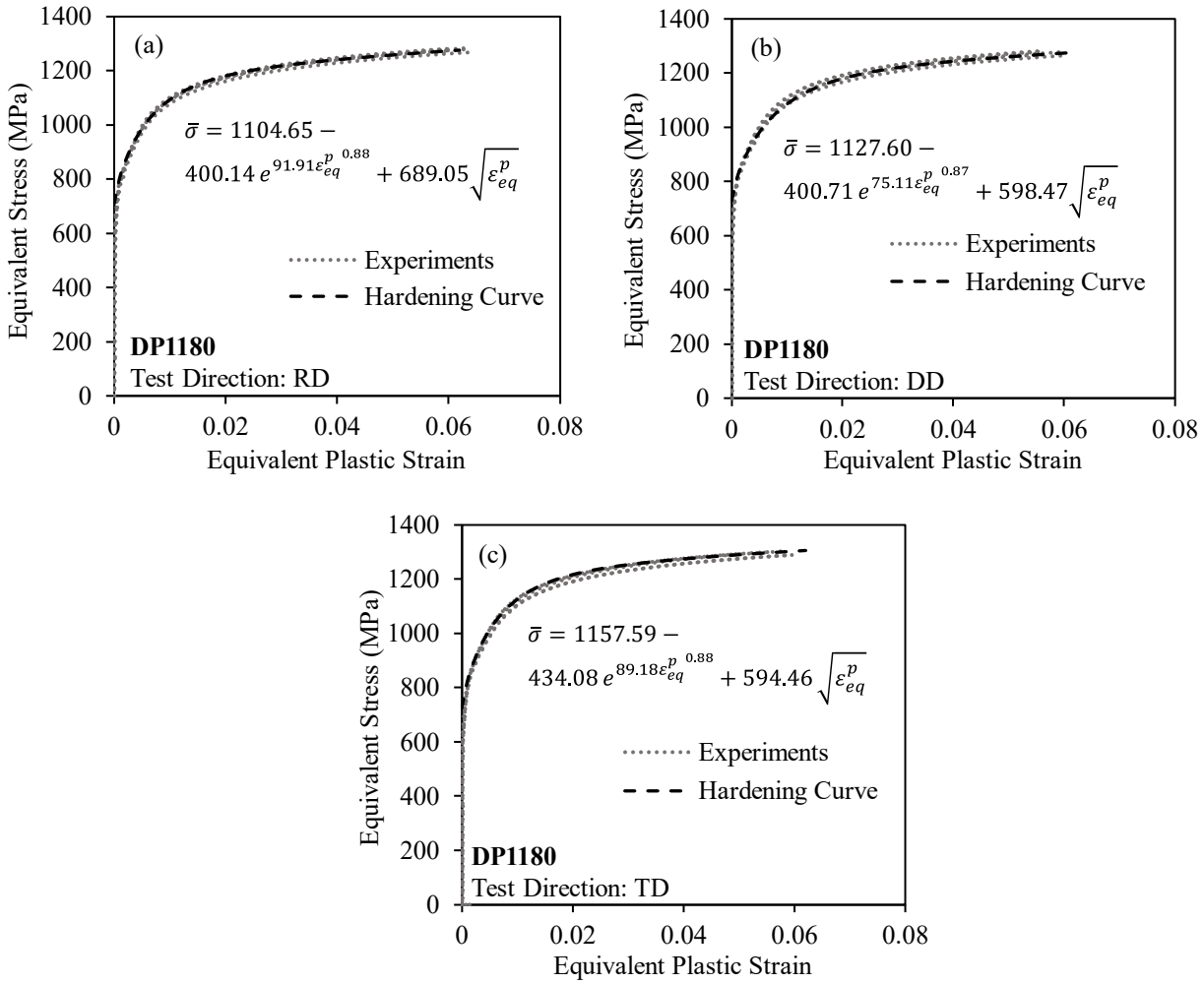

Figure 11: Modified Hockett-Sherby hardening curve fit to experimental data from standard uniaxial tension tests for DP1180 tested along the (a) RD, (b) DD and (c) TD.

The high average R-values in Figure 12 indicates good overall formability and relative agreement with an isotropic value of 1. It should be noted that the linear range of strain for DP1180 is relatively small, due to the limited ductility evidenced by an ultimate tensile strain of just 0.063 to 0.069.

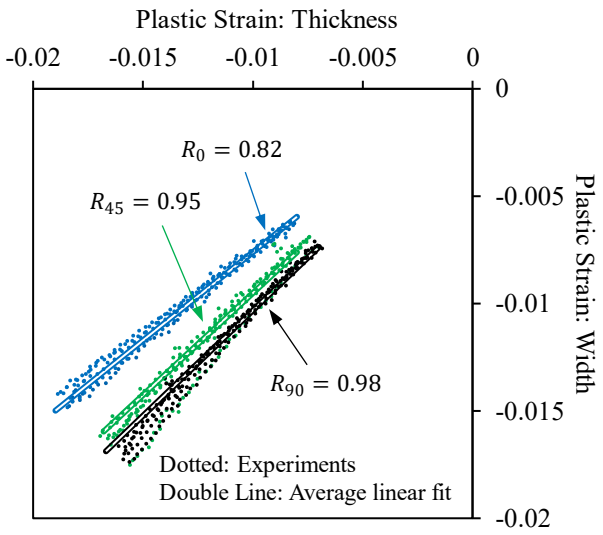

Figure 12: Average uniaxial R-value along the RD, DD and TD compared to the experimental data for each repeat of DP1180.

2.2.4 Properties of AA5182-O

The 5000 series of aluminum is composed of grades having magnesium as the main alloying element. The O temper indicates that annealing was used to eliminate residual stresses and work hardening introduced by the cold rolling process. As a result, the material possesses high ductility but relatively low strength with dynamic strain ageing (DSA) and PLC effects that make it most appropriate for inner closure panels requiring lower surface quality (Davies, 2012).

The basic constitutive characterization data for the 1.5 mm thick sheet material tested in this study are shown in Table 4, as reported by Abedini *et al.* (2020). Based on the excellent fit to the experimental data, the Modified Hockett Sherby model was adopted for the hardening curves shown in Figure 13. Increased scatter in the experimental data is due to the PLC effect.

Table 4: Anisotropic constitutive characterization results for AA5182-O as presented by Abedini *et al*. (2020) for the same lot of material. The equal-biaxial stress was estimated as the in-plane average of the uniaxial tensile stresses. The equal-biaxial R-value was determined using a disc compression test. All values were calculated at a plastic work of 51.50 MJ/m^3. Sample standard deviations are shown in brackets.

	Angle with respect to the rolling direction (RD)							
	0°	15°	22.5°	30°	45°	60°	75°	90°
$\sigma_\theta^{UT}/\sigma_0$	1.000 (0.010)	0.972 (0.003)	-	0.960 (0.002)	0.948 (0.005)	0.935 (0.010)	0.945 (0.004)	0.964 (0.000)
R_θ^{UT}	0.60 (0.04)	0.67 (0.02)	-	0.80 (0.01)	0.91 (0.02)	0.83 (0.01)	0.71 (0.01)	0.70 (0.01)
$\sigma_\theta^{SH}/\sigma_0$	0.540 (0.010)	-	0.517 (0.009)	-	0.540 (0.007)	-	-	-
ε_t^{UE}	0.187	-	-	-	0.251	-	-	0.231
ν	0.33							
E (GPa)	69							
σ_b/σ_0	0.965							
R_b	1.03 (0.03)							

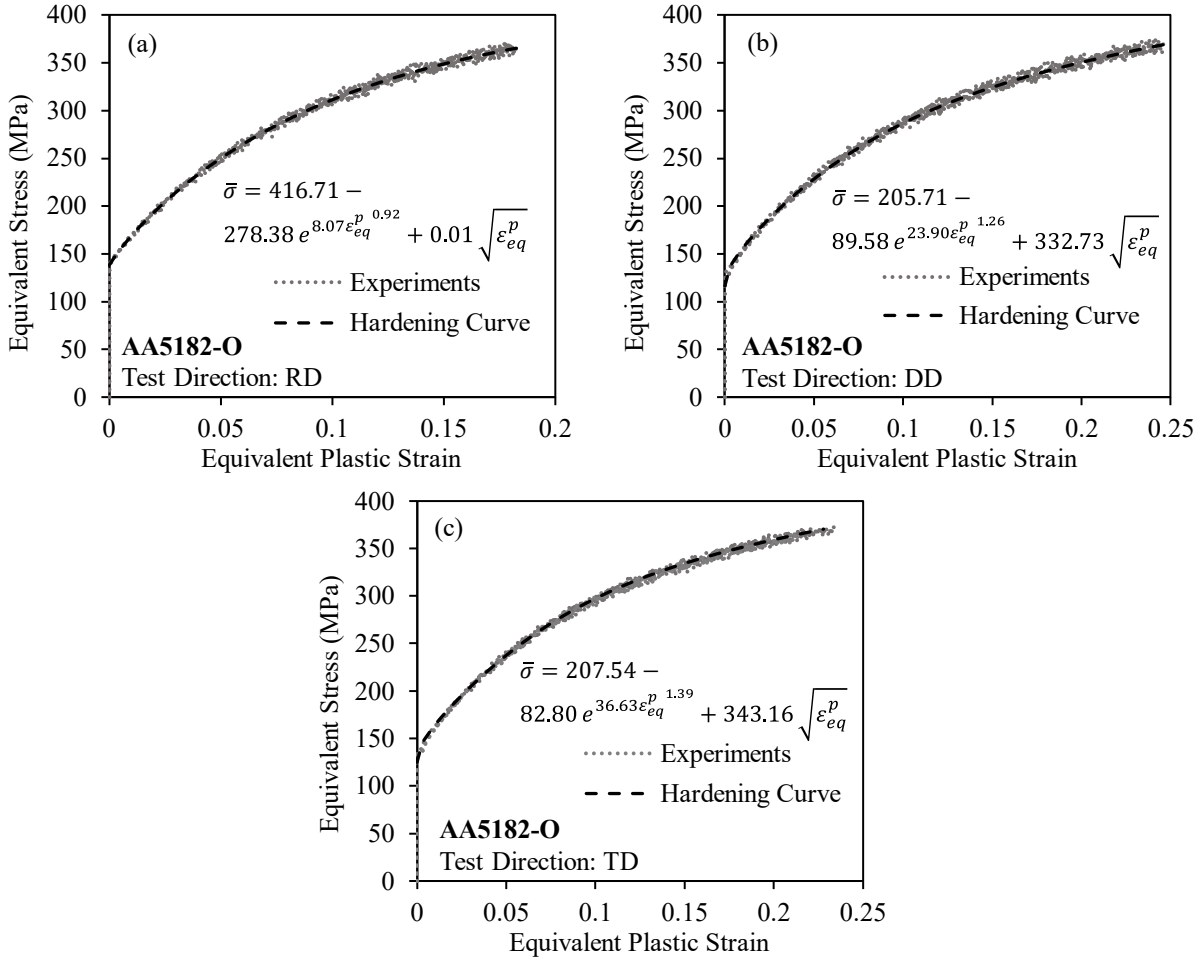

Figure 13: Modified Hockett-Sherby hardening curve fit to experimental data from standard uniaxial tension tests for AA5182-O tested along the (a) RD, (b) DD and (c) TD.

The average R-value is a good fit for the AA5182-O alloy, showing good agreement with the experimental data along each tested direction. The predicted strain path using the average R-value is shown in Figure 14, in comparison to the experimental data, along the RD, DD and TD.

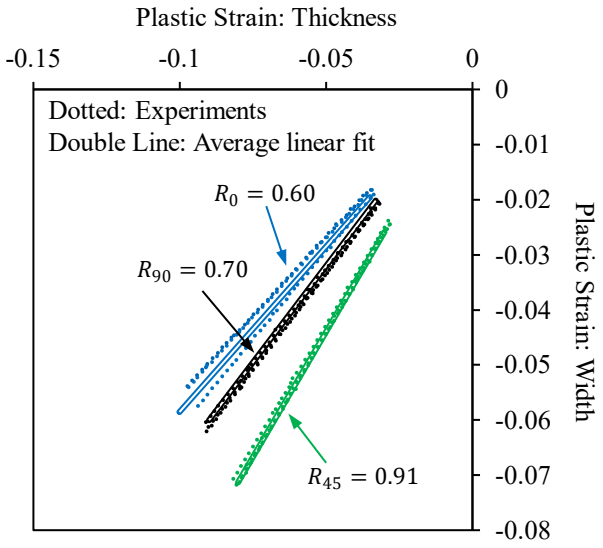

Figure 14: Average uniaxial R-value along the RD, DD and TD compared to the experimental data for each repeat of AA5182-O.

Chapter 3 Methodology for Uniaxial to Plane Strain Tension Characterization[1]

Accurate knowledge of the constitutive response of sheet metals in plane strain tension is of paramount importance to the design of metal forming operations where the majority of failures in stamping occur (Mahmudi, 1999). Plane strain deformation in sheet metal forming is an unavoidable consequence of the mechanics involved. Since the sheet thickness is typically small relative to its planar dimensions, the stress state can be approximated as plane stress for many forming operations. By the same virtue, the large width of the sheet relative to its thickness promotes the development of plane strain conditions in tensile stretching and bending modes (Hill, 1950). In plane strain tension, the material thinning rate and yield strength are at their apex while the strains for localization and fracture are at their lowest values. As described by Hora *et al.* (2013) plane strain tension represents the terminal condition for formability because once the diffuse necking limit is reached, the strain state will begin to transition towards plane strain where the material can sustain a higher stress perpendicular to the neck, to maintain quasi-stable deformation during localization. The transition towards plane strain comes at a cost of increased thinning which reduces the area of the neck and increases the local stress that must by balanced by work hardening and a continued shift towards plane strain. The cycle accelerates until plane strain conditions are met which corresponds to the formation of an acute neck followed by imminent fracture.

Analytical models to predict the onset of localization such as the MK (Marciniak and Kuczynski, 1967) model or predict fracture in a damage-based Modified Mohr Coulomb (MMC) framework (Bai and Wierzbicki, 2008) require precise knowledge of the constitutive response in plane strain and its variation with material direction. Advanced anisotropic yield functions such as Yld2000 (Barlat *et al.*, 2003) and BBC2005 (Banabic *et al.*, 2005) are now routinely used in commercially available finite-element programs such as LS-DYNA® and Autoform® to design stamping operations but the importance of plane strain has been somewhat overlooked. Biaxial and uniaxial tension tests are commonly used to calibrate anisotropic

---

[1] Chapter 3 contains portions of a post-peer-review, pre-copyedit version of an article published in Experimental Mechanics by Springer. Reproduced with permission from Springer Nature. The final authenticated version is available online at:

Fast-Irvine, C., Abedini, A., Noder, J., Butcher, C. (2021). An Experimental Methodology to Characterize the Plasticity of Sheet Metals from Uniaxial to Plane Strain Tension. *Experimental Mechanics*, vol 61, pp. 1381-1404. https://doi.org/10.1007/s11340-021-00744-3.

Section 3.1.2.1 was expanded in this thesis beyond what was included in the accepted manuscript to better demonstrate the suitability of the HF85-PSC function in predicting the intermediate stress and strain values along the uniaxial to plane strain arc.

constitutive models due to the relative simplicity of analyzing the results (Butcher and Abedini, 2019). Variation in the plane strain yield strength due to anisotropy can be predicted by the model but is generally left unvalidated due to the challenges with obtaining reliable plane strain constitutive data.

Experimental methods to determine the constitutive response in plane strain tension include elliptical bulging, cruciform tests, bending, plane strain compression, and notched tensile tests. Elliptical bulging as done by Lanzen and Merklein (Lenzen and Merklein, 2018) is promising but requires specialized equipment and can be sensitive to the curvature measurements and through-thickness gradients as discussed by Min *et al.* (2017) for biaxial bulging. Stress-controlled biaxial cruciform tests, as performed by Kuwabara and Nakajima (2011) and formalized in ISO16842:2014 (International Organization for Standardization, 2014), are perhaps the ideal test for in-plane characterization but also require custom equipment and have been mostly limited to relatively low strain levels due to cracking outside of the gauge area. Techniques including laser deposition can be used to increase the cruciform specimen arm thickness and delay or eliminate cracking, but at additional cost and manufacturing complexity (Hou *et al.*, 2018). Plane strain bending can be performed up to large strain levels, but the mechanics are complicated to extract the constitutive response from the test data as detailed in Yu and Zhang (1996). The shift of the neutral axis towards the concave side of the bend in compression will activate Bauschinger effects as material layers are unloaded in compression and re-loaded in tension. Asymmetry of the response in tension and compression may also be important to consider depending upon the alloy of interest (Kato *et al.*, 2014). Plane strain compression tests can be used to large strain levels but neglect yield asymmetry in the analysis and are complicated by friction, inhomogeneity of the strain rate and lateral spreading of the material under the indenter (Aksenov *et al.*, 2015). Consequently, notched tensile tests are perhaps the most accessible test for plane strain characterization owing to their simplicity and the avoidance of friction or through-thickness strain gradients before the necking limit is reached. Most importantly, the tests can be readily fabricated and tested on a universal test frame at the same time as uniaxial tensile tests required for standard constitutive characterization.

Plane strain tension tests are not without their own challenges. For an ideal geometry, plane stress deformation is limited to the onset of diffuse necking (peak load) which is comparable to the tensile uniform elongation (Swift, 1952). Numerous plane strain test geometries similar to Figure 15 have been proposed based upon the early work of Wagoner (1980) who found that the gauge width, notch radius and notch angle strongly control the size and magnitude of the plane strain region. In a departure from this traditional notched tensile specimen design, Baral *et al.* (2018) recently proposed through-thickness machining as a way of geometrically constraining the region of plastic deformation under plane strain. Regardless of the notched tensile geometry, gradients of strain and stress develop across the specimen width during testing

as shown schematically in Figure 15. Theoretically these gradients are bounded by the limiting states of uniaxial tension at the free edges and plane strain tension in the central region. The initiation of yielding at the edges of the notch before the central region also introduces a gradient in the magnitude of the strain across the width. As a result, every material point along the gauge width is subjected to a different stress state and experiences a different amount of work hardening during the test.

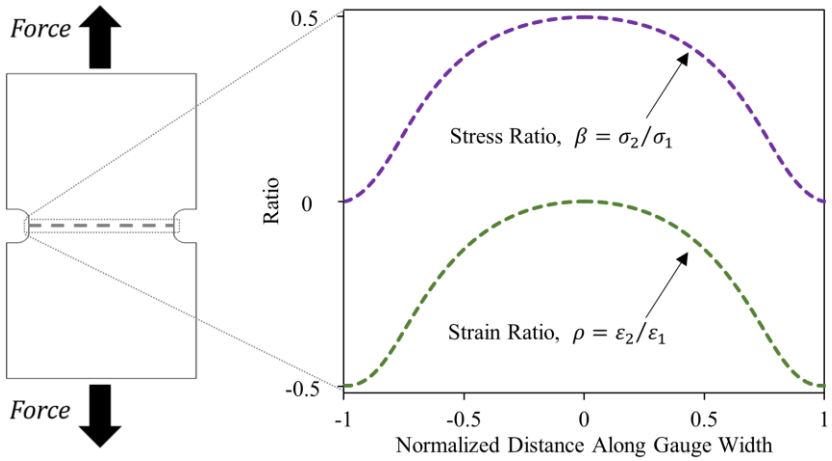

Figure 15: Schematic of the principal stress and strain ratios across the gauge width of an ideal plane strain notch specimen of an isotropic material where the loading transitions from plane strain tension in the center to uniaxial tension at each edge.

Since deformation is not homogenous across the gauge width, the stress calculated by the measured force and gauge area is only an approximation of the plane strain constitutive response. This has prompted the development of several approximate and inverse methods to determine the plane strain yield strength and hardening. An *et al.* (2004) proposed a method to determine the plane strain tensile strength by testing multiple specimens of varying gauge widths to isolate the edge effect. Another empirical relationship derived by Flores *et al.* (2010) relates the plane strain yield strength to the total force by determining the percentage acting over a "homogeneous" zone of plane strain estimated based on the strain gradients. Inverse finite-element analysis has also been used by Dick and Korkolis (2015) and Tian *et al.* (2016) to identify correction factors to account for the non-uniform stress distribution assuming isotropy in plane strain tension experiments.

The *a priori* assumption of isotropy in the numerical analysis of plane strain tests can be directly linked to uncertainty surrounding plane strain behavior in anisotropic yield functions. As reviewed by the authors Butcher and Abedini (2019), it is commonly assumed that the stress state in plane strain tension is unknown and thus must be determined after the conventional calibration of the anisotropic yield function. The inverse problem for plane strain tension is therefore underdetermined since both the magnitude of the yield strength and its location on the yield surface are taken as unknowns. However, Butcher and Abedini (2019) have

recently shown that the stress state for plane strain tension is actually uniquely known for pressure-independent plasticity but is not preserved by anisotropic yield functions developed using linear transformations. Therefore, "generalized plane strain constraints" must be imposed on the normal vectors (or directions of the plastic strain rate) for associated plasticity. By applying these constraints, the plane strain yield strength can be uniquely determined and identified directly from experimental plane strain notch tests of anisotropic sheet materials using inverse analysis.

Inverse methods to identify constitutive model parameters directly from experimental data are possible due to advancements in full-field strain measurement technologies like Digital Image Correlation (DIC) (Rossi *et al.*, 2018). One methodology is to use a constitutive model to calculate stresses from measured strain or displacement data, then optimize the model parameters to balance the internal stresses integrated over a cutting plane with the external force measured by the load cell during the test. This so-called cutting line approach differs from the more general Virtual Fields Method (VFM) in the sense that the former enforces equilibrium only over particular planes of interest while the latter enforces it over the entire deformation field using the principal of virtual work. It should be noted that cutting line methods are in general simpler and less computationally expensive because integration of the entire 2-D or 3-D deformation field is avoided. Cutting line methods have been applied by Marth *et al.* (2016) and Rossi *et al.* (2008) to calibrate hardening functions from tensile experiments assuming isotropic or anisotropic yield functions but the reverse problem of calibrating a yield function given a hardening model has been barely explored. Brosius *et al.* (2018) attempted to calibrate a yield function by applying a cutting line method to shear, uniaxial and plane strain notched tensile tests, but the plane strain point was non-unique and drifted depending on the level of plastic work used for the calibration.

The objective of the present chapter is to develop an experimental methodology to characterize the constitutive behavior of anisotropic sheet metals from uniaxial-to-plane strain tension using standard uniaxial tension and so-called plane strain notched tensile tests. A simple anisotropic yield function, which adheres to the plane strain constraints, is selected to deterministically calibrate the local shape of the yield surface between uniaxial and plane strain tension using a single independent parameter optimized through a cutting line approach. The only inputs are the tensile R-value, elastic parameters, and the experimental hardening curve from uniaxial tension tests until the uniform elongation. By performing uniaxial and plane strain tensile tests in different orientations, multiple uniaxial-to-plane strain arcs of the yield surface can be traced out and used to calibrate a more sophisticated anisotropic yield function such as Yld2000 (Barlat *et al.*, 2003) or Yld2004 (Barlat *et al.*, 2005). The proposed methodology is applied to the four automotive sheet metal alloys introduced in Chapter 2: DP1180, AA5182-O, AA6xxx-T4 and AA6xxx-T81.

3.1. Selection of an Anisotropic Yield Function to Describe Uniaxial-to-Plane Strain Tension

The regions of the plane stress yield surface where deformation ranges from uniaxial tension to plane strain tension in the rolling, diagonal, and transverse directions are shown schematically in Figure 16 for the von Mises yield surface, along with the 2-D projection onto the RD-TD plane. By performing uniaxial and plane strain tension tests in multiple directions, the magnitude and contours of the associated yield surface emerge. While a uniaxial tension test can only provide a single point on the yield surface, the plane strain notch test can provide data over an entire uniaxial to plane strain region that can be used to calibrate anisotropic yield functions. The challenge is to determine a robust methodology to determine each local arc of the associated yield surface without introducing bias due to the choice of yield function or assumptions on the hardening behavior.

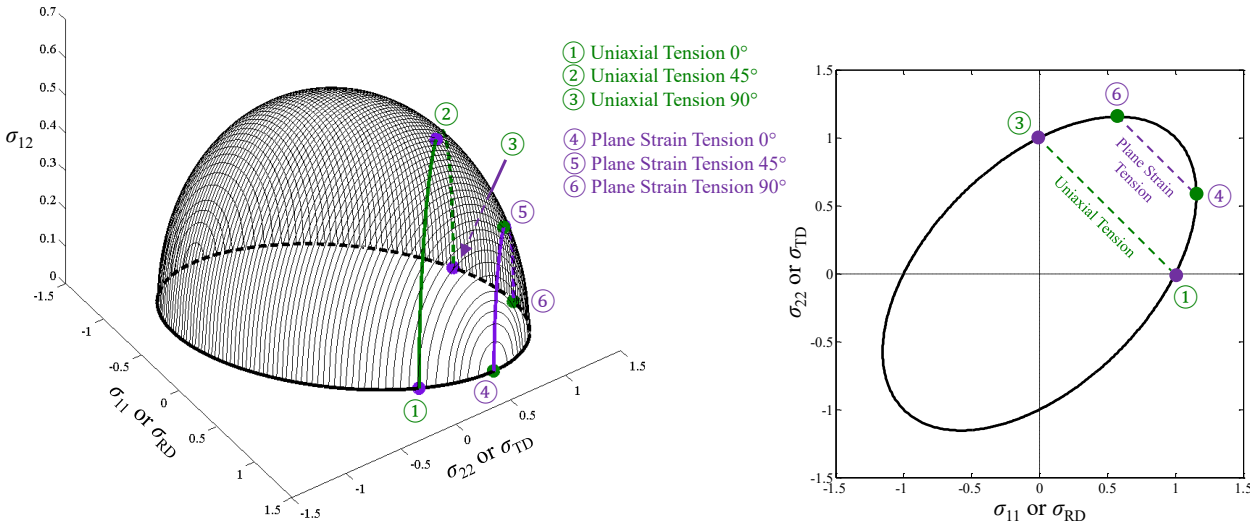

Figure 16: Three dimensional schematic showing locations of uniaxial and plane strain tension on the von Mises yield surface and projection onto the RD-TD plane.

To calibrate the arc of a plane stress yield surface from uniaxial-to-plane strain tension, for a prescribed test orientation, the analyst requires knowledge of:

1. Hardening response in uniaxial tension until the uniform elongation
2. R-value in uniaxial tension
3. Stress state or location on the yield surface where plane strain occurs
4. Anisotropic yield function for local calibration from uniaxial to plane strain tension

The tensile R-value and hardening response in the direction of interest are readily determined from a standard uniaxial tensile test. Each test direction of interest is taken as its own reference direction in this proposed approach. For example, if the transverse direction of the sheet is of interest, then both the plane strain and uniaxial tension tests are performed in that direction. The location of the stress state can be readily

determined using the plane strain constraints of Butcher and Abedini (2019) and justified by an extensive review of experimental biaxial cruciform tests. By modifying a general anisotropic yield function to enforce these constraints, the local arc of the yield surface can be uniquely determined.

3.1.1 Experimental and Theoretical Basis for a Plane Strain Constraint

The analysis of Butcher and Abedini (2019), which concluded that the stress states for generalized plane strain loading of pressure-independent anisotropic metals are known *a priori*, runs counter to conventional wisdom where this is assumed to only apply to isotropic materials. In the conventional approach to calibrate anisotropic plasticity models, the stress state for plane strain tension is permitted to occur anywhere between uniaxial and biaxial tension. In the general case of pressure-dependent anisotropic plasticity, this is the correct approach, but it does not apply for pressure-independent (deviatoric) plasticity. An incompressible material that adheres to deviatoric plasticity, and is constrained to be in a simultaneous state of plane strain and plane stress, is necessarily in plane strain tension (PST) at a minor-to-major principal stress ratio of 1:2. There does appear to be experimental support for the plane strain constraints of Butcher and Abedini (2019) as recently noted by Banabic *et al.* (2020). The present study has performed a comprehensive review of the available biaxial cruciform test data in the literature to evaluate whether the PST points (where the direction of normal vector to yield surface is horizontal/vertical) remain fixed at in-plane stress ratios (σ_{RD}:σ_{TD}) of 1:2 and 2:1, regardless of anisotropy.

Figure 17 and Table 5 were compiled by carefully extracting data from stress-controlled cruciform test results of 22 steel and aluminum alloys provided in 14 different publications from Kuwabara and collaborators to obtain the direction of the plastic strain rate, ϕ, at in-plane stress ratios of 1:2 ($\theta = 26.57°$, see Fig. 3) and 2:1 ($\theta = 63.43°$). The direction of the plastic strain, for a given in-plane loading angle, will differ depending on the plastic anisotropy of the material except at PST where it collapses to a single point at a principal stress ratio of $\sigma_2/\sigma_1 = 1/2$. As representative examples, experimental data for additional stress combinations (σ_{RD}:σ_{TD}) was also extracted for Mat 5 (steel) and Mat 6 (aluminum) to illustrate how the normal vector orientation is material-dependent due to plastic anisotropy but converges at the PST stress states. At PST, the strain-based Lode parameter $v_L = 3d\varepsilon_2/(d\varepsilon_1 - d\varepsilon_3)$ is also equal to zero, since $d\varepsilon_2 = 0$, but will vary with plastic anisotropy for other strain states. Averaging over these 22 BCC and FCC materials, the value of the ratio of the in-plane principal normal vectors is $N_2/N_1 = -0.020 \pm 0.022$ which corresponds to a deviation in the angle of the plastic strain rate from the ideal of $d\phi = -0.084 \pm 1.69^0$ or a strain-based Lode parameter of $v_L = -0.030 \pm 0.033$. It is remarkable that such a wide range of sheet metals exhibit similar behavior at the same nominal stress ratios for plane strain. Some minor deviations from the ideal are expected due to the experimental complexities of maintaining a perfectly balanced true

stress ratio, estimation of the true stress that is accurate to within 2% (Barlat *et al.*, 2018), accounting for elasticity and its change with deformation (Chen *et al.*, 2016), and uncertainty in measuring a plastic strain of near zero. Furthermore, the materials are only assumed to be independent of the pressure when they may possess some measure of pressure-dependence that slightly shifts the plane strain location. Nevertheless, the experimental evidence of Table 5 and Figure 17 clearly highlights that the stress states for plane strain occur very close to $\sigma_2/\sigma_1 = 1/2$, regardless of the plastic anisotropy, and is consistent with the assumption of deviatoric plasticity for FCC and BCC materials.

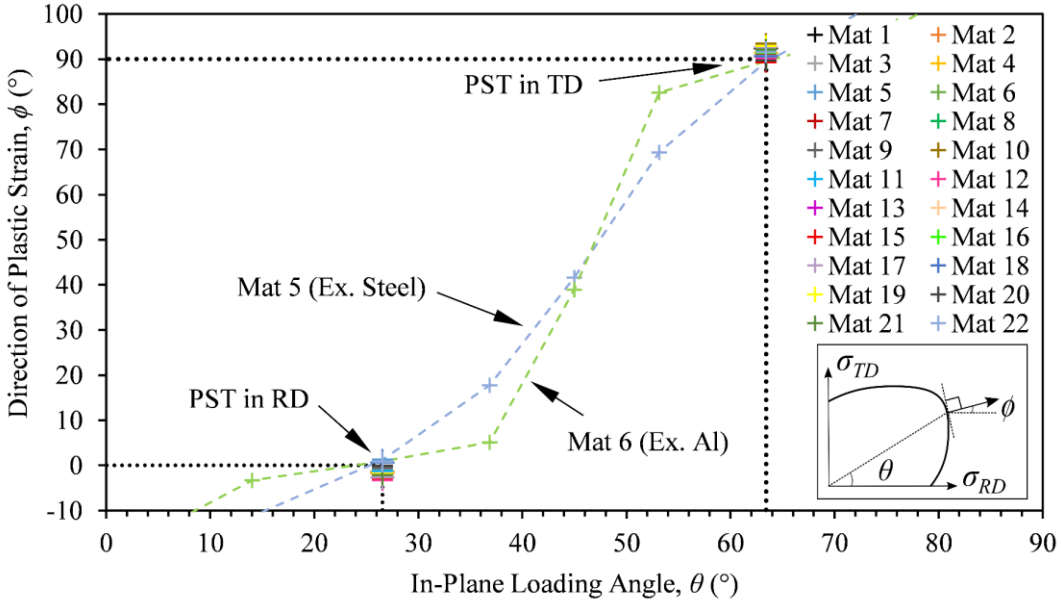

Figure 17: Experimental evidence for the existence of a plane strain constraint from cruciform tests. For plane strain tension, the in-plane loading angle should be $\theta = 26.57°$ in RD and $\theta = 63.43°$ in TD with corresponding plastic strains oriented along normal vectors at $\phi = 0°$ and $\phi = 90°$, respectively.

Table 5: In-plane principal normal vector ratio, strain-based Lode parameter and angle deviation at in-plane stress ratios of 1:2 and 2:1 for 22 steel and aluminum alloys obtained from biaxial cruciform tests.

Label	Material	Crystal Structure	Eq. Strain	N_2/N_1		v_L		$d\phi$ (°)		Reference
				$\frac{\sigma_{RD}}{\sigma_{TD}}=\frac{1}{2}$	$\frac{\sigma_{RD}}{\sigma_{TD}}=2$	$\frac{\sigma_{RD}}{\sigma_{TD}}=\frac{1}{2}$	$\frac{\sigma_{RD}}{\sigma_{TD}}=2$	$\frac{\sigma_{RD}}{\sigma_{TD}}=\frac{1}{2}$	$\frac{\sigma_{RD}}{\sigma_{TD}}=2$	
Mat 1	LC Steel	BCC	0.01	-0.026	-0.043	-0.039	-0.065	-1.468	2.440	(Kuwabara and Ichikawa, 2015)
Mat 2	IF Steel	BCC	0.005	-0.029	-0.012	-0.044	-0.018	-1.639	0.670	(Kuwabara and Sugawara, 2013)
Mat 3	JSC590 Steel	BCC	0.04	-0.012	-0.001	-0.018	-0.002	-0.683	0.080	(Kuwabara, 2014)
Mat 4	DP780 Steel	BCC	0.01	-0.026	-0.026	-0.039	-0.039	-1.480	1.480	(Kuwabara *et al.*, 2011)
Mat 5	DP980 Steel	BCC	0.02	0.022	0.009	0.032	0.013	1.260	-0.500	(Kuwabara and Nakajima, 2011)
Mat 6	AA6016-T4	FCC	0.01	0.016	0.008	0.024	0.012	0.914	-0.450	(Kuwabara *et al.*, 2017)
Mat 7	AA6016-T4, High Cube	FCC	0.04	-0.002	-0.023	-0.003	-0.034	-0.115	1.318	(Yanaga *et al.*, 2012)
Mat 8	AA6016-T4, Low Cube	FCC	0.045	-0.022	-0.030	-0.033	-0.045	-1.253	1.710	(Yanaga *et al.*, 2012)
Mat 9	AA5182	FCC	0.05	-0.009	0.001	-0.014	0.001	-0.540	-0.050	(Yamanaka and Kuwabara, 2015)
Mat 10	BH340 Steel	BCC	0.02	-0.050	-0.060	-0.077	-0.094	-2.860	3.460	(Andar *et al.*, 2010)
Mat 11	DP590 Steel	BCC	0.02	-0.021	-0.009	-0.033	-0.014	-1.230	0.530	(Andar *et al.*, 2010)
Mat 12	AA5xxx-2.5%Mg	FCC	0.06	-0.056	-0.002	-0.086	-0.004	-3.190	0.140	(Kuwabara *et al.*, 2006)
Mat 13	AA5xxx-5.5%Mg	FCC	0.06	-0.040	-0.013	-0.062	-0.020	-2.310	0.750	(Kuwabara *et al.*, 2006)]
Mat 14	ULC IF Steel, R=1.9	BCC	0.002	-0.030	-0.013	-0.045	-0.019	-1.690	0.720	(Kuwabara *et al.*, 2002)
Mat 15	ULC IF Steel, R=1.7	BCC	0.002	-0.049	0.012	-0.075	0.018	-2.810	-0.700	(Kuwabara *et al.*, 2002)
Mat 16	LC, Al Killed Steel	BCC	0.002	-0.041	-0.025	-0.063	-0.038	-2.370	1.420	(Kuwabara *et al.*, 2002)
Mat 17	Cold Rolled DP Steel	BCC	0.002	-0.046	-0.046	-0.071	-0.071	-2.650	2.640	(Kuwabara *et al.*, 2002)
Mat 18	Hot Rolled DP Steel	BCC	0.002	0.012	-0.012	0.018	-0.018	0.700	0.700	(Kuwabara *et al.*, 2002)
Mat 19	LC Steel	BCC	0.1	-0.033	-0.053	-0.050	-0.081	-1.870	3.020	(Lee *et al.*, 2019)
Mat 20	AA6016-O	FCC	0.08	0.000	0.005	-0.001	0.007	-0.020	-0.280	(Kuwabara *et al.*, 2017)
Mat 21	AA6xxx	FCC	0.02	-0.036	-0.038	-0.055	-0.058	-2.070	2.180	(Kuwabara and Kurita, 2000)
Mat 22	SPCE Steel	BCC	0.005	0.014	-0.028	0.021	-0.043	0.810	1.620	(Coppieters *et al.*, 2019)
Average (Std. Dev.)			**0.030**	**-0.020 (0.022)**		**-0.030 (0.033)**		**-0.083 (1.689)**		
Absolute Average (Std. Dev.)			**0.030**	**0.024 (0.017)**		**0.037 (0.026)**		**1.382 (0.952)**		

It can also be shown that this experimental observation can be obtained theoretically from pressure-independent anisotropic plasticity. If only the deviatoric stress is responsible for slip and plastic deformation in a rigid-plastic metal, then by definition under plane strain tension, $d\varepsilon_2 = 0$ and subsequently, $s_2 = 0$. If there is no deviatoric stress in a direction, there can be no plastic strain (displacement) induced even though the applied stress may be non-zero, $\sigma_2 \neq 0$. The condition that $s_2 = 0$ corresponds to the critical deviatoric stress state where the third invariant vanishes, $J_3 = s_1 s_2 s_3 = 0$ and the stress-based Lode parameter is zero, $L = (2s_2 - s_1 - s_3)/(s_1 - s_3) = 0$ since $s_3 = -s_1$ from the first invariant, $J_1 = 0$. Under plane stress conditions, as can often be assumed for thin sheet, $\sigma_3 = 0$ such that $s_2 = (2\sigma_2 - \sigma_1)/3 = 0$ and $\sigma_2/\sigma_1 = 1/2$ in plane strain tension. As shown previously, this conclusion is strongly supported by the experimental cruciform data. It is important to note that materials with HCP crystal structures like titanium and magnesium have been observed to not adhere to the plane strain constraints since deformation is governed by complex twinning and slip mechanisms that are influenced by the hydrostatic stress (Selvarajou *et al.*, 2016; Nagano *et al.*, 2018; Abedini *et al.*, 2018; Abedini *et al.*, 2017). The reader is referred to Butcher and Abedini (2019) for a more rigorous derivation of the plane strain constraints on the calibration of anisotropic yield functions in generalized plane strain stress states. In the present study, where the DP1180 and AA5182 are assumed to adhere to deviatoric plasticity, the stress states where plane strain tension occur must be enforced upon the anisotropic yield surface.

3.1.2 Application to Yield Criteria

For the purposes of this study, HF85 (Hosford, 1985) provides a simple functional form that can be calibrated to notch test experimental data using just a single parameter while enforcing the plane strain constraint. Referring to Eq. (1. 21), it is straightforward to enforce the experimental and theoretical finding that $N_2 = 0$ at $\sigma_2/\sigma_1 = 1/2$ if $R_{\theta+90} = 1$. This so-called HF85-PSC (plane strain constrained) model is then:

$$\sigma_{eq,\theta}^{HF85} = \left(\frac{|\sigma_1|^m + R_\theta |\sigma_2|^m + R_\theta |\sigma_1 - \sigma_2|^m}{1 + R_\theta} \right)^{\frac{1}{m}} \tag{3.1}$$

At a given yield exponent, the ratio of the plane strain yield strength to the tensile strength is

$$\left(\frac{\sigma_1}{\sigma_{eq,\theta}} \right)^{PST} = \left(\frac{1 + R_\theta}{1 + 2R_\theta (1/2)^m} \right)^{\frac{1}{m}} \tag{3.2}$$

where $\sigma_{eq,\theta}$ is the tensile strength in the direction of interest corresponding to the plane strain tensile specimen's orientation (rolling, transverse or diagonal). If isotropy is assumed with $R_\theta = 1$, then Hosford's 1972 non-quadratic extension of the von Mises model is recovered (Hosford, 1972). Figure 18 demonstrates how the shape of the yield surface arc varies with selection of the exponent and R-value at a fixed plane strain yield strength. The R-value is generally defined from a uniaxial tension test. The yield function exponent remains independent and can be used to calibrate the shape of the arc while still enforcing the plane strain constraint. It is important to emphasize that the HF85 yield criterion is only valid if the principal axes are aligned in the coordinate frame upon which the R-values are defined, R_θ and $R_{\theta+90}$. This restriction makes the HF85 model ill-suited for general plane stress loading, but its simple form is ideally suited to analyze the notch tests where only the yield exponent requires calibration.

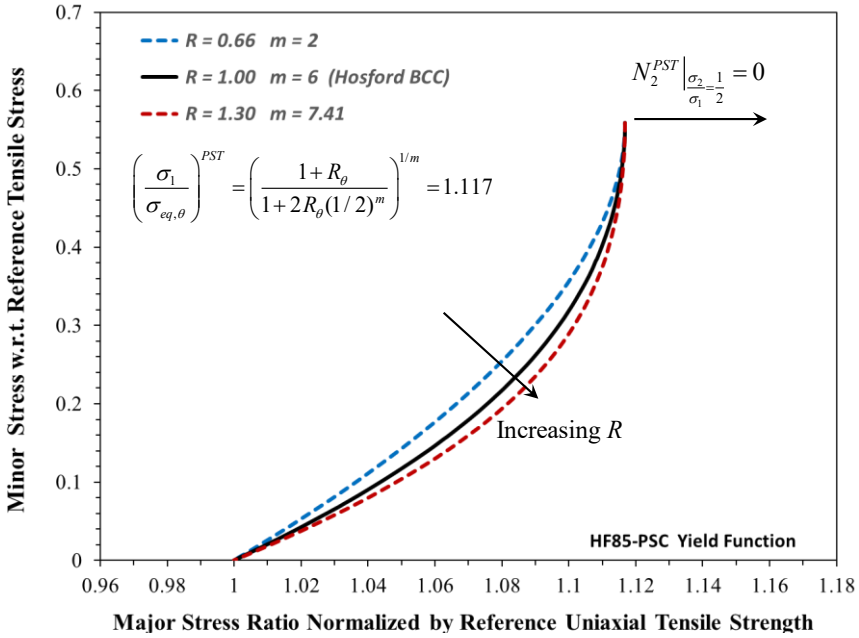

Figure 18: Variation of the HF85-PSC yield surface with the tensile R-value and exponent for a fixed plane strain yield strength. The stress state corresponding to plane strain tension does not vary and remains consistent for pressure-independent plasticity.

Although the HF85-PSC model is not available in common finite-element packages it can be obtained as a special case of higher order anisotropic yield functions built upon Hosford's 1972 model (Hosford, 1972) including the Yld2000 model proposed by Barlat *et al.* (2003). It is relatively straightforward to prove that Yld2000 becomes equivalent to HF85-PSC by setting the eight anisotropy parameters as functions of R_θ and m to:

$$\alpha_1 = \alpha_2 = \alpha_3 = \alpha_4 = \left(\frac{2R_\theta}{1+R_\theta}\right)^{\frac{1}{m}}, \alpha_5 = \alpha_6 = \left(\frac{2}{1+R_\theta}\right)^{\frac{1}{m}}, \alpha_7 = \alpha_8 = \text{undefined} \qquad (3.3)$$

The shear parameters α_7 and α_8 are activated only around the specimen notches where the principal stress axis departs from the loading axis. A value of unity or the average of the other parameters is suggested. More detailed optimization can be accomplished using inverse finite element analysis to match the simulated and experimental local strain response (Narayanan *et al.*, 2022).

It is important to emphasize that the underlying isotropic forms of HF85-PSC and Yld2000 are built upon Hosford's 1972 interpolation between the Tresca and von Mises yield functions (Hosford, 1972) as shown in Figure 19. Consequently, upper and lower bounds for the plane strain yield strength exist based upon the functional form of the yield criterion, the requirements to satisfy convexity, the uniaxial R-value and the plane strain constraint. Using the Hosford-based models, depending upon the R-value and the plane strain yield strength of the material, it may not be possible to select an appropriate yield exponent. For example, no yield exponent exists for a material with an R-value of 0.25 and plane strain yield strength ratio of 1.09 since the upper bound in these Hosford-based models for this condition is about 1.05. The variation of the plane strain yield strength for materials with R-values from 0.25 to 2 within the Hosford framework is presented in Figure 20. Overall, the range of achievable plane strain yield strengths is relatively broad for materials with an R-value greater than 0.25 and should be appropriate for a majority of automotive alloys.

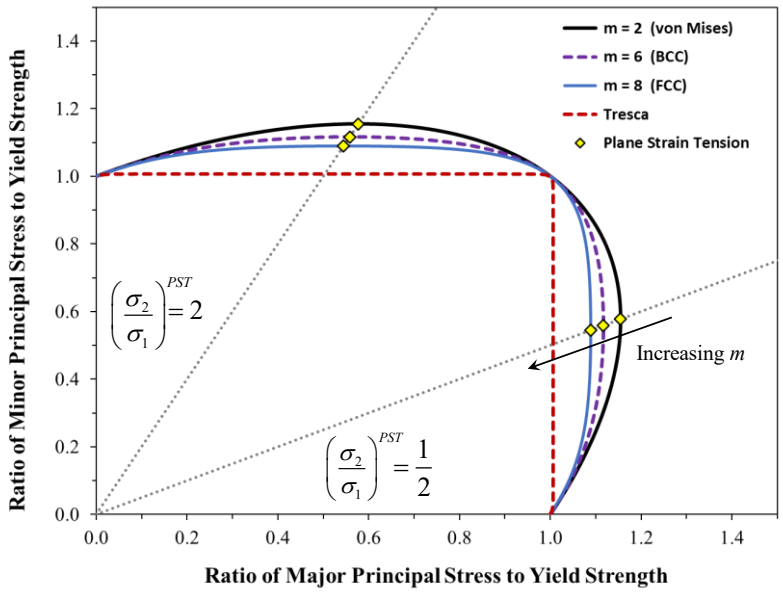

Figure 19: Influence of the yield exponent on the isotropic Hosford yield function. The plane strain tension point is not shown on the Tresca yield function because it is independent of the intermediate principal deviatoric stress.

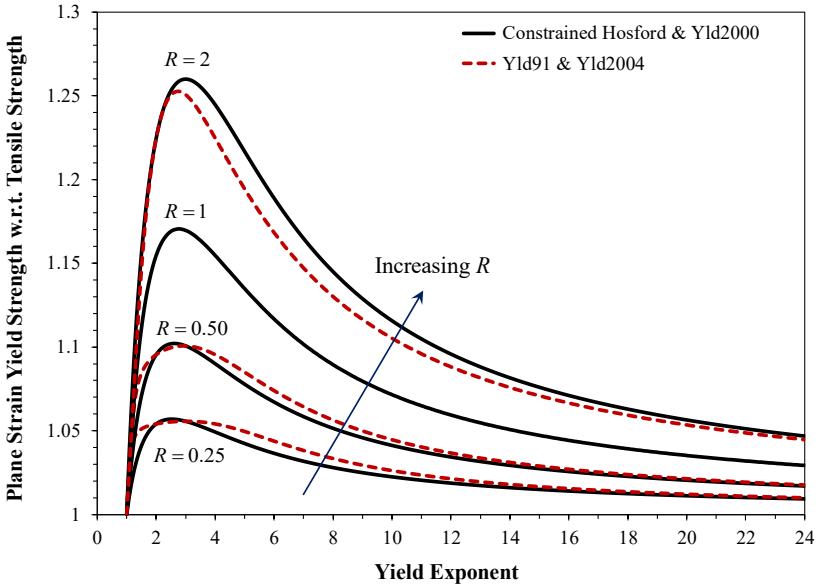

Figure 20: Variation of the plane strain yield strength as a function of R-value and yield exponent for the Hosford-based models of H85-PSC, Yld91/Yld2004 and Yld2000.

3.1.2.1 Justification for Choice of HF85-PSC function

The choice of the Hosford-1985 criterion is not arbitrary. Other yield criteria like Hill48 (Hill, 1948) and Hosford-1979 (Hosford, 1979) are not flexible enough to allow for a plane strain constraint while incorporating material anisotropy. Without the plane strain constraint, the plane strain yield strength and location will be biased to the choice of yield function instead of being an independent material parameter. This was best demonstrated by the notched tensile test analysis of Suh *et al.* (1996) who showed that the constitutive response and location of the plane strain stress state varied with the choice of a Hosford-1979 (Hosford, 1979), Hill-1979 (Hill, 1979) or Yld91 (Barlat *et al.*, 1991) yield function. The observation by Suh *et al.* (1996) that the results from Yld91 and Hosford-1979 were closest at an exponent of 8 directly follows from the plane strain constraint because a higher exponent tempers the error in the model.

Enforcing the plane strain constraint forces the local arc shape to be largely independent of the choice of yield function. To demonstrate the effect of the plane strain constraint, consider two materials with R-values and plane strain yield strengths representative of the range of common engineering materials: Material 1 with an R-value of 0.5 and normalized plane strain yield strength of 1.05 and Material 2 with an R-value of 2.00 and a normalized plain strain yield strength of 1.20. The parameters of the calibrated HF85-PSC and anisotropic Drucker functions are shown in Table 6. Applying the plane strain constraint to the anisotropic Drucker function results in the same local arc shape as the simple HF85-PSC form illustrated in Figure 21.

Table 6: Coefficients of the plane strain constrained anisotropic Drucker function and exponent of the HF85-PSC function corresponding to Materials 1 and 2.

Material	$(\sigma/\sigma_o)^{PST}$	R	HF85-PSC	Anisotropic Drucker		
			m	$c_1, c_3 - c_6$	c_2	c
Mat 1	1.05	0.5	8.243	1.6493	2.0325	2.1879
Mat 2	1.20	2	5.587	1.9971	1.5015	0.5470

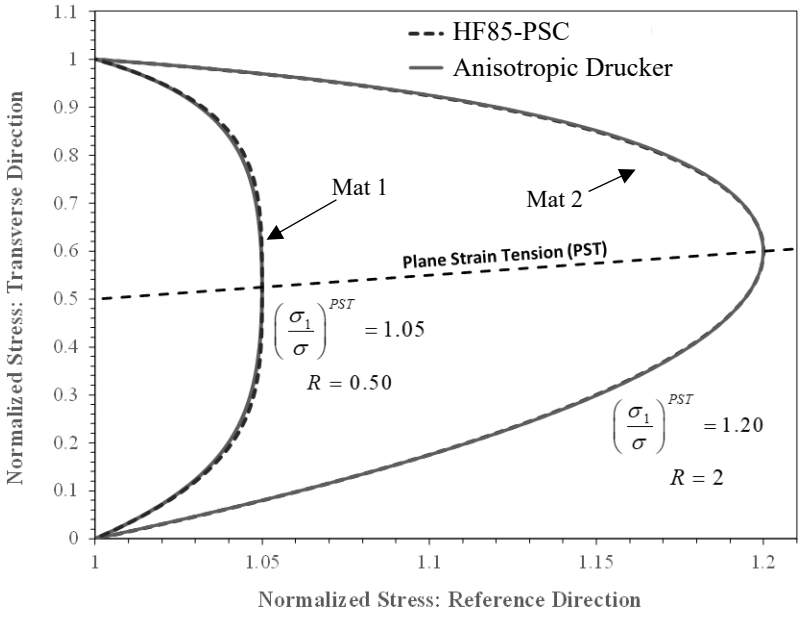

Figure 21: Coincidence of local yield surface arcs between uniaxial tension and plane strain tension for the anisotropic Drucker and HF85-PSC functions after application of the plane strain constraint. Results are shown for two materials to demonstrate coincidence at both extremes of the property ranges encountered for common engineering materials.

Although Figure 21 suggests that the plain strain constraint reduces the UT-PST arc to a unique solution independent of the choice of yield function, the question remains if the arc shape is representative of the material's behaviour at values between those of uniaxial tension and plane strain tension used in the calibration. Fortunately, cruciform studies provide insight into the material yield stress at intermediate points along the UT-PST arc. A typical cruciform study investigates not only the in-plane principal loading states of $\sigma_1 : \sigma_2 = 2:1$ (plane strain tension) and $\sigma_1 : \sigma_2 = 1:0$ (uniaxial tension), but also an intermediate point at $\sigma_1 : \sigma_2 = 4:1$ $(\beta = \sigma_2/\sigma_1 \cong 0.25)$ to better define the plastic work contour. The ideal yield function would perfectly intersect all three stresses, while also satisfying the plane strain constraint and capturing the plastic strain directions. Consider the HF85-PSC criterion represented in the form of Eq. (3.4a, b): the arc exponent m is defined by a normalized major stress at $\sigma_1 : \sigma_2 = 2:1$ $(\beta \cong 0.5)$ and the R-value in the direction of analysis R_θ. Once the exponent is known, the predicted normalized major and minor

stresses at the intermediate point, $\beta \cong 0.25$, may be compared with the experimental values from a cruciform study.

$$\frac{\sigma_1}{\sigma_{eq,\theta}^{HF85-PSC}} = \left(\frac{1 + R_\theta|\beta|^m + R_\theta|1-\beta|^m}{1+R_\theta}\right)^{-\frac{1}{m}}, \quad \frac{\sigma_2}{\sigma_{eq,\theta}^{HF85-PSC}} = \beta\left(\frac{\sigma_1}{\sigma_{eq,\theta}^{HF85-PSC}}\right) \tag{3.4a, b}$$

The strain directions at the intermediate point may also be compared to demonstrate the accuracy of the flow rule and normality principle. The ratio of the major and minor principal strains predicted by the HF85-PSC function is:

$$\rho = \frac{d\varepsilon_2{}^p}{d\varepsilon_1{}^p} = \frac{N_2}{N_1} = R_\theta\left[\frac{|\beta|^{m-1}\text{sign}(\beta) - |1-\beta|^{m-1}\text{sign}(1-\beta)}{1 + R_\theta|1-\beta|^{m-1}\text{sign}(1-\beta)}\right] \tag{3.5}$$

It is more intuitive to consider the angle the strain direction makes with the rolling direction, rather than the strain ratio. Along the UT-PST arc, the principal strain ratio is constrained to fall between $\rho = -R_\theta/(1+R_\theta)$ and $\rho = 0$ whereas the magnitude of the strain angle with the major principal direction will be between $\phi = 0$ and $\phi = \text{atan}[R_\theta/(1+R_\theta)]$.

For each of the materials previously investigated in Table 5, the HF85-PSC exponent was identified based on the plane strain yield strength and R-value, then used to predict the stresses and strain angle at the intermediate cruciform loading condition. The cruciform data was obtained by carefully digitizing the necessary figures in each respective publication. The material R-value in the direction of analysis was obtained from a table, if provided, otherwise from the strain angle. The absolute percent error in the predicted major and minor stresses at the intermediate stress point was evaluated as $\delta = \left|l^{pred} - l^{exp}\right|/l^{exp}$ where $l = \sqrt{\sigma_1^2 + \sigma_2^2}$, or the Euclidean distance between the origin and the stress point. The use of the Euclidean distance simultaneously captures the error in both the major and minor stress.

Table 7 shows that the HF85-PSC function accurately predicts the intermediate experimental loading point from the cruciform tests. The average strain angle deviation is just 2.53°, with a stress error of 1.2%. Four materials (Mat 15-18) were omitted since the corresponding cruciform studies did not include the intermediate loading point. Some materials also had R-value and σ_1^{PST} combinations that were outside the range of the HF85-PSC function illustrated in Figure 20: a low-carbon steel (Mat 19) along both the RD and TD and BH340 (Mat 10) and DP590 (Mat 11) along the RD. Ultimately cruciform tests confirm that the HF85-PSC functional form is consistent with the shape of arc of the yield surface from uniaxial to plane strain tension, and applicable to the majority of common engineering materials.

Table 7: Summary of major stress, minor stress and strain angle predicted by the HF85-PSC yield function compared to the corresponding σ_1:σ_2 = 4:1 experimental value obtained from biaxial cruciform tests.

Label	Dir.	R_θ	m	σ_1/σ_{RD}		σ_2/σ_{RD}		ϕ		$\lvert d\phi \rvert$	$\lvert\delta\rvert$	Reference
				Exp.	Pred.	Exp.	Pred.	Exp.	Pred.	(°)		
Mat 1	RD	1.30	4.00	1.140	1.130	0.289	0.287	-17.05	-18.62	1.56	0.9%	(Kuwabara and Ichikawa, 2015)
	TD	1.50	3.28	1.142	1.126	0.286	0.282	108.85	111.86	3.01	1.5%	
Mat 2	RD	2.27	5.60	1.132	1.156	0.284	0.290	-19.40	-20.45	1.05	2.1%	(Kuwabara and Sugawara, 2013)
	TD	2.65	6.70	1.134	1.178	0.284	0.295	108.57	108.67	0.10	3.8%	
Mat 3	RD	0.42	3.60	1.057	1.058	0.252	0.253	-8.55	-9.19	0.64	0.1%	(Kuwabara, 2014)
	TD	0.63	5.78	1.126	1.117	0.267	0.265	99.67	98.37	1.30	0.8%	
Mat 4	RD	0.93	4.33	1.099	1.100	0.270	0.271	-14.63	-14.59	0.04	0.2%	(Kuwabara *et al.*, 2011)
	TD	1.19	3.72	1.139	1.110	0.277	0.270	107.16	108.86	1.70	2.6%	
Mat 5	RD	0.82	5.44	1.082	1.081	0.254	0.253	-12.74	-11.27	1.47	0.1%	(Kuwabara and Nakajima, 2011)
	TD	0.81	5.13	1.112	1.100	0.272	0.269	104.79	101.38	3.42	1.1%	
Mat 6	RD	0.61	7.26	1.059	1.057	0.264	0.263	-3.56	-5.26	1.70	0.2%	(Kuwabara *et al.*, 2017)
	TD	1.01	7.11	1.066	1.062	0.263	0.262	97.87	98.57	0.70	0.4%	
Mat 7	RD	0.53	10.08	1.048	1.040	0.252	0.250	-4.39	-2.39	1.99	0.8%	(Yanaga *et al.*, 2012)
	TD	0.62	6.27	1.039	1.038	0.246	0.245	97.55	97.43	0.12	0.1%	
Mat 8	RD	0.82	4.61	1.094	1.087	0.256	0.254	-10.60	-13.27	2.67	0.6%	(Yanaga *et al.*, 2012)
	TD	0.70	4.75	1.058	1.040	0.251	0.247	98.72	101.34	2.62	1.7%	
Mat 9	RD	0.79	5.72	1.075	1.082	0.280	0.282	-10.68	-9.02	1.66	0.6%	(Yamanaka and Kuwabara, 2015)
	TD	0.70	5.46	1.044	1.052	0.263	0.265	99.22	99.09	0.13	0.8%	
Mat 10	RD	1.52	-	1.171	-	0.289	-	-18.97	-	-	-	(Andar *et al.*, 2010)
	TD	1.64	3.72	1.187	1.175	0.289	0.286	108.97	112.48	3.51	1.0%	
Mat 11	RD	0.85	-	1.119	-	0.269	-	-12.17	-	-	-	(Andar *et al.*, 2010)
	TD	1.02	3.09	1.155	1.141	0.280	0.276	105.63	108.26	2.63	1.2%	
Mat 12	RD	0.78	3.92	1.102	1.088	0.258	0.255	-9.86	-14.33	4.46	1.2%	(Kuwabara *et al.*, 2006)
	TD	0.66	5.76	1.076	1.068	0.252	0.250	98.90	98.85	0.05	0.7%	
Mat 13	RD	0.67	3.74	1.087	1.082	0.259	0.258	-11.98	-13.01	1.03	0.5%	(Kuwabara *et al.*, 2006)
	TD	0.79	5.13	1.068	1.079	0.252	0.255	101.67	101.57	0.10	1.1%	
Mat 14	RD	2.01	8.33	1.085	1.118	0.271	0.279	-21.60	-11.13	10.47	3.1%	(Kuwabara *et al.*, 2002)
	TD	2.42	8.50	1.133	1.164	0.275	0.283	112.50	103.00	9.50	2.7%	
Mat 20	RD	0.67	20.11	1.026	1.026	0.250	0.250	-6.23	-0.18	6.04	0.0%	(Kuwabara *et al.*, 2017)
	TD	0.85	80.84	1.032	1.028	0.248	0.247	96.72	90.00	6.72	0.4%	
Mat 21	RD	0.78	5.84	1.074	1.078	0.264	0.265	-12.19	-9.35	2.84	0.3%	(Kuwabara and Kurita, 2000)
	TD	0.53	4.01	1.045	1.050	0.251	0.252	102.19	100.30	1.89	0.5%	
Mat 22	RD	1.85	8.27	1.062	1.115	0.275	0.288	-14.00	-9.84	4.16	5.1%	(Coppieters *et al.*, 2019)
	TD	2.82	7.64	1.147	1.173	0.287	0.294	108.11	106.38	1.73	2.2%	
				Average (Std. Dev.)						2.53 (2.57)	1.2% (1.2%)	

3.2 Methodology to Analyze Notched Tensile Tests

A constitutive model was built around the HF85-PSC criterion shown in Eq. (3.2) and the principal of force equilibrium was used as a calibration metric to determine the optimum yield function exponent. Since plane strain notched tensile tests are conducted under quasi-static conditions, a summation of the internal forces (F^{model}) across a cutting plane through the gauge width of the specimen should equal the external force measured by the load cell (F^{exp}), at all values of far-field strain (E_{1y}^{DIC}) captured during the test. Optimum agreement between the calculated force and measured force is achieved when the HF85-PSC yield function exponent is properly selected. The main steps of this methodology are shown in Figure 22.

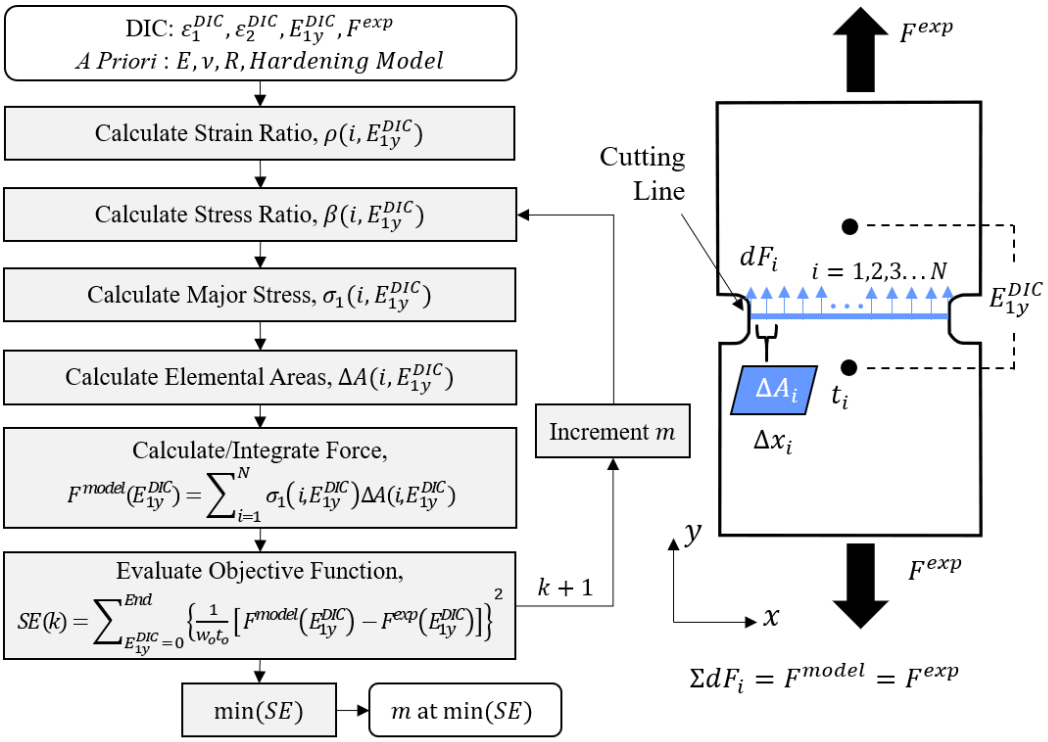

Figure 22: Flowchart showing steps of methodology to calibrate HF85-PSC exponent using strain data captured by DIC along a cutting line through the gauge width of a plane strain notched tensile specimen.

3.2.1 Calculation of Strain and Stress Ratios

Applying the flow rule to the HF85-PSC function, as shown in Eq. (3.5), provides a direct formula for the calculation of stresses given an experimentally measured strain ratio. Note that Eq. (3.5) could be simplified even further for this analysis as β is constrained between 0 and 0.5 along the arc of the yield surface between uniaxial and plane strain tension. The corresponding stress ratio for each strain ratio is solved for using the Newton-Raphson method at a given yield function exponent. Instead of neglecting the elastic strains to simplify the analysis, it is assumed that the applied strain ratio measured by DIC holds for

both the elastic and plastic strain components. The history of the instantaneous strain ratio at every point along the gauge region of the notched specimen is then known as:

$$\rho = \frac{d{\varepsilon_2}^{DIC}}{d{\varepsilon_1}^{DIC}} \approx \frac{N_2}{N_1} \tag{3.6}$$

The ratio of the major principal stress to the equivalent stress can then be evaluated from the HF85-PSC yield criterion shown in Eq. (3.4). From a plastic work balance, assumed hardening model for the flow stress, $\bar{\sigma}\left({\varepsilon_{eq}}^{P}\right)$, and additive decomposition of the strain tensor into elastic and plastic components, a relationship between the equivalent plastic strain increment, $d\varepsilon_{eq}^{P}$, and measured total strain, ε_1^{DIC}, can be derived as:

$${\varepsilon_1}^{DIC} = \left(\frac{1-\nu\beta_j}{E}\right)\left(\frac{\sigma_1}{\sigma_{eq,\theta}^{HF85-PSC}}\right)\bar{\sigma}_j + ({\varepsilon_1}^{P})_{j-1} + \frac{1}{\left(1+\beta_j\rho_j\right)}\left(\frac{\sigma_1}{\sigma_{eq,\theta}^{HF85-PSC}}\right)^{-1}(d{\varepsilon_{eq}}^{P})_j \tag{3.7}$$

where the subscripts *j* and *j-1* correspond to the current and previous time steps (or DIC images), E is the elastic modulus and ν is Poisson's ratio. Any hardening model could be used including the Swift model shown in Eq. (1.9) or the Modified Hockett Sherby model shown in Eq. (1.10). Regardless of the choice of model, at each time step the flow stress is evaluated at $\left(\varepsilon_{eq}^{p}\right)_j = \left(\varepsilon_{eq}^{P}\right)_{j-1} + \left(d\varepsilon_{eq}^{P}\right)_j$. Newton-Raphson iteration of Eq. (3.7) is then used to solve for the equivalent strain increment $\left(d\varepsilon_{eq}^{P}\right)_j$ and the magnitude of the major principal stress is determined from Eq. (3.4).

3.2.2 Area Discretization

Each calculated major principal stress is associated with an area, ΔA. The gauge width, having an initial width, w_o, and thickness, t_o, is discretized into *N* elements corresponding to the *N* discrete strain data points taken along the cutting line. Initially these elements are equally sized with side length Δx, with the exception being the elements at the edges with side length, $\Delta x/2$. The area of each element decreases during the test due to both transverse and out-of-plane thickness strains. The transverse strain, ε_2^{DIC}, is directly measured while the out-of-plane thickness true strain, ε_3, is reconstructed from its elastic and plastic components as:

$$\varepsilon_3 = -\left({\varepsilon_1}^{p} + {\varepsilon_2}^{p} + \frac{\nu}{E}(\beta+1)\sigma_1\right) \tag{3.8}$$

The area of each element is then calculated as:

$$\Delta A_i = \Delta x_i t_i = \Delta x_o t_o e^{\varepsilon_2{}^{DIC} + \varepsilon_3} \tag{3.9}$$

3.2.3 Force Calculation and Stress-Strain Curve Calibration

The total normal force acting on the cutting plane is obtained by numerically integrating the major principal stress over the cross-sectional area. It is important to emphasize that the procedure to calculate the stress and the area outlined in Sections 3.1 and 3.2 is applied at each measured DIC data point, i, along the gauge width of the specimen to calculate the force at a particular step in far-field strain, E_{1y}^{DIC}.

$$F^{model} = \int \sigma_1 dA \approx \sum_{i=1}^{N} \sigma_1\left(i, E_{1y}{}^{DIC}\right) \Delta A\left(i, E_{1y}{}^{DIC}\right) \tag{3.10}$$

Repeating this analysis at each step in far-field strain results in a stress-strain curve. Varying the exponent of the HF85-PSC yield criterion will produce different stress-strain responses, with the correctly calibrated result being the one that minimizes the difference between the modelled and the experimentally obtained curves. This is quantitatively determined using the objective function shown in Eq. (3.11), which is based on the least-squares method and written as

$$SE = \sum_{E_{1y}{}^{DIC}=0}^{End} \left\{ \frac{1}{w_o t_o} \left[F^{model}\left(E_{1y}{}^{DIC}\right) - F^{exp}\left(E_{1y}{}^{DIC}\right) \right] \right\}^2 \tag{3.11}$$

3.3 Finite-Element Model and Identification of the Range of Plane Stress Deformation

A finite-element model of the plane strain notch Geometry A was created to assess the accuracy of the proposed methodology to integrate the constitutive response from DIC surface strain measurements. A half-symmetry model of the specimen geometry shown in Figure 23 was created in LS-DYNA with a sheet thickness of 1 mm and solved using an implicit dynamic formulation. The geometry was only modelled in the free region between the grips. A prescribed motion boundary condition was applied to the nodes at the upper grip using a constant velocity of 0.005 mm/s directed along the vertical axis. The nodes at the lower boundary were fixed in all degrees of freedom to reflect the constraints imposed by the grip of the universal test frame.

3.3.1.1 Validity of Plane Stress Assumption

The proposed methodology relies on a fundamental assumption of plane stress. The validity of this assumption was investigated by comparing the results obtained using shell and solid models, with two different mesh sizes to evaluate mesh sensitivity. For the shell models, a fine mesh comprised of 6786 shell elements with a characteristic dimension of 0.24 mm and a coarse mesh consisting of 263 shell elements having a characteristic dimension of 1.2 mm were used. For both mesh sizes shown in Figure 23, Belytschko-Tsay shell elements with thickness stretch (Type 25 in LS-DYNA) and 7 through-thickness integration points were selected. To be consistent with the DIC measurements used in the physical tests, Lobatto integration was selected instead of Gauss quadrature such that the upper and lower integration points were on the surfaces of the elements.

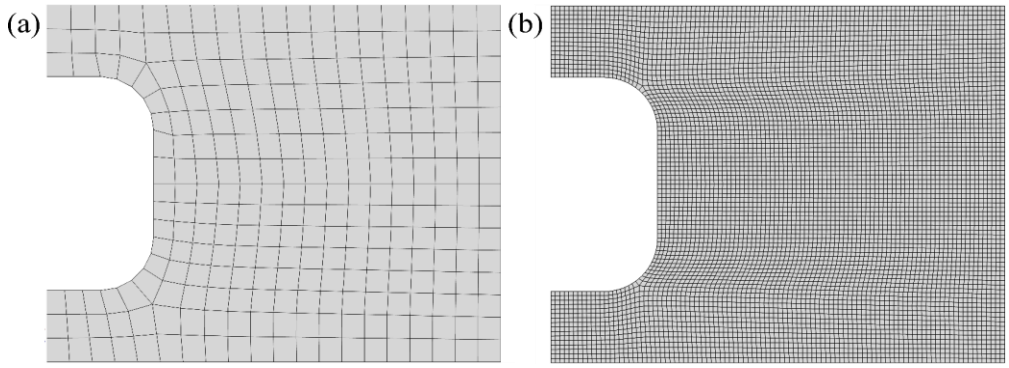

Figure 23: (a) Coarse and (b) fine finite-element meshes of the plane strain notched tensile specimen of Vegter and van den Boogaard (2006).

The solid models were constructed using fully integrated solid elements (Type -2 in LS-DYNA), which are formulated for an accurate solution that is less dependent on aspect ratio. The fine solid mesh had 27,144 elements, arranged with 4 elements through the thickness. The coarse model had 789 elements, with 3 elements through the thickness. The elements had the same in-plane dimensions as the shell models.

Two generic power law hardening, von Mises materials with a strength coefficient of $K = 1000$ MPa and hardening exponents $n = 0.1$ and $n = 0.3$ were considered. The dimensionless form of Swift's hardening model shown in Eq. (1.9) was used with an initial yield strain of $\varepsilon_o = 0.002$. As the shell model will only be comparable to the solid model while the plane stress condition holds, some cut-off criteria must be employed to indicate the start of diffuse necking. The maximum force criteria of Swift (1952) for the onset of diffuse necking can be employed based upon the hardening model selected in Eq. (1.9). If the notch geometry provides a homogeneous plane strain deformation across the gauge width, then diffuse necking begins at an extension strain of $\varepsilon_1^{PST} \approx n$ and an equivalent von Mises strain of $\varepsilon_{eq}^{PST} \approx 1.15n$. Considering that the free edge of the notch specimen will always be in uniaxial tension (UT) by definition, then diffuse

necking at the edge begins when $\varepsilon_1^{UT} = \varepsilon_{eq}^{UT} = n - 0.002$. Since loading will vary between uniaxial and plane strain tension, the start of diffuse necking anywhere across the gauge width occurs when $\varepsilon_1^{UT-PST} \approx n$. Therefore, for simplicity, the range of deformation in the simulations was limited to when the first element in the gauge region exceeded a major strain of $\varepsilon_1^{element} > n$.

As shown in Figure 24, the selected geometry results in strain localization at the notch radii. This influences the strain distribution across the gauge width such that the cut-off strain does not necessarily occur at the free ends of the cutting line, meaning that every point along the cutting line must be checked for the onset of necking. The experimental analog to this criterion using DIC strain measurement would be to end the analysis when the major principal strain at a point along the gauge width exceeds the true strain at uniform elongation (UE) measured in a standard uniaxial tension test and expressed as $\varepsilon_1^{DIC} \geq ln(1 + UE(\%)/100)$.

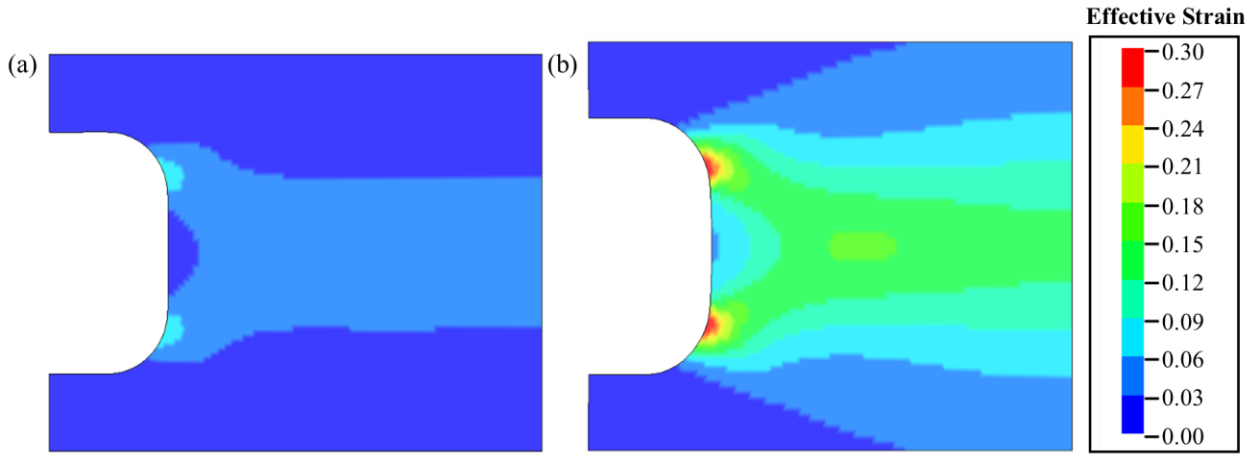

Figure 24: Contours of the equivalent plastic strain obtained from the half-symmetry finite-element model of the notch test using shell elements with a mesh size of 0.24 mm at a far field strain of (a) E_{ly} = 0.028 and after localization at (b) E_{ly} = 0.096 based on an extensometer length of 12 mm. The model employed von Mises plasticity with a hardening exponent of n = 0.1.

A comparison of the engineering stress-strain response for solid and shell elements until $\varepsilon_1^{element} > n$ is presented in Figure 25. The engineering far-field strain was calculated using a gauge length of 12 mm and the engineering stress calculated using the load obtained by summation of the nodal forces at the lower grip as shown in Figure 26. Excellent agreement was observed between the shell and solid models, indicating that the plane stress assumption was appropriate up to the cut-off criterion. Good agreement was also observed between the coarse and fine models, indicating that the global response showed a low sensitivity to the element sizes considered.

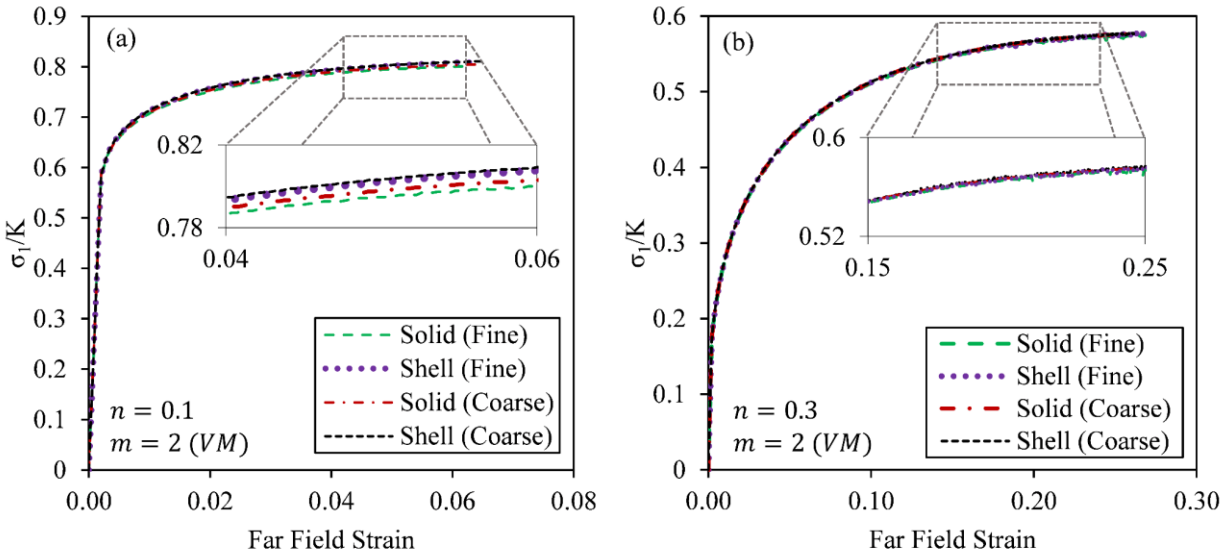

Figure 25: Engineering stress-strain responses up to the start of diffuse necking $\varepsilon_1^{element} > n$ for plane strain notch test simulations comparing fine and coarse meshed shell and solid models for a von Mises material and Swift hardening exponents (a) $n = 0.1$ and (b) $n = 0.3$.

3.3.1.2 Evaluation of DIC Integration Methodology to Calculate HF85-PSC Exponent

With the plane stress assumption validated and a termination criterion identified based on the local strains, the finite-element model was used to evaluate the proposed stress integration methodology using the surface strain measurements across the gauge width. The major and minor strains from the surface integration points were extracted from the model at each node along the gauge width of the modelled specimen and at each solution time step. Analogous to the "experimental" force measured by the load cell, the total force along the loading axis was obtained from the summation of the forces calculated by LS-DYNA at the nodes located at the lower grip. A far field strain was computed from the displacement of two nodes P_1 and P_2 initially 12 mm apart. These extracted values were then imported into a Matlab® script to perform the integration procedure as if the finite-element data had come from the DIC system.

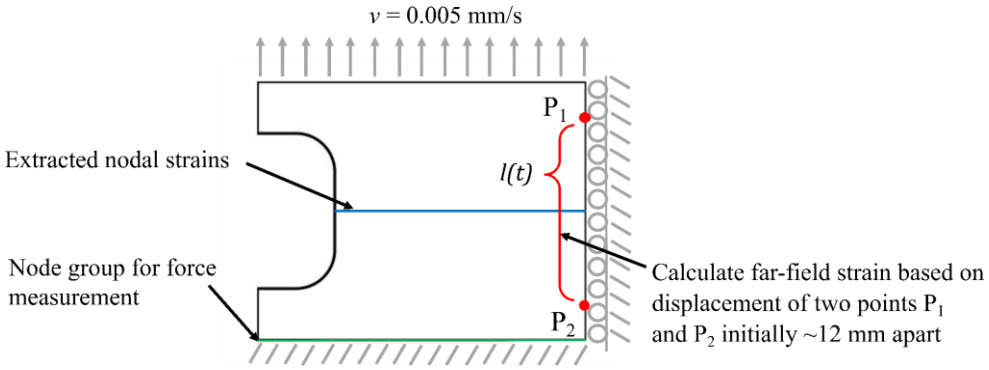

Figure 26: Illustration showing extracted nodal forces and strains for import into the integration script. Procedure is analogous to the treatment of the DIC data.

The stress-strain responses calculated by LS-DYNA and the proposed integration methodology were in excellent agreement when inputting the same hardening curve and yield function exponent ($m = 2$) as shown in Figure 27. Since similar responses were observed for the fine and coarse meshed models, the number of discrete data points had little effect on the accuracy of the integration provided that the local strain distribution was still captured. This suggests that the methodology should have a low sensitivity to the choice of DIC subset and step size, as well as the number of extracted points along the cutting line.

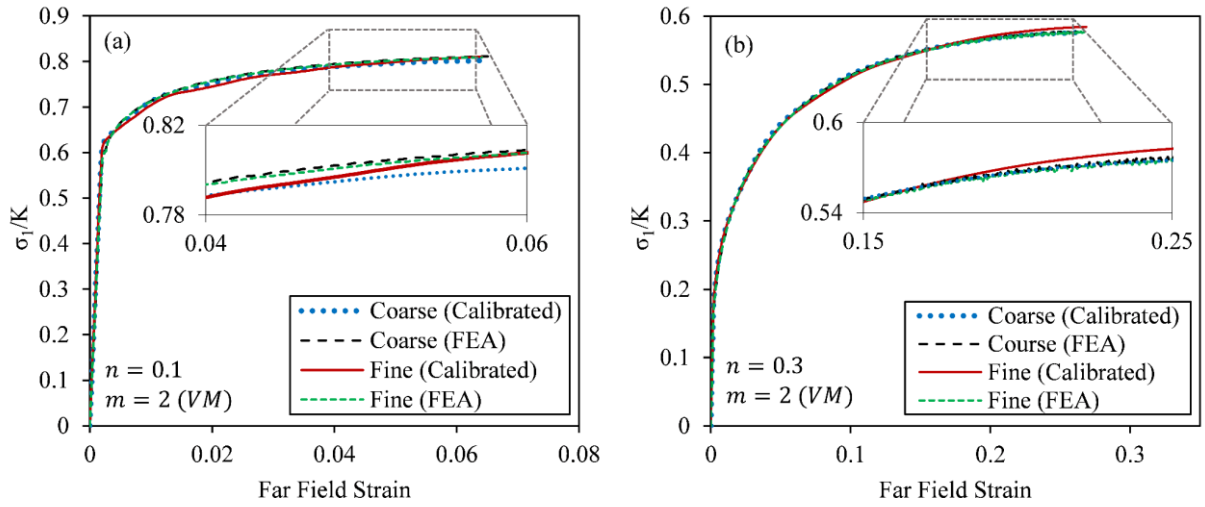

Figure 27: Comparison of calibrated to finite-element calculated engineering stress-strain curves for a von Mises material with Swift hardening exponents (a) $n = 0.1$ and (b) $n = 0.3$. Results for both fine and coarse meshed shell models are shown up to the beginning of diffuse necking.

When the yield function exponent in the LS-DYNA model was changed to reflect anisotropy, the proposed integration methodology at the same yield function exponent accurately reproduced the global stress-strain response. Combinations of Swift hardening exponents n = 0.1 and n = 0.3 with HF85-PSC yield criterion exponents of m = 6 and m = 8 were considered to represent typical values for BCC and FCC materials (Logan and Hosford, 1980). Corresponding R-values of 2.0 and 0.5 were selected as extreme cases with the equivalent Yld2000 coefficients for the HF85-PSC criterion calculated using Eq. (3.3). As seen in Figure 28, excellent agreement was observed for all four anisotropic validation cases when comparing the results from LS-DYNA and the proposed integration methodology.

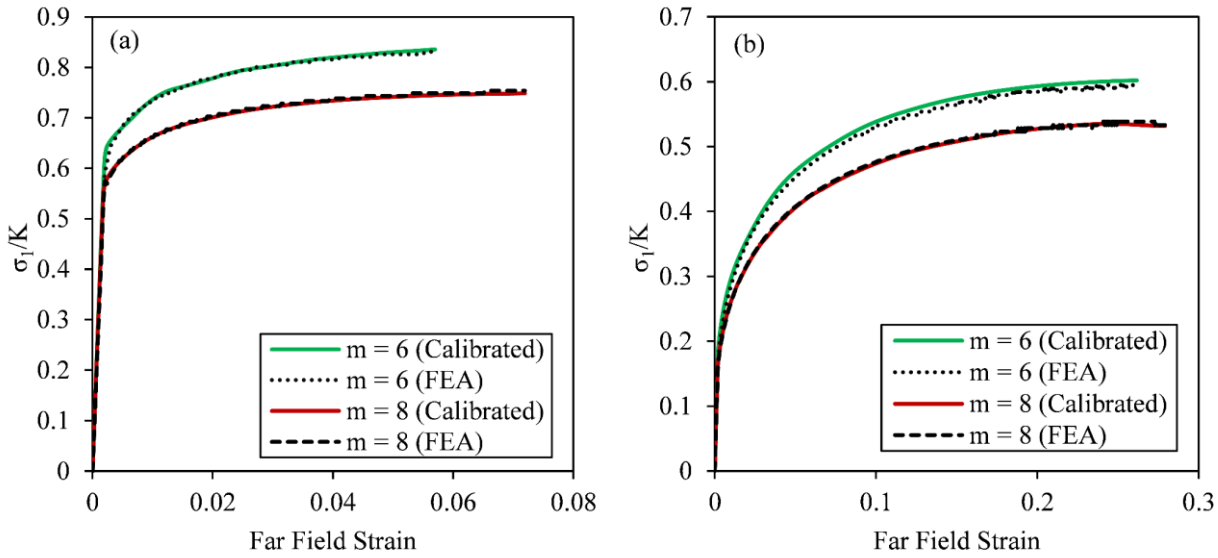

Figure 28: Comparison of calibrated to finite-element calculated engineering stress-strain curves for fine meshed shell models up to the beginning of diffuse necking. Four generic anisotropic materials having HF85-PSC yield function exponents of 6 and 8 with Swift hardening exponents (a) $n = 0.1$ and (b) $n = 0.3$ were considered.

In each of these anisotropic cases, the loading at each point along the gauge width was relatively proportional and between the theoretical limiting states of uniaxial and plane strain tension. As shown in Figure 29 up to the start of diffuse necking, the loading in the middle of the sample was closest to plane strain tension for the higher yield exponent and hardening rate. Nonetheless, the strain state in the center of the gauge width is sufficiently close to the plane strain point in all cases such that the plane strain yield strength can be obtained at the intersection of the calibrated arc with $\beta = 0.5$.

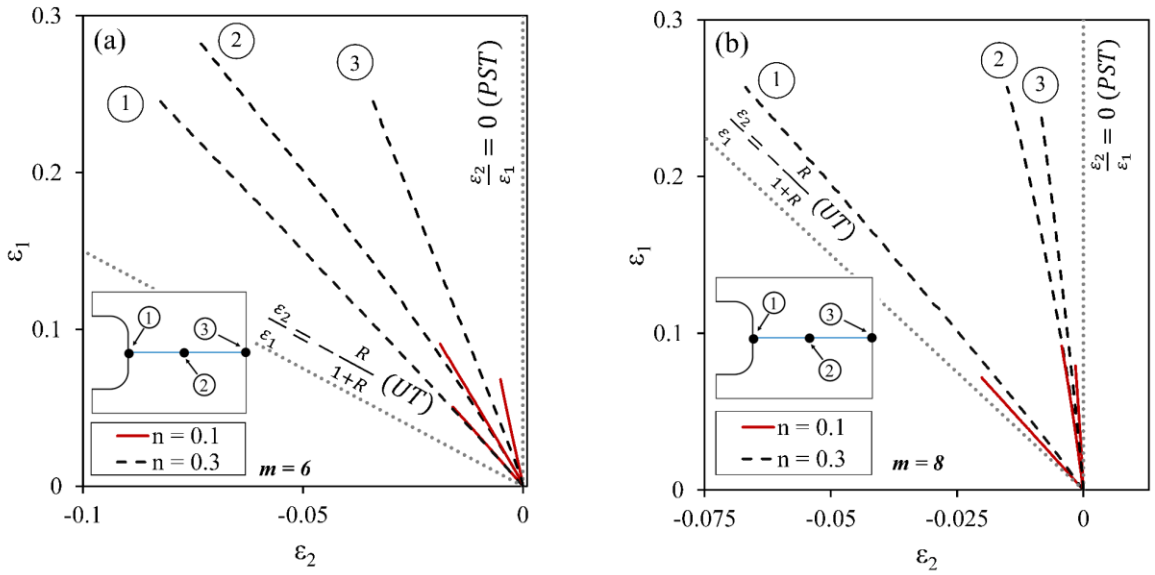

Figure 29: Strain paths corresponding to the edge, middle and centerline nodes of the half symmetry finite-element models up to the beginning of diffuse necking. The four generic materials had Swift hardening exponents of 0.1 and 0.3 and HF85-PSC yield function exponents of (a) 6 and (b) 8.

3.4 Experimental Application

The analysis tools in Vic-3D 8® were used to extract the strain data required for the proposed integration methodology from tests of the Geometry A specimen. The engineering far field strain was measured using a 12 mm virtual extensometer and the strain distribution across the width of the specimen was extracted using the line inspector or "line slice" tool at 200 discrete points. The typical placement of the line slice and extensometer are shown in Figure 30. On average the initial length of the line slice was 37.97 mm and 2.6% smaller than the actual measured gauge width (nominally 39 mm) due to the inability of DIC techniques to capture strain data up to the free edge of a specimen. A scale factor was applied to uniformly stretch the distance between the strain data points to cover the actual measured gauge width. An alternative method of using the strain gradients, at the first and last data points on the line slice, to linearly extrapolate the strains in the missing edge regions, was also considered and found to produce similar results.

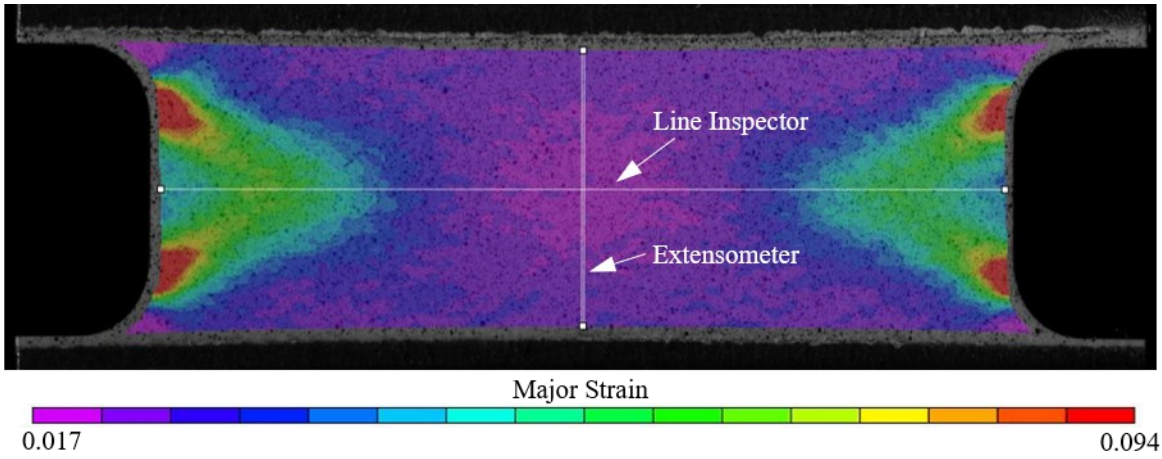

Figure 30: Analysis tools and setup in VIC 3D for a representative repeat of DP1180 in TD at the image corresponding to the necking cut-off.

The extracted strain and load cell data were imported into a custom Matlab® script designed to implement the proposed integration methodology. The DIC data was smoothed using cubic splines and sampled at a maximum major strain increment of 0.2% strain following the work of Min *et al.* (2016). Noise in the strain data was most apparent at the beginning of the test, when strains were small, in the elastic regime and bordering the minimum threshold for DIC measurement. Little noise was observed in the load cell data corresponding to the DP1180, AA6xxx-T4 and AA6xxx-T81 tests, but some oscillations were seen in the hardening response for AA5182-O due to the Portevin-Le Châtelier (PLC) effect. Therefore, the load cell data was also smoothed with cubic splines using approximately 20-30 equally spaced knots. The non-linear region of the hardening response was enforced to be concave down between knots, such that the smoothed curves tracked the average path of the load cell force response between the peaks and valleys of the oscillations. All steps of the methodology described in Section 3 were then performed and the yield function exponent was optimized by calibrating the modelled stress-strain response to match that of the experiment. The procedure was run until the onset of diffuse necking, which was assumed to occur when the major principal strain at any point along the gauge width first exceeded the true strain measured at uniform elongation in a uniaxial tension test in the same direction of analysis.

Due to the discrete nature of the hardening models for the AA6xxx alloys, the code was updated to allow for tabular hardening curve data and improve the optimization algorithm. Rather than evaluate the yield function exponent in increments of 0.05, minimization of the objective functioned employed the more efficient *fmincon* subroutine available in Matlab®. The spline fit hardening curves were inputted as tabular data. At each function call, the table was interpolated using a Piecewise Cubic Hermite Interpolating Polynomial (PCHIP) and the hardening rate obtained using a second order accurate polynomial approximation. Both changes increased the efficiency and accuracy of the integration methodology.

3.5 Results

The modelled engineering stress-strain curve was successfully calibrated to match the experimentally obtained engineering stress-strain curve for each tested repeat along the transverse (TD), rolling (RD) and diagonal (DD) direction of each material. The average calculated HF85-PSC exponent for each direction was used to locally adjust the arc of the yield surface for that material between uniaxial tension (UT) and plane strain tension (PST) to estimate the plane strain yield strength.

3.5.1 Uniaxial-to-Plane Strain Characterization of DP1180

Table 8 shows the selected HF85-PSC yield function exponents that best capture the UT-PST arcs for DP1180, as well as the corresponding plane strain yield strengths in each direction. The average exponents for the TD, RD and DD are 4.89±0.21, 6.12±0.21 and 5.88±0.25, respectively. Although there is some difference in the exponent depending on the material orientation, the results generally agree with the value of 6 commonly taken for BCC materials.

Table 8: HF85-PSC exponents, maximum value of equivalent plastic strain at center point and plane strain yield strengths normalized with respect to direction of analysis and reference direction (RD) for DP1180. Standard deviations are shown in brackets.

	TD				**RD**				**DD**			
	m	$\left(\frac{\sigma_1}{\sigma_o}\right)^{PST}$	$\left(\frac{\sigma_1}{\sigma_o}\right)^{PST}_{Ref}$	ε^p_{eq}	m	$\left(\frac{\sigma_1}{\sigma_o}\right)^{PST}$	$\left(\frac{\sigma_1}{\sigma_o}\right)^{PST}_{Ref}$	ε^p_{eq}	m	$\left(\frac{\sigma_1}{\sigma_o}\right)^{PST}$	$\left(\frac{\sigma_1}{\sigma_o}\right)^{PST}_{Ref}$	ε^p_{eq}
DP1180	4.89 (0.21)	1.135 (0.004)	1.163 (0.004)	0.017 (0.001)	6.12 (0.21)	1.099 (0.003)	1.099 (0.003)	0.022 (0.002)	5.88 (0.25)	1.114 (0.004)	1.119 (0.004)	0.016 (0.001)

The selected exponent for each repeat corresponded to a minimum in the objective function shown in Eq. (3.11). The minimum of the objective function was found by repeating the analysis across yield exponents from 2 to 8 at intervals of 0.05 and then selecting the value of the exponent corresponding to the lowest value of the objective function. The engineering stress-strain curves calibrated for each repeat and direction are shown in Figure 31 through Figure 33. The objective function values are also shown to demonstrate a clear minimization of the least-squared error when the HF85-PSC yield function exponent is correctly selected. Good agreement was observed at the selected exponents between the calibrated and experimental engineering stress-strain curves in each material orientation.

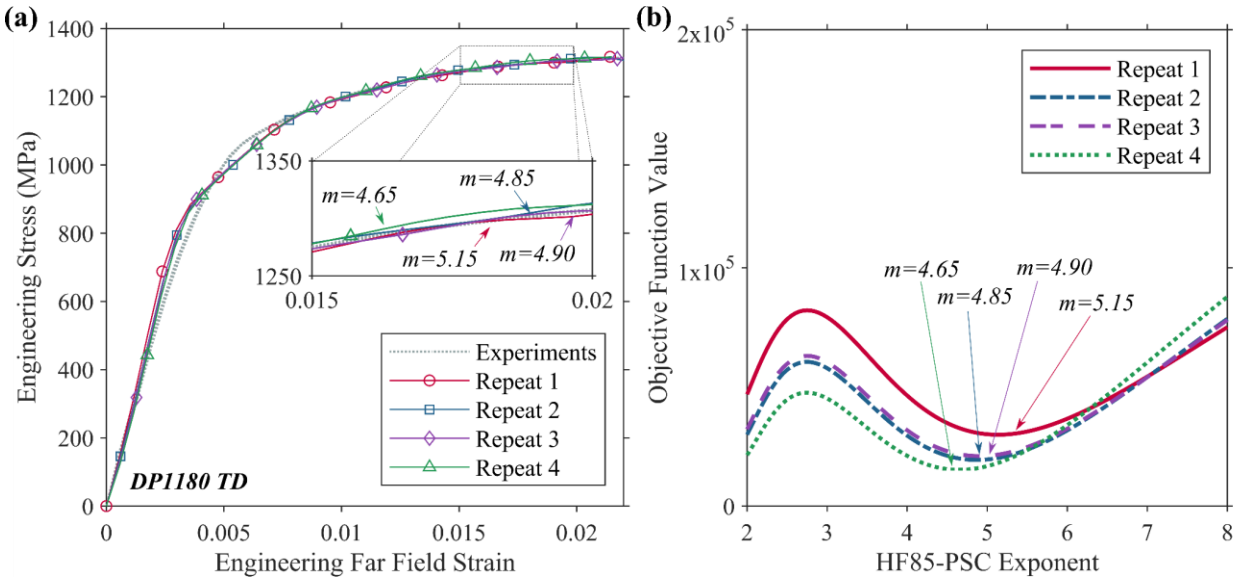

Figure 31: (a) Comparison of calibrated (shown with markers) and experimental engineering stress-strain curves at the selected HF85-PSC exponents that (b) minimize the objective function value for each individual repeat. Results are for DP1180 steel tested in TD.

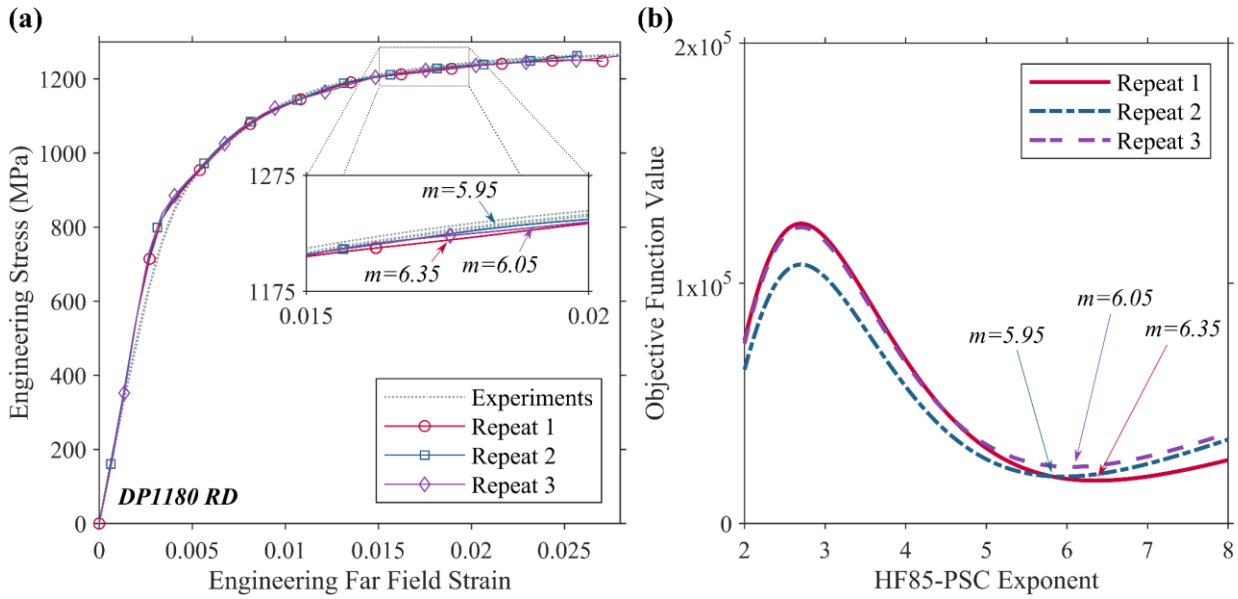

Figure 32: (a) Comparison of calibrated (shown with markers) and experimental engineering stress-strain curves at the selected HF85-PSC exponents that (b) minimize the objective function value for each individual repeat. Results are for DP1180 steel tested in RD.

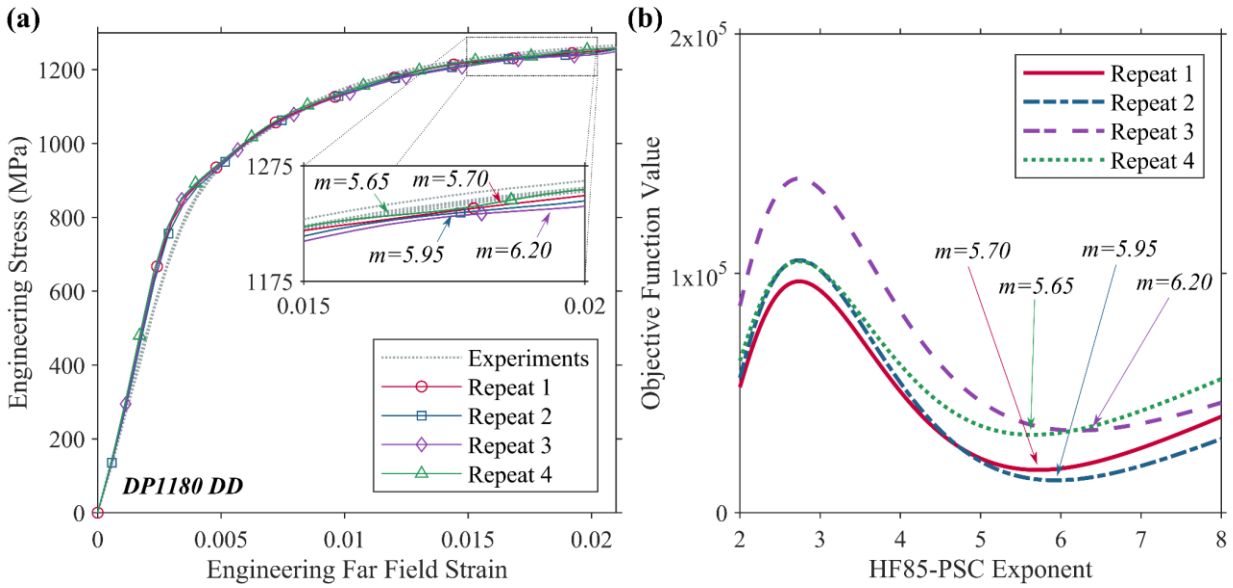

Figure 33: (a) Comparison of calibrated (shown with markers) and experimental engineering stress-strain curves at the selected HF85-PSC exponents that (b) minimize the objective function value for each individual repeat. Results are for DP1180 steel tested in DD.

3.5.2 Uniaxial-to-Plane Strain Characterization of AA5182

Good agreement between each of the calibrated and experimental stress-strain curves was also seen for AA5182-O at the calibrated yield function exponents shown in Table 9. The best calibration was obtained for the RD tests shown in Figure 34 at an average HF85-PSC exponent of 10.68, with a standard deviation of 1.02. In DD and TD, AA5182-O exhibited yield behavior that approximated a Tresca yield surface, which HF85-PSC converges as $m \to \infty$. For practical purposes, values of m up to 50 were considered because the maximum error between the plane strain yield strength at $m = 50$ and as $m \to \infty$ is 1.3% given the R-values for this material. This asymptotic approach to a Tresca surface is illustrated by the objective functions shown in Figure 35 and Figure 36, where further increases to the exponent have little effect on the least-squared error.

Table 9: HF85-PSC exponents, maximum value of equivalent plastic strain at center point and plane strain yield strengths normalized with respect to direction of analysis and reference direction (RD) for AA5182-O. Standard deviations are shown in brackets.

	TD				RD				DD			
	m	$\left(\frac{\sigma_1}{\sigma_o}\right)^{PST}$	$\left(\frac{\sigma_1}{\sigma_o}\right)^{PST}_{Ref}$	ε^p_{eq}	m	$\left(\frac{\sigma_1}{\sigma_o}\right)^{PST}$	$\left(\frac{\sigma_1}{\sigma_o}\right)^{PST}_{Ref}$	ε^p_{eq}	m	$\left(\frac{\sigma_1}{\sigma_o}\right)^{PST}$	$\left(\frac{\sigma_1}{\sigma_o}\right)^{PST}_{Ref}$	ε^p_{eq}
AA5182	50.00 (0.00)	1.011 (0.000)	0.974 (0.000)	0.108 (0.0010)	10.68 (1.02)	1.045 (0.005)	1.045 (0.005)	0.115 (0.007)	50.00 (0.00)	1.013 (0.000)	0.960 (0.000)	0.149 (0.018)

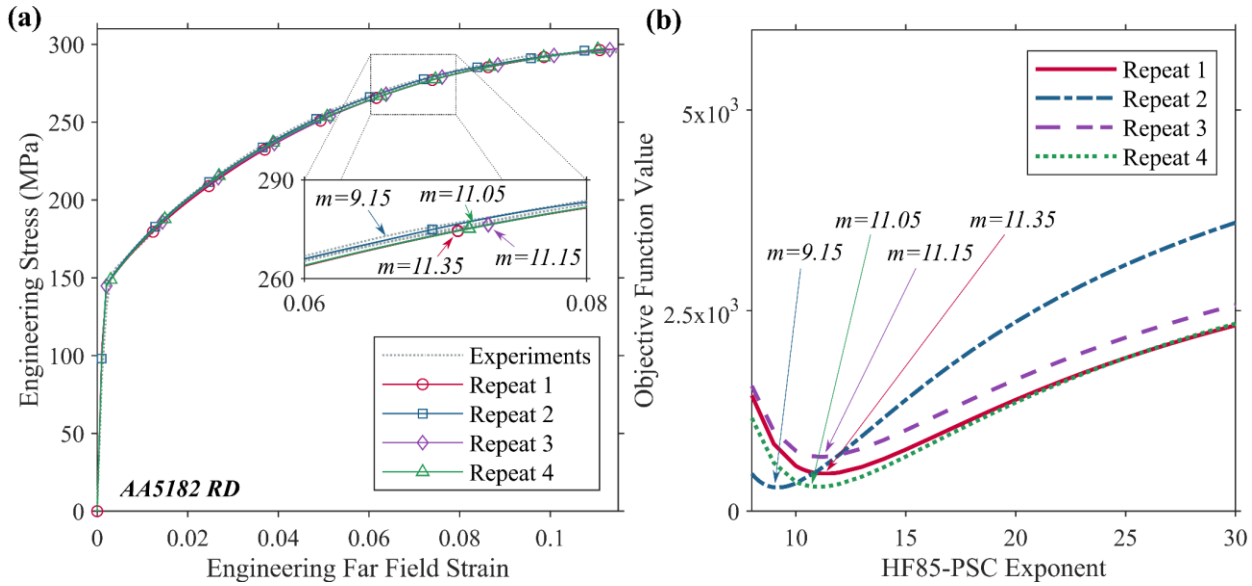

Figure 34: (a) Comparison of calibrated (shown with markers) and experimental engineering stress-strain curves at the selected HF85-PSC exponents that (b) minimize the objective function value for each individual repeat. Results are for AA5182-O aluminum tested in RD.

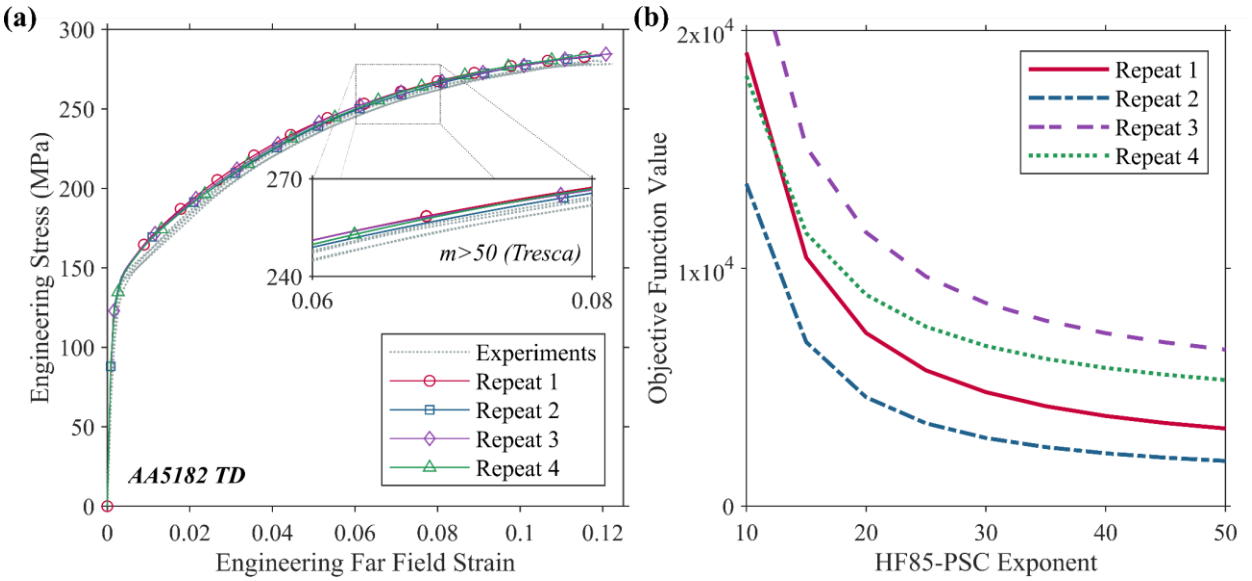

Figure 35: (a) Comparison of calibrated (shown with markers) and experimental engineering stress-strain curves at the selected HF85-PSC exponents that (b) minimize the objective function value for each individual repeat. Results are for AA5182-O aluminum tested in TD.

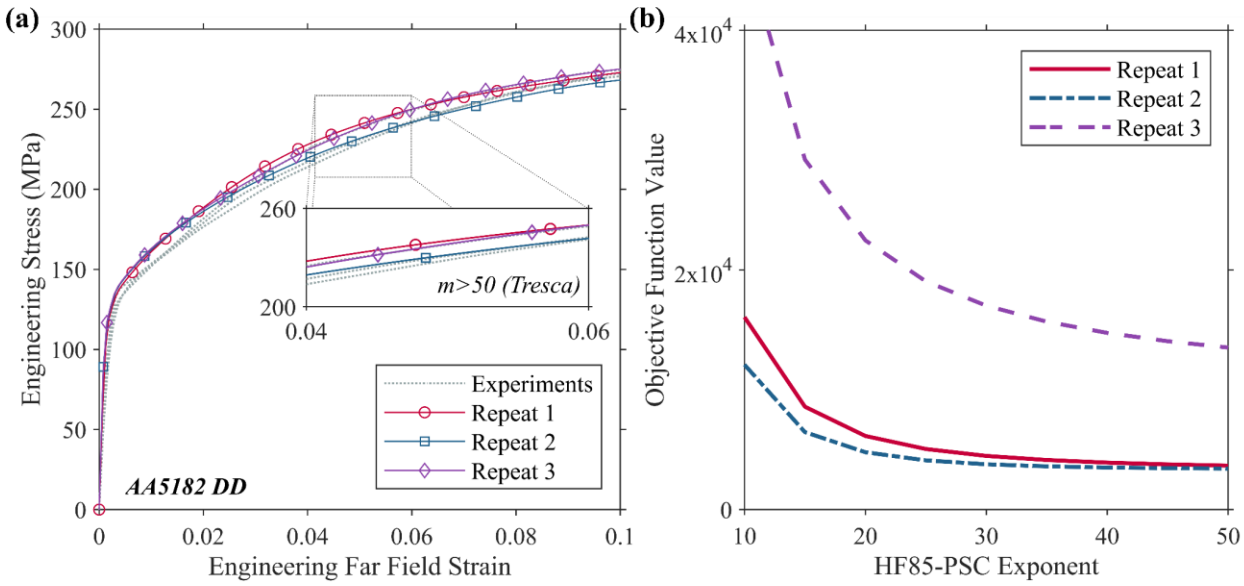

Figure 36: (a) Comparison of calibrated (shown with markers) and experimental engineering stress-strain curves at the selected HF85-PSC exponents that (b) minimize the objective function value for each individual repeat. Results are for AA5182-O aluminum tested in DD.

3.5.3 Uniaxial-to-Plane Strain Characterization of AA6xxx-T4

The selection of Geometry A results in excellent agreement between the experimental and integrated stress strain curves for the AA6xxx-T4 alloy. The integrated curves of Figure 37 were obtained at average HF85-PSC exponents of 4.25±0.46, 6.36±0.42 and 6.28±0.85 along the RD, DD, and TD, respectively. The corresponding plane strain yield strengths, normalized with respect to the rolling direction yield strength, were 1.101±0.006, 1.06±0.005 and 1.055±0.009 along the RD, DD, and TD, respectively. Little anisotropy in the plane strain yield strength was observed for this alloy and the results generally agreed with the plane strain stress ratio of 1.09 for an isotropic FCC material as summarized in Table 10.

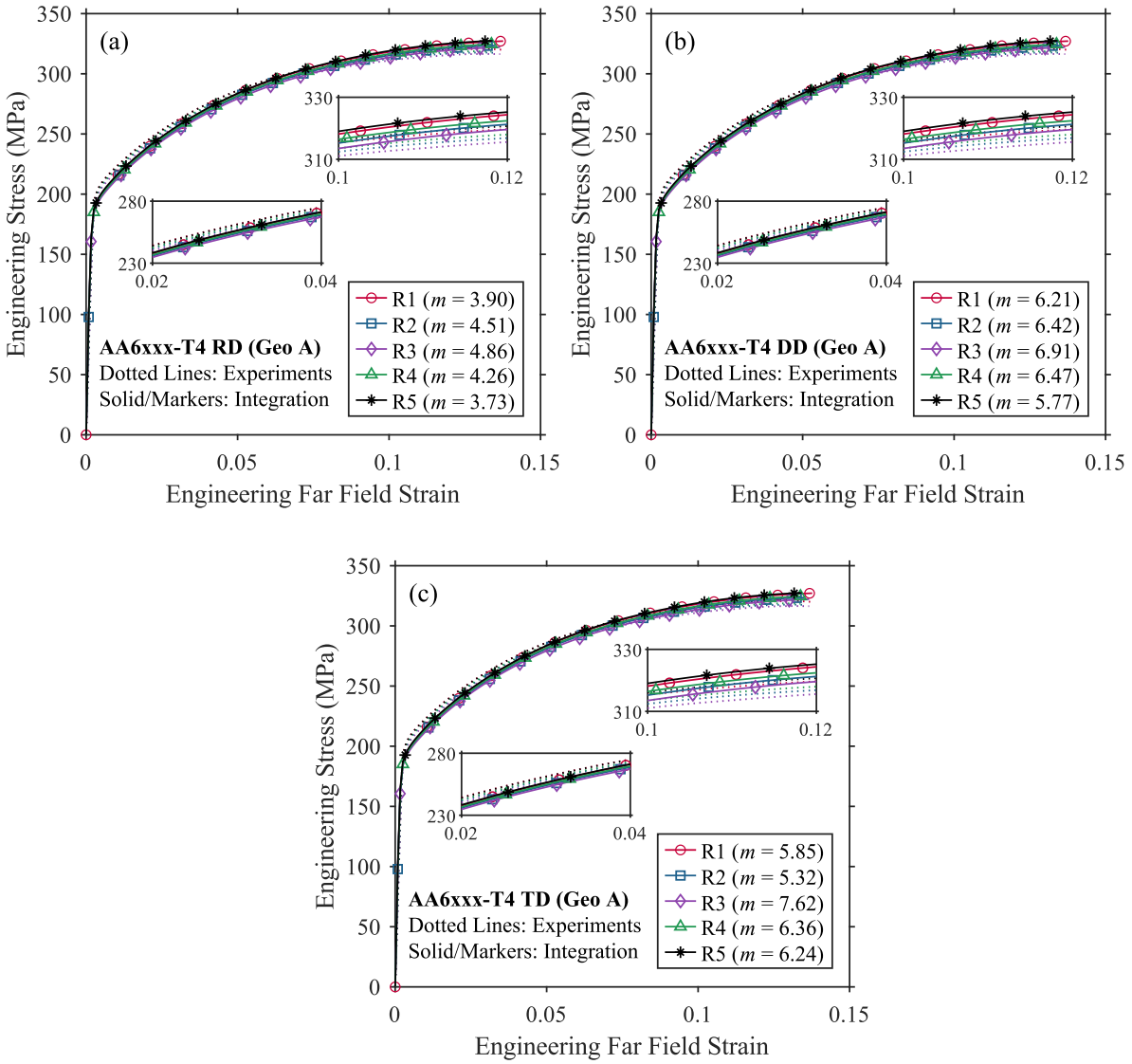

Figure 37: Comparison of integrated and experimental stress-strain curves for each repeat of AA6xxx-T4 tested along the (a) RD, (b) DD and (c) TD. The results are shown for Geometry A at the exponent that minimizes the squared error for each repeat.

Table 10: HF85-PSC exponents and corresponding normalized plane strain yield strengths calibrated up to the indicated equivalent plastic strain reached in the center of the gauge region. Results are shown for the AA6xxx-T4 tested using Geometry A.

Material	RD				DD				TD			
	m	$\left(\frac{\sigma_1}{\sigma_o}\right)^{PST}$	$\left(\frac{\sigma_1}{\sigma_o}\right)^{PST}_{Ref}$	ε^p_{eq}	m	$\left(\frac{\sigma_1}{\sigma_o}\right)^{PST}$	$\left(\frac{\sigma_1}{\sigma_o}\right)^{PST}_{Ref}$	ε^p_{eq}	m	$\left(\frac{\sigma_1}{\sigma_o}\right)^{PST}$	$\left(\frac{\sigma_1}{\sigma_o}\right)^{PST}_{Ref}$	ε^p_{eq}
AA6xxx-T4	4.25 (0.46)	1.101 (0.006)	1.101 (0.006)	0.152 (0.002)	6.36 (0.42)	1.087 (0.005)	1.060 (0.005)	0.159 (0.010)	6.28 (0.85)	1.077 (0.009)	1.055 (0.009)	0.148 (0.008)

3.5.4 Uniaxial-to-Plane Strain Characterization of AA6xxx-T81

For the AA6xxx-T81 alloy, the average yield exponents were found to be 5.06±0.36, 5.88±0.55 and 10.11±1.85 in RD, DD, and TD, respectively. Figure 38 illustrates the excellent agreement between the experiments and the predicted stress-strain curve at these exponents. As summarized in Table 11, corresponding plane strain yield strengths were 1.087±0.005, 1.063±0.006 and 1.030±0.008 along the RD, DD, and TD, respectively. The plane strain yield strength is lower than typically assumed for an isotropic FCC material.

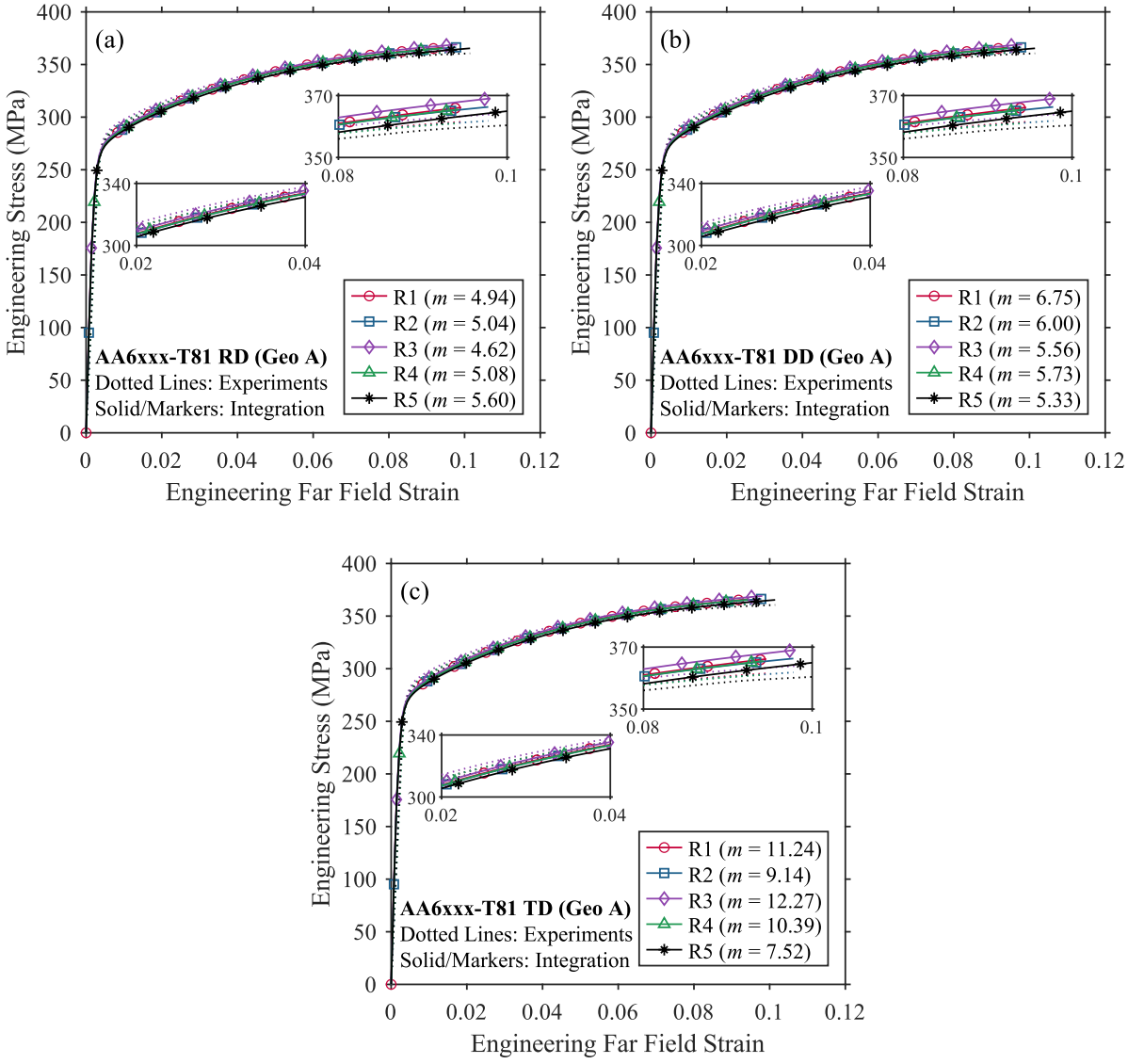

Figure 38: Comparison of integrated and experimental stress-strain curves for each repeat of AA6xxx-T81 tested along the (a) RD, (b) DD and (c) TD. The results are shown for Geometry A at the exponent that minimizes the squared error for each repeat.

Table 11: HF85-PSC exponents and corresponding normalized plane strain yield strengths calibrated up to the indicated equivalent plastic strain reached in the center of the gauge region. Results are shown for the AA6xxx-T81 alloy tested using Geometry A.

Material	RD				DD				TD			
	m	$\left(\frac{\sigma_1}{\sigma_o}\right)^{PST}$	$\left(\frac{\sigma_1}{\sigma_o}\right)^{PST}_{Ref}$	ε^p_{eq}	m	$\left(\frac{\sigma_1}{\sigma_o}\right)^{PST}$	$\left(\frac{\sigma_1}{\sigma_o}\right)^{PST}_{Ref}$	ε^p_{eq}	m	$\left(\frac{\sigma_1}{\sigma_o}\right)^{PST}$	$\left(\frac{\sigma_1}{\sigma_o}\right)^{PST}_{Ref}$	ε^p_{eq}
AA6xxx-T81	5.06 (0.36)	1.087 (0.005)	1.087 (0.005)	0.102 (0.004)	5.88 (0.55)	1.077 (0.006)	1.063 (0.006)	0.089 (0.005)	10.11 (1.85)	1.040 (0.008)	1.030 (0.008)	0.100 (0.006)

3.5.3 Sensitivity to DIC Parameters and Strain Discretization

The sensitivity of the plane strain yield strength to the VSGL, number of points along the line slice and major strain increment size is illustrated in Figure 39 for a representative repeat of DP1180 in the diagonal direction and AA5182-O in the rolling direction. These particular cases are included because they showed the maximum sensitivity out of all the tested directions and materials. The VSGL was calculated as the multiple of the step size (pixels), camera resolution (mm/pixel) and filter size, with values of approximately 0.15, 0.25, 0.5 and 1.0 mm selected for the sensitivity study. The plane strain yield strength, corresponding to the optimized exponent obtained from the integration methodology, was calculated at each combination of VSGL with major principal strain increments of 0.05%, 0.1%, 0.2% or 0.5% strain and with 25, 50, 100, 200 or 400 points extracted along the line slice. Convergence with respect to the number of points along the line slice was obtained at values above 100-200 points. The strain increment had a negligible effect on the results but the effect of the VSGL was difficult to quantify. Nonetheless across the range of parameters considered in this sensitivity study, the maximum variation in the normalized plane strain yield strength was 8×10-3, or a percentage difference of 0.71%. Therefore, in all cases selecting 200 points along the line slice, a 0.5 mm VSGL and 0.2% strain increment was found to be reasonable. It is important that the same parameters be selected for all directions and materials to allow for consistent comparison between the results.

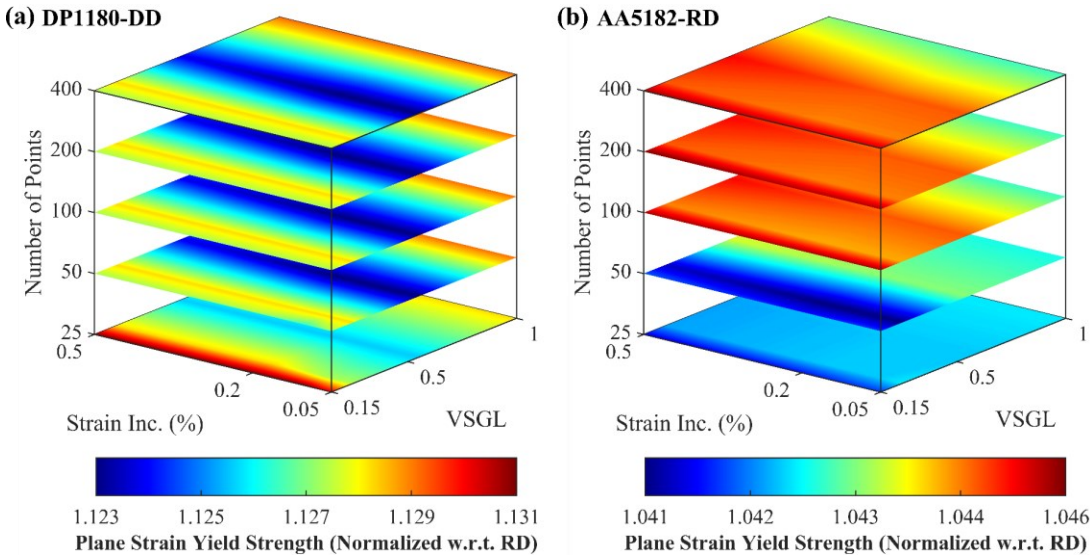

Figure 39: Effect of VSGL, number of points taken along line slice and major strain increment on the normalized plane strain yield strength for a representative repeat of (a) DP1180 tested along the DD and (b) AA5182 tested along the RD.

3.6 Discussion

The developed methodology is a novel, simple method to predict the plane strain yield strength of a sheet metal directly from experimental data using Digital Image Correlation. It is illustrative to compare these results to the cruciform test data available in the literature and already summarized in Table 7. While no studies of DP1180 were found, the other dual phase steels (Materials 3, 4, 5 and 11) showed average normalized plane strain yield strengths of 1.09 along the RD and 1.13 along the TD, within 1-3% of the values determined in this thesis (1.099 along the RD and 1.163 along the TD). Yamanaka and Kuwabara's (2015) analysis of an AA5182 resulted in normalized plane strain yield strengths of 1.075 along the RD and 1.044 along the TD, 3-7% higher than the values of 1.045 along the RD and 0.974 along the TD identified in this thesis. The stronger Tresca-type behavior may be attributed to batch specific texture or non-associated flow. The identified plane strain yield strengths of 1.03 to 1.101 for the AA6xxx alloys are comparable to those obtained in the literature from cruciform tests; the average of Materials 6, 7, 8, 20 and 21 in Table 7 is 1.06 along the RD and 1.05 along the TD, within 2-4% of the results reported in this chapter.

For both the AA6xxx-T4 and AA6xxx-T81 alloys, the integrated engineering stress is lower at small deformations than observed experimentally, while at larger strains the converse is true. Flattening of the yield surface with increasing deformation is an expected consequence of texture evolution in AA6xxx alloys, as reported previously by Kuwabara *et al.* (2017). One exponent cannot adequately model the uniaxial-to-plane strain region of the yield surface over the entire range of deformation because the hardening rate in plane strain tension differs from that in uniaxial tension. Better agreement would be

obtained using a differential hardening model, where the yield surface shape and exponent changes with deformation to match the anisotropic work hardening of different load conditions.

3.7 Summary of a Methodology for Uniaxial to Plane Strain Tension Characterization

Plane strain notch tensile tests are favorable due to their relative simplicity and ease of testing, but accurate determination of the plane strain yield behavior is difficult using conventional means of analysis due to a complicated stress state distribution along the gauge width that varies between uniaxial and plane strain tension. As a novel solution, a constrained form of the Hosford's 1985 (HF85) yield criterion (1985) was identified as an intermediary criterion with the flexibility and simplicity to locally calibrate the arc of a yield surface from uniaxial to plane strain tension and modified to enforce the generalized plane strain constraints of Butcher and Abedini (2019). An elastic-plastic, associated flow constitutive model was built around the plane strain constrained HF85-PSC yield criterion and applied to strain data captured using Digital Image Correlation during plane strain notched tensile tests. The yield function exponent, which controls the shape of the constrained yield surface from uniaxial-to-plane strain tension, was identified based upon equilibrium of the numerically integrated force and experimentally measured force. Finite-element simulations of plane strain notch tests using von Mises, BCC ($m = 6$) and FCC ($m = 8$) materials with moderate ($n = 0.1$) and high hardening ($n = 0.3$) rates were used to show that the proposed methodology accurately and robustly predicts the correct yield function exponent when using an analogous analysis procedure to that developed for the experimental DIC based approach. The methodology was applied to experimental plane strain notch tensile test data for DP1180, AA5182, AA6xxx-T4 and AA6xxx-T81 tested along the transverse, rolling and diagonal directions. The results reported in this analysis were within 1-7% of corresponding cruciform test data available in the literature for similar alloys.

It is important to recognise that the methodology presented in this chapter is a rather narrow application of an associated flow, isotropic hardening model to a single geometry. Some materials are better described by differential hardening or non-associated flow models and numerous notch geometries of different aspect ratios exist. Chapter 4 discusses how to relax the constraints of the methodology to account for non-associated flow and differential hardening while evaluating the choice of Geometry A versus Geometry B.

Chapter 4 Extensions to the Plane Strain Characterization Methodology

The accurate constitutive characterization of sheet materials hinges not only on the assumptions embedded in the analysis, for instance associated flow and isotropic hardening, but also the assumption that the experimentally derived properties are independent of test geometry. The analysis of Chapter 3 suggests that the proposed methodology applies to associated flow, isotropic hardening sheet materials tested using the plane strain notch specimen developed by Vegter and van den Boogaard (2006). However, many different plane strain notch specimens exist (Wagoner, 1980; Aretz *et al.*, 2007; An *et al.*, 2004) and some materials may be better described by a non-associated flow and/or anisotropic hardening model. The intent of this chapter is to extend the methodology from Chapter 3 to differential hardening and non-associated flow as well as compare the results obtained using the Vegter and van den Boogaard (2006) geometry (Geometry A) to those obtained from Geometry B used for plane strain fracture characterization.

4.1. Experimental Testing of AA6xxx-T81 and AA6xxx-T4 Plane Strain Notch Specimens Using Geometry B

AA6xxx-T81 and AA6xxx-T4 were tested using Geometry B and the strains extracted at 200 points along the gauge width using the line slice tool in Vic-3D 8®. However, the optimized exponent was particularly sensitive to the placement of the line slice due to the tangential and radial orientation of the principal stresses around the notch. Only at the notch root is the tangential (major principal) stress exactly aligned with the loading axis. If the line slice were errantly placed higher or lower than the notch root, the major principal stress vector at points near the notch would be at an angle to the loading axis and the overall force would no longer be described by Eq. (3.10). Therefore, the DIC data was carefully extracted by placing the line slice directly through the root of each notch. Geometry A is less sensitive to the placement of the line slice since the notches are outside the area of interest, meaning that the principal stress and loading axes coincide along the entire gauge width.

The missing strain data, between the ends of the line slice and the free edges of the Geometry B specimen, accounts for a larger percentage of the overall gauge width compared to Geometry A. The average line slice was 16% shorter than the measured gauge width for Geometry B, versus only 3% shorter for Geometry A. Therefore, rather than scale the line slice data, the *Fill Boundary* setting in Vic-3D 8® was used to two-dimensionally extrapolate the missing data based on the strain gradients of neighbouring subsets (Correlated Solutions, n.d.). After employing the *Fill Boundary* setting, the required scaling factor decreased to just 1.05. The difference between the strain contours, with and without the setting applied, is clearly visible in Figure 40. Applying the Fill Boundary setting reduced the objective function error by 19-

28%, shown in Figure 41, by improving the agreement between the integrated and experimental stress-strain curves.

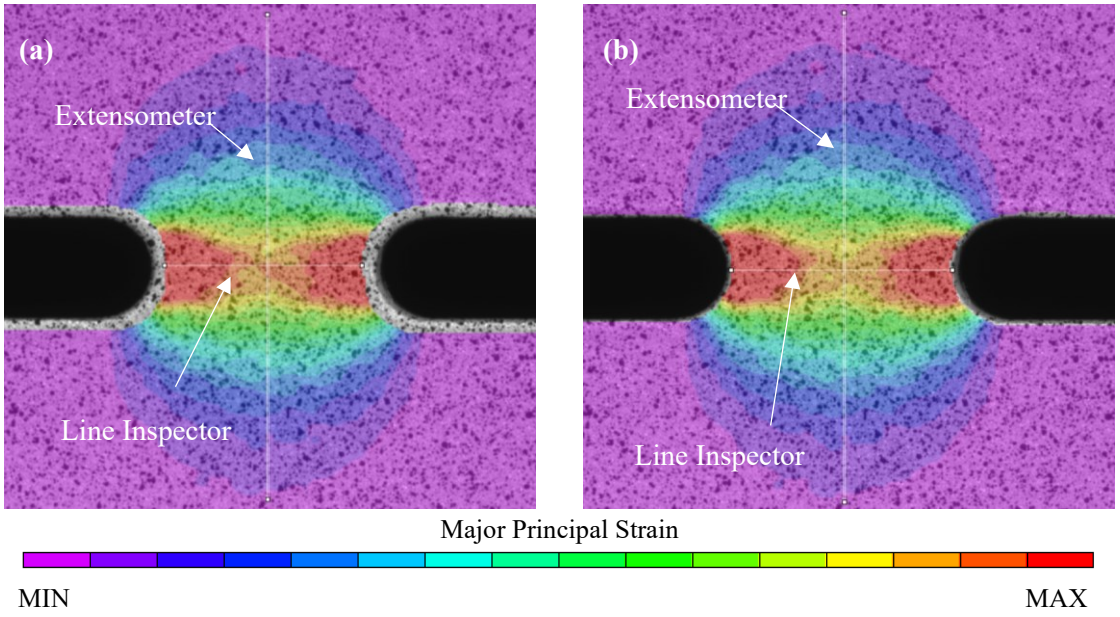

Figure 40: Typical placement of line inspector and extensometer for Geometry B (a) without the *Fill Boundary* setting applied and (b) with the *Fill Boundary* setting applied. Results are shown for a representative repeat of AA6xxx-T4 tested along the RD.

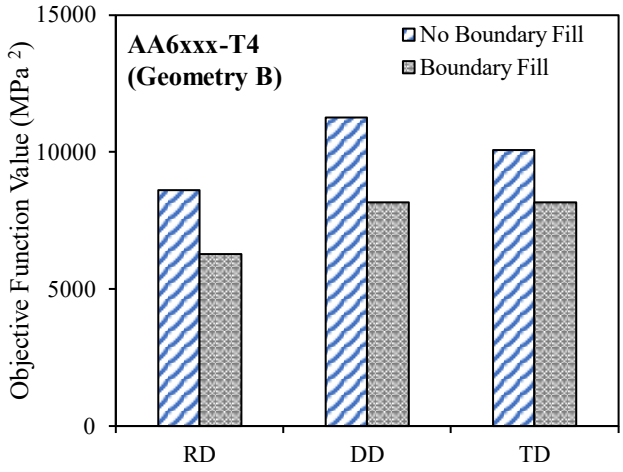

Figure 41: Effect of the Fill Boundary Setting on the objective function error for a representative repeat of the AA6xxx-T4 alloy tested along the RD, DD, and TD. The improvement was of a similar magnitude for the AA6xxx-T81 alloy.

4.2 Experimental Results for AA6xxx-T81 and AA6xxx-T4 Using Geometry B

Overall, good agreement was observed between the integrated and experimental stress-strain curves using Geometry B as shown in Figure 42 and Figure 43 for the AA6xxx-T81 and AA6xxx-T4 alloys, respectively. The exponents identified for AA6xxx-T4 using Geometry B were 4.47±0.38, 4.45±0.19 and

4.72±0.68 along the RD, DD, and TD, respectively. The corresponding normalized plane strain yield strengths were between 1.074±0.009 and 1.098±0.005, and within just 2.5% of the values identified using Geometry A. Exponents of 2.64±0.25, 3.27±0.68 and 3.72±0.53 were calibrated for the AA6xxx-T81 alloy along the RD, DD, and TD, respectively. The corresponding normalized plane strain yield strengths were 1.115, 1.093±0.007 and 1.078±0.005 along RD, DD, and TD, respectively. Note that along the rolling direction, the plane strain yield strength was at the upper bound of the range of the HF85-PSC function (see Figure 20). The identified plane strain yield strengths are within 5% difference of the values identified using Geometry A and on average are representative of the commonly assumed value of 1.09 for an isotropic FCC alloy.

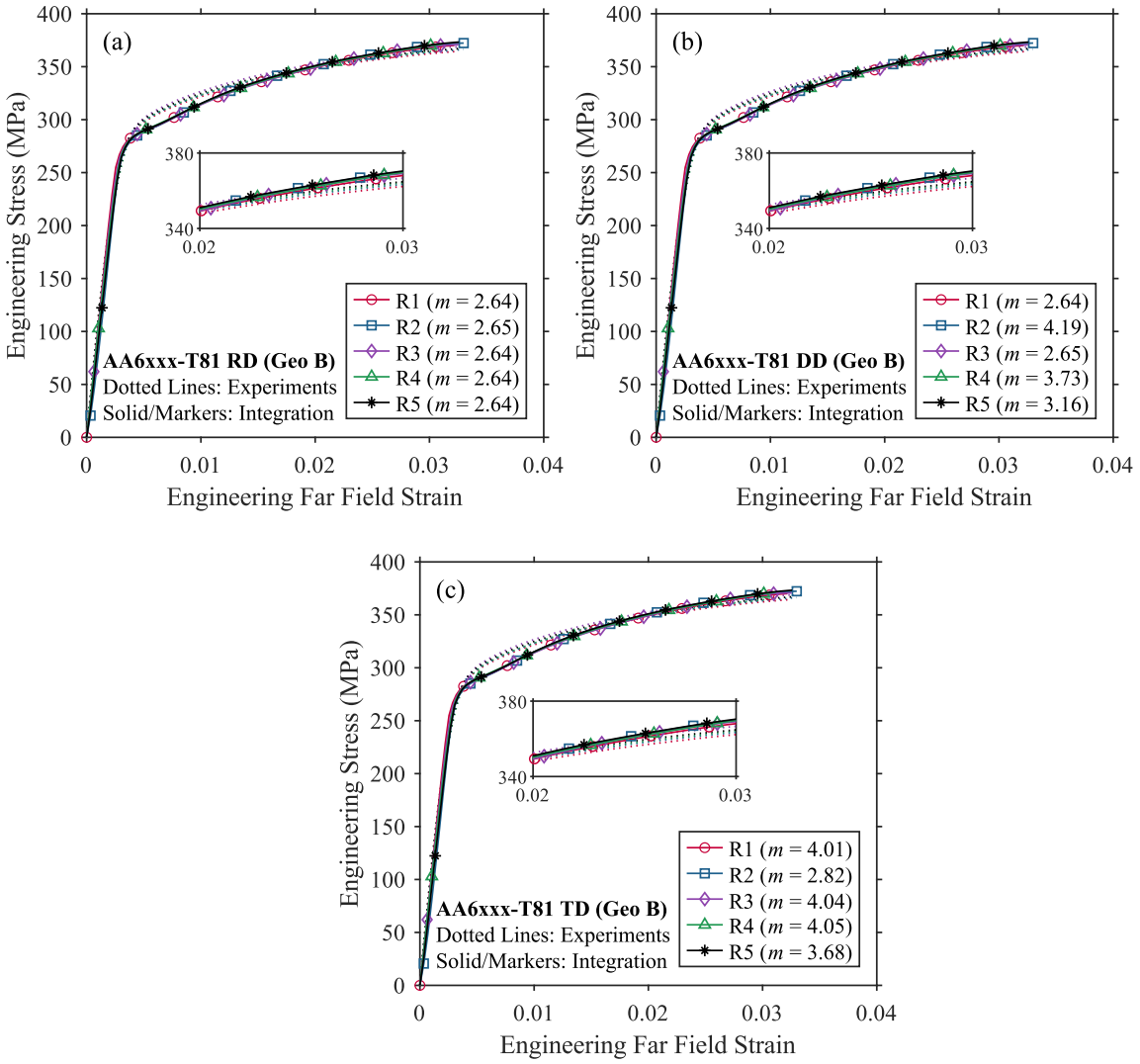

Figure 42: Comparison of integrated and experimental stress-strain curves for each repeat of AA6xxx-T81 tested along the (a) RD, (b) DD and (c) TD. The results are shown for Geometry B at the exponent that minimizes the squared error for each individual repeat. Note that the lower bound of the optimized exponent is 2.64 along the RD and TD and 2.61 along the DD.

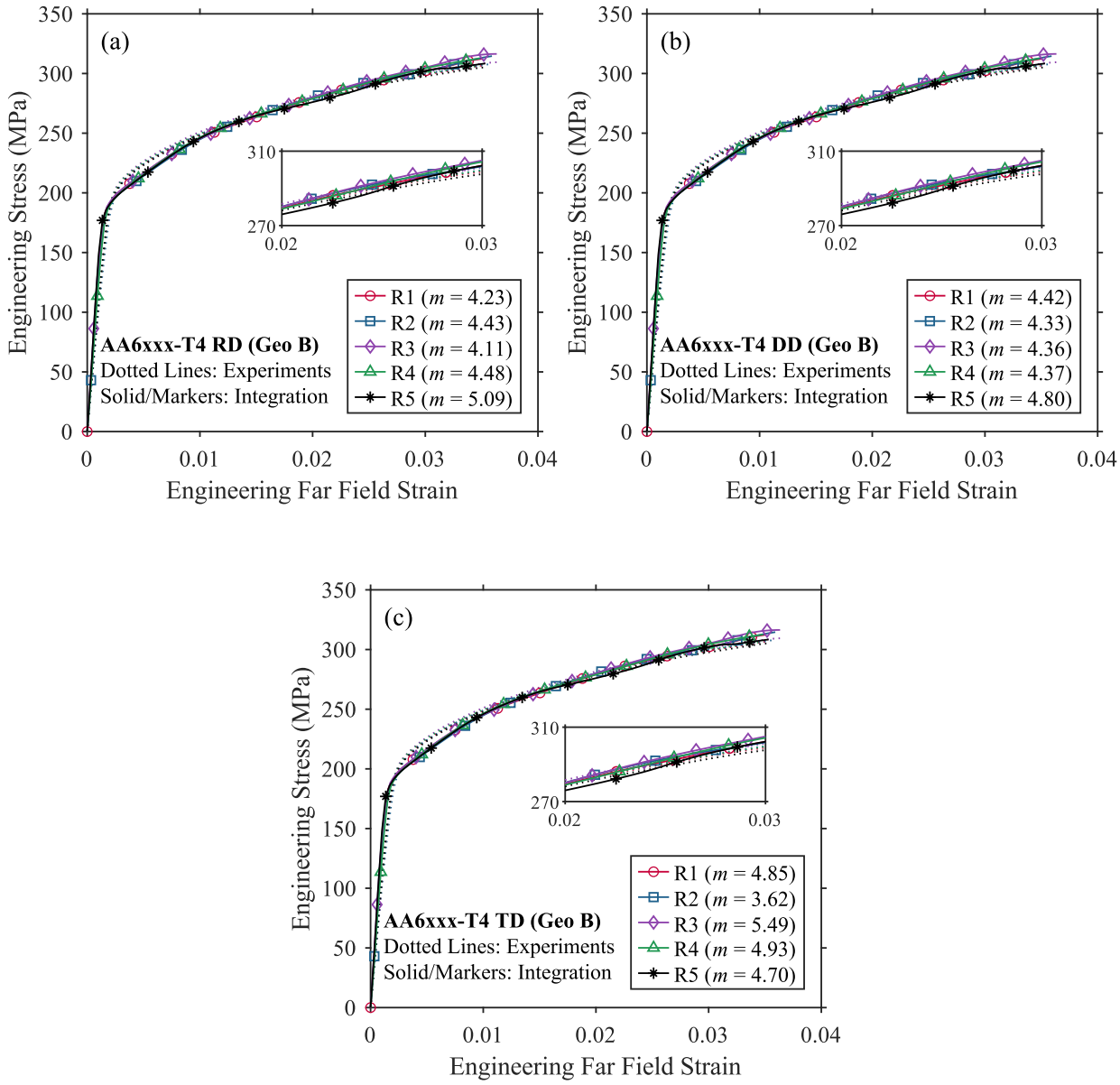

Figure 43: Comparison of integrated and experimental stress-strain curves for each repeat of AA6xxx-T4 tested along the (a) RD, (b) DD and (c) TD. The results are shown for Geometry B at the exponent that minimizes the squared error for each individual repeat.

The test results for Geometry B are summarized in Table 10 and compared to Geometry A in Figure 44. The exponent was calibrated to, on average, a ~50% higher equivalent plastic strain in the center of the gauge region for the Geometry A, compared to Geometry B. For AA6xxx-T4, the calibrated plane strain yield strength is relatively consistent for both geometries. However, for AA6xxx-T81, the plane strain yield strength calibrated using Geometry B is substantially higher than the value obtained using Geometry A.

Table 12: HF85-PSC exponents and corresponding normalized plane strain yield strengths calibrated up to the indicated equivalent plastic strain reached in the center of the gauge region. Results are shown for the AA6xxx-T4 and AA6xxx-T81 alloys tested using Geometry B.

Geo.	Material	RD				DD				TD			
		m	$\left(\frac{\sigma_1}{\sigma_o}\right)^{PST}$	$\left(\frac{\sigma_1}{\sigma_o}\right)^{PST}_{Ref}$	ε^p_{eq}	m	$\left(\frac{\sigma_1}{\sigma_o}\right)^{PST}$	$\left(\frac{\sigma_1}{\sigma_o}\right)^{PST}_{Ref}$	ε^p_{eq}	m	$\left(\frac{\sigma_1}{\sigma_o}\right)^{PST}$	$\left(\frac{\sigma_1}{\sigma_o}\right)^{PST}_{Ref}$	ε^p_{eq}
B	AA6xxx-T4	4.47 (0.38)	1.098 (0.005)	1.098 (0.005)	0.079 (0.002)	4.45 (0.19)	1.115 (0.003)	1.087 (0.003)	0.086 (0.003)	4.72 (0.68)	1.096 (0.009)	1.074 (0.009)	0.083 (0.007)
	AA6xxx-T81	2.64 (0.25)	1.115 (0.000)	1.115 (0.000)	0.082 (0.003)	3.27 (0.68)	1.108 (0.007)	1.093 (0.007)	0.077 (0.005)	3.72 (0.53)	1.088 (0.005)	1.078 (0.005)	0.088 (0.003)

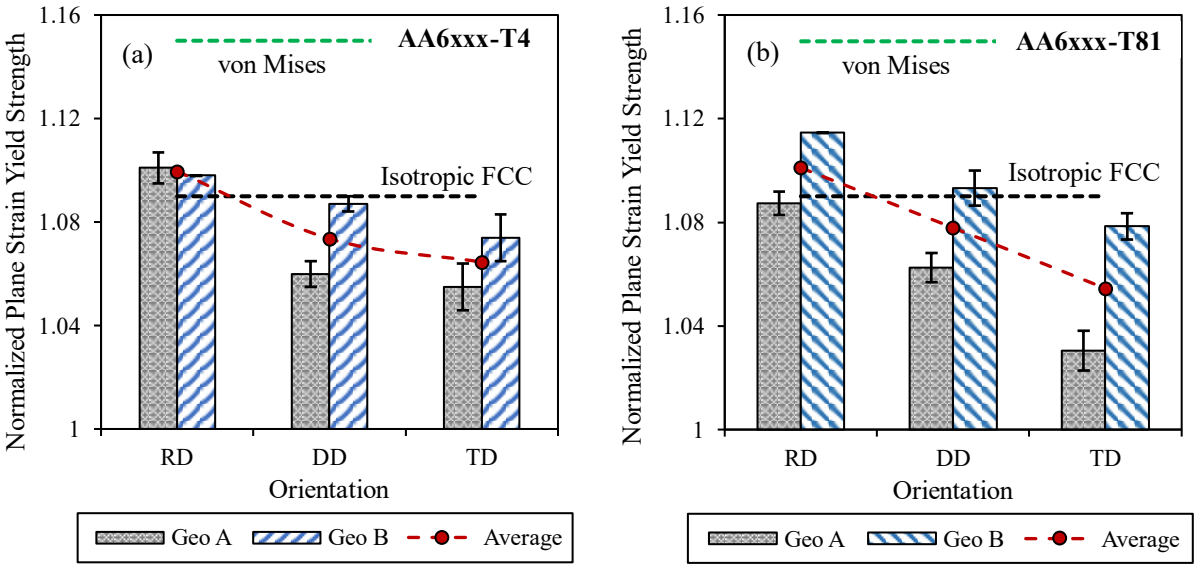

Figure 44: Normalized plane strain yield strengths for each geometry and in each tested direction for (a) AA6xxx-T4 and (b) AA6xxx-T81.

4.3 The Aspect Ratio Effect

The choice of Geometry A or Geometry B has a large influence on the calibrated normalized plane strain yield strength, despite the plane strain yield strength being a material property. As shown in Figure 44, the geometry difference is statistically significant except for the tests along the rolling and transverse directions of AA6xxx-T4. For AA6xxx-T81, there is a 2-5% difference between the normalized plane strain yield strengths identified using each geometry.

The geometry bias is primarily due to the width-to-thickness (aspect) ratio of the specimen and consequent validity of the plane stress assumption. Plane stress occurs if the stress in the through-thickness direction is equal to zero across the gauge width. However, plane stress is only an appropriate assumption for geometries having a small thickness in relation to the other dimensions. Geometry A has a gauge width

of 39 mm, or an aspect ratio of 14.44 for the 2.7 mm thick AA6xxx-T81 material. In contrast, Geometry B has a gauge width of 7.15 mm, or an aspect ratio of just 2.65 for the same material. The smaller the aspect ratio, the larger the departure from plane stress. The free surfaces, where DIC is applied, remain plane stress but a through-thickness stress-gradient develops which cannot be measured and included in the integration which uses the surface strains.

To illustrate, half-symmetry models employing Geometry B and a von Mises material having power law hardening behavior ($n = 0.1$) were simulated in LS-DYNA using explicit dynamic time integration. A shell model and three solid models with thicknesses of 2.7 mm, 1.5 mm and 1 mm were modelled to represent the sheet thicknesses of the actual materials used in this thesis. In all cases, the characteristic element size was 0.25 mm with 10, 6 and 4 elements through the thickness of the 2.7 mm, 1.5 mm, and 1 mm solid models, respectively. In all cases, reduced integration Type 1 solid/shell elements were used with Type 6 hourglass control. The force, engineering strain from using 16 mm extensometer, and major/minor strains along the surface of the gauge width were extracted from the model. Treating each model as a "virtual experiment", the major/minor strains were integrated using an exponent of $m = 2$ following the proposed cutting line approach.

The error between the engineering stress measured in LS-DYNA and the integrated stress increases with the model thickness as shown in Figure 45. As expected, excellent agreement was obtained using shell elements since they are by nature plane stress. As the thickness of the solid model increases, a 3-D stress state develops at the notch root and promotes greater work hardening, flow stress and strain in the interior of the specimen than measured at the surface. Integrating the surface strains underpredicts the stress-strain response since the contribution of the larger stresses and strains acting on elements in the interior of the specimen is not captured.

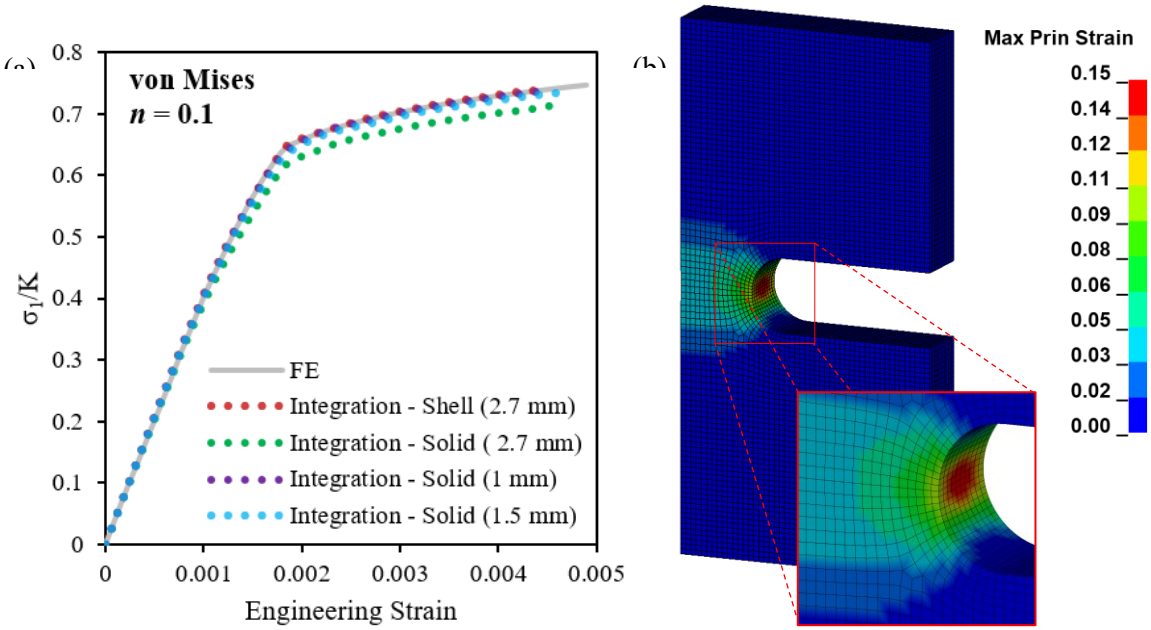

Figure 45: (a) Actual stress-strain response obtained from the LS-DYNA simulated force compared to the integrated stress for shell and solid models of 1 mm, 1.5 mm, and 2.7 mm thickness. All models employed a von Mises material with a power law hardening exponent of 0.1. (b) Contours of major principal strain for the 2.7 mm thick model. At the cutoff point, the maximum major strain on the surface of the specimen is 0.1 but the major strain in the interior of the specimen at the notch root is 0.15.

Since Geometry A does not have a rounded notch in the gauge region, the stress state remains relatively plane stress along the entirety of the line slice where the major and minor strains are extracted for the integration. As a result, it is less sensitive to sheet thickness due to both the absence of the notches and a larger gauge width that promotes plane stress. By the same virtue, Geometry A is less suited for finite-element modelling and fracture characterization since necking and fracture occur at the notch edges, not in the center of the gauge region in plane strain. Extrapolation bias is introduced based on the choice of hardening model as the equivalent strain at the notch is in the post-uniform region of the hardening curve, while the strains along the gauge width are still below the cutoff point. In contrast, Geometry B yields, necks, and fractures in the center of the gauge region making it more suitable for finite-element modelling and especially plane strain fracture characterization. Ideally fracture and constitutive characterization could be completed using one test, making it beneficial to determine the maximum sheet thickness for which Geometry B may be used or alternatively a scaled geometry to suit a particular sheet thickness.

The relationship between the integration error and the specimen aspect ratio was investigated in LS-DYNA comparing Geometry A with single, double, and triple-scaled models of Geometry B at sheet thicknesses of 1 mm, 1.5 mm, and 2.7 mm. In all cases a von Mises material was used with power law hardening exponents of n = 0.1 and n = 0.3. All cases employed Type 1 elements with a characteristic dimension of 0.25 mm in the gauge region. The surface strains were extracted along a line through the

center of the gauge region and integrated in Matlab®, analogous to the DIC based methodology. The percentage error between the integrated and engineering stress from LS-DYNA at the necking cutoff (i.e., when $\varepsilon_1 = 0.1$ or $\varepsilon_1 = 0.3$) was calculated for each material and geometry.

The relationship between the error and the aspect ratio was found to be logarithmic, as shown in Figure 46, with a coefficient of determination of 0.91. At low aspect ratios (as in the case of Geometry B), the integration error was 3-5%. Scaling Geometry B by a factor of three decreased the error to less than 1%. However, Geometry A consistently showed the lowest percentage error of less than 0.24%. The significance of the aspect ratio must be considered in the selection of an appropriate geometry for a given sheet thickness.

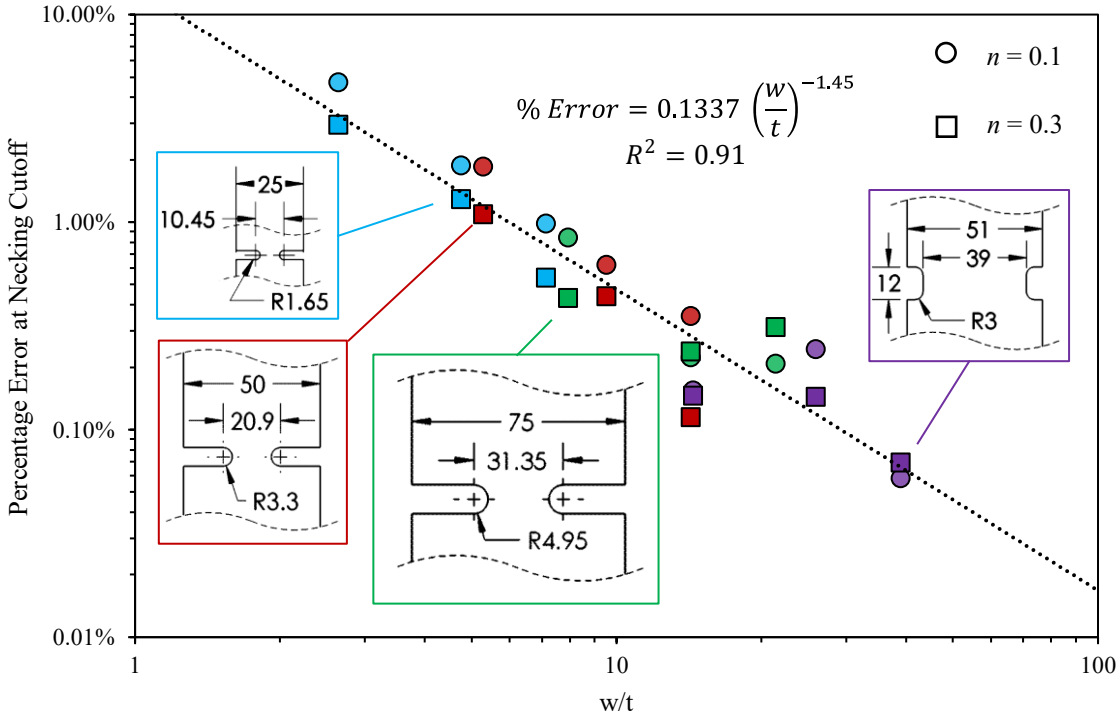

Figure 46: Percentage error at necking cutoff ($\varepsilon_1 = n$) as a function of width to thickness (w/t) ratio for von Mises materials with power law hardening exponents of $n = 0.1$ and $n = 0.3$. The studied geometries include Geometry A and single, double, and triple-scaled versions of Geometry B at sheet thicknesses of 1 mm, 1.5 mm, and 2.7 mm.

4.3.1 Aspect Ratio Correction Factor

The design chart correlation suggests an empirical correction of a given sample geometry to minimize the error caused by a departure from plane stress conditions and a less-than-ideal aspect ratio. As shown in Figure 45, decreasing the aspect ratio decreases the integrated stress response but the hardening rate and percentage error at each point past the proportionality limit remain the same. It follows that a suitable correction would be to scale the integrated stress response, prior to evaluating the objective function of Eq.

(3.11). The modified objective function, incorporating the aspect ratio correct factor f_{geo}, is shown in Eq. (4.1).

$$SE = \sum_{E_{1y}{}^{DIC}=0}^{End} \left\{ \frac{1}{w_o t_o} \left[f_{geo} F^{model}\left(E_{1y}{}^{DIC}\right) - F^{exp}\left(E_{1y}{}^{DIC}\right) \right] \right\}^2 \tag{4.1}$$

The value of f_{geo} is obtained from the design chart curve fit as:

$$f_{geo} = \frac{1}{1 - 0.1337\left(\frac{w_o}{t_o}\right)^{-1.45}} \tag{4.2}$$

4.3.2 Design Chart Evaluation

To evaluate the trend shown in the design chart of Figure 39, three repeats of the triple-scaled notch Geometry B were tested along the RD of the 2.7 mm thick AA6xxx-T81. To be consistent with the post-processing of Geometry A, the *Fill Boundary* setting was turned off. At this aspect ratio of 7.94, the design chart suggests that the percentage error in the engineering stress should be less than 1% and in relative agreement with the results of Geometry A. In practice, the percentage error may be different due to anisotropy and different hardening behavior. Two hundred points were extracted along the line slice through the center of the gauge width. Measurement of the far field strain employed a 48 mm extensometer positioned as shown in Figure 47.

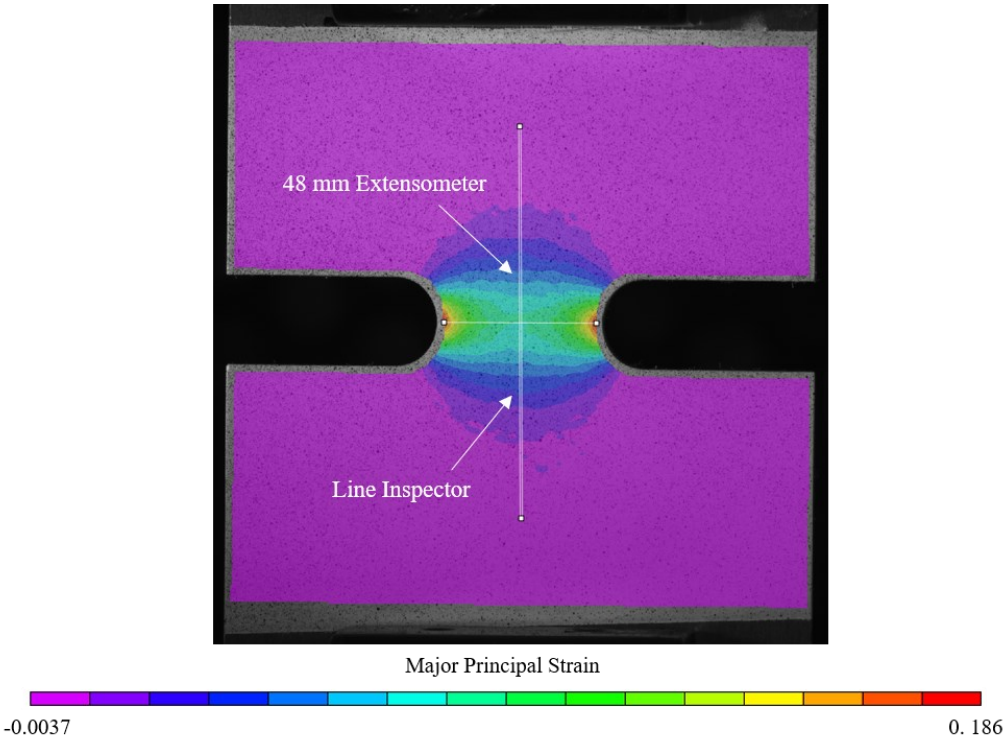

Figure 47: Typical placement of line inspector and extensometer for a representative repeat of the triple-scaled version of Geometry B. The image shown corresponds to the point of necking cutoff.

Scaling or correcting Geometry B causes the plane strain yield strength to collapse to a single geometry-independent value consistent with the findings from Geometry A. Without correction or scaling, the original Geometry B specimen suggested a plane strain yield strength of 1.115 whereas the analysis of Geometry A suggested a plane strain yield strength of 1.087 – a 2.6% error. Integrating the triple-scaled notch Geometry B resulted in a plane strain yield strength of 1.082 ± 0.011, using an exponent of 5.51 ± 0.92 to match each experimental stress response shown in Figure 48 (0.5% error compared to Geometry A). Correcting Geometry B (w/t = 2.7) with a factor of f_{geo} = 1.033 from Section 4.4.1, then repeating the analysis of Section 4.3, produced a plane strain yield strength of 1.088 ± 0.005 (0.1% error compared to Geometry A). The plane strain yield strengths calculated from Geometry A, the triple-scaled Geometry B and the corrected Geometry B all fall within the same statistical confidence window illustrated in Figure 49. Either physically scaling the specimen size to increase the aspect ratio or using the empirical correction in Section 4.3.1 minimizes the error introduced by a departure from plane stress conditions.

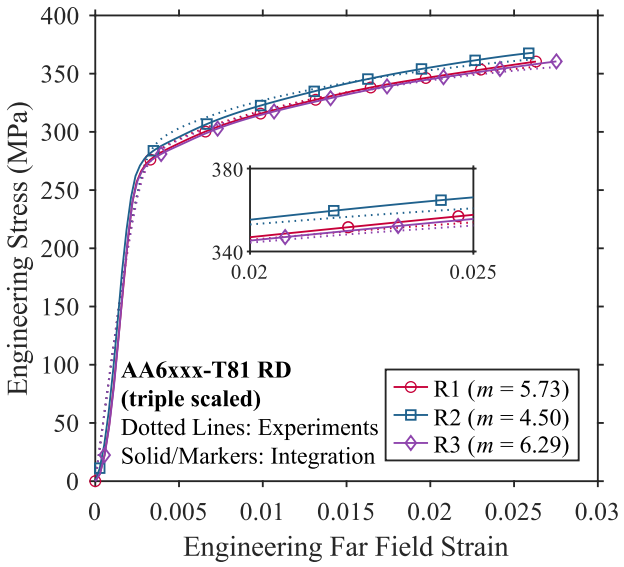

Figure 48: Comparison of integrated and experimental stress-strain curves for each repeat of AA6xxx-T81 tested along the RD. The results are shown for the triple-scaled version of Geometry B at the exponent that minimizes the squared error for each individual repeat.

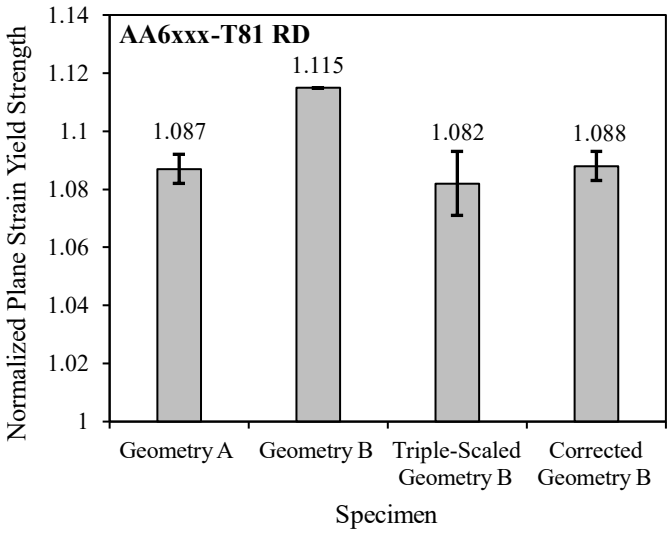

Figure 49: Comparison of HF85-PSC exponent identified by applying the integration methodology to each tested geometry for AA6xxx-T81 along the rolling direction. Increasing the gauge width promotes plane stress conditions along the majority of the gauge width, causing the plane strain yield strength to collapse to a single, geometry independent value. By applying an aspect ratio correction, the plane strain yield strength calculated using Geometry B agrees with the value calculated using Geometry A.

Although scaling Geometry B tailors a combined constitutive/fracture geometry to a given sheet thickness, the selection of Geometry A allows for characterization of the plane strain tensile stress to higher strains before the onset of diffuse necking. As shown in Figure 50, an equivalent strain of $\varepsilon_{eq}^{p} = 0.102$ is reached in the center of the gauge region for the notch Geometry A versus just $\varepsilon_{eq}^{p} = 0.073$ and $\varepsilon_{eq}^{p} =$

0.081 for the triple and single-scaled Geometry B, respectively. Calibrating the exponent to a larger plastic strain ensures that the identified plane strain yield strength is representative of the large deformation seen in typical forming applications. Based on this analysis, the geometry of Vegter and van den Boogaard (2006) is recommended for constitutive characterization as it promotes both a higher strain in the specimen center and plane stress conditions along the gauge width. As a result, this geometry is used for the remainder of the analysis in Chapters 5-7 of this thesis.

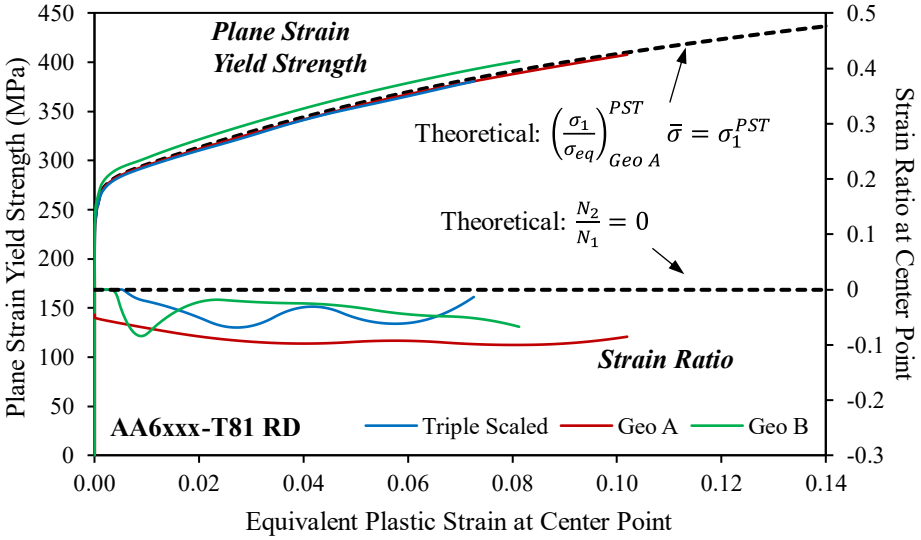

Figure 50: Plane strain yield strength and strain ratio as a function of average equivalent plastic strain at the center point along the gauge width for the three tested geometries. Results are shown for a representative repeat of AA6xxx-T81 tested along the rolling direction.

4.4 Differential Hardening

Adjusting the instantaneous exponent based on the plastic strain would capture differential hardening along the arc of the yield surface from uniaxial to plane strain tension. Previous works by Yanaga *et al*. (2014), Kawaguchi *et al*. (2015) and Ha *et al*. (2018) found that the exponent of a differential hardening yield surface evolves with equivalent plastic strain ε_{eq}^{p} according to the sigmoid relationship shown in Eq. (4.3) with calibration parameters *A* through *D*. While any fitting function is technically valid, including a polynomial or spline, the sigmoid model is most suitable as the exponent is bounded by the coefficients *A* and *B*, avoiding non-physical negative exponents for larger strains outside the fitting window.

$$m = \frac{A - B}{1 + \exp\left(\frac{\varepsilon_{eq}^{p} - C}{D}\right)} + B \tag{4.3}$$

The plane strain yield strength, at a given instantaneous exponent, is defined by:

$$\left(\frac{\sigma_1}{\sigma_{eq}}\right)^{PST} = \left(\frac{1+R_\theta}{1+2R_\theta(1/2)^m}\right)^{\frac{1}{m}}, \qquad m = f\left(\varepsilon_{eq}^P\right) \tag{4.4}$$

Figure 51 illustrates the differential hardening integration and minimization scheme. The process is the same as the isotropic methodology, except that the coefficients A-D of the sigmoid function were optimized using the *fmincon* subroutine in Matlab® (blue blocks) rather than the exponent itself. Since the amount of work hardening varies along the gauge region, direct iteration was used at each point to determine the equivalent strain. To determine a single set of coefficients that best captures all repeats, the *N* experimental repeats were also aggregated together using linear scalarization of the individual objective functions shown in Eq. (4.5). Alternatively, the sigmoid coefficients for an individual repeat can be found by setting *N = 1*.

$$SE = \sum_{k=1}^{N} \sum_{E_{1y}^{DIC}=0}^{End} \left[S_k^{model}\left(E_{1y}^{DIC}\right) - S_k^{exp}\left(E_{1y}^{DIC}\right)\right]^2 \tag{4.5}$$

It is more convenient, for yield function calibration, to determine the yield function exponent as a function of plastic work rather than equivalent strain. The conversion is:

$$W_p = \int \bar{\sigma} d\varepsilon_{eq}^p \tag{4.6}$$

where $\bar{\sigma}$ is the hardening curve in the direction of analysis.

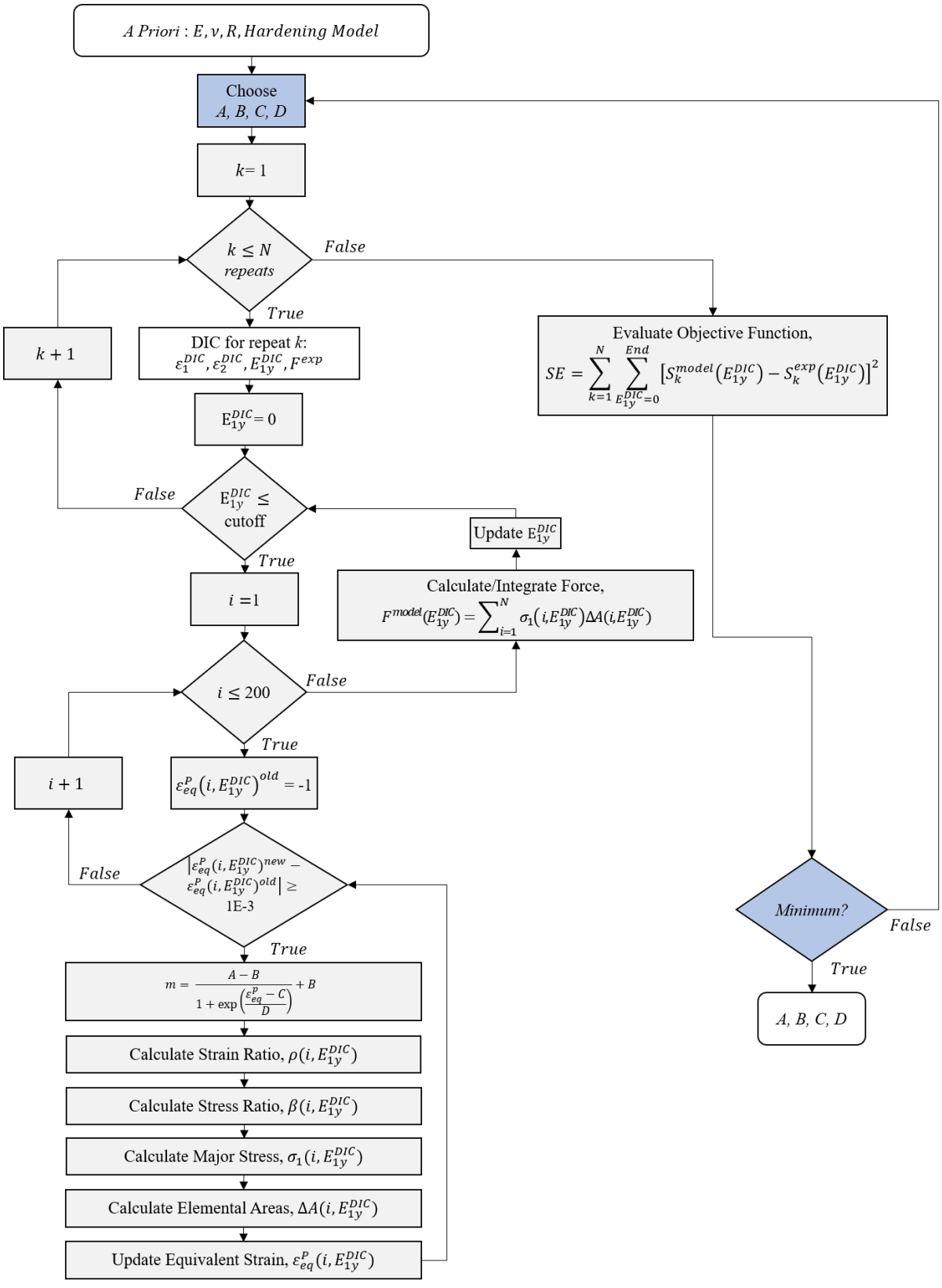

Figure 51: Flowchart showing differential hardening integration methodology.

The differential hardening model better represents the constitutive behavior of the material if the objective function value is lower than that of the isotropic hardening model, keeping all other variables constant. The increased objective function error shown in Table 13 for AA6xxx-T81 along the DD and TD, and AA5182 along all analyzed directions indicates that the isotropic model better described the constitutive response. Conversely, the differential model for DP1180 reduced the aggregate objective function error by 66-88% in RD and DD by improving the agreement between the stress-strain curves at the onset of yielding. Little evidence of differential hardening was observed along the TD. For AA6xxx-T81 the 9% reduction in error observed along the RD indicates a slight differential hardening effect. For the AA6xxx-T4 alloy, the aggregate objective function error decreased by 36-51%, showing strong evidence of differential hardening in all three orientations. Theoretically a material could show both differential hardening and non-associative flow (Hou *et al.*, 2019), although this case was not observed for any of the analyzed materials.

Table 13: Percentage decrease in objective function error by adopting the differential model instead of the isotropic model.

		Individual Repeats					**Aggregate**
		1	2	3	4	5	
AA6xxx-T81	RD	-10%	-6%	-11%	-5%	-6%	-9%
	DD	7%	-37%	3%	3%	-2%	0%
	TD	8%	9%	9%	6%	6%	0%
AA6xxx-T4	RD	-57%	-52%	-49%	-65%	-65%	-51%
	DD	-56%	-54%	-52%	-56%	-46%	-48%
	TD	-46%	-48%	-56%	-39%	-51%	-36%
AA5182-O	RD	1%	1%	0%	1%	-	0%
	DD	8%	5%	4%	-	-	0%
	TD	2%	0%	3%	0%	-	1%
DP1180	RD	-76%	-87%	-64%	-55%	-	-66%
	DD	-82%	-66%	-8%	-71%	-	-88%
	TD	12%	13%	12%	0%	-	-2%

Figure 52 and Figure 53 show the individual and aggregate variation in the HF85-PSC differential hardening exponent as a function of equivalent plastic strain, in comparison to the isotropic solution for the AA6xxx-T4 and T81 alloys. The plane strain yield strength tends to decrease with plastic deformation due to texture evolution. The isotropic solution represents a midrange value that essentially interpolates between the minimum and maximum exponents of the differential hardening model. Differential hardening is relatively muted for the AA6xxx-T81 alloy along the RD but more pronounced for the T4 temper.

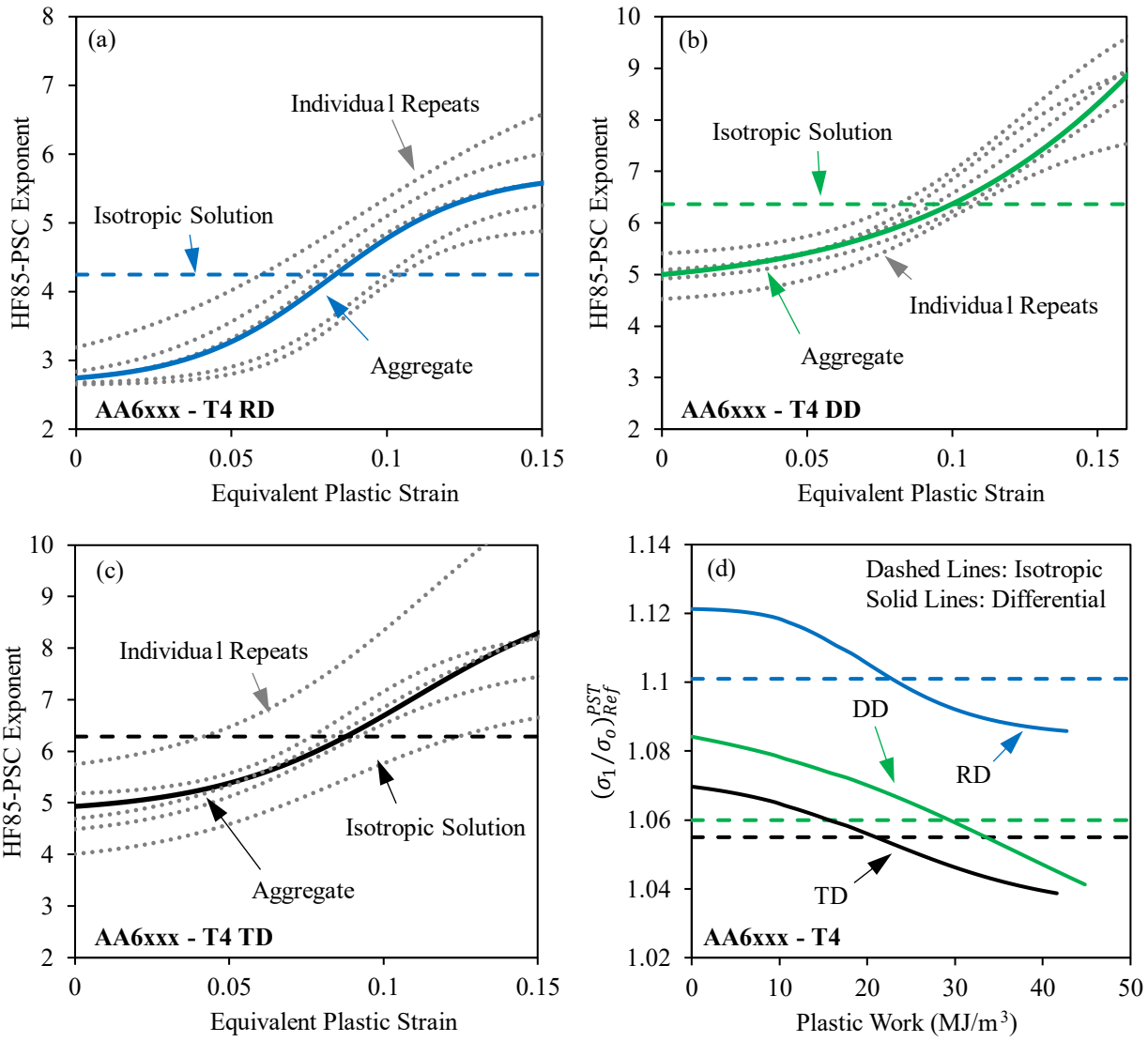

Figure 52: Evolution of yield function exponent versus equivalent plastic strain for AA6xxx-T4 tested along the (a) RD, (b) DD, and (c) TD. As shown in (d), the differential hardening plane strain yield strength is higher at low levels of plastic work than expected under an isotropic hardening assumption. Results are shown up to the average equivalent plastic strain in the center of the gauge region at the onset of necking.

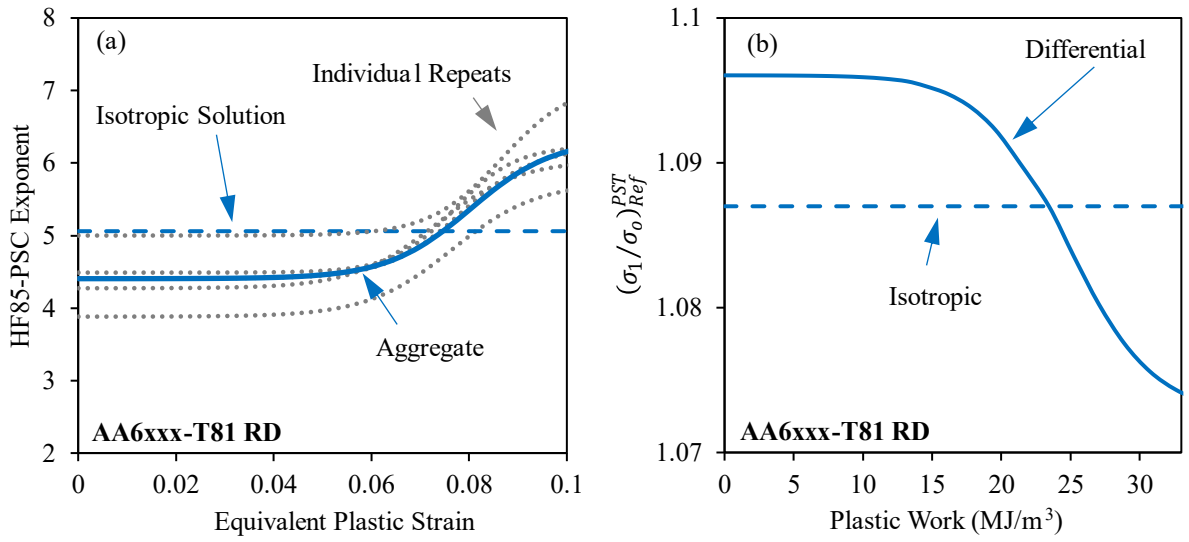

Figure 53: Evolution of yield function exponent versus equivalent plastic strain for AA6xxx-T81 tested along the (a) RD. As shown in (b), the differential hardening plane strain yield strength is higher at low levels of plastic work than expected under an isotropic hardening assumption. Differential hardening was not observed along the transverse or diagonal directions. Results are shown up to the average equivalent plastic strain/work in the center of the gauge region at the onset of necking.

The DP1180 shows a sharp decrease in the HF85-PSC exponent at the onset of yielding, after which the exponent plateaus, as seen in Figure 54. Similar differential behavior has been documented in equal-biaxial tests using interstitial free steel (Mulder *et al.*, 2015), which the authors hypothesized was due to "anelastic strain". Anelastic strain is caused by reversible dislocation movement (van Liempt and Sietsma, 2016), in contrast to linear elastic strain which is caused by the reversible stretch/compression of the intermetallic lattice structure bonds. This dislocation movement causes the lattices to "bow", causing local stresses to develop at the grain boundaries (van Liempt and Sietsma, 2016; Mulder *et al.*, 2015). It follows that this rapid change in lattice structure could cause an initial change in the yield surface shape. Furthermore, not accounting for the residual work caused by the cold rolling process introduces an error that is most prominent at small strains. Due to various yield point effects, conventional extraction of material properties omits the response around yielding by adopting, for example, a 0.2% offset in the case of the yield strength or a higher value of plastic work in the case of the yield surface calibration.

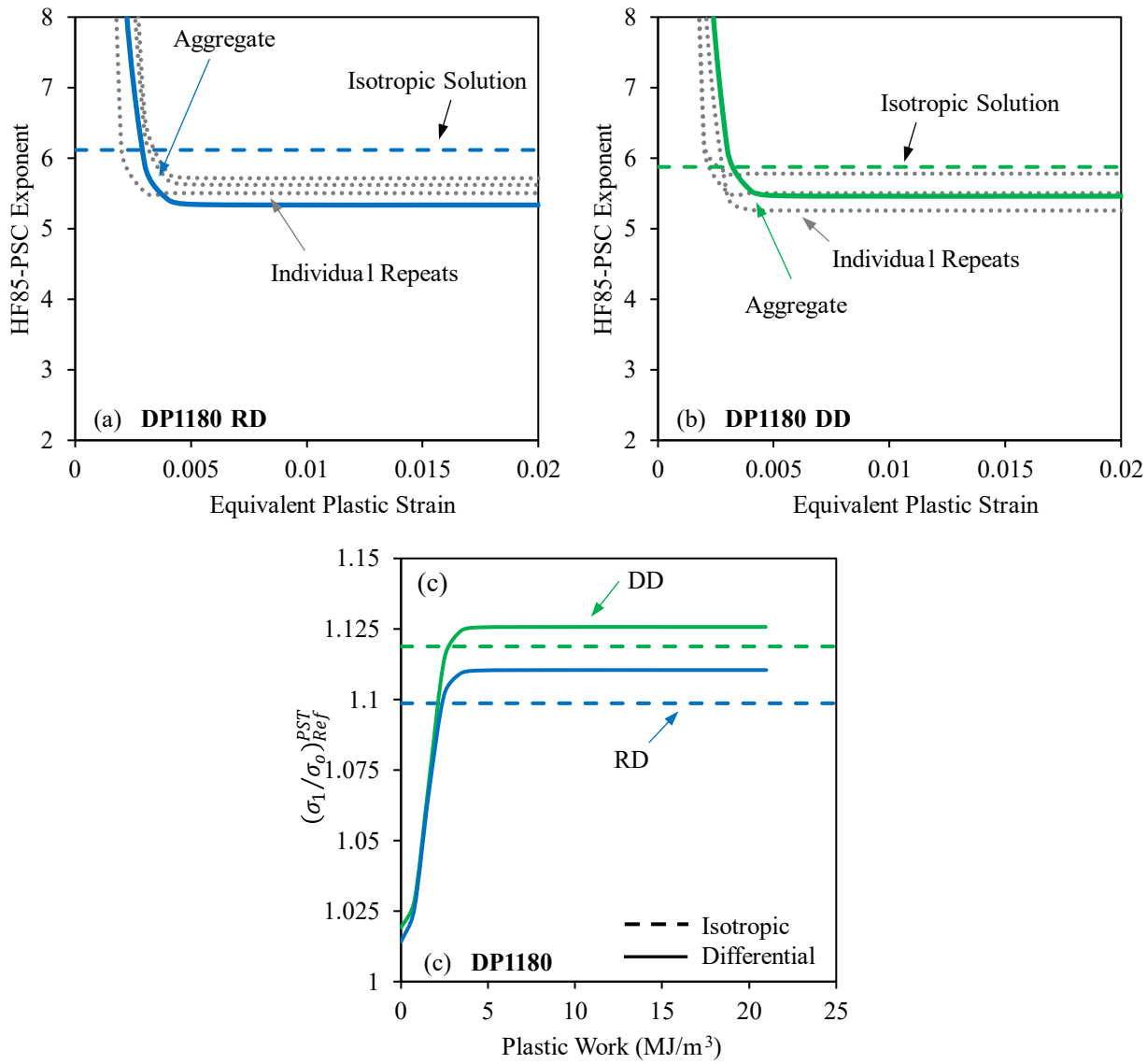

Figure 54: Evolution of yield function exponent versus equivalent plastic strain for DP1180 tested along the (a) RD and (b) DD. As shown in (c), the differential hardening plane strain yield strength is higher at low levels of plastic work than expected under an isotropic hardening assumption. Differential hardening was not observed along the transverse direction. Results are shown up to the average equivalent plastic strain in the center of the gauge region at the onset of necking.

Table 14 shows the coefficients for each of the aggregate fits. The equivalent plastic strain represents the average value seen in the center of the gauge region at the onset of necking and termination of the integration and optimization methodology. The equivalent plastic strain is comparable to or greater than that achieved in biaxial cruciform tests of similar materials (Kuwabara *et al.*, 2017; Yanaga *et al.*, 2012; Kuwabara and Nakajima, 2011; Kuwabara *et al.*, 2011), making the proposed method particularly suited for accurate material characterization to strain levels typical of forming operations.

Table 14: Coefficients of the HF85-PSC differential hardening sigmoid model calibrated up to the indicated average equivalent plastic strain at the center point of the gauge region.

Material	Direction	ε_{eq}^{p}	Sigmoid Coefficients			
			A	*B*	*C*	*D*
AA6xxx-T4	RD	0.15	5.723	2.662	0.082	-0.023
	DD	0.16	21.313	4.7046	0.220	-0.055
	TD	0.15	9.256	4.796	0.110	-0.032
AA6xxx-T81	RD	0.10	4.408	6.328	0.080	0.0085
DP1180	RD	0.02	49.724	5.334	0.0008	0.0005
	DD	0.02	49.675	5.465	0.0010	0.0005

4.5 Non-Associated Flow Rule

Separate functions for the yield surface and plastic potential may be adopted to better capture the plastic flow behavior in some materials under a non-associative flow framework (Stoughton, 2002; Stoughton and Yoon, 2009; Cvitanic *et al.*, 2008). Local non-associative flow along the uniaxial to plane strain arc can be modelled using the HF85-PSC criterion as both the plastic potential and yield function. The same steps of the original methodology apply, except that an exponent m_y is calibrated for the yield function σ_{eq} and a separate exponent m_p is calibrated for the plastic potential ψ.

The modifications to the methodology needed to implement non-associated flow involve using the plastic potential when operating on the strains and the yield function when operating on the stresses. The DIC measured strain ratio describes the ratio of the plastic potential function normal vectors. By applying the flow rule to the HF85-PSC plastic potential function, the strain ratio is given by:

$$\rho = \frac{N_2}{N_1} = \frac{\partial\psi/\partial\sigma_2}{\partial\psi/\partial\sigma_1} = \frac{R_\theta(\beta^{m_p-1} - |\beta - 1|^{m_p-1})}{1 + R_\theta|\beta - 1|^{m_p-1}}, \beta = \frac{\sigma_2}{\sigma_1} \tag{4.7}$$

In this case, m_p is the plastic potential exponent and the stress ratio β is found using Newton-Raphson iteration as before. After determining β from the plastic potential function, the increment in equivalent plastic strain at the current timestep is:

$$\varepsilon_1{}^{DIC} = \left(\frac{1-\nu\beta}{E}\right)\left(\frac{\sigma_1}{\sigma_{eq}^{HF85}}\right)\bar{\sigma} + (\varepsilon_1{}^{P})_{n-1} + \frac{1}{(1+\beta\rho)}\left(\frac{\sigma_1}{\sigma_{eq}^{HF85}}\right)^{-1}(d\varepsilon_{eq}{}^{P})_n \tag{4.8}$$

The ratio of the major principal stress to the equivalent stress is calculated from the yield function with exponent m_y shown in Eq. (4.9). The question becomes how to select R_θ^y, since R-values are only relevant

to the plastic potential in the non-associated case. Possible solutions include considering R_θ^y as a free variable and including it in the multivariable optimization, assuming isotropy ($R_\theta^y = 1$) or assuming associative flow just at uniaxial tension such that $R_\theta^y = R_\theta$.

$$\frac{\sigma_1}{\sigma_{eq,\theta}^{HF85}} = \left(\frac{1 + R_\theta^y|\beta|^{m_y} + R_\theta^y|1-\beta|^{m_y}}{1 + R_\theta^y}\right)^{-\frac{1}{m_y}} \tag{4.9}$$

Since Eq. (4.7-4.9) are based on the strain and stress ratios, calculation of the scalar multiplier $d\lambda$ is avoided.

The methodology described in Figure 55 was applied to all materials, considering all three solutions for R_θ^y. Only AA5182 exhibited non-associated flow. Conveniently, the curvature of the AA5182 yield surface at uniaxial tension is of little significance because the arc approximates a Tresca shape. Therefore, the variable R_θ^y was set equal to R_θ in this analysis. However, it is stressed that this assumption may not be appropriate for other materials.

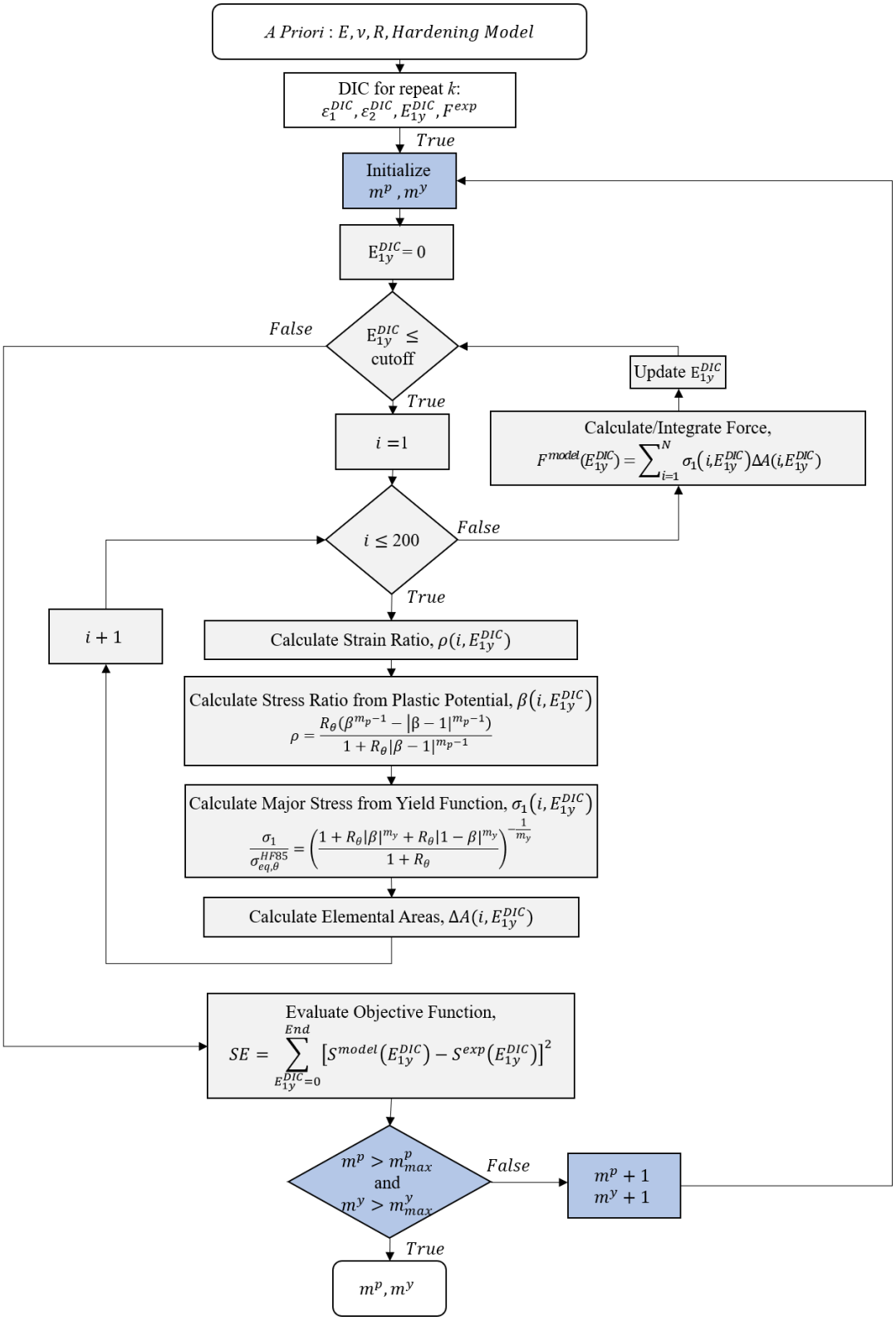

Figure 55: Flowchart showing non-associated flow integration methodology. The blue blocks represent the optimization and selection of the exponents, accomplished using a grid search to visualize the objective function surfaces. Alternatively, the *fmincon* subroutine in Matlab® could be used as a more efficient, gradient based algorithm.

A convenient optimization approach for two free variables is a so-called grid search over the possible solution space, which allows for visualization of the objective function surface seen in Figure 56. The error at each evaluation point in Figure 56 is normalized with respect to the error at the optimum point. For AA5182 along the TD, the objective function error decreased by 30% versus the isotropic, associated flow solution using m_p = 2.7 and $m_y = 50$. Note that an exponent of 2.7 is the lowest possible for the HF85-PSC yield function given the R-value of the material. Along the DD, only a 0.5% reduction in error occurred with $m_p = 6$ and $m_y = 50$. The low sensitivity to the plastic potential exponent in this direction indicates that practically any exponent between m_p = 6 and m_p = 50 is a valid choice. In general, from the viewpoint of stability in numerical simulations, lower exponents prevent spurious localizations driven by a relatively flat yield surface.

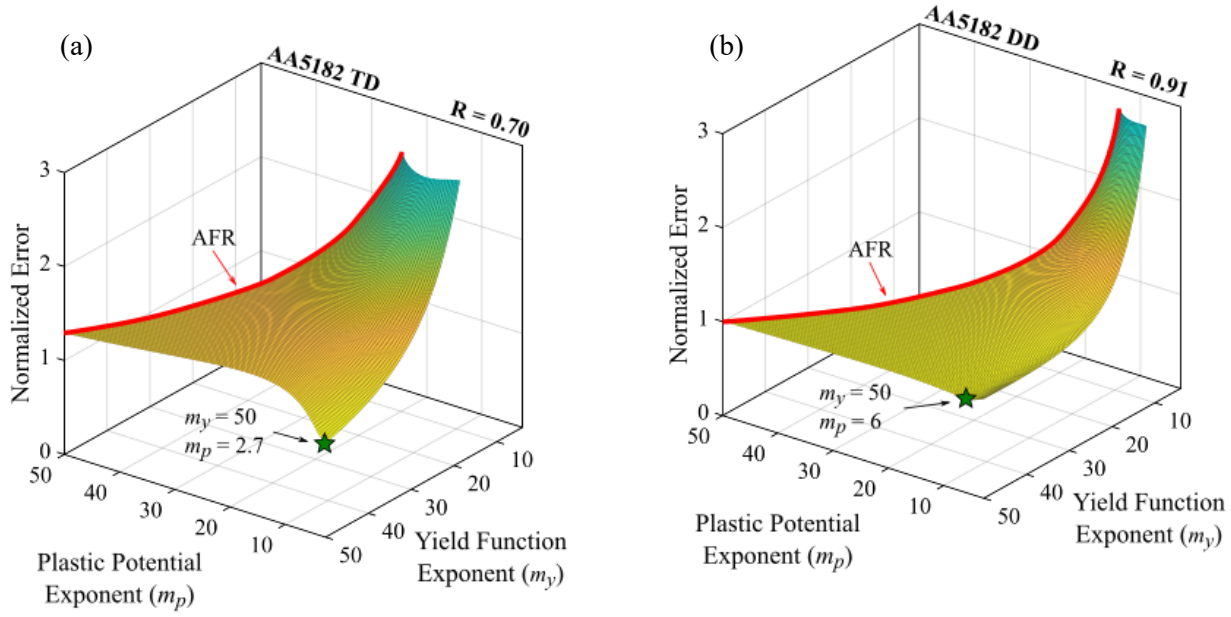

Figure 56: Objective function surface showing minima at the NAFR solution for AA5182 tested along the (a) TD and (b) DD. The red line represents the AFR solution, where both the yield function and plastic potential exponents are equal.

Adopting non-associated flow also permits the direct use of a Tresca type surface for the yield function. The HF85-PSC yield function approaches Tresca when the yield function exponent increases to infinity, as seen in this case with $m_y = 50$ fixed at the upper bound of the solution space. However, a Tresca yield surface is inadmissible in the AFR-based methodology because unique identification of the stress ratio from the strain ratio at each point is impossible if $\rho = 0$ along the entire arc. The NAFR-based methodology avoids this problem because the stress ratio can be determined from a lower-exponent plastic potential, while the equivalent stress is found from the Tresca yield function. Calibrating the HF85-PSC function for

the lower-exponent plastic potential and directly adopting Tresca for the yield surface with $\sigma_1/\sigma_{eq,\theta}^{HF85} = 1$ in Eq. (4.8) further reduces the error by 25-44%.

The modelled stress-strain curves from the integration methodology are in good agreement with the experimental responses under both non-associated flow models. Compared to the associated flow calibrations of Figure 35 and Figure 36, the non-associated models shown in Figure 57 offer improved agreement. Furthermore, directly adopting the Tresca criterion as the yield function visibly improves the agreement between the modelled and experimental stress-strain curves at small strains.

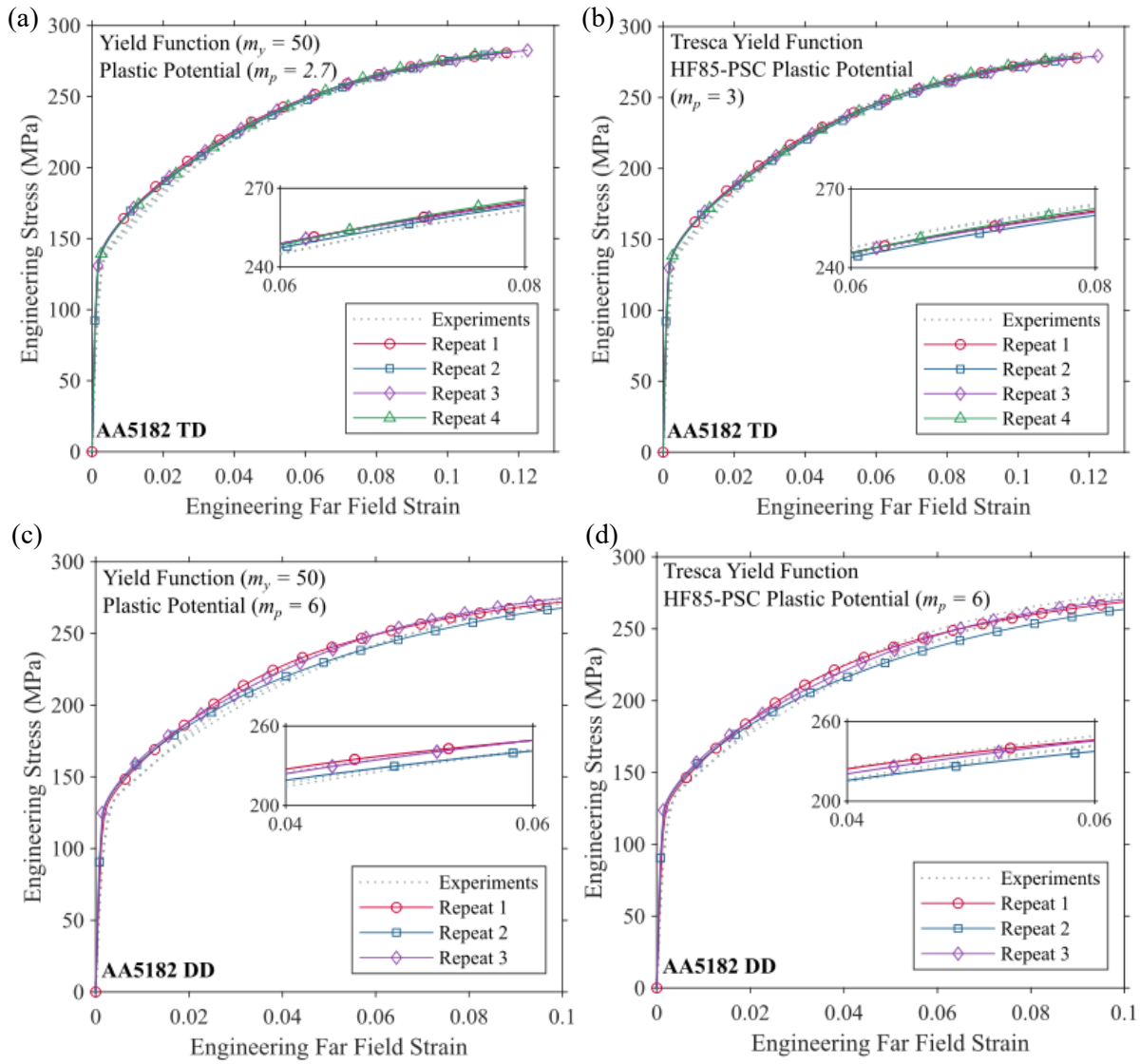

Figure 57: Comparison of experimental and integrated stress-strain curves evaluated using the NAFR model. As shown in (a), an HF85-PSC yield function exponent of 50 and a plastic potential exponent of 2.7 capture the plastic behavior of the AA5182 material along the TD. As shown in (c), an HF85-PSC yield function exponent of 50 and a plastic potential exponent of 6 capture the plastic behavior of the AA5182 material along the DD. As shown in (b) for the TD and (d) for the DD, directly adopting the Tresca criterion as the yield function improves the agreement with the experimental stress-strain curves at small strains.

4.6 Summary of Extensions to the Plane Strain Characterization Methodology

The constitutive behavior along the uniaxial to plane strain arc was characterized for AA6xxx-T4 and AA6xxx-T81 alloys by applying the integration methodology established in Chapter 3 to the smaller notch Geometry B. Discrepancies between the HF85-PSC exponents identified from experimental notch tests using so-called Geometry A, adapted from Vegter and van den Boogaard (2006), and Geometry B suggested a geometry bias linked to the aspect ratio of the selected specimen. Using Geometry A, the A6xxx-T4 and AA6xxx-T81 alloys showed HF85-PSC exponents of between 4.25-6.36 and 5.06-10.11, respectively. The corresponding normalized plane strain yield strengths were between 1.030 and 1.087 for the AA6xxx-T81 alloy and between 1.06 and 1.1 for the AA6xxx-T4 alloy. In comparison, the plane strain yield strength for an isotropic FCC material with an exponent of 8 is 1.09. Applying the integration methodology to Geometry B suggested exponents for the AA6xxx-T4 and AA6xxx-T81 alloys of between 4.45-4.72 and 2.64-3.72, respectively. The corresponding normalized plane strain yield strengths were between 1.078 and 1.115 for the AA6xxx-T81 alloy and between 1.07 and 1.1 for the AA6xxx-T4 alloy. The plane strain yield strengths calibrated using Geometry B were within just 2.5% of the results obtained with Geometry A for the AA6xxx-T4 alloy, but up to 5% different for AA6xxx-T81.

The sensitivity of the calibrated exponent to the geometry, especially for the AA6xxx-T81 material, was attributed to the thickness of the sheet (2.7 mm). Plane stress is only a valid approximation for thin sheet, relative to the planar dimensions. However, the Geometry B gauge width is only 7.15 mm, making the width-to-thickness aspect ratio of 2.65 too small to promote plane stress across much of the gauge width. Geometry A showed less sensitivity to the material thickness because the notches, where the greatest deviation from plane stress occurs, were outside the area subject to the integration. Furthermore, the larger gauge width of 39 mm resulted in an aspect ratio of 14.4 which promoted plane stress conditions across the sample width. Successive finite-element simulations showed that a triple-scaled Geometry B, with an aspect ratio 7.95, adequately tempered the error in the plane stress approximation. Experimental tests of the triple-scaled Geometry B confirmed that the integrated exponent was in closer agreement with that identified from the analysis of Geometry A. Similarly applying a correction factor based on the experimental error observed in finite element simulations collapsed the plane strain yield strength derived from the original Geometry B to that obtained from the triple-scaled Geometry B and Geometry A specimens. Based on the findings of the sensitivity study, Geometry A was selected for the remainder of the analysis in the thesis.

The proposed integration methodology is easily extendable to non-associated flow. Calibrating the exponents of two separate HF85-PSC functions, one to serve as the plastic potential and one to serve as the yield function, enables characterization of non-associated flow along the uniaxial to plane strain arc of the yield surface. Only the AA5182 material showed non-associated flow in the TD and DD, with an HF85-

PSC yield function exponent of $m^y \rightarrow \infty$. The corresponding plastic potential exponents were 3 and 6 along the TD and DD, respectively. Adopting non-associated flow enabled direct adoption of the Tresca yield function, which was not possible under the associated flow model due to a lack of uniqueness between the stress and strain ratios. Adopting the Tresca yield function reduced the error in the integrated AA5182 stress-strain curve by 25-44% compared to the associated flow model of Chapter 3.

Based on other works in the literature, a sigmoid function was selected to represent the evolution of the HF85-PSC yield function exponent under differential hardening as a function of the equivalent plastic strain. Calibrating the four coefficients of the sigmoid distribution, using constrained multivariable optimization in Matlab®, indicated the presence of differential hardening for the AA6xxx-T4 material in all directions, AA6xxx-T81 along the RD and DP1180 along the RD and DD. Differential hardening was not observed for the AA5182 material, avoiding the need for a combined differential and non-associated analysis. Adopting differential hardening reduced the aggregate objective function error by 9-88% depending on the alloy and direction, compared to the isotropic, associated flow model. For the AA6xxx-T4 alloy, the plane strain yield strength was inversely proportional to plastic deformation, decreasing from 1.12 to 1.09, 1.08 to 1.04 and 1.07 to 1.04 along the RD, DD, and TD, respectively. The muted differential hardening for AA6xxx-T81 generated a similar decrease in normalized plane strain yield strength from 1.096 to 1.074 in the RD. In the case of the DP1180, the normalized plane strain yield strength sharply increased around initial yielding from approximately 1.01 to saturated values of 1.11 along the RD and between 1.11-1.13 along the DD, depending on whether the instantaneous or average R-value was used. Sources of this unique yield point behavior may include anelastic strain causing reversible dislocation movement and residual cold work due to rolling.

Chapter 5 Evaluation of Plane Strain Characterization Methodology

This chapter evaluates the integrated plane strain yield strength for each material determined in Chapters 3-4 against the established empirical method of Flores *et al*. (2010) and by comparison of detailed finite-element simulations of the coupon tests. The finite-element method makes it possible to not only simulate the isotropic, associated flow case (HF85-PSC-ISO), but also the differential hardening (or evolving exponent model, HF85-PSC-EVO) and non-associated flow (HF85-PSC-NAFR) models. The differential hardening and non-associated flow models were implemented in the finite-element software LS-DYNA as User Defined Materials (UMATs).

5.1 Comparison to Other Experimental Methods

Based on experimental and numerical observations that there exists a linear relationship between the size of the homogenous zone of plane strain (W_H) and the portion of the applied load attributed to that zone (F_H), Flores *et al*. (2010) developed an empirical correlation to calculate the plane strain yield strength of a sheet metal. Eq. (5.1) defines the size of the homogenous zone as the distance between the two boundaries where the major principal strain gradient ($d\varepsilon_1/dx$) exceeds 2% of the magnitude of the major principal strain in the center of the specimen, ε_1^{CP} (Flores *et al.*, 2010).

$$W_H = x\left(\frac{d\varepsilon_1}{dx} = \zeta\right) - x\left(\frac{d\varepsilon_1}{dx} = -\zeta\right), \qquad \zeta = 0.02\ \varepsilon_1^{CP}\ \text{mm}^{-1} \tag{5.1}$$

Applying volume conservation with $\varepsilon_2^p = 0$ and neglecting the elastic strains gives the instantaneous thickness of the homogeneous zone as:

$$t_H = t_o \exp(-\varepsilon_1^P) \tag{5.2}$$

where t_o is the initial measured specimen thickness. The uniform stress acting over the homogeneous zone is:

$$\sigma_1^{PST} = \frac{F_H}{W_H t_H} \tag{5.3}$$

Since the load F_H is unknown, a correlation was developed between W_H, the total specimen width W_T, the total applied force measured at the load cell F_T and the homogeneous zone thickness. As done by Flores *et al*. (2010), applying the correlation to Eq. (5.3) gives:

$$\sigma_1^{PST} = 0.978\left(\frac{F_T}{W_T t_H}\right) + 0.022\left(\frac{F_T}{W_H t_H}\right) \tag{5.4}$$

Flores *et al*. (2010) observed that Eq. (5.4) was relatively independent of the two studied geometries and five materials with varying R-values and hardening exponents.

For each material studied in this thesis, all repeats of Geometry A were analyzed using the method of Flores *et al*. (2010) applied in the rolling direction. The major strain distribution was smoothed using cubic splines and constrained to have a global minimum at the center of the gauge region, where plane strain is assumed to occur under ideal test conditions. The size and thickness of the homogeneous zone were then estimated using Eq. (5.1-5.2) before applying Eq. (5.4) to obtain the stress history as a function of the major principal strain at the center point of the gauge region. The coordinate data from Vic-3D 8® was exported in the deformed configuration, to track the small specimen width change. A scale factor was applied so that the initial width matched the measured width of the specimen, to correct for the missing DIC edge data.

Each $\sigma_1^{PST} - \varepsilon_1^P$ curve was compared with the response calibrated from the integration methodology proposed in this thesis. Using the flow stress $\bar{\sigma}$ and calibrated normalized plane strain yield strength $\sigma_1^{PST}/\sigma_{eq}$, the plane strain yield strength as a function of the equivalent plastic strain $\sigma_1^{PST}(\varepsilon_{eq}^P)$ is:

$$\sigma_1^{PST}\left(\varepsilon_{eq}^P\right) = \frac{\sigma_1^{PST}}{\sigma_{eq}}\bar{\sigma} \tag{5.5}$$

The plane stress-plane strain plastic work balance of Eq. (5.6) applies

$$\sigma_{eq} d\varepsilon_{eq}^P = \sigma_1^{PST} d\varepsilon_1^P \tag{5.6}$$

Integrating Eq. (5.6) assuming isotropic hardening (constant $\sigma_1^{PST}/\sigma_{eq}$) and proportional loading gives:

$$\left(\frac{\sigma_1^{PST}}{\sigma_{eq}}\right)^{-1} \varepsilon_{eq}^P = \varepsilon_1^P \tag{5.7}$$

Figure 58 shows that the methodology of Flores *et al*. (2010) is in relatively poor agreement with the proposed integration methodology for all materials, tending to predict a higher stress in plane strain tension. Neglecting the elastic strains in the prediction of Flores *et al*. (2010) causes a deviation from the integrated response at small strains, particularly for DP1180. At the necking cutoff, the percentage difference between the method of Flores *et al*. (2010) and the integration methodology proposed in this thesis is between 1% (AA6xxx-T4) and 7% (AA5182).

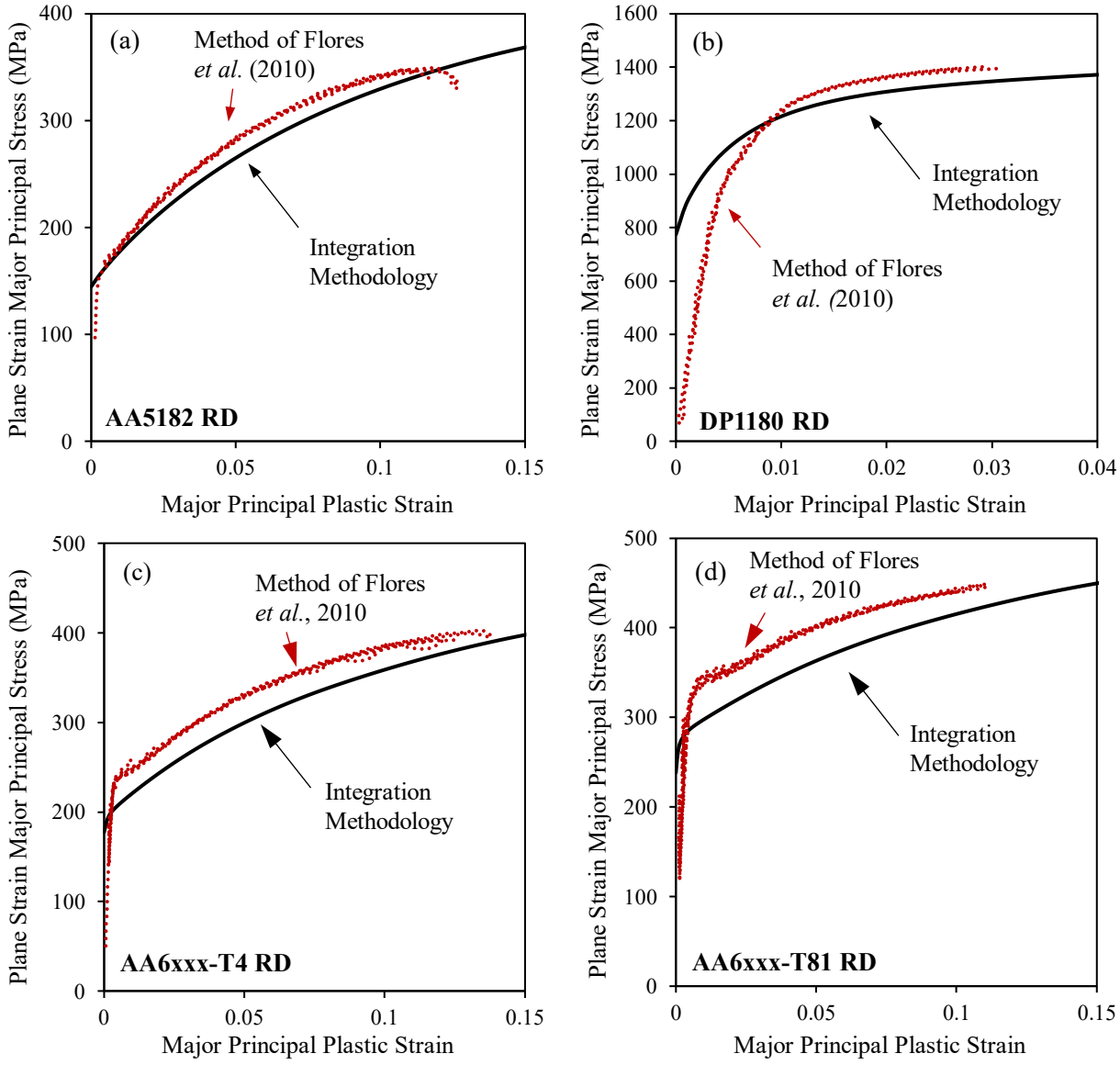

Figure 58: Comparison of plane strain major stress versus major principal plastic strain along the rolling direction using the analysis method of Flores *et al*. (2010) and the proposed integration methodology applied to (a) AA5182, (b) DP1180, (c) AA6xxx-T4 and (d) AA6xxx-T81. The discrepancy at initial yielding is due to neglecting the elastic strains in the method of Flores *et al*. (2010).

The 1-7% difference between the predicted plane strain yield stress at necking obtained from the method of Flores *et al*. (2010) and the method proposed in this thesis is reflective of the restrictive assumptions adopted in the model of Flores *et al*. (2010). Elastic strains are omitted in the analysis by Flores *et al*. (2010) causing large errors at low strains, more so for steel than aluminum due to a higher elastic modulus. Since the boundary of the homogenous zone is obtained from the strain gradient, it is particularly sensitive to the derivative of the spline fit to the experimental data. The assumption of a homogenous zone of plane strain is convenient for empirical analysis but not applicable to many materials and sample geometries. Depending

on the material properties (see Figure 29), the center of the gauge width may not be in exactly plane strain tension. For conventional analysis of a notched tensile test assuming a homogeneous zone of plane strain, the absence of plane strain tension introduces an error into the results. In the proposed integration methodology, the deviation from plane strain is less relevant. Provided that stress states along the gauge width sufficiently probe the envelope between uniaxial tension and plane strain tension, the exponent identified in the integration methodology still defines the local arc shape. Applying the calibrated exponent in the HF85-PSC yield function gives the plane strain yield strength at the intersection of the arc with a principal stress ratio of $\sigma_2/\sigma_1 = 0.5$. By accounting for elasticity and not making any assumptions about the shape of the strain distribution along the specimen gauge width or degree of plane strain conditions in the center of the specimen, the methodology proposed in this thesis provides a more accurate characterization of the yielding response.

5.2 Finite-Element Validation

Finite-element validation permits not only simulation of the isotropic results (HF85-PSC-ISO), but also the differential (HF85-PSC-EVO) and non-associative (HF85-PSC-NAFR) extensions to the integration methodology. Non-associative flow and differential hardening were implemented in LS-DYNA as user-defined materials (UMATs). Half-symmetry, finite-element shell models of the Vegter and van den Boogaard (2006) geometry (Geometry A) were employed to validate the HF85-PSC models calibrated in Chapters 3-4 for all materials and directions. The model used explicit time integration and the same mesh shown in Figure 23. Type 2 constant stress and strain elements were used as they are most consistent with the experimental integration discretization approach. The HF85-PSC-ISO model was run for all cases, as well as the HF85-PSC-EVO or HF85-PSC-NAFR models if also applicable.

Two metrics were selected to evaluate the agreement between the simulated and experimental responses: the global engineering stress-strain response and local response of the major principal strain in the center of the gauge region. Comparison of the stress-strain curves indicate how well the model captures the overall response of the material and geometry under the applied tensile load. Since the deformation is not homogeneous over the gauge region, comparing the local strain evolution in the center of the gauge region indicates how well the model predicts the constitutive behavior specifically in plane strain tension and how well the flow rule predicts the direction of the plastic strains.

The Yld2000 model natively available in LS-DYNA was used to simulate the HF85-PSC-ISO calibrations, by calculating the corresponding coefficients $\alpha_1 - \alpha_8$ from Eq. (3.3). The parameters α_7 and α_8 are shear parameters, activated only around the notches of the specimen where the axes of principal stress do not coincide with the loading axis. In this analysis, the shear parameters were selected as the

average of α_1 and α_6, which was close to unity. A value close to unity is recommended to promote agreement between the experimental and simulated local strain response (Narayanan *et al.*, 2022).

5.2.1 Development of a UMAT for Differential Hardening

An existing Yld2000 UMAT, written by Professor Clifford Butcher, was modified to implement differential hardening. At each call to lookup the yield function coefficients, an additional script was added to retrieve the values of the experimentally calibrated sigmoid coefficients and R-value from an input table, obtain the cumulative equivalent plastic strain from the LS-DYNA data files and calculate the corresponding instantaneous yield function exponent. The Yld2000 coefficients were then updated using Eq. (3.3).

Validating the UMAT with single element simulations showed good agreement between the simulated normalized instantaneous plane strain yield strength predicted by LS-DYNA and the value expected from the input sigmoid function at the same equivalent plastic strain. The single-element model was implemented using a 2 mm x 2 mm shell element, with plane strain boundary conditions enforced by constraining movement along the y-axis (v = 0). Explicit time integration with a minimum time step of 2E-4 seconds was used to reduce simulation time. Repeating the analysis with both Type 2 and Type 16 elements produced the same responses shown in Figure 59. The same generic materials with power law hardening exponents of $n = 0.1$ and R-values of $R = 0.5$ and $R = 2$ from Chapter 3 were adopted. Selecting sigmoid coefficients of A = 3, B = 50, C = 0.11 and D = 0.035 represented the strongest possible case of differential hardening, where the exponent evolved between the upper and lower bounds of m = 3 and m = 50 adopted in this thesis. To ensure that the UMAT could represent materials with exponents that both increased and decreased with plastic strain, additional simulations were conducted with sigmoid coefficients of A = 50, B = 3, C = 0.11 and D = 0.035. Excellent agreement between the LS-DYNA predicted and expected plane strain yield strength was observed over the entire range of deformation regardless of material, or an increasing or decreasing exponent.

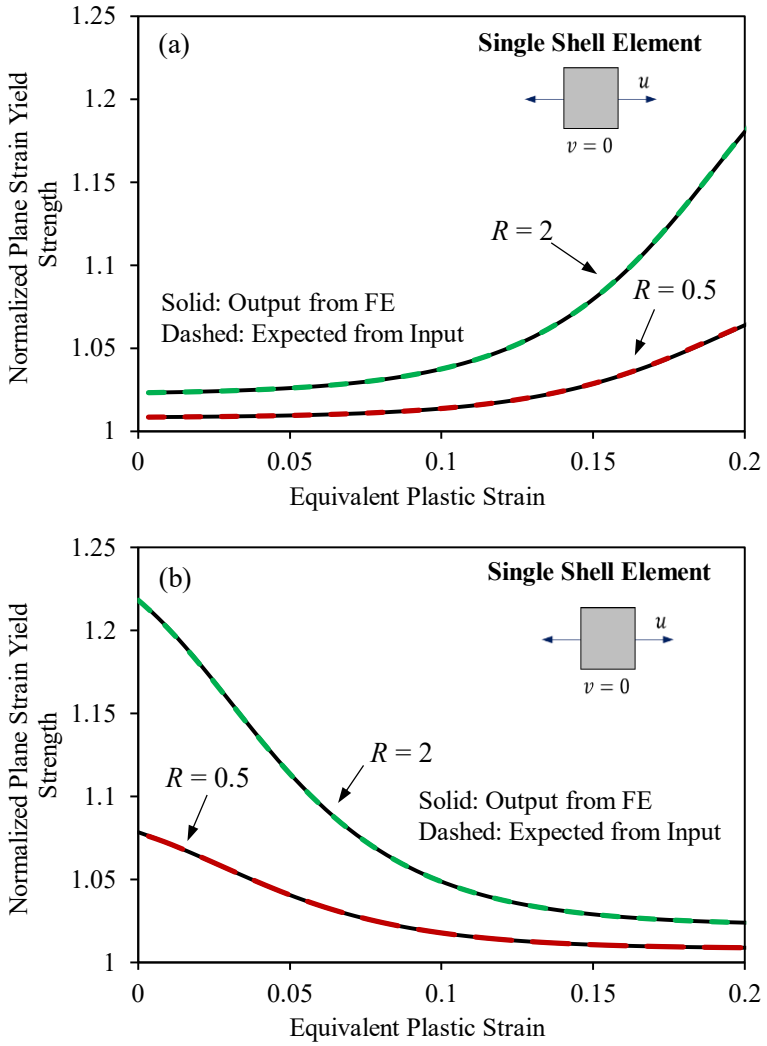

Figure 59: Results of single shell, plane strain element simulations for an evolving yield function exponent. Regardless of whether the HF85-PSC-EVO exponent (a) increases or (b) decreases with plastic strain, the UMAT perfectly predicts the normalized plane strain yield strength response.

5.2.2 Comparison of Finite-Element and Experimental Results

Figure 60 compares the LS-DYNA simulated and experimental results for DP1180. One representative integration from Chapter 3 was included in each direction for comparison. The simulations show good agreement with the experiments in all directions, although they underestimate the initial stress-strain response near the proportional limit. The major principal strain at the center of the gauge region also trends higher in the models than in the experiments, possibly because the material could show some minor pressure sensitivity that shifted the location of plane strain tension slightly from the theoretical, pressure-independent value of $\beta = 0.5$. The differential hardening models, applicable to the RD and DD, better predicted the stress-response at small strains but had little effect on the strain evolution.

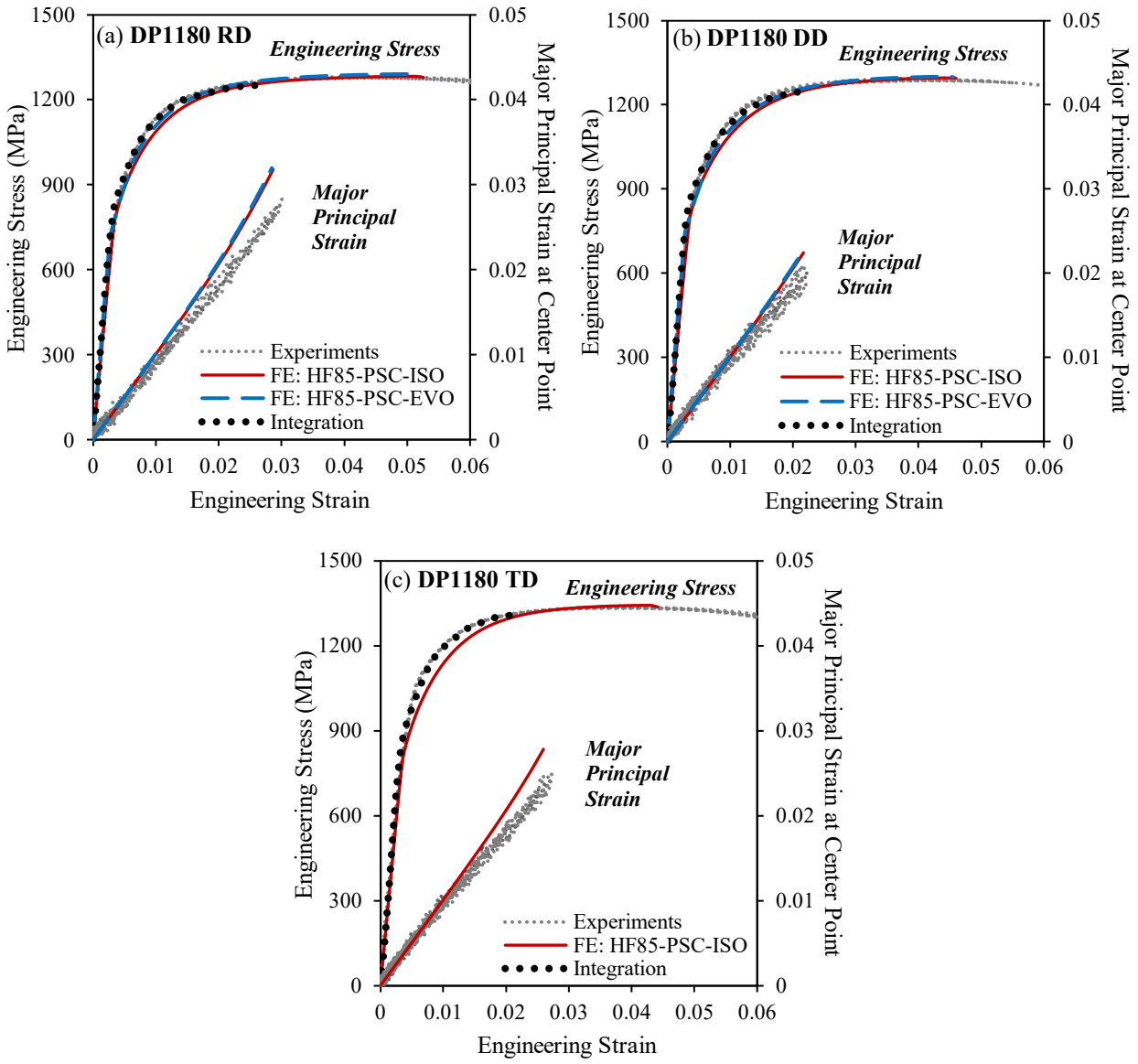

Figure 60: Comparison of finite-element modelled, integrated, and experimental stress and strain responses for DP1180 tested along the (a) RD, (b) DD and (c) TD. The engineering stress-strain response is shown up to the peak load, whereas the representative integration and local strain response are only shown up to the necking cutoff used in the integration methodology.

It is important to emphasize the difference between the integration and the finite-element method. In all cases, the representative integration shows the best agreement with the experimental stress strain response because it operates directly on the DIC identified strains. In contrast, both the stress and strain fields are unknowns that must be identified from the boundary conditions and constitutive model in the finite-element method. In the standard finite-element approach, the nodal displacements are obtained from the global stiffness matrix and boundary conditions. The displacements are then post-processed for strains and stresses using strain-displacement functions and a constitutive model. Consequently, any difference in the

prediction of strains will result in a different prediction of stress compared to the integration. This layer of uncertainty is avoided in the integration methodology since the strains are already known exactly.

By comparing the finite-element and experimental strain contours, one can assess whether the error in the stress prediction stems from a discrepancy in the strain prediction. As can be seen in Figure 61 for DP1180 tested along the limiting transverse direction, the strain at the notch drives the strain distribution along the gauge width, giving rise to "humps" in the major and minor strain distributions at a distance from the center of approximately 17 mm. The strains captured by DIC along the cutting line are higher than predicted in the finite-element method, which result in greater work hardening and a higher flow stress at each point. This observation explains why the integration methodology, which operates directly on the DIC strains, can match the experimental stress-strain response whereas the finite-element software underpredicts the strains and hence the stress. At the necking cutoff, $E_{1y} = 0.021$, the magnitude of the major strain at the notch is 34% higher in the DIC contour image versus the strain at the corresponding finite-element timestep.

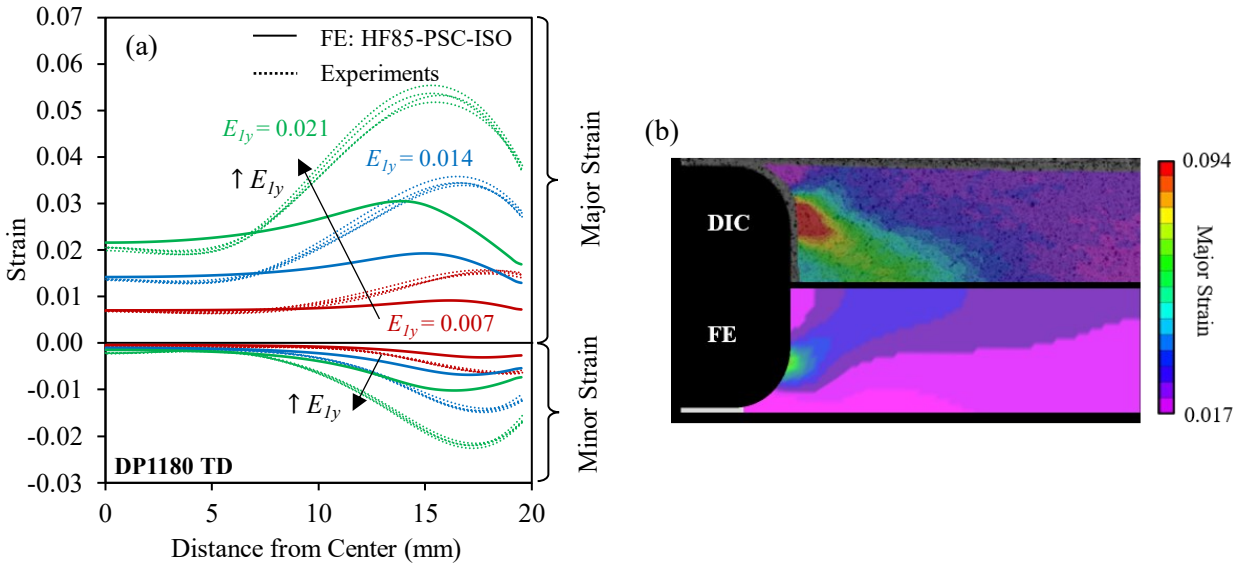

Figure 61: (a) Comparison of finite-element and experimental local strain distributions for DP1180 tested along the TD and (b) comparison of finite-element and DIC major principal strain contours at the cutoff extensometer strain of $E_{1y} = 0.021$.

Clearly the localization of the strain at the notch is at least somewhat responsible for the difference between the integrated and finite-element predictions. The following sources for the discrepancy were evaluated:

- Mesh design and grid independence. A finer mesh results in greater resolution in the calculation of the strains and stresses, especially in regions subject to high gradients like a notch. Various mesh designs and sizes were considered down to a characteristic dimension of 0.05 mm with little effect.

- Element type. It is well known that different element formulations have varying degrees of accuracy. A fully integrated element results in greater local resolution than a reduced, single point integration element. Type 16 (fully integrated), Type 25 (fully integrated with thickness stretch) and Type 2 (reduced integration) elements were all tested, with little effect on the stress response.
- Machining Defects. The machining of the specimens could have introduced microscopic stress raisers along the free edges (Kalpakjian and Schmid, 2008). An additional stress concentration could promote greater localization at the notch than predicted in the finite-element model which does not consider surface roughness or edge quality. Since CNC machining was used and the edge quality was discernably smooth, it is unlikely that this had a pronounced effect. Furthermore, the other materials were machined in the same manner and did not show the same discrepancy in the stress-strain response.
- Hardening model. Necking occurs at the notch before it is detected using the cutoff criterion at the cutting line along the gauge region. Consequently, the hardening curve is extrapolated beyond uniform elongation for elements at the notch, which could introduce uncertainty into the results. Since the discrepancy in the stress-strain responses is observed early in the test, when the notch stress is still below the ultimate tensile strength, it is unlikely that post-uniform extrapolation of the hardening curve is responsible.
- Strain rate sensitivity. The notches localize faster than elements along the gauge region, meaning that the strain rate is higher at the notch than in the surrounding material. Rahmaan (2015) documented the rate sensitivity of dual phase steels, observing that an increase in strain rate prompted an increase in the flow stress. It follows that a rate sensitive model would predict higher work hardening at the notches, driving larger strains along the gauge region and an overall higher global stress strain response. More work is required to assess this hypothesis.

The simulated, experimental, and integrated results also agree reasonably well for AA5182 but subject to more variation in the experimental measurements. Figure 62 compares the stress and strain responses, showing excellent agreement between the predicted and experimental data along the rolling direction but discrepancies in the responses obtained along the diagonal and transverse. The experimental variation in the strain data is likely due to the PLC effect, which was particularly severe in the TD and DD, but relatively mild in comparison along the RD. Due to this high experimental variation, the predicted strain responses along DD and TD remain within the experimental margin of error. At the necking cutoff, the strains predicted by LS-DYNA were $\varepsilon_1^{cp} = 0.12$ along the diagonal direction and $\varepsilon_1^{cp} = 0.13$ along the transverse direction, which are within the experimental 95% confidence interval of 0.16 ± 0.09 and 0.11 ± 0.08, respectively.

While the Tresca-type yield surface is a good match for the TD yield surface arc, the exponent of m = 50 appears too high in the DD as the average experimental stress is underpredicted by a maximum of about 5%. This can be traced back to the objective function convergence characteristics illustrated in Figure 36. Rather than a well-defined minimum, the objective function behaves asymptotically beginning at approximately m = 30 and continuing as the exponent increases to infinity. Therefore, any exponent could be selected along this asymptotic approach, while remaining within the experimental margin of error.

The non-associated model calibrated in the TD is reasonably consistent with the experimental results, although it underpredicts the average experimental engineering stress-strain by a maximum of about 4%. This is contrary to the analysis of Chapter 4 which indicated that the HF85-PSC-NAFR model showed a lower objective function error than the HF85-PSC-ISO model. Nonetheless, both models closely predict the experimental results considering the uncertainty introduced by the PLC effect.

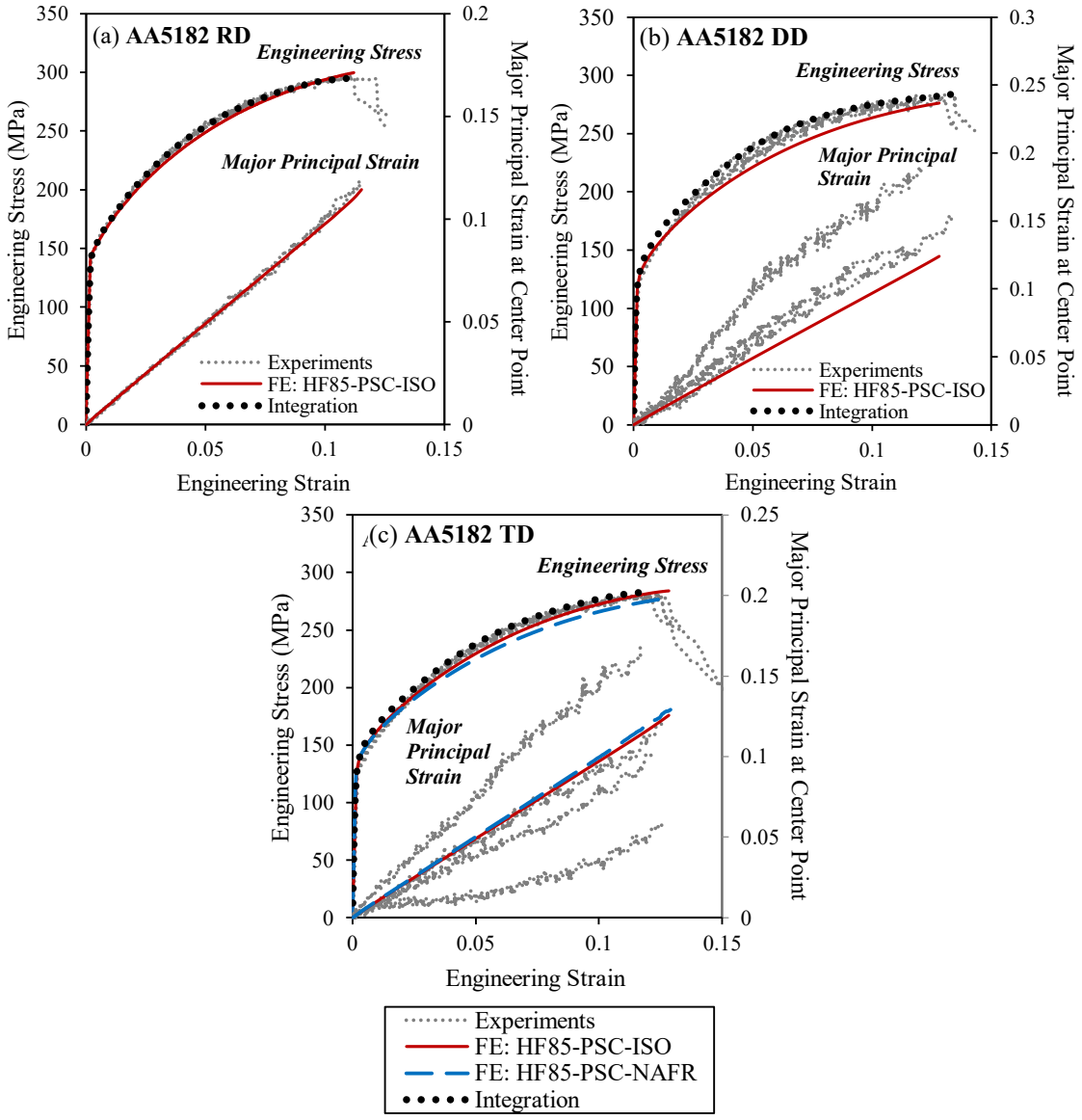

Figure 62: Comparison of finite-element modelled, integrated, and experimental stress and strain responses for AA5182 tested along the (a) RD, (b) DD and (c) TD. The engineering stress-strain response is shown up to the peak load, whereas the representative integration and local strain response are only shown up to the necking cutoff used in the integration methodology.

Figure 63 shows the close agreement between the experimental and simulated responses in all tested directions of AA6xxx-T81. For simplicity, differential hardening was ignored due to the muted response observed in Chapter 4. Nonetheless, the engineering stress and strain responses are well predicted by the isotropic model up to the onset of necking.

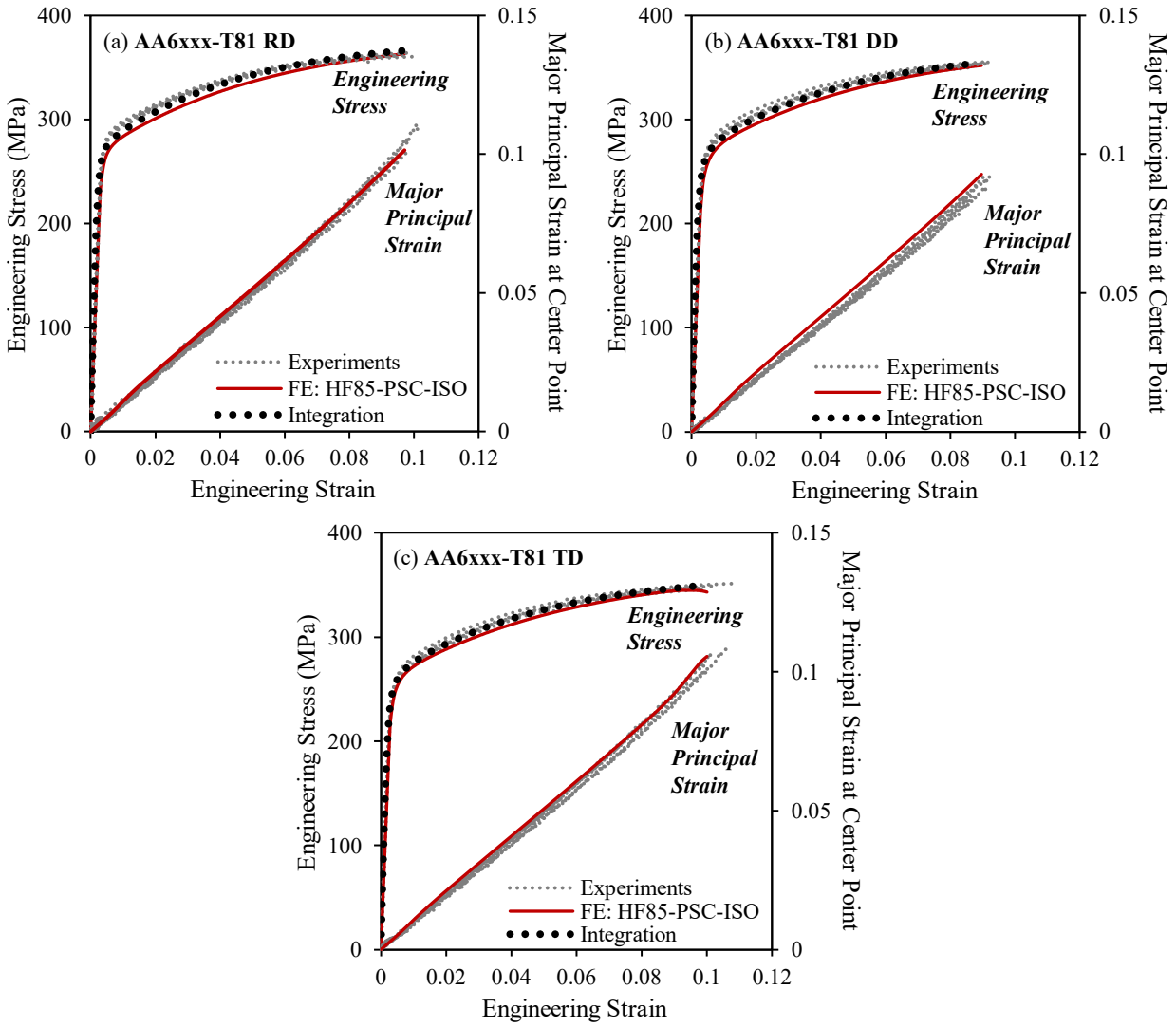

Figure 63: Comparison of finite-element modelled, integrated, and experimental stress and strain responses for AA6xxx-T81 tested along the (a) RD, (b) DD and (c) TD. The engineering stress-strain response is shown up to the peak load, whereas the representative integration and local strain response are only shown up to the necking cutoff used in the integration methodology.

Figure 64 shows the excellent agreement between the experimental results, integration, and isotropic HF5-PSC-ISO models for the AA6xxx-T4 alloy up to necking in all tested directions. Differential hardening was again ignored since the plane strain yield strength only decreased by approximately 4% over the measured range of plastic work. The evolution of the major principal strain, as a function of engineering strain, is in excellent agreement with the experimental results along the DD and TD. Along the RD, a non-linearity in the experimental response develops at an engineering strain of 0.11, possibly as a result of premature necking and localization that was not captured in the cutoff criterion.

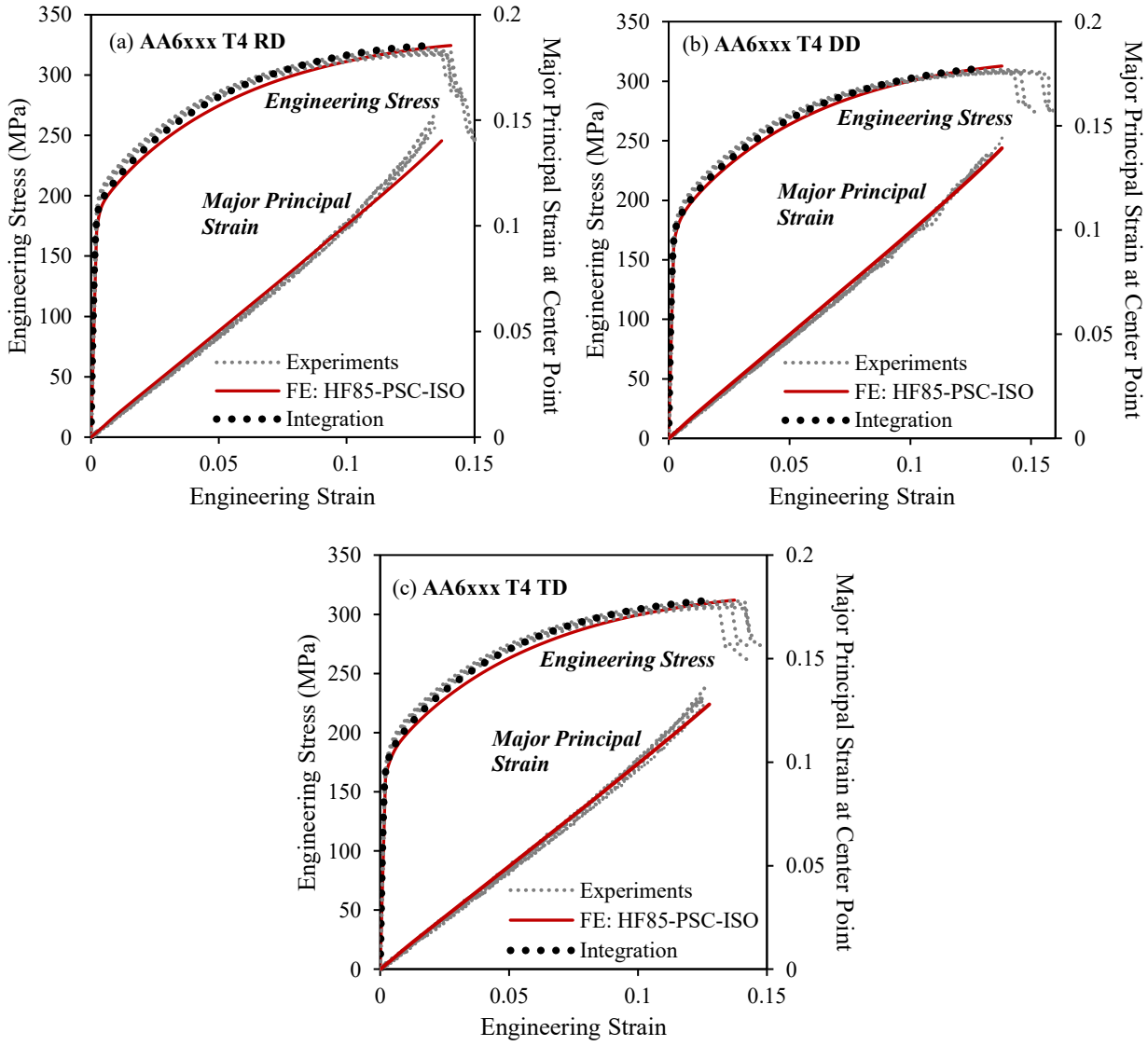

Figure 64: Comparison of finite-element modelled, integrated, and experimental stress and strain responses for AA6xxx-T4 tested along the (a) RD, (b) DD and (c) TD. The engineering stress-strain response is shown up to the peak load, whereas the representative integration and local strain response are only shown up to the necking cutoff used in the integration methodology.

5.3 Summary of Model Evaluation

The integration methodology, and its extensions to cases of differential hardening and non-associated flow, accurately captures the stress and strain responses of the four studied materials. The isotropic associated flow (HF85-PSC-ISO), non-associated flow (HF85-PSC-NAFR) and differential, associated flow (HF85-PSC-EVO) models were evaluated using finite-element simulations and by comparison with the empirical method of Flores *et al.* (2010). Compared to the latter, the present approach does not require

perfect plane strain loading in the center of the specimen and is not sensitive to the size of the so-called homogeneous zone.

Finite-element models of the tested Geometry A confirmed good agreement between the experimental, integrated, and simulated engineering stress-strain and local strain responses for all alloys. Differential hardening was relatively muted for all studied materials; the good agreement between the isotropic models and the experimental results shows that it can be reasonably neglected in component level simulations for the four studied materials. The simulated test for DP1180 was in excellent agreement with the experimental stress and strain response outside the small strain regime of between 0.01-0.02. Greater strain localization, on the order of 34%, occurred at the notches in the experiments compared to the simulated responses, causing a difference in the strain distribution along the gauge region. The increased localization may be due to strain rate sensitivity, which was omitted from the finite-element model. The AA6xxx-T81 and T4 alloys showed excellent agreement between the calibrated models and experimental results. The presence of the PLC effect led to small inaccuracies on the order of 5% in the calibrated DD and TD models for AA5182. Ultimately, the proposed integration methodology acts as a complete toolkit for accurately characterizing the local arc of a yield surface from uniaxial to plane strain tension under isotropic or differential hardening and associated or non-associated flow.

Chapter 6 Constitutive Characterization in Through-Thickness Shear

Through-thickness shear is the second generalized plane strain stress state evaluated in this thesis. As reviewed in Chapter 1, limited investigations into this loading condition for metals have mostly focused on fracture and not constitutive characterization. This chapter outlines the development of a novel test for through-thickness shear characterization along the RD in 1 mm DP1180 and 2.7 mm AA6xxx-T81, considering specimen geometry, test fixture design and DIC pattern generation. These alloys were selected to evaluate both a steel and aluminum and consider the effect of widely different sheet thicknesses.

While both blanking and double notched specimens will initiate through-thickness shear, the double notched specimen introduced in Chapter 2 was selected for experimental convenience and based on the assumed orthotropic behavior of the selected materials. As suggested by Gu *et al*. (2020), the properties identified from a setup modelling a blanking operation, with the applied load orientated parallel to the normal axis of the sheet, may be different from the properties identified from a double-notched test with the applied load directed along the RD or TD. For example, the yield strength may not be the same along complimentary shear planes (i.e.: $\sigma_{xz}^{yield} \neq \sigma_{zx}^{yield}$ and $\sigma_{yz}^{yield} \neq \sigma_{zy}^{yield}$) due to microstructural differences even though the applied shear stress on perpendicular planes of a material volume element must be equal (i.e.: $\sigma_{xz}^{applied} = \sigma_{zx}^{applied}$ and $\sigma_{yz}^{applied} = \sigma_{zy}^{applied}$). Fracture experiments by Wang and Wierzbicki (2015) and Hartmann *et al*. (2021) resemble blanking type setups while those of Gu *et al*. (2020) and Li *et al*. (2018) are of the double-notched variety. However, assuming orthotropy, as is common in the case of aluminum and steel sheet, makes this distinction unnecessary.

6.1 Specimen Design, Manufacturing and Gauge Length Selection

As discussed by Gu *et al*. (2020), the length of the specimen gauge region h must be selected to promote a shear fracture in the gauge region before necking occurs elsewhere in the specimen under uniaxial tension. The maximum uniaxial tensile stress shown in Eq. (6.1) occurs at the notch root, where the cross-sectional area is lowest.

$$\sigma_{eq} = \frac{F}{w\left(\frac{t}{2} - r\right)} = \frac{2F}{w(t - 2r)} \tag{6.1}$$

In Eq. (6.1), F is the applied force, t is the sheet thickness, w is the specimen width and r is the notch radius. The average shear stress in the gauge region is:

$$\tau = \frac{F}{w(h-2r)} \tag{6.2}$$

Assuming the von Mises criterion for design purposes and substituting $\sigma_{eq} = \sqrt{3}\tau$ defines the equivalent stress inside the gauge region as:

$$\sigma_{eq} = \frac{\sqrt{3}F}{w(h-2r)} \tag{6.3}$$

For the specimen to fail in shear before tension, the equivalent stress in the gauge region must be greater than the equivalent stress at the notch root. Including a design factor of n_d, the design condition is defined by the inequality in Eq. (6.4).

$$\frac{\sqrt{3}F}{w(h-2r)} > n_d \frac{2F}{w(t-2r)} \tag{6.4}$$

Simplifying Eq. (6.4) leads to Eq. (6.5), which may be solved for the maximum length of the sample gauge region for any sheet thickness.

$$\frac{h-2r}{t-2r} < \frac{\sqrt{3}}{2n_d} \tag{6.5}$$

A design factor of two was adopted and the notch radius was set to r = 0.15 mm, corresponding to the minimum commonly available wire size for the electrical discharge machining (EDM) process used to make each specimen. Consequently $h = 0.6$ mm and $h = 1.34$ mm, for the 1 mm and 2.7 mm thick sheets, respectively.

Wire EDM was used to make each specimen since it is uniquely suited for precision machining of parts with small features. By creating a spark between the metal workpiece and a wire electrode, the wire EDM process melts or vaporizes the material at temperatures between 8,000-12,000°C to form the desired geometry (Azam *et al.*, 2016). A dielectric fluid, often deionized water, simultaneously cools the workpiece and flushes the eroded workpiece and electrode fragments. By measuring each machined specimen with a Keyence VHX-5000 optical microscope, it was observed that the wire EDM process resulted in good dimensional accuracy and repeatability. As shown in Table 15, the as-machined gauge length was, on average, approximately 47 μm larger than nominal. The notch radii were machined 30 μm larger than designed, but within the expected tolerances.

Table 15: Measurements of through-thickness shear geometry features machined using wire EDM. All dimensions are in millimeters. The average value is presented with the standard deviation in brackets.

Material	Notch Radius	Gauge Length
DP1180	0.176 (0.007)	0.346 (0.010)
AA6xxx-T81	0.184 (0.005)	1.047 (0.014)

Optical microscopy revealed some other interesting features of the machined specimens. Figure 65(a) shows typically 55 μm thick black "burn marks" around each notch of the DP1180 specimens. Some DP1180 specimens, like the one in (b), also showed orange rust possibly because of oxidation induced by electrolysis of the water during machining (Azam *et al.*, 2016). The rust was removed by light sanding prior to DIC pattern application. In contrast, the AA6xxx-T81 specimens did not show any discoloration or visible defects as shown in (c).

(a)

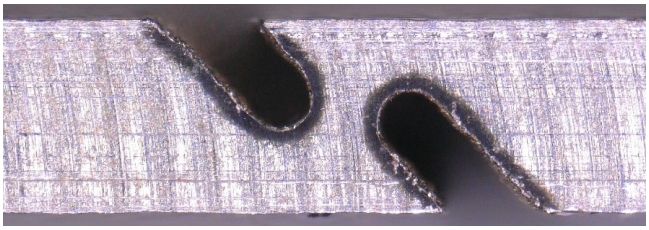

(b)

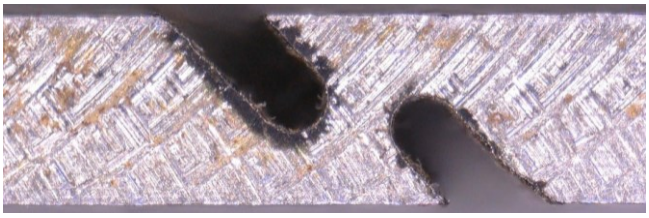

(c)

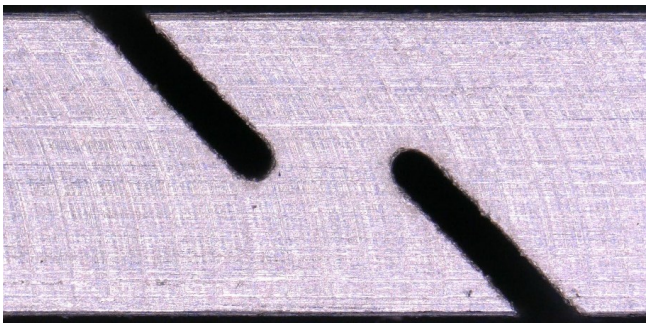

Figure 65: (a) Discoloration, or so called "burn marks", on the surface of the DP1180 through-thickness shear specimens subjected to wire EDM. The average measured thickness of each burn mark was 55 μm. (b) Regions of orange rust on DP1180 specimens produced by wire EDM. (c) Representative AA6xxx-T81 through-thickness shear specimen produced by wire EDM.

6.2 Test Fixture Design and Parameter Selection

A clamping force is required to reduce rotation of the gauge region, decrease bending moments, and promote a stress state of simple shear. As shown in Figure 66, localization occurs outside the gauge region at the notch root if the sample is unrestrained. Rather than fail in a state of shear, the specimen necks in uniaxial tension. A rigid fixture must be designed to provide clamping force that minimizes rotation and encourages a shear failure in the center of the gauge region.

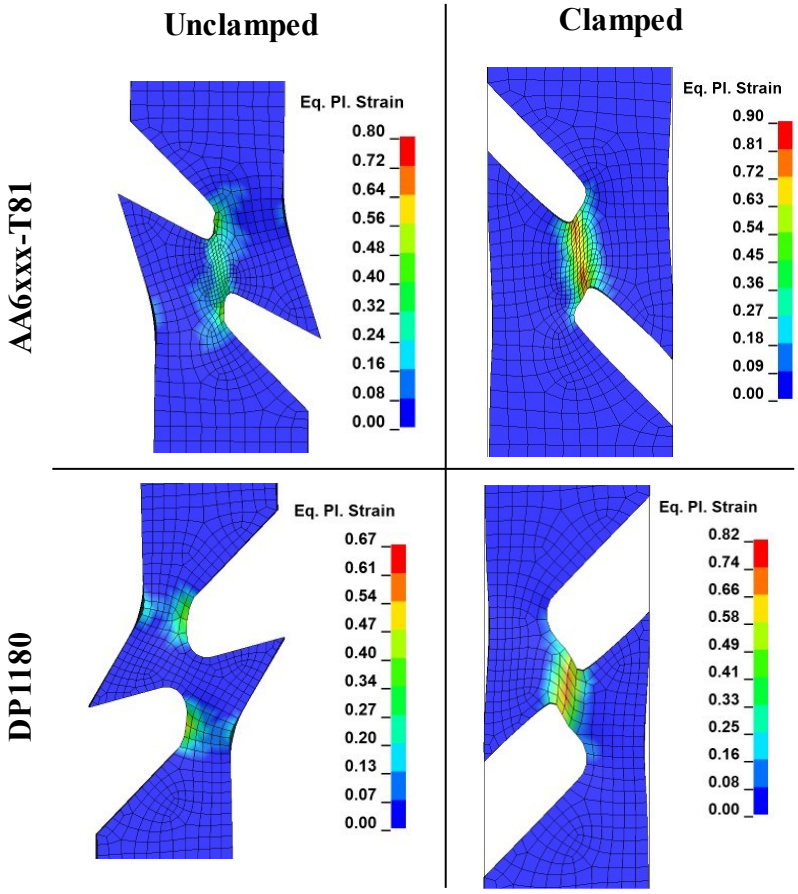

Figure 66: Contours of equivalent plastic strain from simulated clamped and unclamped through-thickness shear tests. The solid models consisted of Type 1 elements, with a characteristic dimension of 0.05 mm in the gauge region. The von Mises yield surface was employed along with the material hardening curves from Chapters 3 and 4.

An existing cyclic tension-compression fixture, under development by Jacqueline Noder at the University of Waterloo, was adapted for through-thickness shear testing. The fixture was based on a design proposed by Kupke (2017). It consists of two steel plates compressed against the specimen using a nitrogen spring with a maximum on-contact force of 15 kN. Suspending the entire clamping fixture from springs allows it to move with the elongating specimen, minimizing relative velocity and sliding friction. To adapt the fixture for through-thickness shear testing, two 25.4 mm x 45 mm x 110 mm dies were fabricated so

that a microscope lens could be placed between the clamping plates in close proximity to the specimen surface. Figure 67 shows the final fixture design, configured for through-thickness shear testing.

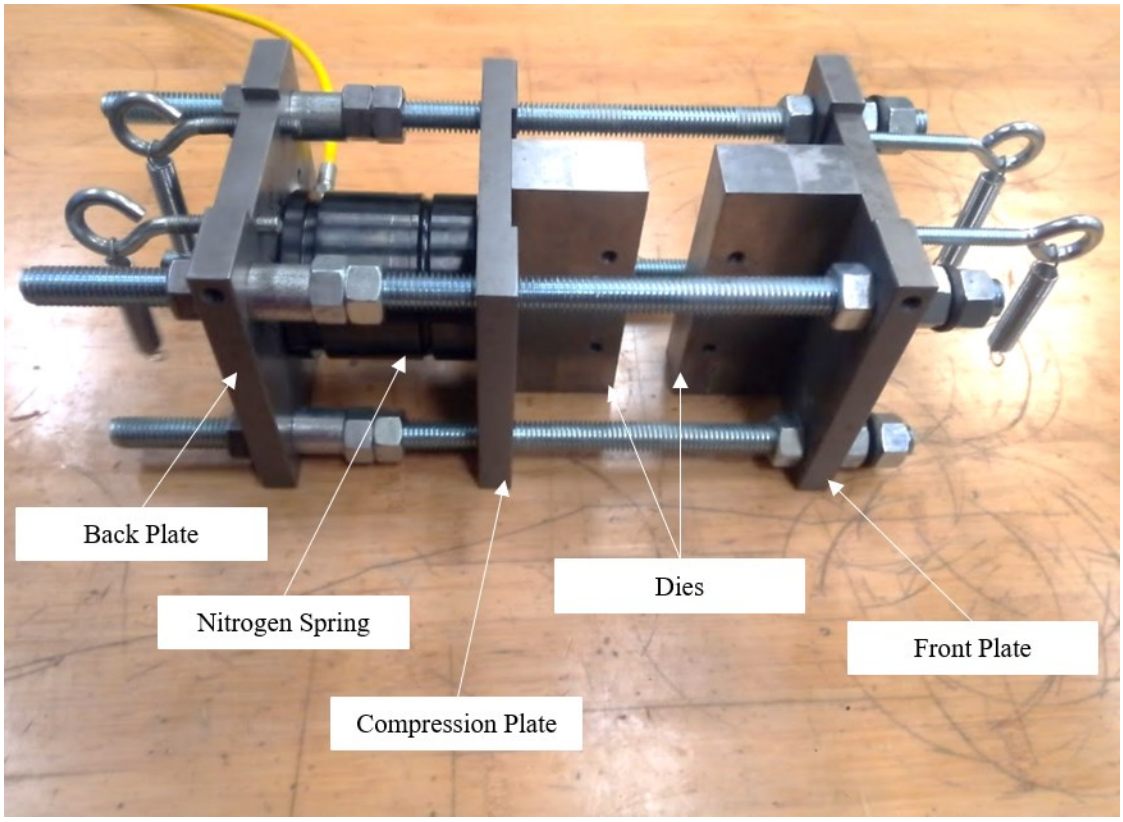

Figure 67: Through-thickness shear fixture. The nitrogen spring provides the required clamping force to minimize gauge region rotation of the specimen.

6.2.1 Selection of a Clamping Pressure

The selection of the clamping force is subject to two competing objectives; the force must be high enough to reduce rotation but also as low as possible to minimize friction and the superimposed biaxial stress. A finite-element study was used to select a clamping force, F_c in advance of the experimental tests by evaluating the gauge region rotation at values between F_c = 0 and F_c = 12 kN. The 1 mm and 2.7 mm sheets were modelled under half-symmetry using an explicit dynamic formulation. The actual hardening curves for each material were used, but the yield surface was assumed to be von Mises since the through-thickness properties were unknown in advance of the experiments. Type 1 solid elements were used with a characteristic dimension of 0.05 mm in the gauge region. Two rigid shell plates were also modelled to be representative of the clamping fixture. The clamping force was applied to the rigid plates and contact was enforced between the sheet and plates assuming a coefficient of static and dynamic friction of μ = 0.03. Figure 68 shows the boundary conditions and mesh design.

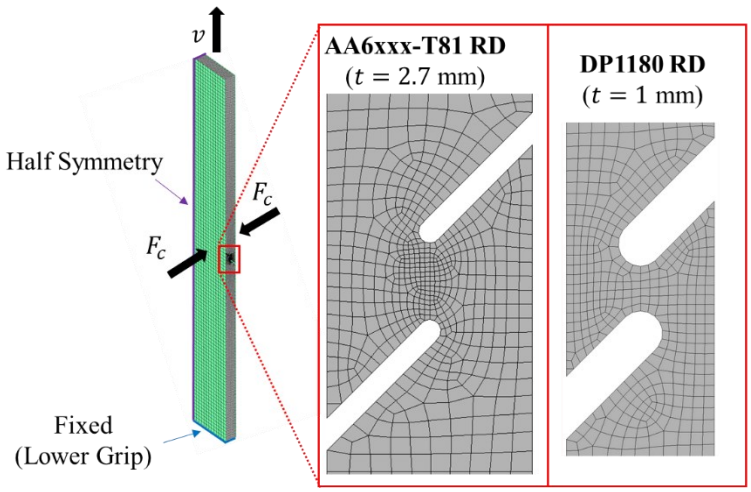

Figure 68: FE through-thickness shear model showing mesh and boundary conditions. The sheet thicknesses are not to scale to illustrate the mesh design.

As shown in Figure 69, gauge region rotation decreases with increasing clamping force. For each value of F_c, the rotation was evaluated at the same crosshead displacement of 0.47 mm for DP1180 and 0.81 mm for AA6xxx-T81. As a first estimate, the selected displacements correspond to the point at which the equivalent plastic strain in the gauge region begins to exceed the equivalent fracture strain obtained from in-plane shear tests of the same material. The equivalent in-plane fracture strain is approximately $\varepsilon_{eq}^{f} = 0.6$ for DP1180 (Abedini *et al.*, 2020) and $\varepsilon_{eq}^{f} = 0.8$ for AA6xxx-T81. Convergence was observed at F_c = 4 kN for AA6xxx-T81 ($\theta = 4°$) and $F_c = 8$ kN ($\theta = 7°$) for DP1180.

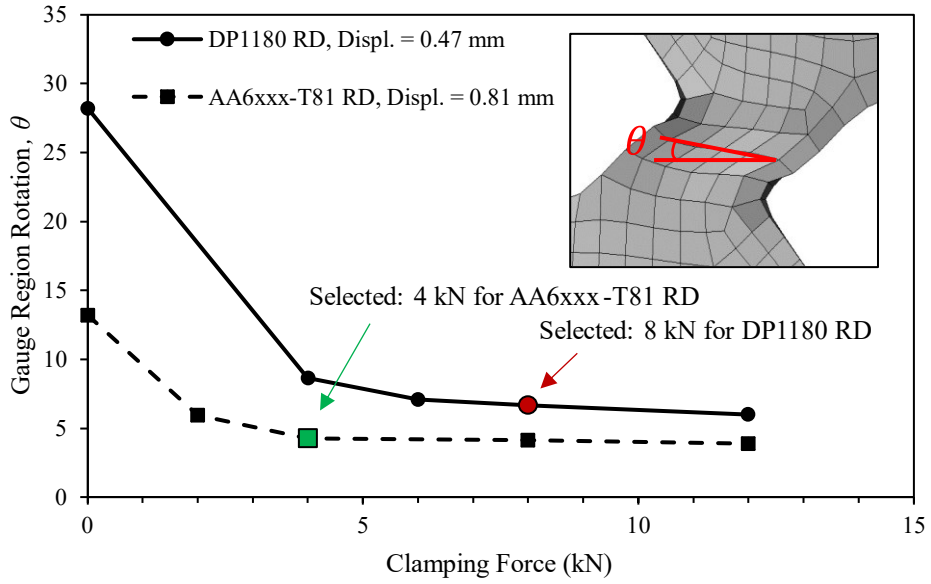

Figure 69: Dependency of gauge region rotation on clamping force. Convergence was obtained at a clamping force of F_c = 4 kN for AA6xxx-T81 and F_c = 8 kN for DP1180.

The force-displacement, triaxiality (T), equivalent plastic strain and Lode parameter (L) evolution were evaluated at the selected clamping forces as shown in Figure 70. The Lode parameter, in the middle of the specimen at the half-symmetry plane, is equal to zero for most of the deformation indicating plane strain loading. At the free surface, the Lode parameter increases with deformation, indicating a departure from plane strain. Similarly, the triaxiality at both locations increases with plastic strain. For both alloys, the initial stress state is compressive due to the clamping force of the dies. The average triaxiality and Lode parameter were calculated using Eq. (6.6) to quantify the average state of stress and strain over the range of deformation.

$$f_{avg} = \frac{1}{\varepsilon_{eq}^{p}} \int_{0}^{\varepsilon_{eq}^{p}} f d\varepsilon_{eq}^{p} \approx \frac{1}{\varepsilon_{eq}^{p}} \sum_{i=1}^{N} \bar{f}_i \Delta\varepsilon_{eq}^{p}, \; f = \begin{cases} L \\ T \end{cases} \tag{6.6}$$

For the AA6xxx-T81, the average Lode parameter and triaxiality were -0.018 and -0.065, respectively. For DP1180, the average Lode parameter and triaxiality were 0.01 and 0.07, respectively. The average values are sufficiently close to a simple shear stress state with $L = T = 0$ such that both specimens are appropriate for constitutive characterization in through-thickness shear.

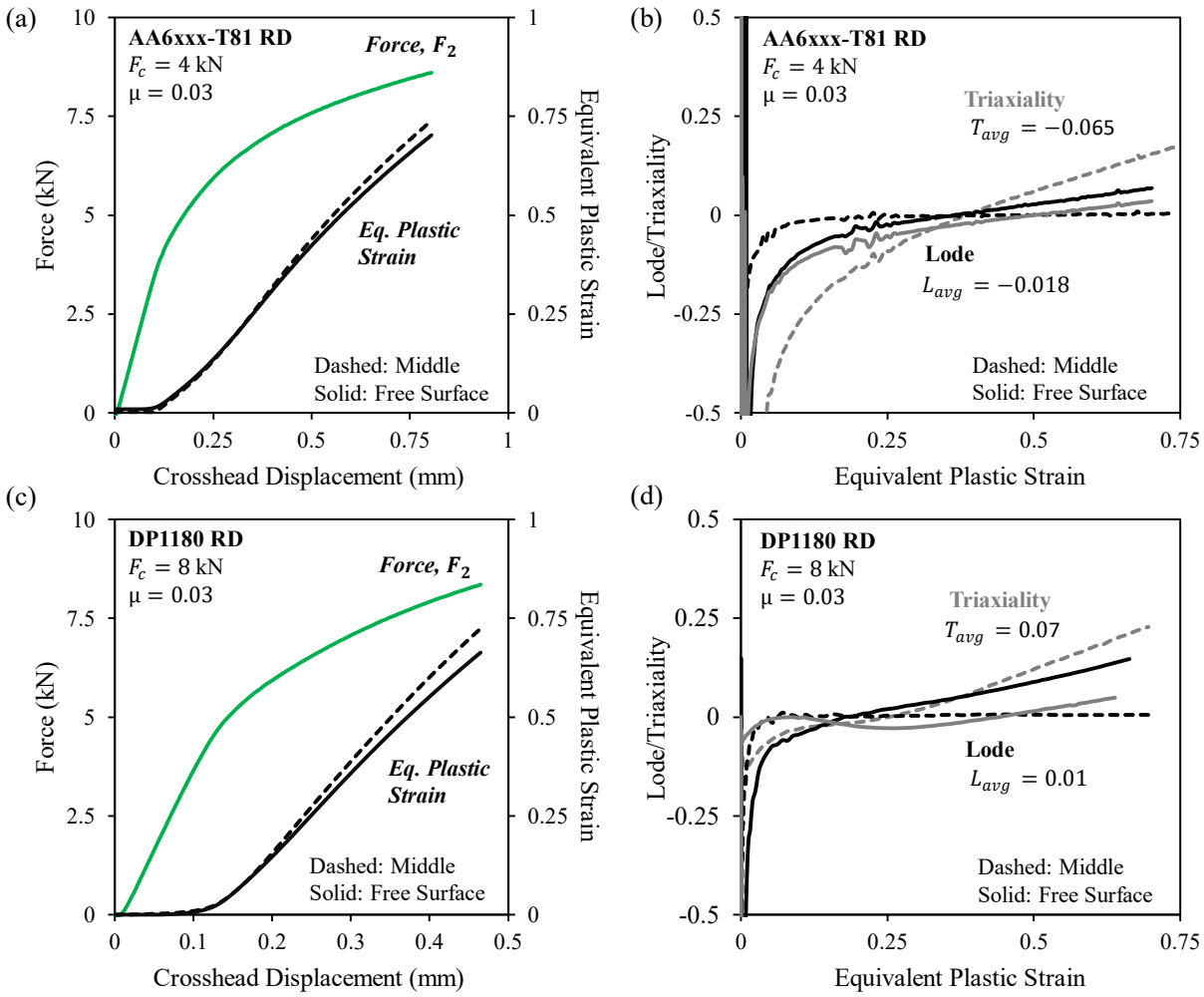

Figure 70: Force, equivalent plastic strain, Lode parameter and triaxiality at the selected clamping forces for (a, b) AA6xxx-T81 and (c, d) DP1180. The dashed lines represent values extracted from the midplane of the specimen, at the element in the center of the gauge region, while the solid lines represent values extracted from the free surface where DIC measurements occur.

6.2.2 Sensitivity to Friction

The clamping force introduces friction into the load response. If the upper grip force is denoted as F_1 and the lower grip force as F_2 then the frictional force F_f is in the same direction as F_2. Figure 71 represents the free body diagram of the through-thickness shear specimen. Since the load cell is located at the upper grip (denoted F_1), the frictional force F_f must be subtracted from the measured force. Using the standard Coulomb model, the friction-free force F_2 is

$$F_2 = F_1 - 2F_f = F_1 - 2\mu F_c \tag{6.7}$$

where μ is the coefficient of friction.

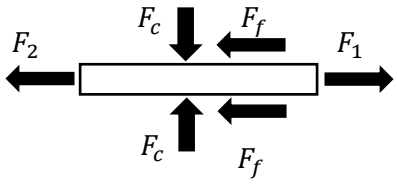

Figure 71: Free body diagram of through-thickness shear specimen. The frictional force F_f opposes the direction of the force F_1 at the upper grip where the load cell is located.

The challenge is in determining the value of the coefficient of friction. It is common to perform both clamped and unclamped tensile tests in uniaxial tension-compression tests, the closest existing experimental analogue to the proposed through-thickness shear setup. By subtracting the unclamped force value from the clamped force at a given displacement, the friction coefficient is obtained for a given clamping force and material. A correction for the superimposed biaxial stress, due to the clamping force, is applied before subtraction (Boger *et al.*, 2005; Kupke, 2017). Although the method of clamped/unclamped curve subtraction is perhaps ideal for accurate friction measurement in uniaxial tensile specimens, it is poorly suited for the present geometry since the gauge region rotation causes dramatic differences in the slope and magnitude of the stress-strain response of an unclamped specimen.

A review of the tension-compression test literature, summarized in Table 16, suggests a coefficient of friction of between 0.03 and 0.11 for a Teflon-steel or Teflon-aluminum interface. Fixture design is responsible for some of the variation; a fixture that moves with the deforming specimen is advantageous to limit relative velocity and friction (Kupke, 2017; Boger *et al.*, 2005; Kuwabara *et al.*, 2009). Ultimately, the Coulomb model is only an approximate idealization of the complex characteristics of friction. Surface roughness, contact interface pressure (Tamai and Manabe, 2013), velocity (Hwang and Chen, 2020), material, lubrication, and breakdown (Noder, 2017) all affect the coefficient of friction. Therefore, it is important that the friction coefficient is determined under test conditions as close as possible to the through-thickness shear experiments.

Table 16: Summary of friction coefficients reported in the literature for a Teflon-metal interface in tension-compression tests. Tension-compression tests are perhaps the closest existing experimental setup to the proposed through-thickness shear tests.

Material	Coefficient of Friction	Clamping Force (kN)	Contact Pressure (MPa)	Reference
AA6022-T4	0.03-0.06	7	-	(Boger *et al.*, 2005)
DQSK/HSLA/AA6022-T4	0.06-0.09	5	-	(Balakrishnan, 1999; Geng *et al.*, 2002)
DP780	0.11	5/10	-	(Kupke, 2017)
DP590	0.04	2.23/3.35	0.83/1.25	(Sun and Wagoner, 2013)
DP780	0.067	2.23/3.35	0.83/1.25	(Sun and Wagoner, 2013)
DP980	0.105	2.23/3.35	0.83/1.25	(Sun and Wagoner, 2013)
DQ	0.07	2.03	-	(Joo *et al.*, 2016)
DP590		3.15	-	(Joo *et al.*, 2016)
SPCC	0.06	2.003	-	(Bae and Huh, 2011)
DP590	0.08	2.275	-	(Bae and Huh, 2011)

To assess the sensitivity of the through-thickness shear setup to friction, the coefficient was adjusted between 0.03 and 0.11 in finite-element simulations to probe the change in the stress-strain response. The maximum range of the expected measurement error can be estimated from two extreme cases: the actual coefficient is 0.03 but the coefficient was overcorrected with 0.11 or the actual coefficient was 0.11 but it was under-corrected with 0.03. As shown in Figure 72, there is a maximum 37 MPa, or 12% error in the stress for the AA6xxx-T81 and a 239 MPa or 26% error in the shear stress for DP1180. The lower error for the AA6xxx-T81 is attributable to the clamping force, which is only half the value required for DP1180 to inhibit rotation. Although selection of the friction coefficient introduces uncertainty into the load response, simulated fracture strains were independent of friction. Only the load cell force requires a correction for constitutive characterization.

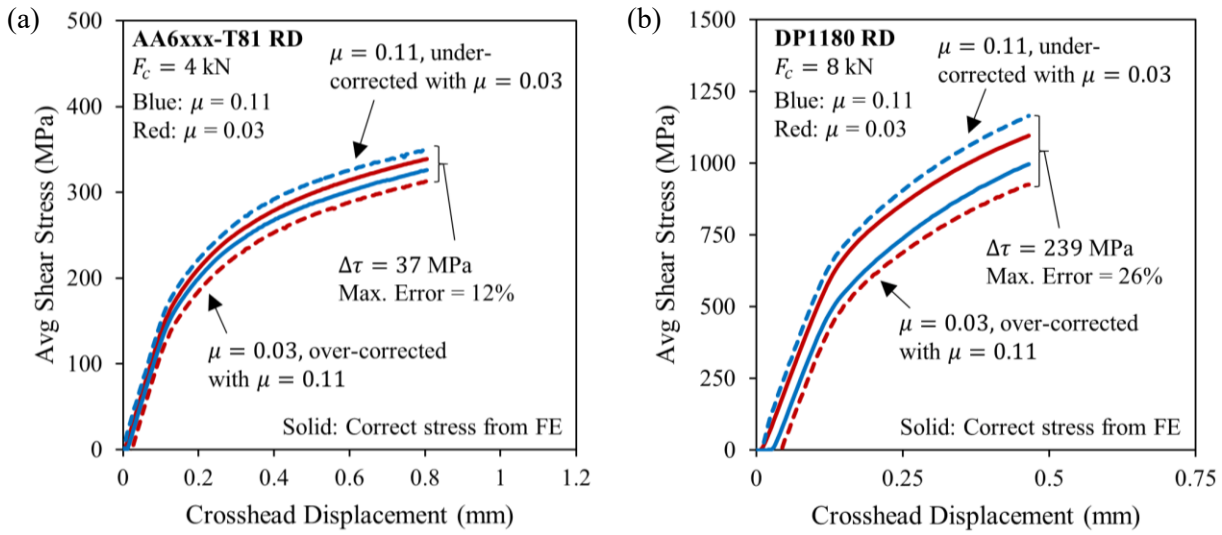

Figure 72: Illustration of error caused by improper selection of the friction coefficient in simulated through-thickness shear tests of (a) AA6xxx-T81 and (b) DP1180. The blue curves illustrate the results obtained at a friction coefficient of μ = 0.11 and the red curves illustrate the results at μ = 0.03. The solid curves represent the stress obtained from the load at the lower grip, F_2 which is friction-free and the target stress for the friction correction. If μ = 0.03, but the response is overcorrected with μ = 0.11, then the red dashed curve is obtained. If μ = 0.11, but the response is under-corrected with μ = 0.03, then the blue dashed curve is obtained. The difference between these extremes is the range of the possible experimental error.

6.2.2.1 Friction characterization using clamped rectangular strip tests

Based on the non-negligible influence of friction on the proposed experimental setup and variability of the coefficient in literature, a method was developed to characterize the friction coefficient under analogous conditions to the through-thickness shear tests. Between three and four 25.4 mm x 200 mm rectangular strips were clamped in the test fixture and tested until fracture, maintaining approximately the same contact area, sliding velocity, lubrication, and pressure distribution as the through-thickness shear tests. As the stress state within the strip is uniaxial tension up to uniform elongation, the true stress strain curve obtained from the clamped rectangular strip tests can be directly subtracted from the material flow stress curve presented in Chapters 3-4 to isolate the friction coefficient using Eq. (6.7).

The so-called friction strip test must be corrected for both biaxial stress and friction (Kupke, 2017; Boger *et al.*, 2005). The clamping force applied by the fixture induces a biaxial stress in the specimen, which may be estimated using the von Mises criterion as:

$$\sigma_{eq} = \sqrt{\sigma_a^2 - \sigma_a\sigma_t + \sigma_t^2} \tag{6.8}$$

where σ_a is the stress in the axial loading direction and σ_t is the through-thickness stress component introduced by the clamping pressure obtained from Eq. (6.9). The contact area, A_c is 2794 mm^2 (25.4 mm x 110 mm) for the dies used in this study.

$$\sigma_t = \frac{F_c}{A_c} \tag{6.9}$$

As discussed by Boger *et al*. (2005), adopting the von Mises yield criterion for an anisotropic material introduces minimal error due to the small magnitude of the biaxial stress. After biaxial correction, the Coulomb friction coefficient is iteratively adjusted to bring the clamped stress-strain curve into agreement with the average stress-strain curve of the unclamped repeats.

6.3 DIC Pattern Generation

Considering the small size of the through-thickness shear specimen gauge regions, conventional spray paint produces large speckles unconducive for selection of a subset size with sufficient spatial resolution of the DIC captured strain field. A method of generating smaller speckles using an Iwata Eclipse® airbrush with a 0.35 mm needle at 30 psi was evaluated by applying various inks and paints to the surface of the 1 mm thick DP1180 geometry. Some of the spray mediums were selected from a review of the literature including Golden Artist® High Flow Acrylic Paint (Kramer *et al.*, 2016) and spray paint collected from the can and re-atomized with the airbrush (Blaber, n.d.). The other mediums tested in the airbrush were PEBEO® India ink and FW® acrylic ink. Two brands of conventional spray paints, with different nozzle sizes, were also used for comparison. Images of each speckle pattern were captured at the same magnification and field of view using a Keyence VHX-5000 digital microscope for comparison and particle size analysis.

To quantify the speckle size distribution, a representative 1 mm x 1 mm region was extracted from each image seen in Figure 73, binarized then analyzed using the *bwlabel* and *imfindcircles* commands in Matlab®. The *imfindcircles* command employs a Circular Hough Transform (CHT) algorithm to identify the size and center point of each circle in the image. Consider one black circle on a white background, for simplicity: the edges of the circle are defined where the color gradient is greatest (i.e.: transition from black foreground to white background). At each edge pixel, possible coordinates for the center of the circle are collected by sweeping a radial line outward in all directions. By repeating this procedure at each edge pixel around the perimeter of the circle, an array of possible center coordinates for the circle is obtained, with the correct location being the one that is common to all of the edge pixels (MathWorks, n.d.). Whereas application of the CHT algorithm is complicated by the presence of non-circular, coalesced “blobs” of droplets, the *bwlabel* command, as used by Dong *et al*. (2015), simply defines the equivalent diameter of a circle occupying the same area as each blob.

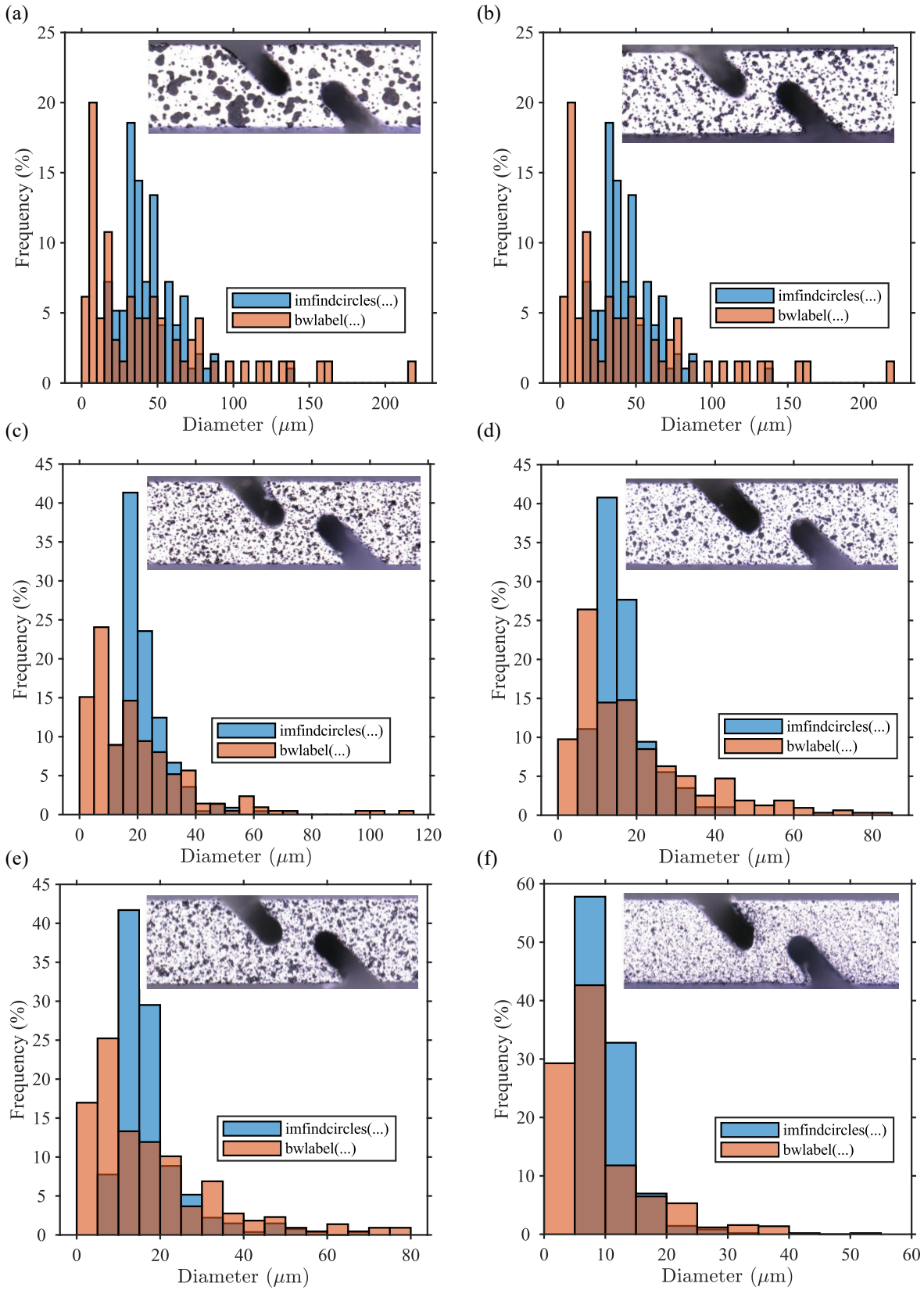

Figure 73: Speckles generated using (a) Rustoleum® spray paint, (b) Zynolyte® spray paint, (c) PEBEO® India ink, (d) FW® acrylic ink, (e) Golden Artist® High Flow paint and (f) Re-atomized Rustoleum® paint. Patterns (c-f) were applied using an airbrush.

Despite the differences in the methodologies of the two particle processing methods, both indicate a left-skewed frequency distribution with a similar average speckle size. Table 17 shows the summary statistics of the frequency histograms for both processing methods and all tested inks and paints. FW® acrylic ink was selected for the present study since it resulted in a small average speckle size of ~18 μm. Although the re-atomized Rustoleum® resulted in the smallest speckles, transferring the paint from the can to the airbrush was impractical. Due to the fast-drying nature of spray paint, the adhesion properties may also have been affected by transfer and re-atomization. The PEBEO® India Ink was too glossy when dry, which caused bright spots in the DIC images. Regardless of the selected medium, the airbrush can produce a much finer speckle pattern than conventional spray paint.

Table 17: Diameter and standard deviation (in brackets) of the speckles in six different DIC patterns analyzed using two particle counting methods. Speckle diameter is given in micrometers.

Particle Counting Method	Conventional Spray Paint		Airbrush			
	Rustoleum®	Zynolyte®	PEBEO® India Ink	FW® Acrylic Ink	Golden Artist® High Flow Acrylic Paint	Re-atomized Rustoleum®
imfindcircles	45.02 (18.99)	24.34 (8.77)	17.20 (6.55)	18.11 (8.66)	22.71 (8.50)	10.59 (3.65)
bwlabel	45.37 (46.34)	25.62 (20.09)	19.26 (15.49)	17.99 (15.74)	19.73 (17.77)	9.25 (7.44)

6.4 Experimental Testing

The friction and shear specimens were tested on the Shimadzu 50 kN electro-pneumatic test frame introduced in Chapter 2. The clamping fixture was suspended from hooks attached to aluminum extrusion side rails. The supporting side rails were bolted to the tensile frame bed. The fixture was then levelled and plumbed to minimize rotation and bending of the specimen as shown in Figure 74. The grips of the test frame were rotated 90 degrees from their nominal position to allow for 2-D DIC measurement on the edge of the sheet specimens.

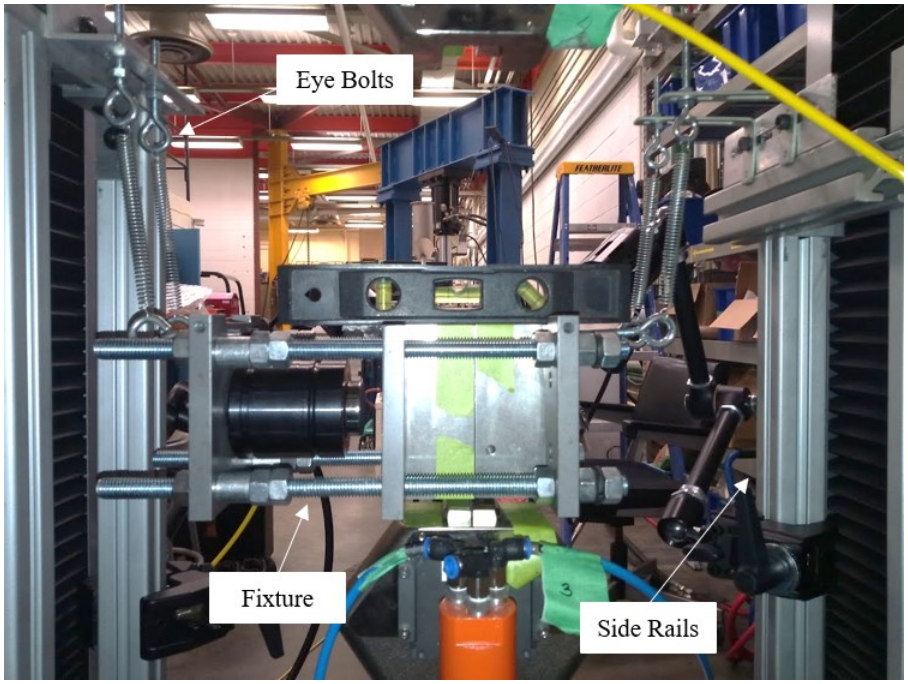

Figure 74: Setup and attachment of through-thickness shear fixture to the Shimadzu uniaxial test frame.

Each specimen was carefully prepared for testing. The gauge length was measured with the optical microscope, as discussed in Section 6.1, and the width was measured with calipers. The edge of the sample was then cleaned with alcohol and lightly sanded to improve adhesion prior to applying the white spray paint base coat. The FW® acrylic ink speckle pattern was applied with the airbrush as discussed in Section 6.3.

The clamping fixture and nitrogen spring were controlled using a 2000 psi [138 bar] compressed nitrogen canister with a regulator and transducer to accurately measure the pressure. After clamping the specimen in the Shimadzu grips, the nitrogen spring was pressurized to the target clamping pressure, P_{target}. The target clamping pressure was determined from the target force (F_{target}) based on the rated on-contact force (F_{rated}) and pressure (P_{rated}) of the spring as shown in Eq. (6.10). At full extension, the nitrogen spring had a rated on-contact force of 15.7 kN at a pressure of 150 bar. The force provided by a nitrogen spring increases as the cylinder volume decreases due to Boyle's Law. However, since the spring was positioned such that contact occurred at approximately full extension, the on-contact force was taken as the rated force provided by the spring without any correction for volume compression.

$$P_{target} = \frac{F_{rated} P_{rated}}{F_{target}} \tag{6.10}$$

Combined application of 0.1 mm thick Teflon sheets, Petrolatum and PTFE spray lubricant minimized friction between the dies and the specimen. A thin layer of Petrolatum was applied between two Teflon sheets, which were then inserted between the specimen and each of the PTFE lubricated dies. The Petrolatum tended to "squeeze out" once the spring was pressurized, so the Teflon sheets were folded to direct the excess away from the sample surface and avoid damaging the speckle pattern.

Figure 75 shows the setup of the test equipment. Images were captured at 1 frame per second (FPS) by a single 12 MP Flir Systems® camera with an InfiniProbe® MS microscopic lens. The crosshead speed of the uniaxial tensile frame was set to 5E-4 mm/s for the DP1180 and 0.017 mm/s for the AA6xxx-T81 shear specimens to obtain a quasi-static von Mises equivalent strain rate of approximately 0.001 s^{-1} in the center of the gauge region.

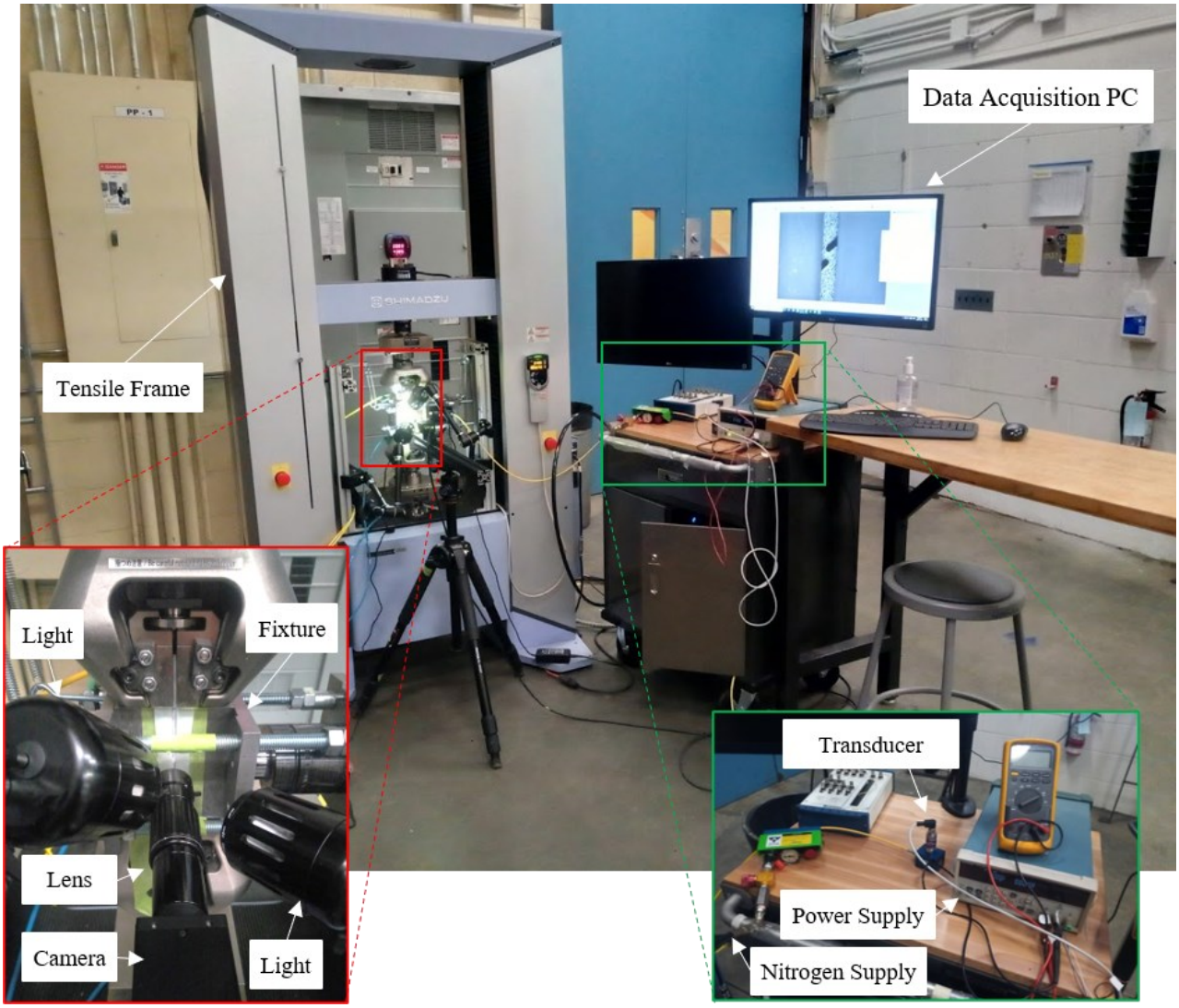

Figure 75: Experimental setup of through-thickness shear test equipment.

Four repeats of AA6xxx-T81 and three repeats of DP1180 through-thickness shear were performed at a nominal clamping force of 6 kN and 12 kN, respectively. Each clamping force is 50% higher than those identified in the finite-element study of Chapter 6.2 to implement a design factor and guard against experimental uncertainty. Due to the low fracture strains encountered in the DP1180 tests and excessive rotation that affected the localization of strain in the gauge region (even with the 50% larger clamping force than simulated), one specimen was cut in half using water jet machining. The two smaller specimens were then tested at 6 kN and 12 kN of clamping force to assess whether a higher contact pressure would decrease rotation and increase the fracture strain and localization in the gauge region. Strains were then extracted with 4 circle inspectors and a 6 mm extensometer as shown in Figure 76 and Figure 77. The VSGL was selected to correspond to the width of the shear zone seen in the DIC contours. A VSGL of 0.1 mm was used for the DP1180 and 0.3 mm for the AA6xxx-T81.

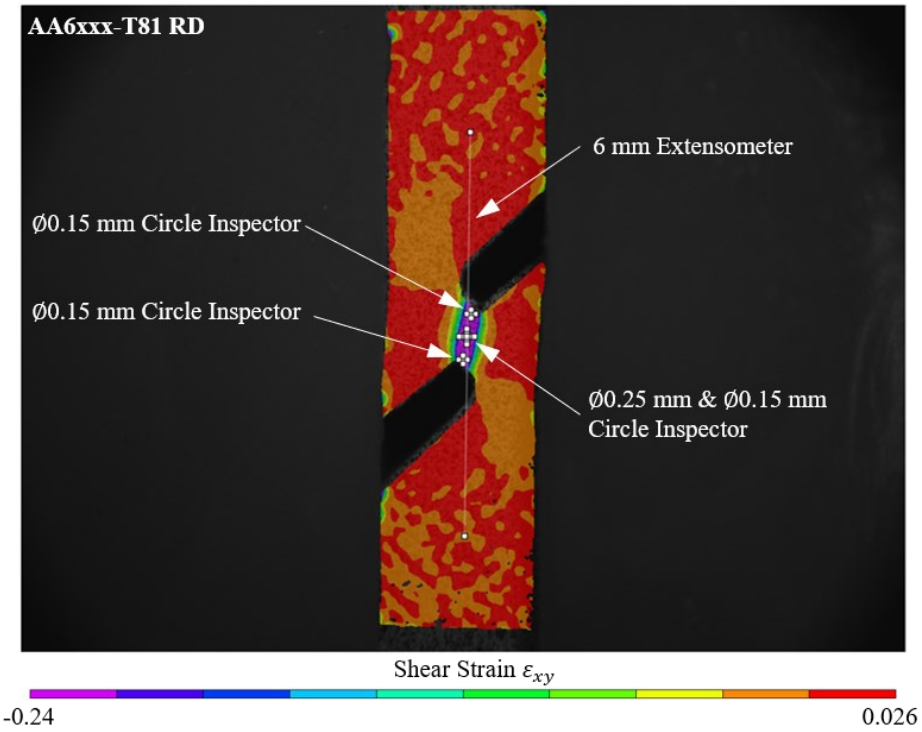

Figure 76: Contour plot showing shear strain at the image prior to fracture for a representative through-thickness shear test of AA6xxx-T81 tested along the RD.

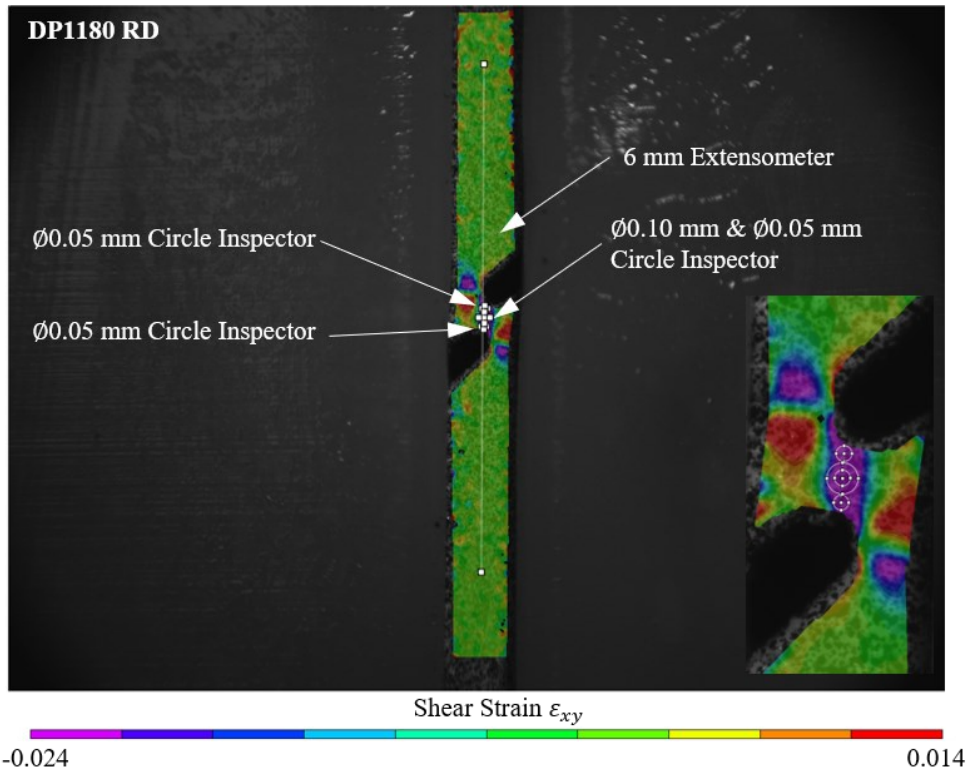

Figure 77: Contour plot showing shear strain at the image prior to fracture for a representative through-thickness shear test of DP1180 tested along the RD.

The friction strips were tested at 0.017 mm/s for the AA6xxx-T81 and 0.083 mm/s for the DP1180. Ideally, both the shear and friction tests should be performed at the same velocity, but the test time for the DP1180 was over two hours to fracture at 5E-4 mm/s. Therefore, the velocity was increased to 0.083 mm/s to equalize the strain rates over the 50 mm extensometer gauge length of the friction strip specimen and the 6 mm extensometer length employed for the shear specimen. Representative DIC images and placement of the extensometer is shown in Figure 78. Two friction strip repeats were performed at each clamping force of 6 kN and 12 kN for both alloys. The same VSGL as the through-thickness shear tests was used for the friction strip tests.

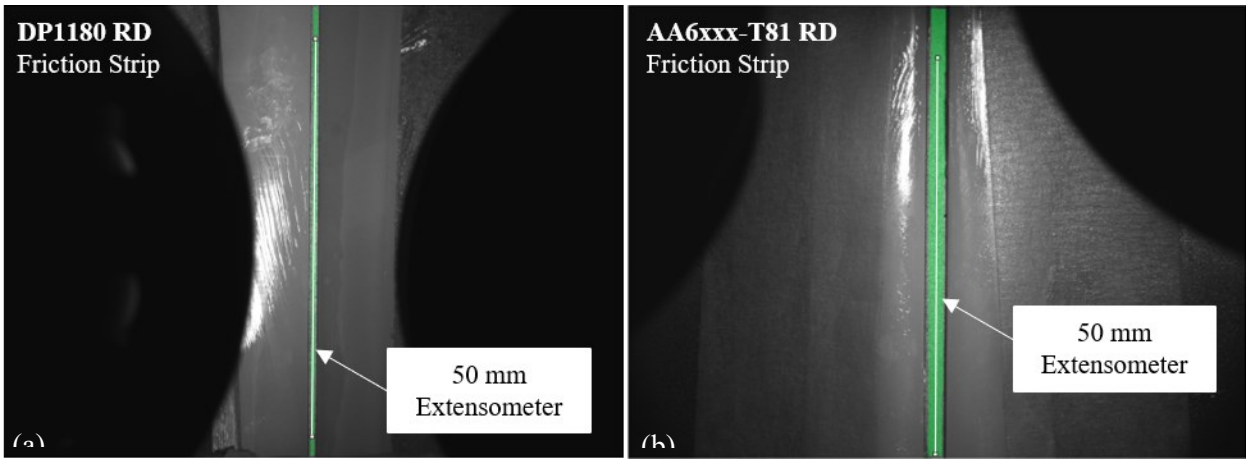

Figure 78: Typical field of view for DIC of friction strip tests showing 50 mm extensometer. Images shown are for (a) DP1180 and (b) AA6xxx-T81.

6.5 Results

The coefficient of friction was first estimated from the strip tests, then used to correct the through-thickness shear stress at the same clamping force. After correcting for friction, the normalized shear stress was obtained using the method of Rahmaan *et al.* (2017) for use in yield surface calibration. To assess the quality of the test results, post-mortem optical microscopy photographs were taken of the shear specimens. The surface roughness of each material was also correlated with the measured coefficient of friction.

6.5.1 Friction Tests

A representative correction procedure is illustrated in Figure 79. The uncorrected, clamped friction strip test has a higher equivalent stress than standard uniaxial "dogbone" tests in the same direction due to the presence of friction. Subtracting the biaxial stress and friction collapses the clamped curve to those of the unclamped dogbone tests. In all cases, the biaxial stress was negligible, and the biaxial corrected response overlapped the uncorrected curve. For the repeat shown below, a coefficient of friction of $\mu = 0.1$ was needed to bring the curves into agreement.

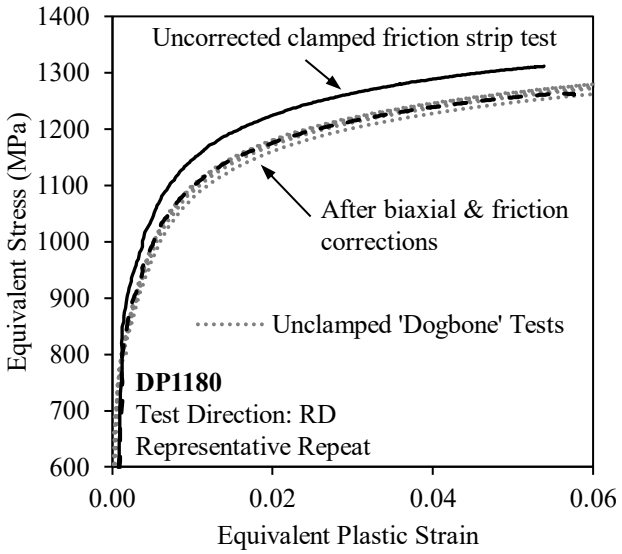

Figure 79: Illustration of correction procedure to obtain the coefficient of friction from a clamped friction strip test.

The final friction and biaxial corrected stress versus equivalent plastic strain curves are presented in Figure 80. The unclamped tensile curves are the same as those shown in Figure 11 and Figure 7 for the DP1180 and AA6xxx-T81, respectively. Excellent agreement between the hardening curves fit to the unclamped data and the corrected friction strip tests occurs with proper selection of the coefficient of friction.

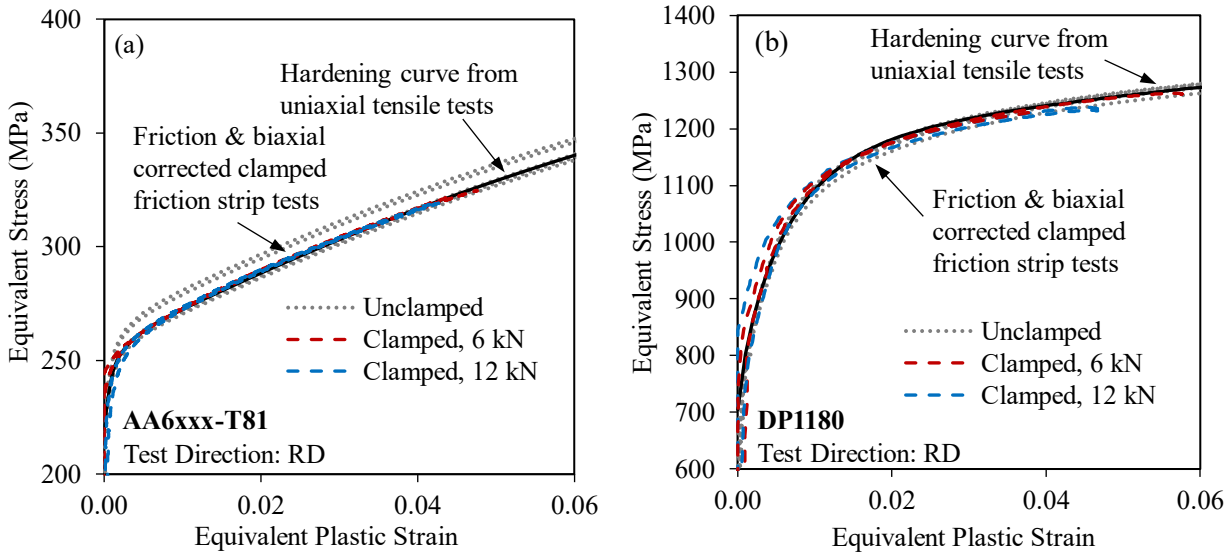

Figure 80: Stress-strain curves for clamped and unclamped tensile tests of (a) AA6xxx-T81 and (b) DP1180 at 6 kN and 12 kN of clamping force. After biaxial and friction correction, each clamped tensile (friction strip test) agrees well with the hardening curve fit to the unclamped tensile tests.

The coefficients of friction that were used to bring each clamped curve into agreement with the hardening curve and unclamped dogbone tests are shown in Figure 81. For DP1180, $\mu = 0.09 \pm 0.01$ at $F_c = 6$ kN and $\mu = 0.02 \pm 0.03$ at $F_c = 12$ kN. For AA6xxx-T81, $\mu = 0.08 \pm 0.01$ at $F_c = 6$ kN and $\mu = 0.03 \pm 0.01$ at $F_c = 12$ kN. The calculated values are in excellent agreement with the range of 0.03-0.11 suggested by the literature review of Section 6.2.2.

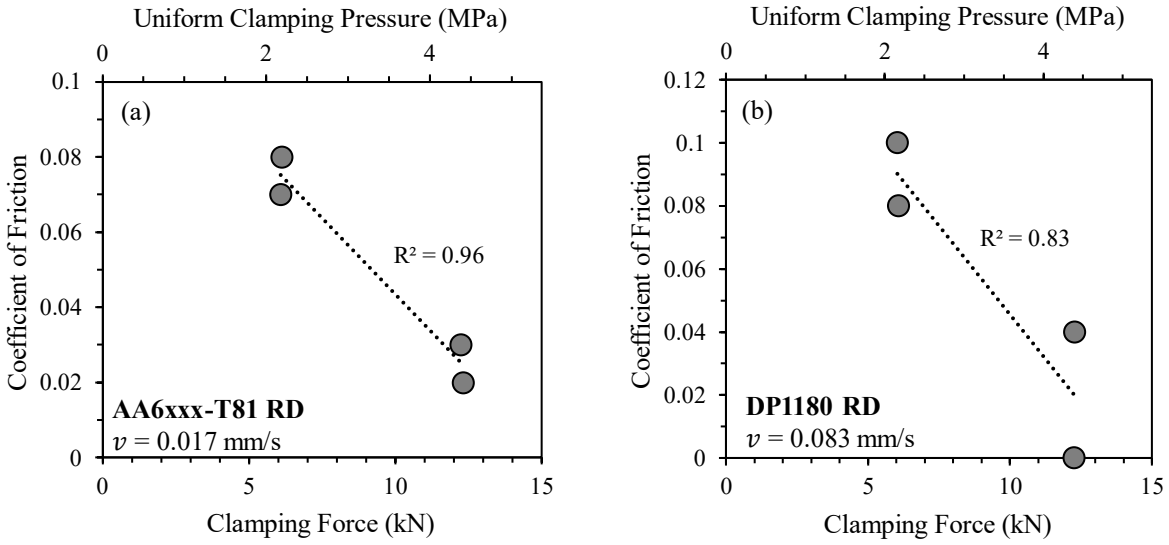

Figure 81: Coefficient of friction as a function of clamping force or pressure. For both (a) AA6xxx-T81 and (b) DP1180, the coefficient of friction decreases with clamping force holding the test velocity constant.

The surface roughness was measured using a Taylor-Hobson Surtronic 3+ meter with a characteristic gauge length of $L_c = 0.25$ mm to be representative of the small sliding length encountered in the actual shear tests. Considering that the surface of a material consists of peaks and valleys, different measures can be defined to quantity the roughness as shown in Figure 82. The parameter R_a is the average deviation from the mean line between the peaks and valleys. The parameter R_y is the largest peak-to-valley measurement and R_z is the average of the peak-to-valley measurements over the evaluation length L_n (Taylor-Hobson, n.d.). A minimum of six repeated measurements were taken for each alloy.

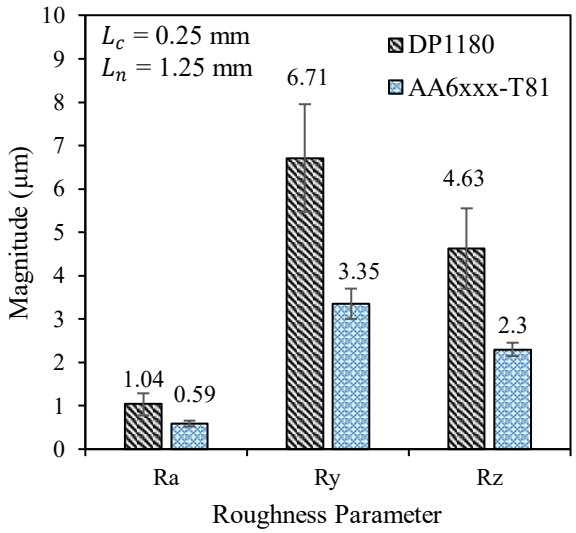

Figure 82: Surface roughness of DP1180 and AA6xxx-T81 calculated using a gauge length of 0.25 mm. The average and standard deviation of three parameters, R_a, R_y and R_z are presented as different measures of the surface roughness.

The surface roughness measurements support the relative values of the friction coefficients estimated for DP1180 and AA6xxx-T81. The friction coefficient is higher for DP1180, which has the higher surface roughness. The DP1180 coefficient of friction is approximately 50% higher than that of the AA6xxx-T81, whereas the surface roughness is approximately 70% higher. The surface roughness is not the only independent variable affecting the coefficient of friction, but it does account for some of the difference in the material responses and supports the relative magnitude of the coefficients estimated for each material.

6.5.2 Through-Thickness Shear Tests

The shear stress versus shear strain responses are presented in Figure 83. Excellent repeatability was observed for the AA6xxx-T81 material at a clamping force of 6 kN, with a fracture strain of $\varepsilon_{xy}^{f} = 0.30 \pm 0.02$. The responses shown below were corrected for friction using $\mu = 0.08$ for all repeats. The three repeats of the full width DP1180 samples showed reasonable repeatability at a clamping force of 12 kN but were limited to an average fracture strain of only $\varepsilon_{xy}^{f} = 0.05 \pm 0.02$. Decreasing the width of the specimens significantly increased the fracture strain to $\varepsilon_{y}^{f} = 0.13 \pm 0.01$. The full-width repeats clamped at 12 kN were corrected with $\mu = 0.02$. The half width repeats were subjected to double the clamping pressure, for the same clamping force, and as such were corrected with $\mu = 0.02$ and $\mu = 0$ for F_c = 6 kN and F_c = 12 kN, respectively.

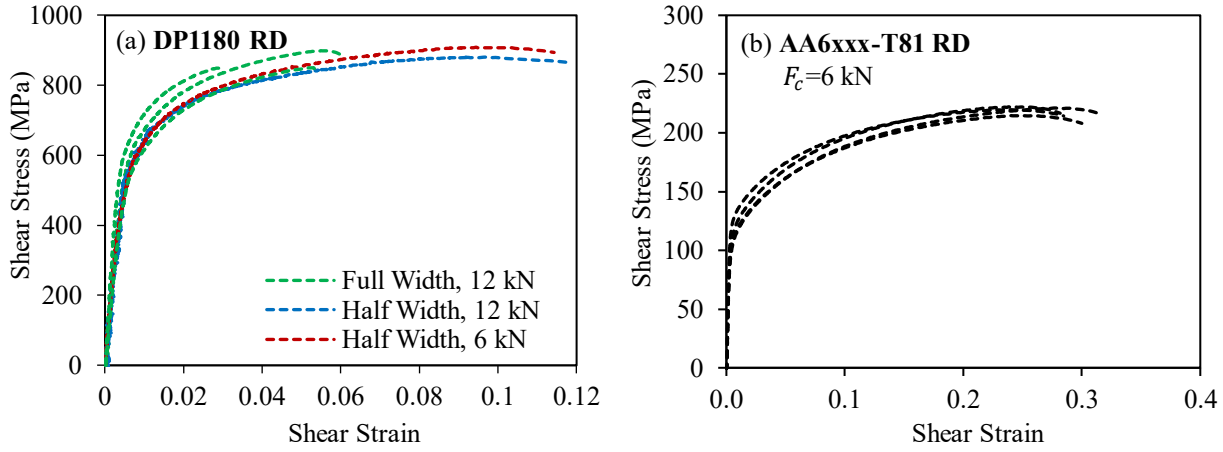

Figure 83: Through-thickness shear stress versus shear strain curves for (a) DP1180 and (b) AA6xxx-T81 after correction for friction. The half width specimens refer to the samples that were cut in half using water jet machining to investigate the effect of a decreased width on the fracture strain.

For both alloys, the strains paths extracted from the circle inspector in the middle of the gauge region confim that the deformation is primarily shear. The strain ratio for AA6xxx-T81 closely tracks the theoretical ratio of $\rho = -1$ for shear, as shown in Figure 84 and is relatively constant up to fracture. The average strain ratio for the full width DP1180 specimens is approximately $\rho = -0.86$. The half width specimens show initial non-linearity which quickly transitions to simple shear. The fracture strain is 78% higher than obtained using the full width specimens.

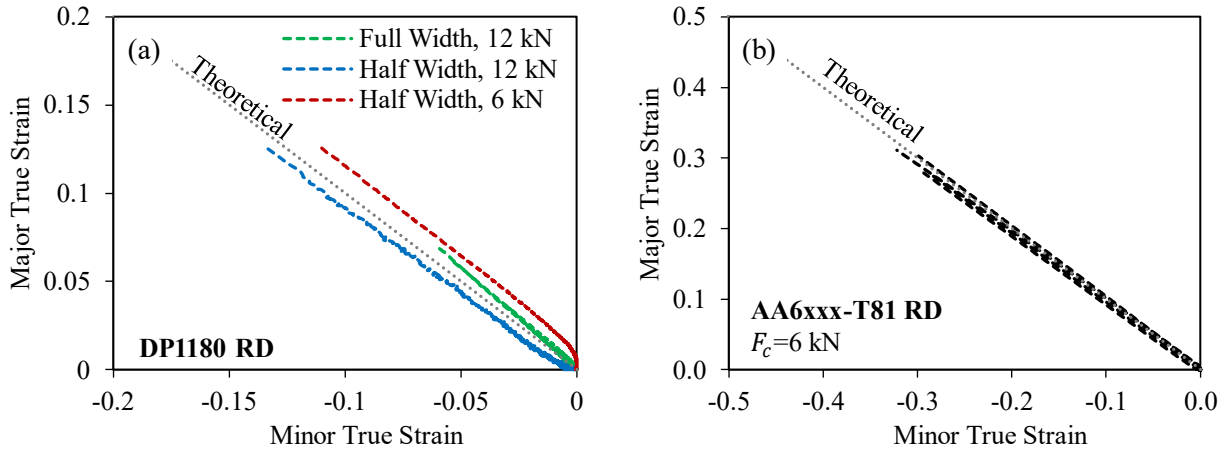

Figure 84: Strain path at center point of (a) DP1180 and (b) AA6xxx-T81 through-thickness shear specimens. The DP1180 results are shown at the two tested clamping forces of F_c = 6 kN and F_c = 12 kN.

For a specimen to be valid for constitutive characterization, the stress state should be both shear and uniform across the gauge region. The major strain distribution at fracture across the gauge region of each specimen is shown in Figure 85. A uniform state of shear was generated across 60% of the AA6xxx-T81 gauge region, with a transition to uniaxial tension at each edge. The loading was also relatively uniform

across the gauge region of the DP1180 full width specimens. Although cutting the specimens in half increased the major strain at fracture, the water jet process likely introduced microscopic defects that caused the loading to be non-uniform across the gauge region.

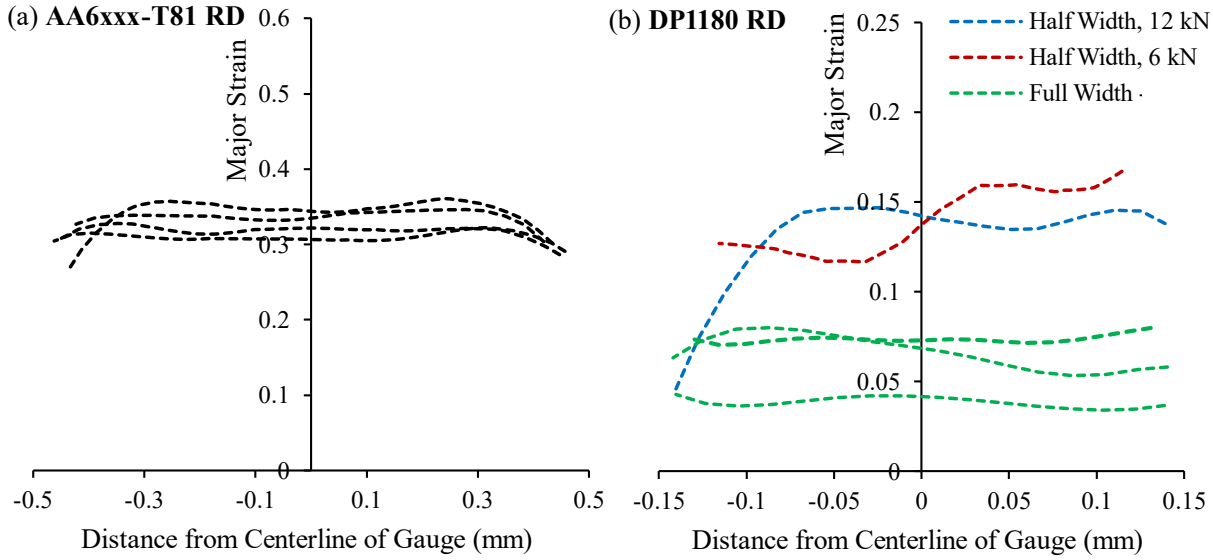

Figure 85: Major strain distribution across gauge width for through-thickness shear tests of (a) AA6xxx-T81 and (b) DP1180. Results are shown for each repeat at the DIC image immediately preceding fracture.

The post-mortem optical microscopy revealed that the specimens underwent significant gauge region rotation, more than predicted from the finite-element simulations. The AA6xxx-T81 fracture plane was orientated at an angle of 19°, but the free surfaces of the specimen in contact with the clamping dies only rotated by approximately 5° which is in good agreement with the simulated response. In contrast, the free surface of both the DP1180 full width and half width specimens rotated by approximately 15°, inducing bending at each notch as shown in Figure 86. Bending results in a superimposed tensile stress in the gauge region, which is the source of the combined shear-tensile strain path observed for the DP1180 in Figure 84.

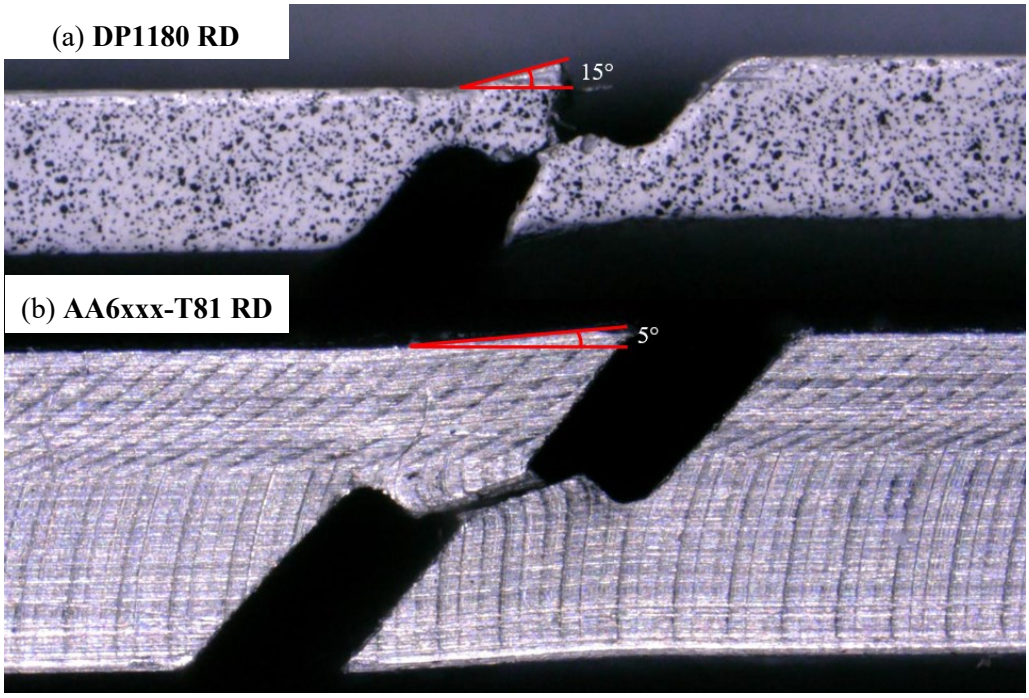

Figure 86: Post-mortem optical microscope measurements of through-thickness shear specimen rotation. (a) The DP1180 specimen, clamped with a force of 12 kN, rotates more than the (b) AA6xxx-T81 specimen, clamped with a force of 6 kN. Significant bending and deformation occur at the notches in the DP1180 tests, resulting in the combined tensile-shear loading measured at the center of the gauge region.

6.5.3 Calculation of Shear Stress

The shear stress ratios σ_{13}/σ_{RD} were calculated from the load and strain data following the general approach described in Rahmaan *et al*. (2017). For each alloy and repeat, the plastic work was estimated from the shear strain and friction-corrected shear stress. The ratio of the shear stress to the equivalent stress along the rolling direction, obtained from uniaxial tensile tests, was then calculated at the same level of plastic work.

The instantaneous stress ratio is shown in Figure 87, compared to a von Mises material with $\sigma_{13}/\sigma_{RD} = 0.577$ and a Tresca material with $\sigma_{13}/\sigma_{RD} = 0.5$. At the onset of localization, as shown in Table 18, the average normalized shear yield stress for the DP1180 and AA6xxx-T81 alloys was 0.68 ± 0.018 and 0.50 ± 0.006, respectively. The shear yield stress for AA6xxx-T81 is in good agreement with a Tresca type yield surface whereas the DP1180 shows a higher yield strength in shear than expected if assuming von Mises type behavior. In both cases, the shear yield stress is relatively independent of plastic work.

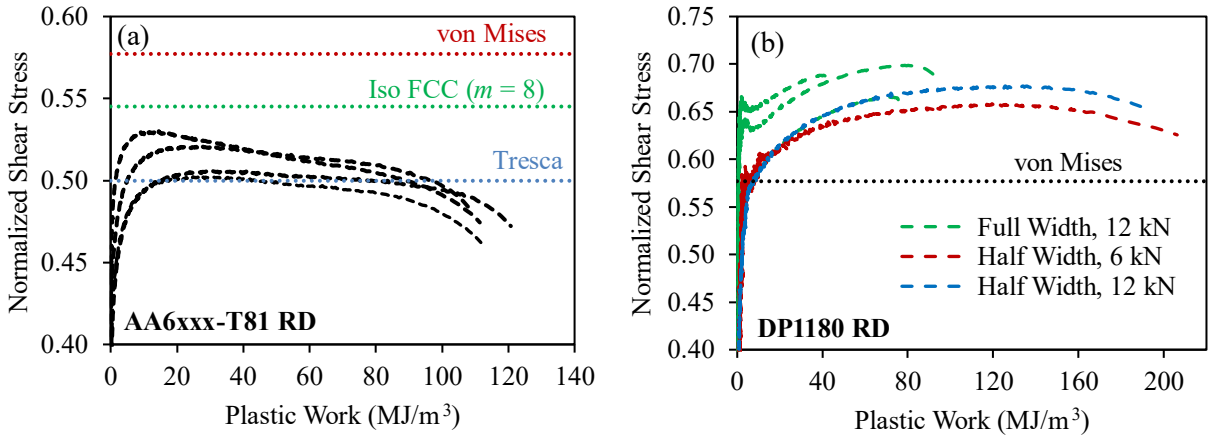

Figure 87: Instantaneous normalized shear yield stress as a function of plastic work for (a) AA6xxx-T81 and (b) DP1180.

Table 18: Average normalized through-thickness shear stress at the onset of localization for AA6xxx-T81 and DP1180. The sample standard deviation is shown in brackets.

Material	Geometry	Clamping Force (kN)	σ_{13}/σ_{RD}
AA6xxx-T81 RD	Full (w = 25.4 mm)	6	0.50 (0.006)
DP1180 RD	Full (w = 25.4 mm)	12	0.68 (0.017)
	Half (w = 12.7 mm)	6	0.65 (-)
		12	0.67 (-)
	Overall		0.68 (0.018)

6.6 Discussion

The friction and shear tests presented in Section 6.5 collectively represent a novel and simple method for constitutive and fracture characterization of through-thickness shear in sheet metals. The strip friction tests are a simple, efficient method for accurately determining the friction correction under the same conditions as the shear tests. The ability to minimize relative velocity is a significant advantage to the test fixture: one repeat of the DP1180 at a clamping force of 12 kN showed a coefficient of friction of zero because, as the DIC images revealed, the test fixture moved with the sample due to the high clamping pressure. Therefore, little friction is reflected in the load cell measurement due to minimal relative velocity between the components.

For both alloys, the constitutive results are reasonable and repeatable. The DP1180 shear to tensile stress ratio of 0.68±0.02 is within 12% of the average in-plane shear ratio of 0.60 shown in Table 3. Although the half width specimens generated a higher fracture strain for DP1180, the constitutive response is in good

agreement with the results obtained from the full width specimens. While in-plane shear constitutive results for AA6xxx-T81 are unavailable, the ratio of 0.50 ± 0.006 is in agreement with the in-plane Tresca-type shear behavior of the other tested aluminum, AA5182.

Although the objective of this thesis is constitutive characterization, the through-thickness shear specimens should also be evaluated based on fracture performance. The ideal specimen is valid for both constitutive and fracture characterization, to limit the number of tests and fully define a material's properties between yielding and fracture. Furthermore, delaying fracture increases the range of plastic work over which to evaluate the constitutive response to large strains. The fracture strain of $\varepsilon_{xy}^{f} = 0.30$ reported for the AA6xxx-T81 is 58% lower than the in-plane average of $\varepsilon_{xy}^{f} = 0.71$ obtained by Amir Zhumagulov using mini-shear tests. The DP1180 fracture strain was even lower, just 0.05-0.13 versus 0.68 in-plane (Abedini *et al.*, 2020).

A fracture strain of just 7-19% of the in-plane values is unrealistic for the DP1180. Although some directional difference is expected due to microstructure and texture variation between the in-plane and out-of-plane directions (Gu *et al.*, 2020), the large discrepancy seen in these results warrants further discussion. Necking initiation at the notch root in uniaxial tension could lead to premature fracture as commonly documented for in-plane shear tests (Peirs *et al.*, 2012). However, Figure 53 reveals that the strain state is relatively uniform in the tested geometry. Implementing eccentricity between the notches could suppress gauge region rotation and increase fracture strains, as observed for in-plane shear tests by Peirs *et al*. (2012). The wire EDM machining process and specimen width are two other potential sources of error which are discussed in detail in Section 6.6.1.

6.6.1 Influence of the Wire EDM Process on DP1180 Fracture Strains

Wire EDM significantly alters the properties of the material in the vicinity of the machined feature, in this case the notches. The heating/melting caused by the electric spark, followed by quenching/re-solidification by the dielectric fluid induces a heat-affected zone around the notch. This zone, commonly referred to as the "white" or "recast" layer is finer grained, harder, and more brittle than the base material (Straka *et al.*, 2016). Inside the white layer, the water quenching encourages martensite formation in steels, further assisted by diffusion of carbon from the electrode into the workpiece (Azam *et al.*, 2016; Uddeholm, 2007; Arooj *et al.*, 2014). Amplifying the situation, the machined surface is characteristically dimpled, porous, and rough as each arc strike removes a crater of material, while some molten metal globules are re-cast onto the surface due to the high fluid quench rate (Azam *et al.*, 2016; Arooj *et al.*, 2014; Holmberg *et al.*, 2018). Numerous cracks may also exist in this region (Azam *et al.*, 2016). As a result, failures in steel

components produced by EDM often initiate inside the white layer (Klocke *et al.*, 2016) where the material is more brittle, and stress concentrations exist due to the roughness and machining defects.

The influence of the white layer on the measured constitutive properties depends on the depth of penetration and the amount of base material present in the gauge region. The depth of the EDM heat affected zone may approach 50 μm (Straka *et al.*, 2016; Uddeholm, 2007), depending on the wire speed and pulse-time settings (Azam *et al.*, 2016; Uddeholm, 2007), which is in close agreement with the measured depth of the burn marks in Figure 65. Considering that the DP1180 gauge length is nominally 0.3 mm, the heat affected material makes up 37% of the gauge length. Assuming the same depth for the AA6xxx-T81, only 11% of the gauge region consists of the heat affected material. Therefore, the characterized yield strength and fracture strain are more typical of the base material for AA6xxx-T81 while more strongly influenced by the brittle, heat-affected white layer for the DP1180. Future work could consider specifying and optimizing the EDM parameters to decrease the white layer depth or adopting a micromachining method (Mativenga, 2018).

It is also important to consider the specimen width. The larger width increases the probability of encountering a crack or other machining defect along the notch. This could explain the three-fold increase in fracture strains using the half width specimens versus the original 25.4 mm wide design. If the specimen width had been machined using CNC rather than abrasive water jetting, an even higher fracture strain may have been realized. Unfortunately, water jetting the already machined specimens produced workpiece chatter and gouging defects due to the difficulty in clamping the small specimen in the water jet machine. The poor surface quality of the cut, shown in Figure 88 could have negated some of the positive effects of decreasing the specimen width. Future work could consider trials using different specimen widths to determine the ideal dimensions.

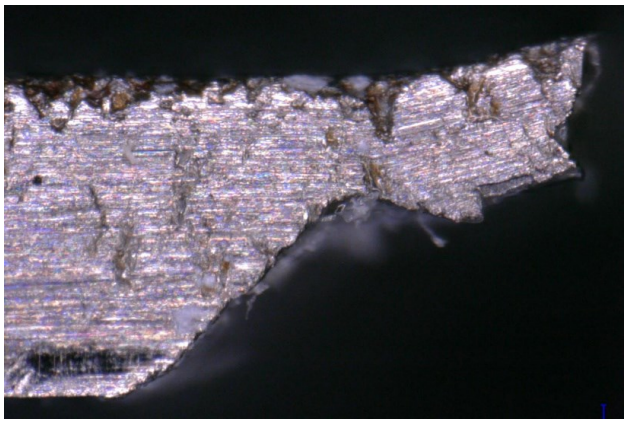

Figure 88: Gouging defects on the surface of a representative half width through-thickness shear specimen caused by water jet machining.

6.7 Summary of Through-thickness Shear Test Development

This chapter presented a novel, simple method for constitutive characterization of through-thickness shear in sheet metals. One-millimeter thick DP1180 and 2.7 mm thick AA6xx-T81 sheet metals were selected for the experimental study to evaluate the difference in properties between a representative steel and aluminum, as well as the influence of sheet thickness. The specimen proposed by Gu *et al*. (2020) for through-thickness fracture characterization was adapted for use in an existing clamping fixture available at the University of Waterloo. Shear was promoted by two notches machined through the sheet thickness using wire electric discharge machining (EDM). The gauge length, between the notches, was selected to be 0.3 mm for the DP1180 and 1 mm for the AA6xxx-T81 to ensure a shear failure inside the gauge region.

The clamping fixture was required to reduce sample rotation, which promoted bending in the gauge region rather than shear. The clamping fixture consists of two dies, with the clamping force controlled by a nitrogen spring. Minimum clamping forces of 8 kN for DP1180 and 4 kN for AA6xxx-T81 were determined based on a finite-element study. The potential error in the shear stress response due to friction was estimated as 12-26%, prompting the development of a so-called friction strip test to accurately determine the coefficient of friction under analogous conditions as the through-thickness shear tests.

DIC speckle patterns generated by airbrushing and conventional spray painting were compared to determine a suitable medium and method for speckling the through-thickness shear and friction strip specimens. The ideal pattern was generated using acrylic ink and an Iwata Eclipse airbrush with a 0.35 mm needle at 30 psi. The average speckle size was 18 μm, which resulted in excellent spatial resolution over the 0.3 mm gauge length of the DP1180 shear specimens.

Four to five repeats of the through-thickness shear tests were conducted for both DP1180 and AAxxx-T81, with the rolling direction of the sheet parallel to the loading direction. A nearly ideal and uniform simple shear stress state was observed for the AA6xxx-T81 in the gauge region, while the DP1180 results showed more variation and a combination of tension and shear. Each shear stress response was corrected for friction, by identifying the coefficient of friction under a similar contact pressure, test speed and lubrication conditions. The through-thickness shear yield strength, normalized with respect to the uniaxial tensile yield strength in the rolling direction, was found to be 0.50 and 0.68 for the AA6xxx-T81 and DP1180, respectively.

The measured fracture strains of 0.3 for AA6xxx-T81 and 0.05 for DP1180 were lower than expected, possibly due to specimen width, EDM related defects and gauge region rotation. Cutting a DP1180 specimen with water jet machining to decrease the width to 12 mm increased the fracture strain to 0.13, possibly since a smaller width decreases the statistical likelihood of defects along the notch resulting from

the EDM process. EDM of high-strength steels produces a brittle, martensitic and defect prone heat-affected "white layer", in which fracture initiates at a lower strain level than otherwise expected for the base material. The influence of this white layer was highest for the DP1180, where 37% of the gauge length consisted of material in the heat affected zone, versus only 11% in the AA6xxx-T81. Future work could consider optimizations to the specimen design, including implementing eccentricity between the notches to minimize rotation, adjusting the EDM parameters to minimize the white layer depth and testing various specimen widths.

Chapter 7 Calibration of Advanced Anisotropic Yield Functions under States of Generalized Plane Strain

A master yield surface that fully captures the anisotropic yielding behavior of the material across all stress states and sheet orientations is required for entry into finite element simulations used for formability modelling. During a typical forming operation, different areas of the component will be subjected to different stress states, orientated along different sheet orientations. Consider again the deep drawn cup used for illustration in Chapter 1: the walls are in plane-strain tension, center in equal-biaxial tension, flange in shear and bends in combined uniaxial tension and through-thickness shear. Rotating around the cup activates different sheet orientations (RD, DD, TD). To properly simulate the forming of such a component, a master yield surface is required that accurately predicts all stress states and interpolates intermediate values, with respect to all sheet orientations.

As shown in Figure 89, each of the tested materials shows different yield behavior along the uniaxial to plane strain arc calibrated with the HF85-PSC function. Ideally, the calibrated master yield surface should duplicate the local arc shape, predict the through thickness shear stress and include the baseline characterization data provided in Chapter 2. The plane stress Yld2000, plane stress Vegter and 3-D Yld2004 models were selected due to their popularity in industry and calibration flexibility.

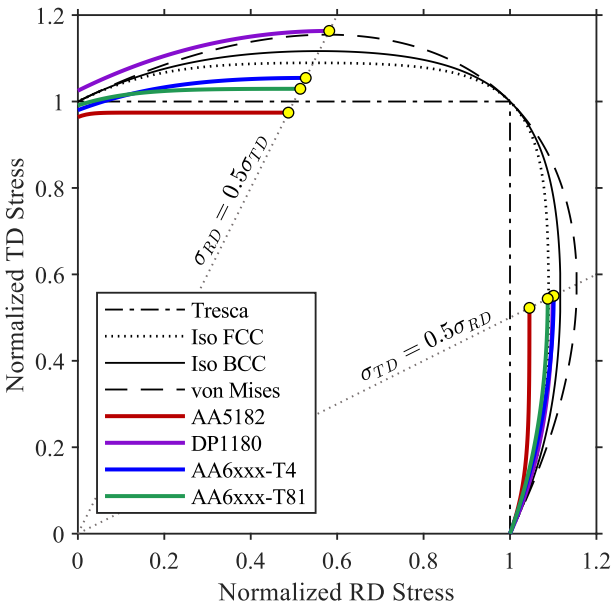

Figure 89: Yield surface arcs calibrated along RD and TD between uniaxial tension and plane strain tension for each of the four studied materials. Tresca, von Mises and isotropic Hosford yield criteria with exponents of 6 (BCC) and 8 (FCC) are included for comparison.

For any calibration procedure, the number of experimental data points must be greater than or equal to the number of calibration parameters. The plane stress Barlat Yld2000 model has eight parameters ($\alpha_1 - \alpha_8$), which are commonly calibrated using three uniaxial tension yield stresses and R-values at 0°, 45° and 90° from the rolling direction ($\sigma_0, \sigma_{45}, \sigma_{90}, R_0, R_{45}, R_{90}$), plus an equal-biaxial yield stress (σ_b) and R-value (R_b). The exponent is commonly set to 6 or 8, for a BCC or FCC material, respectively. Calibrating the 18 parameters of 3D Yld2004 conventionally requires seven uniaxial tension yield stress and R-values in 15° increments from the rolling direction ($\sigma_0, \sigma_{15}, \sigma_{30}, \sigma_{45}, \sigma_{60}, \sigma_{75}, \sigma_{90}, R_0, R_{15}, R_{30}, R_{45}, R_{60}, R_{75}, R_{90}$). The additional 4 data points generally include the equal-biaxial yield stress and R-value, plus through-thickness data which is often unavailable. Therefore, the 4 parameters corresponding to the through-thickness shear terms are conventionally set to unity ($C'_{55} = C'_{66} = C''_{55} = C''_{66} = 1$), implying isotropy in these loading conditions. Simplifying with isotropy reduces the number of parameters requiring calibration to only 14 such that the uniaxial and equal-biaxial yield stresses and R-values are sufficient. Yld2004 may be simplified further by recognizing that two parameters are redundant, leaving only 16 independent calibration parameters in the case of full 3-D or 12 in the case of plane stress (van den Boogaard *et al.*, 2015). Including the exponent as another free variable in the calibration therefore requires a minimum of 17 data points for 3-D and 13 for plane stress. Experimental data points in plane strain tension, along each uniaxial to plane strain arc, and through-thickness shear provide additional inputs, not commonly available in conventional yield surface calibrations. With the addition of these parameters, the number of available experimental data points greatly exceeds the minimum required.

At its core, a phenomenological anisotropic yield function is a non-linear interpolation technique for which the prediction should improve with additional data and parameters. The practical limitations of the models include balancing ease-of-calibration and accuracy with the expense of the comprehensive material testing needed to characterize the material across a range of stress states. Therefore, it would be advantageous to determine if some experimental tests could be eliminated with minimal effect on the accuracy of the calibration. For instance, hydraulic bulge and cruciform testing machines are inaccessible for the average laboratory, making it difficult to obtain the equal-biaxial R-value and yield strength. Although the introduction of the disc compression test has permitted evaluation of the equal-biaxial R-value on a standard test frame, friction negatively affects the accuracy (Aretz and Barlat, 2014) and the test enforces tension-compression symmetry which is not a valid assumption for all materials. In an attempt to eliminate the need for equal-biaxial constitutive properties, Aretz *et al*. (2007) predicted the equal-biaxial yield strength and R-value using Yld2000 and only plane strain and uniaxial tension tests along the RD, DD and TD of four materials. While the method reasonably predicted the equal-biaxial yield strength in each case, the error in the prediction of the equal-biaxial R-value exceeded 41% for the IF steel and 35%

for the 5000 series aluminum (Aretz *et al.*, 2007). It is worth considering if the additional arc data and plane strain constraint introduced in the present approach would improve the prediction of the equal-biaxial R-value.

The calibration schemes considered in this analysis are shown in Table 19 and Table 20 for Yld2000 and Yld2004, respectively. Each subsequent calibration scheme adds an additional loading condition to the input data to determine the effect on the prediction. A calibration with no equal-biaxial data is also included to determine if the equal-biaxial yield strength and R-value can be predicted using only the other data. Two calibrations with a variable exponent are also considered to assess the impact of additional calibration flexibility. Yld2004 schemes 5, 6, 8 and 9 consider using only data along the RD, DD, and TD rather than the conventional 7-directions. All schemes include the generalized plane strain constraints, and five equally spaced stresses S^{1-5} and normal vectors N^{1-5} along each uniaxial to plane strain tension arc.

Table 19: Calibration schemes for Yld2000. Recommended exponent indicates a calibration at either m = 6 or m = 8 for a BCC and FCC material, respectively. The variable exponent calibrations include the exponent as an additional free parameter.

	Calibration Scheme							
	Recommended Exponent						***Variable Exponent***	
	1	2	3	4	5	6	7	8
	Conventional	*Cal 1 + PST*	*Cal 1 + PST + Arcs*	*Cal 1 + PST + Arcs + Shear*	*All Data*	*No Equal-Biaxial*	*All Data*	*No Equal-Biaxial*
σ_0	X	X	X	X	X	X	X	X
σ_{15}					X	X	X	X
σ_{30}					X	X	X	X
σ_{45}	X	X	X	X	X	X	X	X
σ_{60}					X	X	X	X
σ_{75}					X	X	X	X
σ_{90}	X	X	X	X	X	X	X	X
R_0	X	X	X	X	X	X	X	X
R_{15}					X	X	X	X
R_{30}					X	X	X	X
R_{45}	X	X	X	X	X	X	X	X
R_{60}					X	X	X	X
R_{75}					X	X	X	X
R_{90}	X	X	X	X	X	X	X	X
σ_b	X	X	X	X	X		X	
R_b	X	X	X	X	X		X	
σ_0^{PST}		X	X	X	X	X	X	X
σ_{45}^{PST}		X	X	X	X	X	X	X
σ_{90}^{PST}		X	X	X	X	X	X	X
S_0^{1-5}			X	X	X	X	X	X
S_{45}^{1-5}			X	X	X	X	X	X
S_{90}^{1-5}			X	X	X	X	X	X
N_0^{1-5}			X	X	X	X	X	X
N_{45}^{1-5}			X	X	X	X	X	X
N_{90}^{1-5}			X	X	X	X	X	X
σ_0^{xy}				X	X	X	X	X
$\sigma_{22.5}^{xy}$				X	X	X	X	X
σ_{45}^{xy}				X	X	X	X	X

Table 20: Calibration schemes for Yld2004. Recommended exponent indicates a calibration at either $m = 6$ or $m = 8$ for a BCC and FCC material, respectively. The variable exponent calibrations include the exponent as an additional free parameter.

	Calibration Scheme									
	Recommended Exponent						***Variable Exponent***			
	1	2	3	4	5	6	7	8	9	10
	Conv.	*Cal 1 + PST*	*Cal 1 + PST + Arcs*	*All Data*	*3 x UT + PST + Arcs + TTS + SH + EB*	*3 x UT + PST + Arcs + TTS + SH*	*All Data*	*3 x UT + PST + Arcs + TTS + SH + EB*	*3 x UT + PST + Arcs + TTS + SH*	*7 x UT + PST + Arcs + TTS + SH*
σ_0	X	X	X	X	X	X	X	X	X	X
σ_{15}	X	X	X	X			X			X
σ_{30}	X	X	X	X			X			X
σ_{45}	X	X	X	X	X	X	X	X	X	X
σ_{60}	X	X	X	X			X			X
σ_{75}	X	X	X	X			X			X
σ_{90}	X	X	X	X	X	X	X	X	X	X
R_0	X	X	X	X	X	X	X	X	X	X
R_{15}	X	X	X	X			X			X
R_{30}	X	X	X	X			X			X
R_{45}	X	X	X	X	X	X	X	X	X	X
R_{60}	X	X	X	X			X			X
R_{75}	X	X	X	X			X			X
R_{90}	X	X	X	X	X	X	X	X	X	X
σ_b	X	X	X	X	X		X	X		
R_b	X	X	X	X	X		X	X		
σ_0^{PST}		X	X	X	X	X	X	X	X	X
σ_{45}^{PST}		X	X	X	X	X	X	X	X	X
σ_{90}^{PST}		X	X	X	X	X	X	X	X	X
S_0^{1-5}			X	X	X	X	X	X	X	X
S_{45}^{1-5}			X	X	X	X	X	X	X	X
S_{90}^{1-5}			X	X	X	X	X	X	X	X
N_0^{1-5}			X	X	X	X	X	X	X	X
N_{45}^{1-5}			X	X	X	X	X	X	X	X
N_{90}^{1-5}			X	X	X	X	X	X	X	X
σ_0^{xy}				X	X	X	X	X	X	X
$\sigma_{22.5}^{xy}$				X	X	X	X	X	X	X
σ_{45}^{xy}				X	X	X	X	X	X	X
σ_0^{xz}	Iso	Iso	Iso	X	X	X	X	X	X	X

UT = uniaxial tension
PST = plane strain tension
EB = equal-biaxial tension
Arcs = HF85-PSC calibrations stresses and normal vectors from UT-PST
SH = in-plane shear
TTS = through-thickness shear

To properly compare the objective function error of each calibration scheme, a consistent set of weighting parameters w_i must be selected and kept constant. However, the selection of the correct weighting parameters *a priori* of the calibration is unknown as adjusting the weights can affect the goodness of fit by prioritizing different loading conditions. Often the weights are determined manually by the analyst through trial and error. Alternatively, these weights could be set equal to one, corresponding to an ordinary least-squares (OLS) minimization as done by Khalfallah *et al*. (2015), set equal to the reciprocal of the variance to favor experimental tests with greater repeatability or biased toward the stresses to favor a more accurate load response in subsequent simulations (Abedini *et al.*, 2018; Barlat *et al.*, 2005). Four different weighting approaches were considered in this analysis: $w_\sigma = w_R = w_N = 1$ (unweighted), $w_\sigma = 0.9$ and $w_R = w_N = 0.1$ (stress-biased), $w_\sigma = 0.9/n$ and $w_R = w_N = 0.1/n$ (normalized stress-biased) and $w_i = 1/s_i^2$ (inverse variance) where w_σ is the weight applied to the stresses, w_R is the weight applied to the R-values and w_N is the weight applied to the normal vectors along the UT-PST arc. The weights in the normalized stress-biased approach are divided by the number of tests under a particular loading condition, n. The intent of the normalized stress-biased approach is to enforce the same overall influence of each loading condition on the calibration, regardless of the number of directions tested. For instance, in the case of 7 uniaxial stresses, 3 plane strain stresses and 1 equal-biaxial stress, the weights would be $w_\sigma^{UT} = 0.129$, $w_\sigma^{PST} = 0.3$ and $w_\sigma^{EB} = 0.9$.

To minimize dependency of the starting point on the optimization, the *MultiStart* Matlab® subroutine was used to search for a global minimum in the objective function represented by Eq. (7.1). *MultiStart* tests multiple trial points generated from a random scatter algorithm and reports the point with the lowest objective function value (MathWorks, n.d.). A minimum of 20 trial points were evaluated.

$$error = \sum_{i=1}^{N} w_{\sigma i}\left(\frac{\sigma_i^{pred}}{\sigma_i^{exp}} - 1\right)^2 + \sum_{i=1}^{N} w_{R i}\left(\frac{R_i^{pred}}{R_i^{exp}} - 1\right)^2 + \sum_{i=1}^{N} w_{N i}\left(\frac{\boldsymbol{N_i^{pred}}\cdot\boldsymbol{N_i^{exp}}}{\left|\boldsymbol{N_i^{pred}}\right|*\left|\boldsymbol{N_i^{exp}}\right|} - 1\right)^2 \tag{7.1}$$

The squared error (*SE*) formula of Eq. (7.2) was used to compare each calibration and weighting scheme to determine the best method.

$$SE = \sum\left(x^{model} - x^{exp}\right)^2 \tag{7.2}$$

The variable x represents the error under a particular loading condition, for example plane strain tension or through-thickness shear. When comparing weighting schemes, and using the unweighted approach as a baseline, the increase or decrease in squared error is given by Eq. (7.3).

$$\Delta SE = SE^{weighted} - SE^{unweighted} \tag{7.3}$$

Similarly using the conventional calibration as the baseline, the increase or decrease in squared error for each alternate calibration method is given by Eq. (7.4).

$$\Delta SE = SE^{Cal\ i} - SE^{Cal\ 1\ (Conventional)} \tag{7.4}$$

In this manner, the optimum weighting and calibration approaches may be quantitatively identified as those which result in the lowest squared error.

7.1 Calibration of a Master Yield Surface for DP1180

The DP1180 shows relatively mild anisotropy, with normalized plane strain tensile yield stresses close to expected for a typical BCC material. However, as will be demonstrated in this analysis, a more optimal calibration may be obtained by adopting a variable yield function exponent, rather than using the recommended value of m = 6. Yld2000, Yld2004 and Vegter criteria all capture the experimentally measured constitutive behavior.

7.1.1 Impact of Weighting Approach for DP1180

Table 21 through Table 23 summarize the difference in objective function error for each Yld2000 calibration scheme. Green cells/negative values indicate an improved calibration under the respective loading condition compared to the unweighted scheme. Red cells/positive values indicate a higher error. In general, the stress-biased approach improves the response under plane strain tension and shear at the expense of the other loading conditions and the overall error. The normalized stress-biased approach generally favors the equal-biaxial stress, due to its proportionally higher weight in the calibration, compared to the other stress states. The inverse variance approach favors shear and plane strain tension, due to the comparatively lower experimental standard deviations. Overall, the unweighted approach consistently offers the better calibration.

Table 21: Error between the stress-biased and unweighted Yld2000 calibrations for DP1180. Green highlighted cells indicate decreased error compared to the unweighted approach while red highlighted cells indicate a higher error compared to the unweighted approach. Except for the conventional calibration, the stress-biased approach generally results in greater error than the unweighted approach.

#	Description	σ_{UT}	R_{UT}	σ_{PST}	σ_b	R_b	σ_{Sh}	Overall
1	Conventional	-1.5E-04	-1.5E-04	-2.2E-04	-1.4E-05	-2.8E-04	-5.9E-04	-1.4E-03
2	Cal 1 + PST	2.6E-04	2.0E-03	3.2E-04	7.0E-05	5.0E-03	6.0E-04	8.3E-03
3	Cal 1 + PST + Arcs	1.3E-04	1.1E-03	5.0E-05	2.3E-05	1.2E-02	5.2E-04	1.4E-02
4	Cal 1 + PST + Arcs + Shear	-4.3E-04	1.0E-02	-9.4E-05	-4.6E-06	1.9E-02	6.0E-04	2.9E-02
5	All Data (m = 6)	4.7E-05	4.3E-03	-1.8E-04	-1.6E-05	5.1E-04	-2.7E-04	4.4E-03
6	No EB (m = 6)	4.8E-05	4.5E-03	-6.2E-05	3.5E-05	2.5E-03	-3.3E-04	6.6E-03
7	All Data (Variable Exponent)	6.0E-05	3.6E-03	-5.2E-04	8.8E-05	1.1E-02	-2.9E-04	1.4E-02
8	No EB (Variable Exponent)	-2.6E-06	4.6E-03	-3.4E-04	1.6E-04	6.2E-03	-8.5E-05	1.0E-02

Table 22: Error between the normalized stress-biased and unweighted Yld2000 calibrations for DP1180. Green highlighted cells indicate decreased error compared to the unweighted approach while red highlighted cells indicate a higher error compared to the unweighted approach. Except for the conventional calibration, the stress-biased approach generally results in greater error than the unweighted approach.

#	Description	σ_{UT}	R_{UT}	σ_{PST}	σ_b	R_b	σ_{Sh}	Overall
1	Conventional	-1.3E-04	-1.4E-04	-2.0E-04	-1.4E-05	-2.8E-04	-5.7E-04	-1.3E-03
2	Cal 1 + PST	2.5E-04	3.2E-04	2.7E-04	-1.3E-05	2.3E-04	-8.3E-05	9.7E-04
3	Cal 1 + PST + Arcs	1.1E-04	8.2E-06	3.3E-04	-2.8E-05	2.9E-04	1.9E-04	9.1E-04
4	Cal 1 + PST + Arcs + Shear	-2.4E-04	2.6E-02	8.1E-04	4.9E-05	2.7E-03	6.6E-04	3.0E-02
5	All Data (m = 6)	1.3E-03	7.1E-02	4.7E-03	-2.1E-05	1.3E-04	-1.7E-03	7.6E-02
6	No EB (m = 6)	8.4E-04	1.8E-02	1.1E-04	-2.5E-05	2.2E-03	-1.1E-03	2.0E-02
7	All Data (Variable Exponent)	2.3E-04	9.4E-03	3.0E-05	6.1E-05	3.2E-04	-7.7E-04	9.3E-03
8	No EB (Variable Exponent)	1.3E-04	1.3E-02	4.5E-05	-1.0E-03	1.1E-02	-1.7E-04	2.3E-02

Table 23: Error between the inverse variance method and unweighted Yld2000 calibrations for DP1180. Green highlighted cells indicate decreased error compared to the unweighted approach while red highlighted cells indicate a higher error compared to the unweighted approach. The calibrations improve under plane strain and shear loading, due to the low experimental variance under these conditions, but overall have a higher error than the corresponding unweighted calibrations.

#	Description	σ_{UT}	R_{UT}	σ_{PST}	σ_b	R_b	σ_{Sh}	Overall
1	Conventional	-1.5E-04	-1.0E-04	-3.9E-04	-1.4E-05	-2.8E-04	-7.4E-04	-1.7E-03
2	Cal 1 + PST	8.9E-04	-1.8E-05	-6.3E-04	3.4E-05	5.7E-03	-7.7E-04	5.2E-03
3	Cal 1 + PST + Arcs	8.6E-04	-1.2E-06	-4.5E-04	1.6E-05	5.7E-03	-5.8E-04	5.5E-03
4	Cal 1 + PST + Arcs + Shear	1.3E-03	1.8E-03	-3.8E-04	6.9E-05	1.3E-02	-3.5E-04	1.6E-02
5	All Data (m = 6)	-1.5E-04	1.4E-03	8.4E-05	-2.1E-05	1.1E-02	1.0E-03	1.4E-02
6	No EB (m = 6)	-3.9E-05	5.8E-04	-2.1E-04	-5.0E-04	1.1E-02	4.7E-04	1.2E-02
7	All Data (Variable Exponent)	1.9E-04	5.7E-04	7.3E-05	5.7E-04	1.4E-02	-1.0E-03	1.5E-02
8	No EB (Variable Exponent)	2.7E-04	7.4E-04	4.2E-04	-2.9E-04	4.2E-03	-3.9E-04	5.0E-03

The unweighted approach also produces the optimal calibration of Yld2004. As shown in Table 24, the stress-biased approach predominantly favors plane strain tension and shear, although with a worse calibration overall. The normalized stress-biased approach, summarized in Table 25, improves calibration 6 the most by eliminating oscillations in the R-values and uniaxial stresses when calibrating to data along only the RD, DD, and TD. The inverse variance method, shown in Table 26, does not offer any consistent improvement and is not recommended.

Table 24: Error between the stress-biased and unweighted Yld2004 calibrations for DP1180. Green highlighted cells indicate decreased error compared to the unweighted approach while red highlighted cells indicate a higher error compared to the unweighted approach. The stress-biased approach generally results in greater error than the unweighted approach.

#	Description	σ_{UT}	R_{UT}	σ_{PST}	σ_b	R_b	σ_{Sh}	Overall
1	Conventional	1.2E-05	2.8E-04	-3.6E-05	3.1E-06	4.8E-04	-1.2E-05	7.2E-04
2	Cal 1 + PST	-1.4E-06	2.2E-05	-1.9E-04	4.8E-06	2.0E-03	-7.2E-05	1.8E-03
3	Cal 1 + PST + Arcs	-2.0E-05	5.7E-04	-3.1E-04	7.9E-06	4.3E-03	-7.5E-05	4.5E-03
4	All Data *(m = 6)*	-2.0E-05	1.7E-03	-2.9E-04	9.4E-06	4.4E-03	-1.9E-04	5.6E-03
5	All Data along RD/TD/DD + TTS + EB (*m = 6)*	4.0E-05	3.2E-02	-3.4E-04	1.5E-05	4.5E-03	-3.8E-04	3.6E-02
6	All Data along RD/TD/DD + TTS (*m = 6)* – No EB	2.6E-04	6.6E-02	-1.4E-04	-7.9E-06	6.5E-03	-2.2E-04	7.2E-02
7	All Data (Variable Exponent)	2.3E-05	3.2E-04	1.6E-05	-5.2E-06	4.9E-04	9.9E-06	8.5E-04
8	All Data along RD/TD/DD + TTS + EB (Variable Exponent*)*	1.4E-05	1.0E-03	1.8E-06	-2.5E-06	4.0E-04	2.7E-06	1.4E-03
9	All Data along RD/TD/DD + TTS (Variable Exponent*)* – No EB	-1.1E-05	1.1E-04	-3.7E-06	-4.7E-05	6.4E-03	4.0E-05	6.5E-03
10	No EB (Variable Exponent)	-3.2E-06	4.0E-05	-2.0E-06	3.0E-05	3.0E-03	1.8E-05	3.1E-03

Table 25: Error between the normalized stress-biased and unweighted Yld2004 calibrations for DP1180. Green highlighted cells indicate decreased error compared to the unweighted approach while red highlighted cells indicate a higher error compared to the unweighted approach. In 7 out of 10 calibrations, the normalized stress-biased calibrations have a higher objective function error than the corresponding unweighted calibrations.

#	Description	σ_{UT}	R_{UT}	σ_{PST}	σ_b	R_b	σ_{Sh}	Overall
1	Conventional	1.8E-04	3.4E-03	3.4E-04	1.5E-05	9.8E-05	1.6E-04	4.2E-03
2	Cal 1 + PST	1.5E-04	2.2E-03	1.3E-04	1.7E-05	4.4E-04	-3.3E-05	2.9E-03
3	Cal 1 + PST + Arcs	1.8E-04	1.4E-03	1.7E-04	4.0E-05	6.2E-04	-3.8E-04	2.1E-03
4	All Data *(m = 6)*	1.8E-04	4.8E-03	3.5E-04	3.8E-05	6.9E-04	-8.2E-04	5.2E-03
5	All Data along RD/TD/DD + TTS + EB *(m = 6)*	-2.4E-05	-5.8E-02	3.5E-04	2.7E-05	7.9E-04	-3.4E-04	-5.7E-02
6	All Data along RD/TD/DD + TTS *(m = 6)* – No EB	-8.1E-05	-6.7E-02	2.5E-04	-4.2E-06	-6.4E-03	-3.4E-04	-7.4E-02
7	All Data (Variable Exponent)	3.3E-05	6.6E-04	-2.0E-06	-1.9E-06	1.4E-05	2.1E-06	7.0E-04
8	All Data along RD/TD/DD + TTS + EB (Variable Exponent)	5.3E-06	7.5E-04	-2.1E-06	1.1E-07	1.6E-05	1.2E-06	7.7E-04
9	All Data along RD/TD/DD + TTS (Variable Exponent) – No EB	1.8E-05	4.3E-05	3.4E-06	5.3E-05	8.0E-03	-3.1E-07	8.1E-03
10	No EB (Variable Exponent)	1.3E-05	1.7E-04	-2.8E-07	5.4E-05	-3.2E-04	-7.9E-06	-9.0E-05

Table 26: Error between the inverse variance method and unweighted Yld2004 calibrations for DP1180. Green highlighted cells indicate decreased error compared to the unweighted approach while red highlighted cells indicate a higher error compared to the unweighted approach. In all cases, the invers variance calibrations have a higher overall objective function error than the corresponding unweighted calibrations.

#	Description	σ_{UT}	R_{UT}	σ_{PST}	σ_b	R_b	σ_{Sh}	Overall
1	Conventional	1.8E-03	5.0E-02	-7.9E-04	-4.7E-05	1.5E-02	-3.2E-03	6.3E-02
2	Cal 1 + PST	2.4E-04	5.1E-02	4.6E-04	-2.5E-05	9.9E-04	2.5E-04	5.3E-02
3	Cal 1 + PST + Arcs	6.0E-05	5.2E-03	1.4E-04	1.7E-04	4.8E-03	1.6E-04	1.1E-02
4	All Data *(m = 6)*	-8.7E-06	2.1E-02	1.3E-04	3.6E-04	4.9E-03	2.3E-03	2.8E-02
5	All Data along RD/TD/DD + TTS + EB *(m = 6)*	7.5E-04	6.8E-02	-6.5E-04	1.8E-04	2.1E-02	-4.9E-04	8.9E-02
6	All Data along RD/TD/DD + TTS *(m = 6)* – No EB	7.0E-04	5.3E-02	-1.6E-04	4.0E-04	2.2E-02	-4.2E-04	7.6E-02
7	All Data (Variable Exponent)	1.6E-03	9.3E-02	4.7E-03	1.2E-05	1.4E-02	2.3E-03	1.1E-01
8	All Data along RD/TD/DD + TTS + EB (Variable Exponent)	2.2E-04	4.8E-02	-4.5E-05	4.8E-05	5.2E-06	-5.3E-06	4.9E-02
9	All Data along RD/TD/DD + TTS (Variable Exponent) – No EB	1.7E-04	5.2E-02	-2.3E-05	3.5E-04	-1.3E-02	4.6E-05	3.9E-02
10	No EB (Variable Exponent)	1.0E-03	6.4E-02	2.4E-03	3.9E-06	-1.7E-02	5.9E-03	5.6E-02

7.1.2 Impact of Calibration Scheme for DP1180

The performance of each calibration scheme is evaluated against the conventional calibration following the same approach as Section 7.1.1. The red cells/positive values in Table 27 indicate a higher error than the conventional calibration while green cells/negative values indicate a lower error. By adding more data, the calibration tends to improve under each loading condition except equal-biaxial yielding. Omitting the equal-biaxial R-value and stress in Calibrations 6 and 8 results in a large error in the prediction under these loading conditions. Even with the plane strain tension data and additional intermediate points along the arc, the equal-biaxial point cannot be accurately predicted. The best overall calibration, selected as the master yield surface for this material, is obtained by including all data and adopting a variable exponent as done in Calibration 7.

Table 27: Error between each calibration scheme and the conventional calibration for Yld2000 and DP1180. Green highlighted cells indicate decreased error compared to the conventional scheme while red highlighted cells indicate a higher error compared to the conventional scheme. The additional data consistently decreased the error under most loading conditions except for the equal-biaxial yield stress. All calibrations adopt the unweighted approach.

#	Description	σ_{UT}	R_{UT}	σ_{PST}	σ_b	R_b	σ_{Sh}	Overall
1	Conventional	0	0	0	0	0	0	0
2	Cal 1 + PST	-1.9E-04	-1.5E-04	-3.3E-04	1.1E-06	-2.8E-04	-6.2E-04	-1.6E-03
3	Cal 1 + PST + Arcs	-1.5E-04	-1.6E-04	-5.1E-04	1.9E-05	-2.7E-04	-8.0E-04	-1.9E-03
4	Cal 1 + PST + Arcs + Shear	4.1E-04	3.4E-04	-4.9E-04	5.5E-05	-2.7E-04	-1.7E-03	-1.6E-03
5	All Data (m = 6)	1.4E-04	-1.5E-04	-5.0E-04	6.3E-05	-2.7E-04	-1.3E-03	-2.1E-03
6	No EB (m = 6)	-2.0E-05	-1.5E-04	-9.8E-04	4.9E-04	4.0E-02	-1.4E-03	3.8E-02
7	All Data (Variable Exponent)	-1.9E-04	-1.5E-04	9.4E-05	1.8E-05	-2.4E-04	-2.9E-03	-3.4E-03
8	No EB (Variable Exponent)	-1.9E-04	-1.3E-04	-5.0E-04	1.1E-03	9.7E-03	-3.6E-03	6.5E-03

Figure 90 shows the predicted stresses and R-values for each calibration scheme with respect to sheet orientation. Except for calibrations 6 and 8, where the equal-biaxial data is omitted from the calibration, the Yld2000 model is in good agreement with the experimental data collected under each loading condition. Calibration 7, the master yield surface for this material, still overpredicts the plane strain yield strength along the rolling direction by 3% since the Yld2000 model does not have enough flexibility to perfectly capture the full anisotropic yielding behavior.

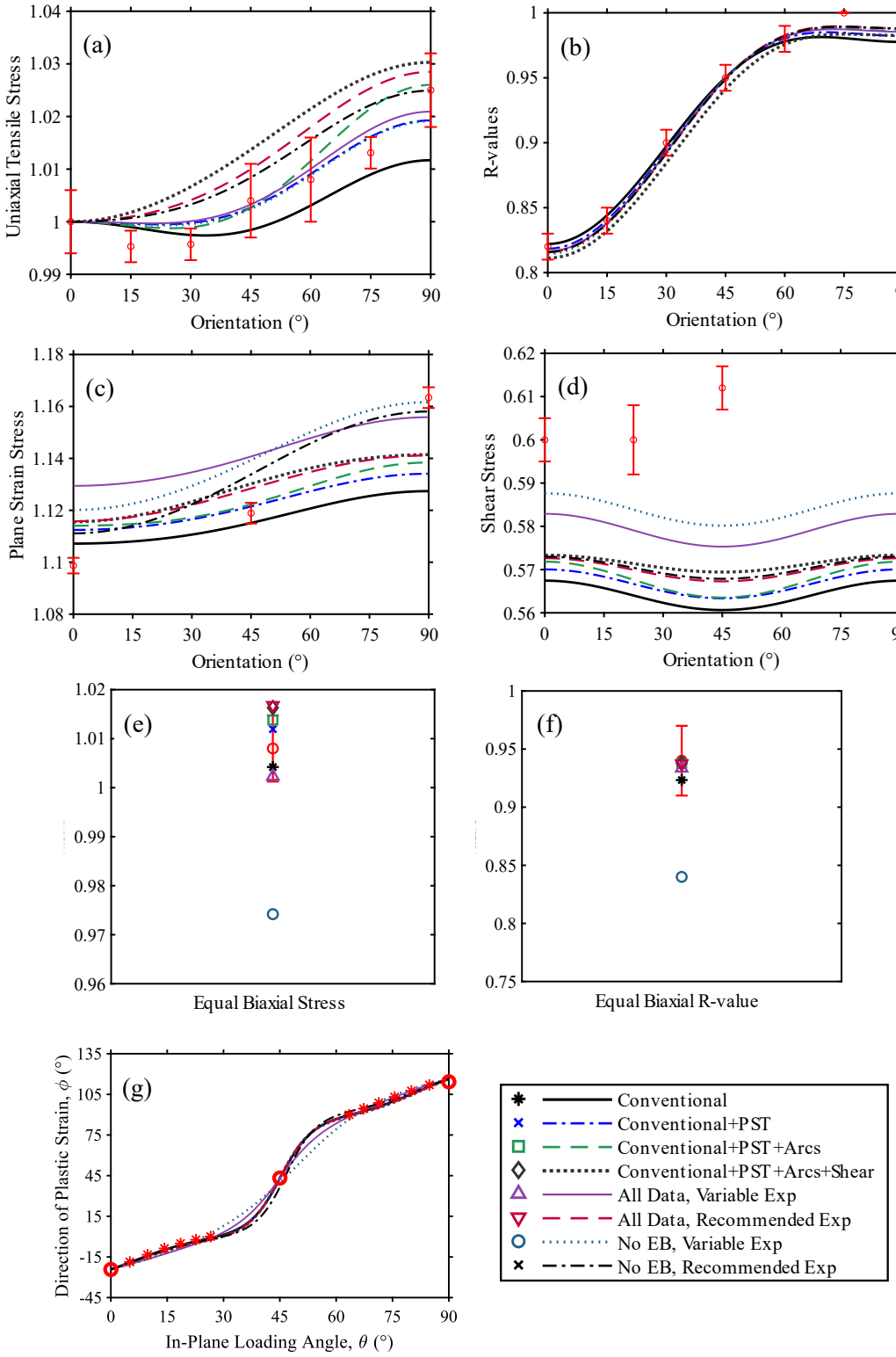

Figure 90: (a, c, d, e) Normalized stresses, (b, f) R-values and (g) plastic strain directions for the unweighted Yld2000 calibrations fit to the experimental data for DP1180. Red circles and asterisks represent the available experimental data with the error bars corresponding to the experimental standard deviations. Due to the absence of bulge or cruciform test data, the equal-biaxial yield stress was estimated as the average of the in-plane uniaxial tensile stresses with the average of the corresponding standard deviations.

As shown in Table 28, the best Yld2004 model is obtained by including all data in the calibration and adopting a variable exponent. Compared to the conventional calibration, Calibration 7 – the selected Yld2004 master yield surface – offers a 97% improvement in predictive accuracy under plane strain loading and a 95% improvement under shear loading. As observed using Yld2000, the equal-biaxial stress and R-value cannot be predicted using plane strain, uniaxial and shear data alone. Even with the additional arc and plane strain data, the equal-biaxial data point cannot be eliminated, nor can the number of tensile tests be down selected to only three directions without compromising the accuracy of the calibration.

Table 28: Error between each calibration scheme and the conventional calibration for Yld2004 and DP1180. Green highlighted cells indicate decreased error compared to the conventional scheme while red highlighted cells indicate a higher error compared to the conventional scheme. The additional data consistently decreased the error under uniaxial tension, plane strain tension and shear. All calibrations adopt the unweighted approach.

#	Description	σ_{UT}	R_{UT}	σ_{PST}	σ_b	R_b	σ_{Sh}	Overall
1	Conventional	0	0	0	0	0	0	0
2	Cal 1 + PST	-3.7E-05	-3.3E-06	-5.2E-04	-7.8E-06	2.8E-05	-5.7E-04	-1.1E-03
3	Cal 1 + PST + Arcs	-1.0E-04	-2.6E-05	-6.1E-04	-2.7E-05	6.6E-05	-5.7E-04	-1.3E-03
4	All Data *(m = 6)*	-9.2E-05	1.0E-05	-4.6E-04	8.0E-06	7.1E-05	-1.6E-03	-2.0E-03
5	All Data along RD/TD/DD + TTS + EB *(m = 6)*	1.3E-04	6.5E-02	-4.9E-04	7.6E-06	7.3E-05	-2.1E-03	6.3E-02
6	All Data along RD/TD/DD + TTS *(m = 6)* – No EB	4.3E-05	7.7E-02	-1.1E-03	5.0E-05	3.4E-02	-2.2E-03	1.1E-01
7	All Data (Variable Exponent)	-1.0E-04	5.4E-05	-1.4E-03	-4.2E-05	-7.7E-06	-4.2E-03	-5.7E-03
8	All Data along RD/TD/DD + TTS + EB (Variable Exponent)	-9.5E-05	2.4E-04	-1.4E-03	-4.4E-05	-6.6E-06	-4.2E-03	-5.5E-03
9	All Data along RD/TD/DD + TTS (Variable Exponent) – No EB	-7.3E-05	1.4E-04	-1.4E-03	1.6E-04	2.1E-02	-4.3E-03	1.5E-02
10	No EB (Variable Exponent)	-1.1E-04	4.9E-05	-1.4E-03	1.7E-04	2.6E-02	-4.2E-03	2.0E-02

Figure 91(c, d) illustrate how the plane strain tensile stress and shear stress are not well predicted under the conventional approach, but near perfectly predicted by including the additional data and adopting a variable exponent. Under the conventional approach, the error in the predicted plane strain yield strength is up to 3%. Optimizing the exponent adjusts the local curvature of the surface, allowing the function to match the range of plane strain tensile and shear stresses, which is not possible using the recommended exponent of 6. Oscillations in the uniaxial stress (a) and R-value (b) predictions of Calibrations 5 and 6 result from the inclusion of data along only the RD, DD, and TD in the calibration. The equal-biaxial point must be included to prevent erroneous predictions of the R-value (e) and stress (f).

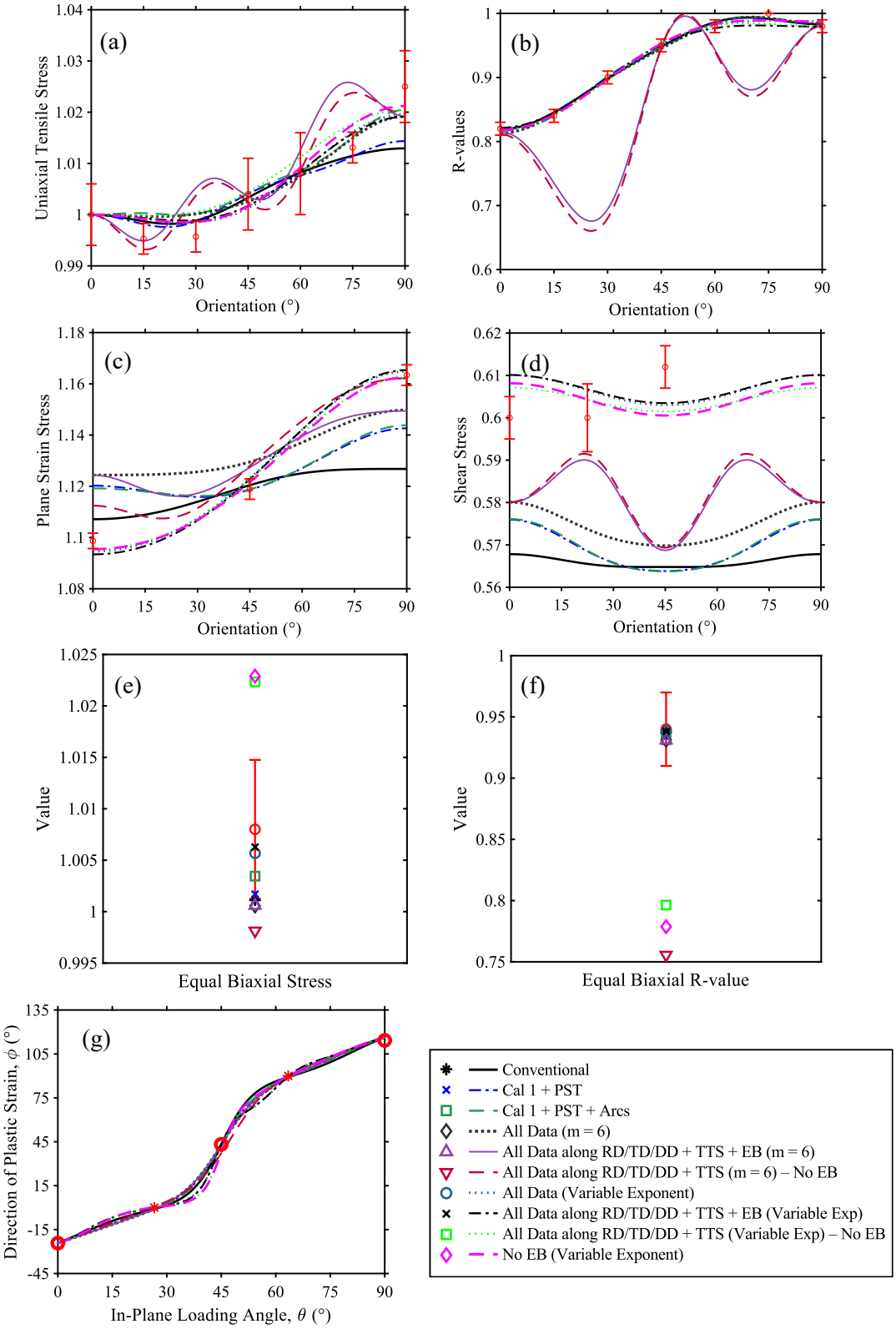

Figure 91: (a, c, d, e) Normalized stresses, (b, f) R-values and (g) plastic strain directions for the unweighted Yld2004 calibrations fit to the experimental data for DP1180. Red circles and asterisks represent the available experimental data with the error bars corresponding to the experimental standard deviations. The equal-biaxial yield stress was estimated as the average of the in-plane uniaxial tensile stresses with the average of the corresponding standard deviations.

7.3 Selection of Master Yield Criteria for DP1180

For both Yld2000 and Yld2004, the optimal master yield surfaces were obtained by calibrating to all experimental data points, adopting a variable exponent and setting all weights equal to 1. The variable exponent acts as an additional calibration parameter which "fine-tunes" the overall curvature of the surface, particularly in the shear and plane strain regions. The predicted plane strain yield strengths are within 0.4% of the experimental values using Yld2004 and 3% using Yld2000. Figure 92 illustrates the stark difference in the shapes of the Yld2004 and Yld2000 surfaces, particularly in the shear and plane strain conditions. Yld2004 is also able to perfectly predict the through-thickness shear stress of σ_{TTS} = 0.675 whereas Yld2000 is by nature plane stress and only suitable for two-dimensional applications. The coefficients of both functions are presented in Table 29 and Table 30.

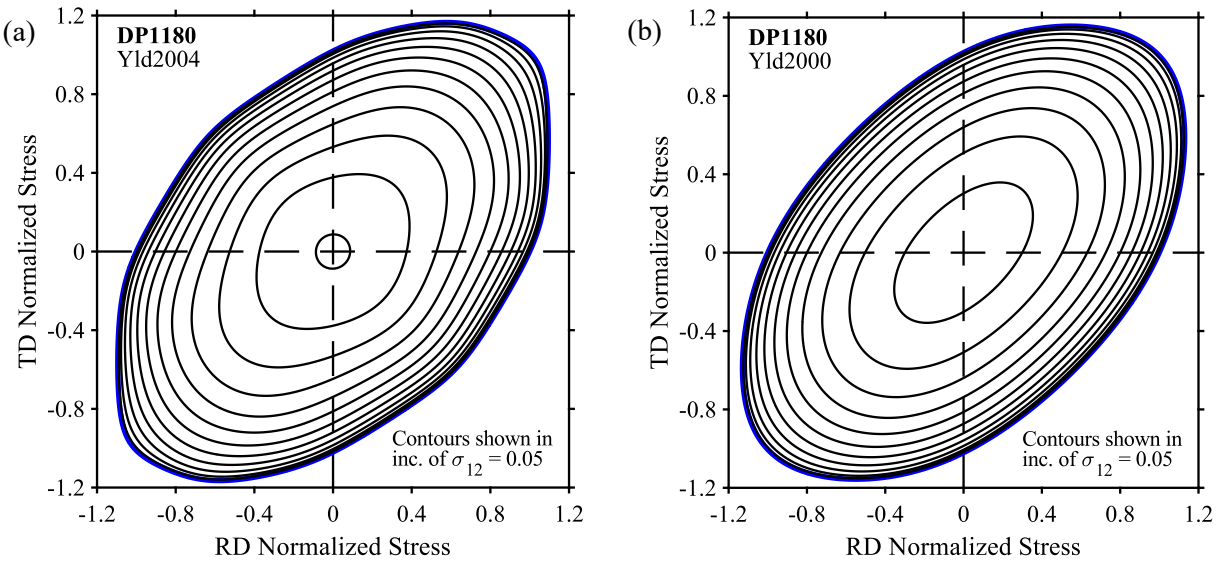

Figure 92: Calibrated (a) Yld2004 and (b) Yld2000 yield surfaces represented in plane stress $\sigma_{11} - \sigma_{22} - \sigma_{12}$ space for DP1180.

Table 29: Coefficients of the selected Yld2000 master yield surface for DP1180.

Material	m	α_1	α_2	α_3	α_4	α_5	α_6	α_7	α_8
DP1180	4.7123	0.8965	1.0527	1.0759	0.9863	1.0105	0.9126	0.9898	1.0090

Table 30: Coefficients of the selected Yld2004 master yield surface for DP1180.

Material	m	C'_{12}	C'_{13}	C'_{21}	C'_{23}	C'_{31}	C'_{32}	C'_{44}	C'_{55}
DP1180	19.3417	0.2654	0.4864	0.8357	0.8325	0.4413	0.1913	0.5622	-0.5355
cont'd	C'_{66}	C''_{12}	C''_{13}	C''_{21}	C''_{23}	C''_{31}	C''_{32}	C''_{44}	C''_{55}	C''_{66}
DP1180	-0.5355	0.8554	1.4708	1.4404	1.6083	1.3841	0.9212	1.1567	1.0000	1.0000

The Vegter, Yld2000 and Yld2004 master yield surfaces are compared in Figure 93 with $\sigma_1 = \sigma_{RD}$, $\sigma_2 = \sigma_{TD}$ and $\sigma_{12} = 0$. The Vegter criterion discussed in Section 1.3.2.3 is the optimal 2-D (plane stress) model because of its flexible design. Shear, plane strain tension, uniaxial tension and equal-biaxial tension are all perfectly predicted because they are hinge points in the Bezier curve interpolation. The generalized plane strain constraints are straightforward to enforce in the Vegter model by setting $n_1 = n_2 = -1$ and $A_2 = A_1$ at simple shear and $n_1 = 1$, $n_2 = 0$ and $A_2 = A_1/2$ at plane strain tension. The plane strain constraints resolve a fundamental uncertainty with the original Vegter function where σ_2^{PST} was unknown and had to be arbitrarily selected along the arc between uniaxial and equal-biaxial tension. Although the calibration of the Vegter criterion does not include the points along the uniaxial to plane strain tension arc, the intermediate stress and strain values are well captured. Coincidence of the Vegter and HF85-PSC yield functions, between uniaxial and plane strain tension, is further evidence of the suitability of the HF85-PSC function and the role of the plane strain constraint in collapsing the profiles of disparate yield functions onto a single, unique arc.

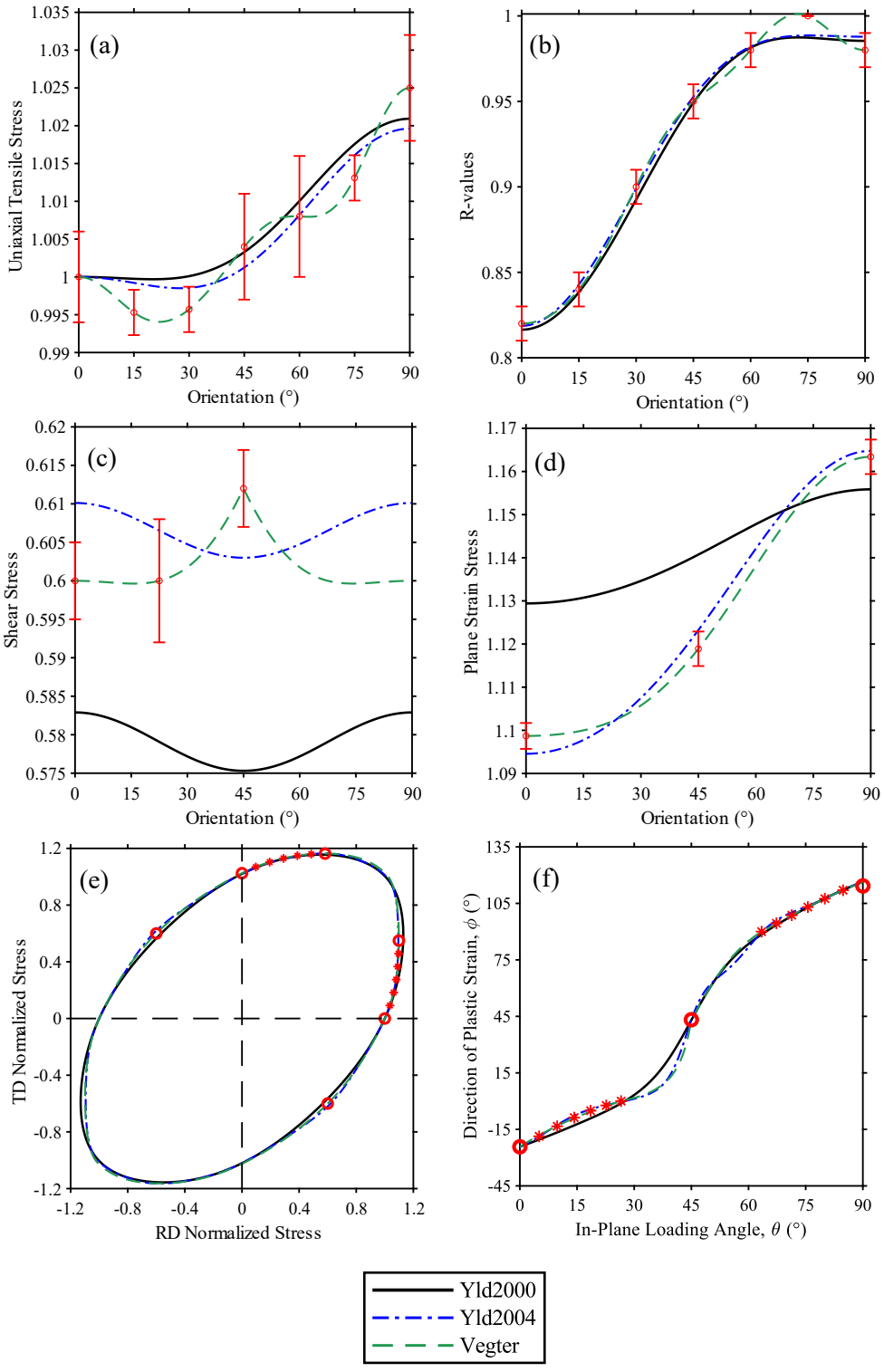

Figure 93: Yld2000, Yld2004 and Vegter master yield surfaces calibrated for DP1180 comparing (a, c, d) predicted and experimental stresses, (b) R-values, (f) plastic strain directions and (e) the overall plane stress surface. The predicted equal-biaxial yield stresses are $\sigma_b = 1.006$ and $\sigma_b = 1.002$ for Yld2004 and Yld2000, respectively. The predicted equal-biaxial R-values are $R_b = 0.939$ and $R_b = 0.933$ for Yld2004 and Yld2000, respectively.

7.2 Calibration of a Master Yield Surface for AA5182

The AA5182 shows much more severe anisotropy than the DP1180, with a high plane strain yield stress along the RD, but a transition to Tresca-like behavior along the DD and TD. No through-thickness shear tests were conducted for this material and thus the Yld2004 out-of-plane parameters were set equal to 1, corresponding to their isotropic values. The Vegter criterion is preferred for 2-D simulations, since Yld2000 cannot capture the directional variation of the plane strain yield strength. The extra flexibility of the Yld2004 criterion allows it to better capture the anisotropic plane strain yield strength in 3-D applications.

7.2.1 Impact of Weighting Approach for AA5182

Following the same approach described in Section 7.1, the stress-biased and normalized weighting schemes were evaluated against the unweighted approach as a baseline. The inverse variance method was not considered since it did not produce reliable results for the DP1180. The stress-biased approach, shown in Table 31 for Yld2000, resulted in a comparatively better calibration that the unweighted approach, particularly under uniaxial tension, plane strain tension and shear. The normalized approach, shown in Table 32 for Yld2000, resulted in a generally higher error, particularly under plane strain tension.

Table 31: Error between the stress-biased and unweighted Yld2000 calibrations for AA5182. Green highlighted cells indicate decreased error compared to the unweighted approach while red highlighted cells indicate a higher error compared to the unweighted approach. The stress-biased approach generally results in comparable, or lower overall error than the unweighted approach.

#	Description	σ_{UT}	R_{UT}	σ_{PST}	σ_b	R_b	σ_{Sh}	Overall
1	Conventional	-6.9E-04	6.3E-03	4.8E-04	9.2E-05	-2.5E-04	-2.0E-05	5.9E-03
2	Cal 1 + PST	-9.6E-05	-5.1E-04	-4.0E-04	-6.2E-06	8.1E-04	-2.1E-05	-2.2E-04
3	Cal 1 + PST + Arcs	-3.2E-04	2.6E-02	-1.9E-03	9.9E-05	1.1E-02	-2.3E-05	3.4E-02
4	Cal 1 + PST + Arcs + Shear	-6.6E-04	3.2E-02	-1.7E-03	2.9E-05	8.8E-03	-2.3E-04	3.9E-02
5	All Data (m = 8)	-7.9E-03	1.2E-02	-1.5E-02	4.4E-04	5.7E-03	-3.7E-04	-5.0E-03
6	No EB (m = 8)	-3.3E-04	2.3E-02	-2.0E-03	5.1E-04	8.2E-02	-7.7E-05	1.0E-01
7	All Data (Variable Exponent)	-4.4E-03	3.0E-03	-1.5E-03	-1.3E-04	1.0E-04	4.1E-04	-2.6E-03
8	No EB (Variable Exponent)	-5.9E-05	2.7E-03	-4.7E-05	2.3E-05	-2.4E-01	-2.1E-04	-2.4E-01

Table 32: Error between the normalized stress-biased and unweighted Yld2000 calibrations for AA5182. Green highlighted cells indicate decreased error compared to the unweighted approach while red highlighted cells indicate a higher error compared to the unweighted approach. The normalized approach generally results in higher error than the unweighted approach.

#	Description	σ_{UT}	R_{UT}	σ_{PST}	σ_b	R_b	σ_{Sh}	Overall
1	Conventional	-1.4E-04	3.7E-03	9.7E-04	1.1E-04	-9.6E-04	2.2E-05	3.7E-03
2	Cal 1 + PST	5.5E-04	2.1E-03	7.1E-04	-1.9E-04	-4.3E-06	2.6E-05	3.2E-03
3	Cal 1 + PST + Arcs	-7.8E-06	1.0E-02	6.6E-04	-1.7E-04	-1.4E-04	-2.2E-05	1.1E-02
4	Cal 1 + PST + Arcs + Shear	-4.5E-04	1.3E-02	1.0E-03	-2.0E-04	5.9E-06	-2.4E-04	1.3E-02
5	All Data (*m = 8)*	-8.0E-03	1.8E-02	-1.2E-02	1.6E-04	-6.7E-05	-4.8E-04	-2.4E-03
6	No EB (*m = 8*)	-4.5E-04	3.5E-02	-6.9E-04	9.9E-05	4.1E-02	-1.7E-04	7.4E-02
7	All Data (Variable Exponent)	5.8E-03	9.9E-03	3.8E-03	3.8E-04	-1.4E-04	-1.4E-03	1.8E-02
8	No EB (Variable Exponent)	1.2E-03	1.2E-02	1.9E-03	7.8E-05	-2.4E+00	-1.4E-03	-2.3E+00

While the stress-biased approach offers the best overall calibrations of the Yld2000 yield function to the AA5182 experimental data, the unweighted approach is preferred for the Yld2004 function as illustrated in Table 33 and Table 34. Seven out of the 10 calibrations were worse than the corresponding unweighted calibration using the stress-biased approach and eight out of the 10 calibrations were worse using the normalized approach.

Table 33: Error between the stress-biased and unweighted Yld2004 calibrations for AA5182. Green highlighted cells indicate decreased error compared to the unweighted approach while red highlighted cells indicate a higher error compared to the unweighted approach. The stress-biased approach generally results in greater error than the unweighted approach.

#	Description	σ_{UT}	R_{UT}	σ_{PST}	σ_b	R_b	σ_{Sh}	Overall
1	Conventional	-3.1E-04	2.6E-03	6.9E-03	2.4E-05	9.0E-06	2.7E-03	1.2E-02
2	Cal 1 + PST	-1.6E-04	7.7E-03	-1.2E-03	4.1E-05	6.5E-04	-1.2E-04	6.9E-03
3	Cal 1 + PST + Arcs	1.7E-05	3.5E-02	-1.9E-03	2.1E-04	8.1E-03	-3.4E-05	4.1E-02
4	All Data *(m = 8)*	-1.1E-04	3.5E-02	-1.9E-03	2.0E-04	8.1E-03	-1.2E-04	4.1E-02
5	All Data along RD/TD/DD + TTS + EB (*m = 8)*	1.7E-04	7.9E-03	-2.2E-03	1.9E-04	1.1E-02	-1.4E-05	1.7E-02
6	All Data along RD/TD/DD + TTS (*m = 8)* – No EB	3.1E-04	5.1E-02	-2.6E-03	8.9E-04	2.2E-01	-7.8E-05	2.7E-01
7	All Data (Variable Exponent)	2.5E-04	4.0E-04	7.1E-04	-6.1E-04	3.6E-04	6.3E-05	1.2E-03
8	All Data along RD/TD/DD + TTS + EB (Variable Exponent)	4.0E-05	3.8E-04	-1.3E-03	5.5E-04	1.5E-05	-2.3E-05	-3.6E-04
9	All Data along RD/TD/DD + TTS (Variable Exponent) – No EB	2.1E-05	-5.7E-01	1.1E-05	1.5E-05	-8.2E+00	-4.3E-06	-8.8E+00
10	No EB (Variable Exponent)	1.1E-04	2.6E-04	-4.1E-05	-7.7E-06	-2.7E+01	-1.0E-05	-2.7E+01

Table 34: Error between the normalized stress-biased and unweighted Yld2004 calibrations for AA5182. Green highlighted cells indicate decreased error compared to the unweighted approach while red highlighted cells indicate a higher error compared to the unweighted approach. The normalized approach generally results in greater error than the unweighted approach.

#	Description	σ_{UT}	R_{UT}	σ_{PST}	σ_b	R_b	σ_{Sh}	Overall
1	Conventional	4.2E-04	3.5E-03	1.2E-02	-3.3E-05	-2.7E-06	4.3E-03	2.0E-02
2	Cal 1 + PST	7.0E-04	3.6E-02	1.3E-03	-3.1E-04	3.6E-04	-6.9E-05	3.8E-02
3	Cal 1 + PST + Arcs	-7.2E-04	5.5E-02	1.6E-03	-2.3E-04	6.5E-04	-8.7E-05	5.6E-02
4	All Data *(m = 8)*	-7.6E-04	5.2E-02	1.6E-03	-2.3E-04	6.9E-04	-2.5E-04	5.3E-02
5	All Data along RD/TD/DD + TTS + EB (*m = 8)*	-1.6E-03	7.9E-02	2.5E-03	-3.1E-04	5.1E-04	-5.3E-04	8.0E-02
6	All Data along RD/TD/DD + TTS (*m = 8)* – No EB	-1.9E-03	1.9E-01	1.0E-03	-3.9E-04	1.7E-01	-5.0E-04	3.6E-01
7	All Data (Variable Exponent)	2.1E-03	7.7E-03	1.1E-03	-5.1E-04	1.1E-05	-1.7E-04	1.0E-02
8	All Data along RD/TD/DD + TTS + EB (Variable Exponent)	2.7E-03	-2.3E-04	-2.5E-05	1.8E-04	4.2E-06	-2.4E-04	2.3E-03
9	All Data along RD/TD/DD + TTS (Variable Exponent) – No EB	9.9E-04	-1.6E+00	3.3E-04	6.7E-05	-1.0E+01	-1.7E-04	-1.2E+01
10	No EB (Variable Exponent)	4.8E-04	5.3E-04	7.7E-04	2.7E-03	-9.7E+01	-2.0E-04	-9.7E+01

7.2.2 Impact of Calibration Scheme for AA5182

Considering the stress-biased calibrations for Yld2000, the optimal master yield surface was obtained by including all data in the calibration and adopting a variable exponent (Calibration 7). As indicated in Table 35, pronounced errors appear in the equal-biaxial stress and R-value when omitting these data points from the calibration. As a result of the Tresca-like shape, a corner is promoted at the equal-biaxial point. The R-value is therefore extremely sensitive to small changes in the curvature in this region. Without the actual experimental data to anchor the calibration, the predicted equal-biaxial R-value tends toward artificially high values ($R_b > 2$).

Table 35: Error between each calibration scheme and the conventional calibration for Yld2000 and AA5182. Green highlighted cells indicate decreased error compared to the conventional scheme while red highlighted cells indicate a higher error compared to the conventional scheme. The additional data consistently decreased the error under most loading conditions except for the equal-biaxial yield stress. All calibrations adopt the stress-biased weighting approach.

#	Description	σ_{UT}	R_{UT}	σ_{PST}	σ_b	R_b	σ_{Sh}	Overall
1	Conventional	0	0	0	0	0	0	0
2	Cal 1 + PST	-6.7E-03	-5.7E-03	-1.3E-02	4.3E-04	-2.1E-04	-6.8E-05	-2.5E-02
3	Cal 1 + PST + Arcs	-7.2E-03	1.9E-02	-1.5E-02	5.3E-04	1.0E-02	-6.8E-05	7.0E-03
4	Cal 1 + PST + Arcs + Shear	-7.7E-03	2.6E-02	-1.5E-02	4.4E-04	7.9E-03	-3.1E-04	1.1E-02
5	All Data ($m = 8$)	-7.5E-03	9.7E-03	-1.5E-02	4.3E-04	5.0E-03	-2.5E-04	-7.4E-03
6	No EB ($m = 8$)	-7.3E-03	1.7E-02	-1.6E-02	1.2E-03	9.1E-02	-1.8E-04	8.5E-02
7	All Data (Variable Exponent)	-8.0E-03	-4.1E-03	-1.7E-02	-9.1E-05	-7.3E-04	9.9E-04	-2.9E-02
8	No EB (Variable Exponent)	-8.3E-03	-4.1E-03	-1.8E-02	1.7E-04	2.2E+00	1.1E-03	2.1E+00

Figure 94 shows the predicted stresses and R-values for each calibration scheme with respect to sheet orientation. In general, Calibration 7 accurately captures the material response along each loading condition. The conventional calibration overpredicts the plane strain yield strength by 2-11% since the Tresca-type yielding observed along the DD and TD cannot be captured by the recommended exponent of 8 for FCC materials.

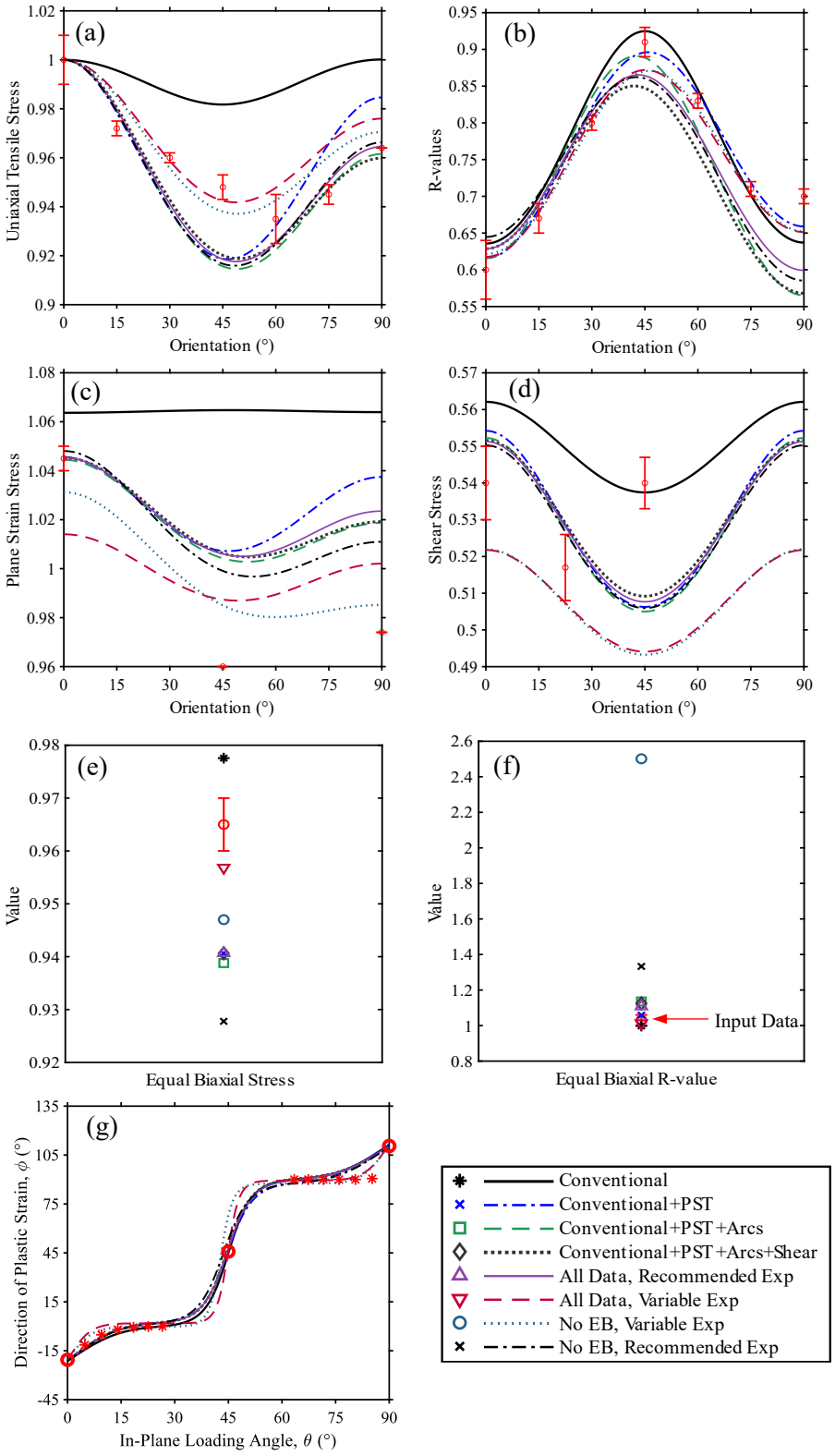

Figure 94: (a, c, d, e) Normalized stresses, (b, f) R-values and (g) plastic strain directions for the stress-biased Yld2000 calibrations fit to the experimental data for AA5182. Red circles and asterisks represent the available experimental data with the error bars corresponding to the experimental standard deviations. The equal-biaxial yield stress was estimated as the average of the in-plane uniaxial tensile stresses with the average of the corresponding standard deviations.

The Yld2004 calibrations also improve with additional data beyond that typically included in the conventional calibration. Table 36 indicates that including the plane strain and arc data improves the calibration accuracy in the respective regions of the yield surface. By omitting the equal-biaxial R-value, the variable exponent calibrations tend towards a sharp-cornered Tresca-type response to suit the plane strain yield strength along DD and TD. The sharp corner is sensitive to small changes in curvature at the equal-biaxial point, producing an equal-biaxial R-value of 7 or higher. As observed with the Yld2000 calibration and analysis for the DP1180, the equal-biaxial constitutive behavior cannot be accurately predicted using only plane strain, tensile, arc and shear data. Calibration 7 is selected as the optimal calibration for AA5182 and as the Yld2004 master yield surface.

Table 36: Error between each calibration scheme and the conventional calibration for Yld2004 and AA5182. Green highlighted cells indicate decreased error compared to the conventional scheme while red highlighted cells indicate a higher error compared to the conventional scheme. The additional data and assumption of a variable exponent consistently decreased the error under most loading conditions except for the equal-biaxial yield stress. All calibrations adopt the unweighted approach.

#	Description	σ_{UT}	R_{UT}	σ_{PST}	σ_b	R_b	σ_{Sh}	Overall
1	Conventional	0.0E+00	0.0E+00	0.0E+00	0.0E+00	0.0E+00	0.0E+00	0.0E+00
2	Cal 1 + PST	-2.8E-04	9.9E-04	-2.0E-02	3.9E-04	-2.4E-06	-3.0E-03	-2.2E-02
3	Cal 1 + PST + Arcs	4.1E-04	3.4E-03	-2.2E-02	4.8E-04	9.5E-05	-2.8E-03	-2.1E-02
4	All Data *(m = 8)*	3.4E-04	3.4E-03	-2.2E-02	4.7E-04	8.4E-05	-2.9E-03	-2.1E-02
5	All Data along RD/TD/DD + TTS + EB (*m = 8)*	9.2E-04	9.1E-02	-2.2E-02	4.4E-04	1.1E-04	-3.0E-03	6.7E-02
6	All Data along RD/TD/DD + TTS (*m = 8)* – No EB	1.4E-03	9.5E-02	-2.4E-02	9.5E-04	2.9E-02	-2.8E-03	9.9E-02
7	All Data (Variable Exponent)	-8.4E-04	1.3E-03	-2.7E-02	6.0E-04	-3.6E-06	-3.6E-03	-3.0E-02
8	All Data along RD/TD/DD + TTS + EB (Variable Exp)	-8.6E-04	2.9E-03	-2.6E-02	-5.2E-05	5.1E-06	-3.6E-03	-2.7E-02
9	All Data along RD/TD/DD + TTS (Variable Exp) – No EB	-2.7E-04	4.6E+00	-2.8E-02	-1.8E-05	3.8E+01	-3.7E-03	4.2E+01
10	No EB (Variable Exponent)	-4.9E-04	1.6E-03	-2.8E-02	4.5E-05	1.0E+02	-3.6E-03	1.0E+02

Comparing the ten Yld2004 models in Figure 95 illustrates the effect of each calibration scheme. The plane strain yield stresses (c) are overpredicted under the conventional calibration by 3-13%. The uniaxial R-values (b) at 15°, 30°, 60° and 75° orientations are not well predicted by Calibrations 5, 6 and 9, which were only calibrated to the test data captured along RD, DD, and TD. Ultimately, all available experimental data should be included for the most accurate calibration.

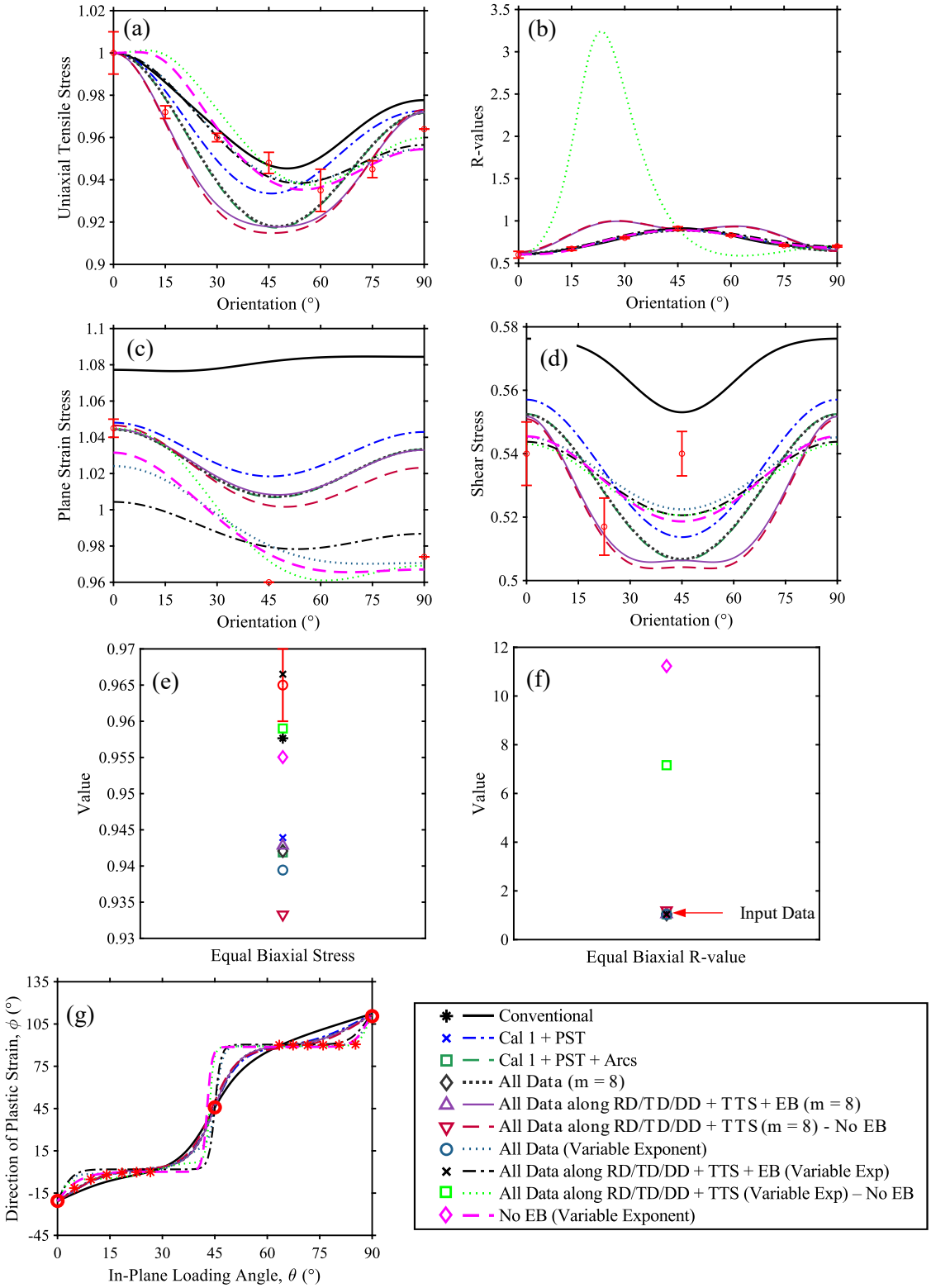

Figure 95: (a, c, d, e) Normalized stresses, (b, f) R-values and (g) plastic strain directions for the unweighted Yld2004 calibrations fit to the experimental data for AA5182. Red circles and asterisks represent the available experimental data with the error bars corresponding to the experimental standard deviations. Due to the absence of bulge or cruciform test data, the equal-biaxial yield stress was estimated as the average of the in-plane uniaxial tensile stresses with the average of the corresponding standard deviations.

7.2.3 Selection of Master Yield Criteria for AA5182

Although the contours of the Yld2000 and Yld2004 models appear largely similar under plane stress conditions, as illustrated in Figure 96, the Yld2004 model offers an improved prediction under plane strain tension and shear. The improved prediction of the Yld2004 model is particular apparent for off-axis loading where the principal stresses are not coincident with the RD-TD directions. Table 37 and Table 38 provide the coefficients of the master Yld2000 and Yld2004 models, respectively.

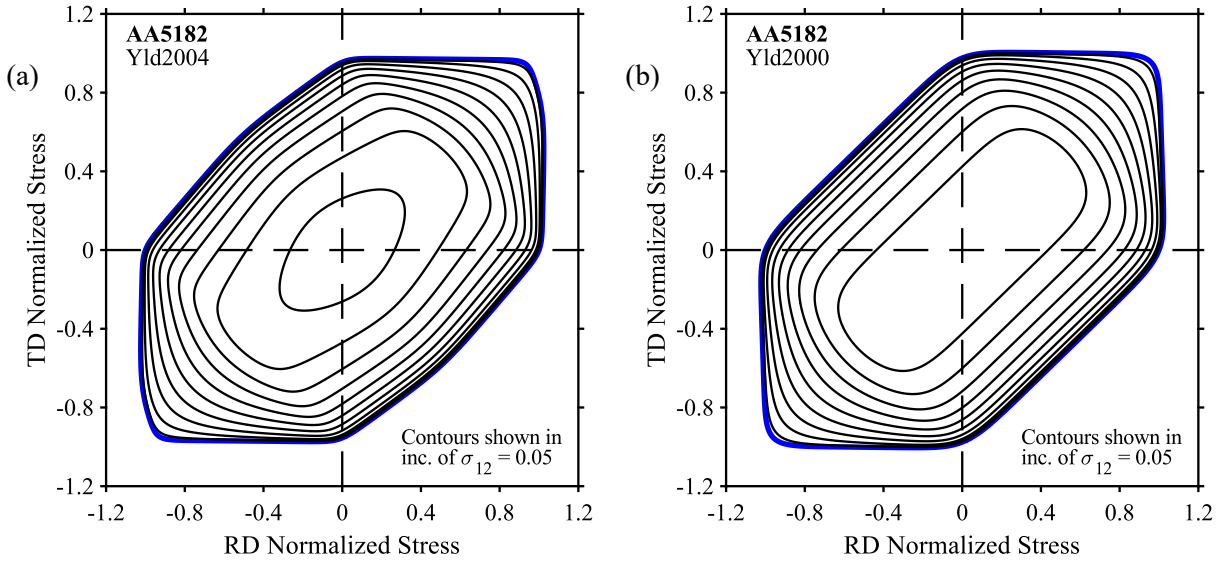

Figure 96: Calibrated (a) Yld2004 and (b) Yld2000 yield surfaces represented in plane stress $\sigma_{11} - \sigma_{22} - \sigma_{12}$ space for AA5182.

Table 37: Coefficients of the selected Yld2000 master yield surface for AA5182.

Material	m	α_1	α_2	α_3	α_4	α_5	α_6	α_7	α_8
AA5182	16.6551	0.9577	1.0403	1.0576	1.0403	1.0280	1.0762	1.0550	1.0879

Table 38: Coefficients of the selected Yld2004 master yield surface for AA5182.

Material	m	C'_{12}	C'_{13}	C'_{21}	C'_{23}	C'_{31}	C'_{32}	C'_{44}	C'_{55}
AA5182	38.5288	1.0890	0.8017	1.0088	0.8739	-0.6740	-0.1167	1.1160	1
cont'd	C'_{66}	C''_{12}	C''_{13}	C''_{21}	C''_{23}	C''_{31}	C''_{32}	C''_{44}	C''_{55}	C''_{66}
AA5182	1	0.8731	1.0242	0.7585	1.0745	1.2187	1.2622	0.8328	1	1

Under plane stress loading, Yld2004 and the Vegter criterion are in good agreement, as illustrated in Figure 97. Yld2000 lacks the calibration flexibility to capture the highly anisotropic plane strain response. The Vegter criterion accurately predicts the intermediate points along the uniaxial to plane strain arcs, locally obtained from the HF85-PSC criterion. The error in the predicted plane strain yield strength is less than 2% for Yld2004 and 3% for Yld2000.

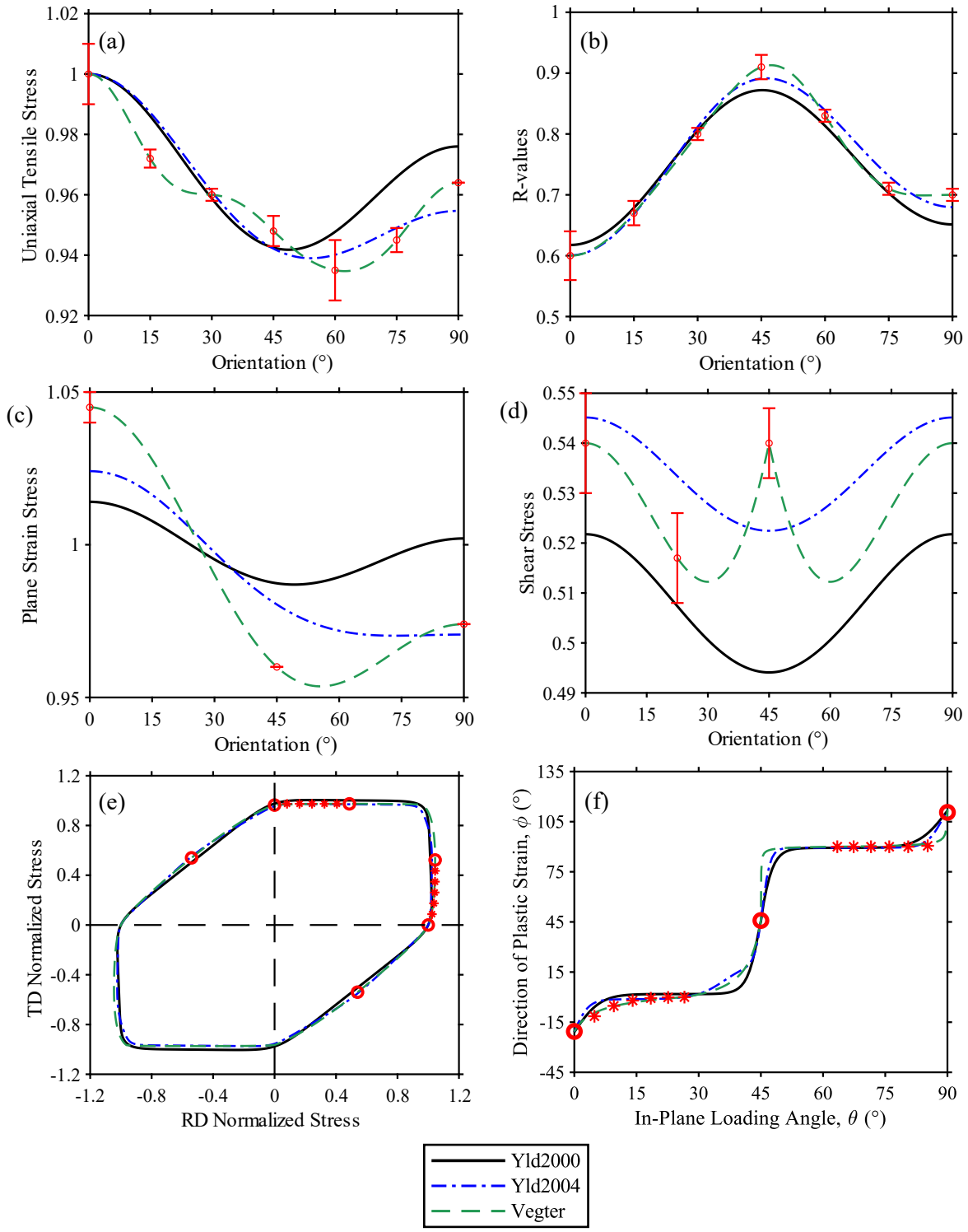

Figure 97: Yld2000, Yld2004 and Vegter master yield surfaces calibrated for AA5182 comparing (a, c, d) predicted and experimental stresses, (b) R-values, (f) plastic strain directions and (e) the overall plane stress surface. The predicted equal-biaxial yield stresses are $\sigma_b = 0.9394$ and $\sigma_b = 0.9568$ for Yld2004 and Yld2000, respectively. The predicted equal-biaxial R-values are $R_b = 1.031$ and $R_b = 1.013$ for Yld2004 and Yld2000, respectively.

7.3 Calibration of a Master Yield Surface for AA6xxx-T81

The AA6xxx-T81 alloy is mildly anisotropic and thus well modelled by the Yld2000, Yld2004 and Vegter criteria. Unweighted and stress-biased weighting approaches were compared to demonstrate that the best calibrations were consistently achieved with all weights set equal to unity. The inclusion of additional experimental data improves the yield surface predictions, particularly under shear and plane strain loading, which are not well captured in the conventional calibration approach. The Vegter criterion should be employed for two-dimensional finite-element simulations using shell elements, whereas Yld2004 must be used for three-dimensional solid element simulations.

7.3.1 Impact of Weighting Approach for AA6xxx-T81

The unweighted approach produces the best calibrations for AA6xxx-T81. Since the normalized stress-biased and inverse variance methods produced poor calibrations of the previous DP1180 and AA5182 master yield surfaces, only the unweighted and stress-biased approaches were considered for AA6xxx-T81 and AA6xxx-T4. As shown in Table 39, the unweighted calibration approach produced the better overall Yld2000 calibration in all cases except Calibration 3. Similarly, for Yld2004, Table 40 illustrates that the unweighted calibration produced the better overall calibration.

Table 39: Error between the stress-biased and unweighted Yld2000 calibrations for AA6xxx-T81. Green highlighted cells indicate decreased error compared to the unweighted approach while red highlighted cells indicate a higher error compared to the unweighted approach. Although the predictions in plane strain tension and equal-biaxial tension are improved, the stress-biased approach generally results in higher overall error compared to the unweighted approach

#	Description	σ_{UT}	R_{UT}	σ_{PST}	σ_b	R_b	σ_{Sh}	Overall
1	Conventional	1.6E-04	2.6E-03	-2.6E-04	-1.2E-04	6.9E-04	1.5E-04	3.2E-03
2	Cal 1 + PST	1.5E-04	2.4E-04	-2.0E-04	-8.9E-05	2.4E-04	3.3E-05	3.7E-04
3	Cal 1 + PST + Arcs	5.4E-05	-2.7E-04	-8.9E-05	-2.9E-05	-1.5E-05	-3.5E-06	-3.6E-04
4	Cal 1 + PST + Arcs + Shear	7.8E-05	8.9E-03	-3.2E-05	7.4E-05	5.7E-03	-7.8E-05	1.5E-02
5	All Data (m = *8*)	8.6E-05	1.2E-03	-8.0E-05	-2.8E-05	-1.2E-05	-5.4E-05	1.1E-03
6	No EB (m = *8*)	1.4E-04	2.1E-03	-6.5E-05	-4.1E-05	4.2E-04	-1.1E-04	2.5E-03
7	All Data (Variable Exponent)	1.2E-04	2.5E-03	2.5E-04	-1.1E-04	8.9E-04	5.0E-04	4.1E-03
8	No EB (Variable Exponent)	1.1E-04	1.2E-02	1.3E-03	-4.3E-04	6.3E-03	1.4E-03	2.0E-02

Table 40: Error between the stress-biased and unweighted Yld2004 calibrations for AA6xxx-T81. Green highlighted cells indicate decreased error compared to the unweighted approach while red highlighted cells indicate a higher error compared to the unweighted approach. The stress-biased approach generally results in greater error than the unweighted approach.

#	Description	σ_{UT}	R_{UT}	σ_{PST}	σ_b	R_b	σ_{Sh}	Overall
1	Conventional	3.5E-05	1.7E-03	-4.1E-05	-2.2E-05	4.8E-06	4.7E-05	1.7E-03
2	Cal 1 + PST	3.2E-05	2.3E-03	-1.8E-04	-4.6E-05	2.4E-06	-1.2E-04	2.0E-03
3	Cal 1 + PST + Arcs	-4.1E-05	1.4E-03	-3.5E-04	-5.3E-04	4.3E-04	2.1E-04	1.1E-03
4	All Data *(m = 8)*	1.0E-04	1.9E-03	7.4E-05	-2.3E-04	1.6E-04	3.3E-04	2.3E-03
5	All Data along RD/TD/DD + TTS + EB *(m = 8)*	9.7E-05	3.0E-03	-1.3E-04	-1.4E-04	3.1E-04	-2.5E-04	2.9E-03
6	All Data along RD/TD/DD + TTS *(m = 8)* – No EB	5.0E-05	-2.3E-04	7.2E-06	-3.6E-04	5.1E-03	-2.5E-05	4.5E-03
7	All Data (Variable Exponent)	-2.8E-06	3.3E-04	-2.0E-04	1.3E-04	7.1E-04	-2.4E-04	7.3E-04
8	All Data along RD/TD/DD + TTS + EB (Variable Exponent)	3.2E-04	7.6E-03	3.1E-04	-7.8E-05	3.0E-05	7.4E-04	9.0E-03
9	All Data along RD/TD/DD + TTS (Variable Exponent) – No EB	-9.0E-05	1.7E-02	1.9E-04	-3.1E-03	-8.0E-03	2.8E-04	6.2E-03
10	No EB (Variable Exponent)	1.3E-04	4.5E-03	2.8E-05	-1.6E-04	5.1E-04	1.4E-04	5.2E-03

7.3.2 Impact of Calibration Scheme for AA6xxx-T81

The optimal calibration is achieved for Yld2000 and Yld2004 when all data is included in the calibration and the yield exponent is selected to best fit the experimental data. Calibration 7 represents the master Yld2000 yield surface for this material. The addition of the plane strain and arc data improves the accuracy of the fit in the plane strain region, versus the conventional calibration that lacks this data. As shown in Table 41 and Figure 98, the equal-biaxial yield stress and R-value are inaccurately predicted when the corresponding experimental data is omitted from the calibration.

Table 41: Error between each calibration scheme and the conventional calibration for Yld2000 and AA6xxx-T81. Green highlighted cells indicate decreased error compared to the conventional scheme while red highlighted cells indicate a higher error compared to the conventional scheme. The additional data and the assumption of a variable exponent decreased the error under most loading conditions except for the equal-biaxial yield stress. All calibrations adopt the unweighted approach.

#	Description	σ_{UT}	R_{UT}	σ_{PST}	σ_b	R_b	σ_{Sh}	Overall
1	Conventional	0	0	0	0	0	0	0
2	Cal 1 + PST	-3.3E-06	-9.0E-05	4.7E-08	1.4E-06	-5.2E-06	7.1E-06	-9.0E-05
3	Cal 1 + PST + Arcs	4.6E-06	-2.2E-04	-9.1E-06	-6.0E-06	1.9E-05	1.7E-06	-2.1E-04
4	Cal 1 + PST + Arcs + Shear	6.7E-06	1.1E-04	-5.2E-06	-2.3E-06	2.1E-06	-9.4E-06	9.9E-05
5	All Data *(m = 8)*	8.7E-06	-1.8E-03	-9.6E-05	-3.6E-05	2.0E-05	9.7E-05	-1.8E-03
6	No EB (Variable Exponent)	1.1E-05	-1.8E-03	-9.0E-05	-3.9E-05	8.3E-05	9.0E-05	-1.7E-03
7	All Data (Variable Exponent)	-2.7E-05	-1.8E-03	-6.7E-04	1.1E-04	-7.9E-06	-6.6E-04	-3.0E-03
8	No EB *(m = 8)*	-1.8E-05	-1.8E-03	-6.9E-04	3.6E-04	3.3E-05	-6.7E-04	-2.7E-03

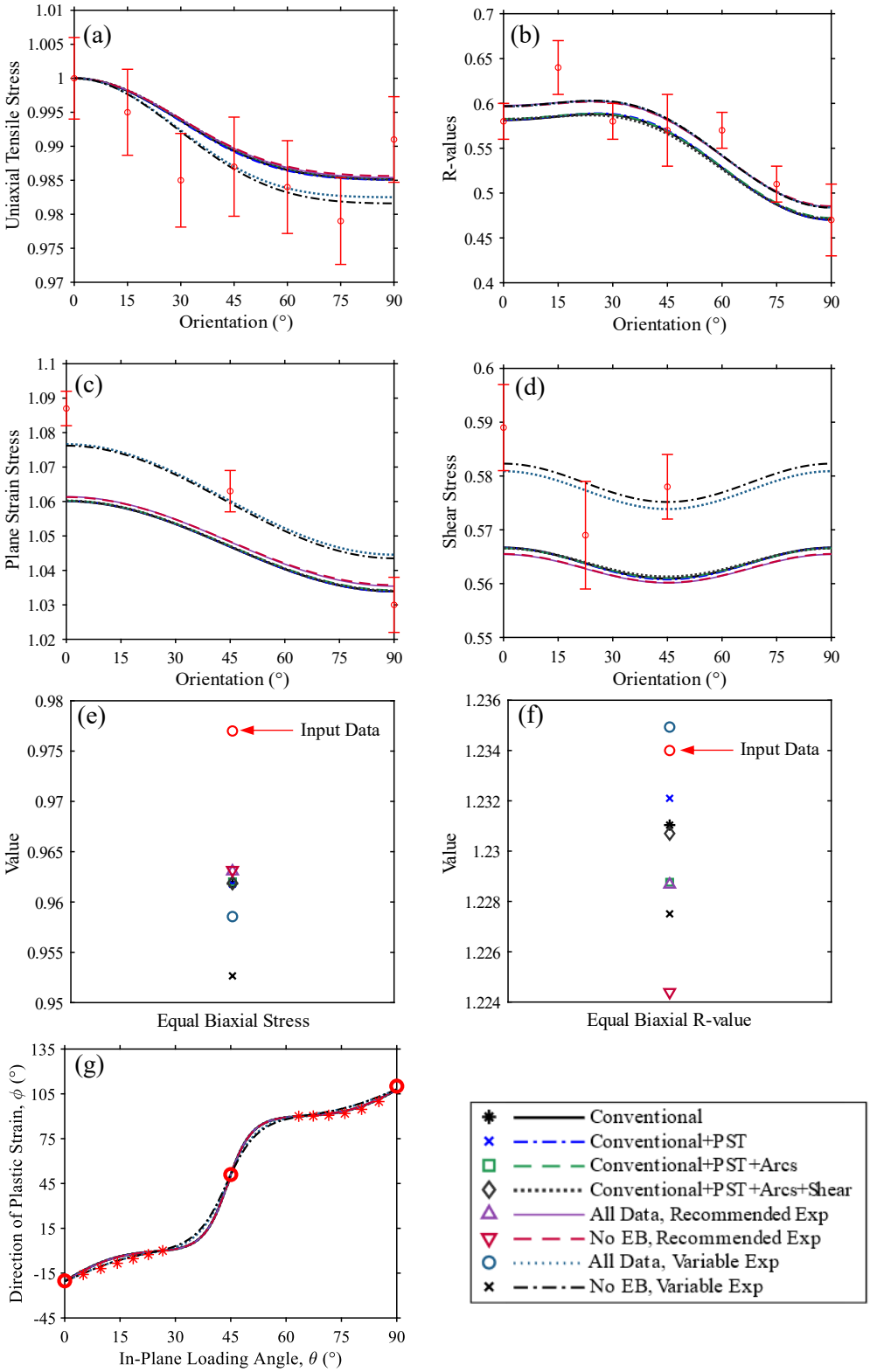

Figure 98: (a, c, d, e) Normalized stresses, (b, f) R-values and (g) plastic strain directions for the unweighted Yld2000 calibrations fit to the experimental data for AA6xxx-T81. Red circles and asterisks represent the available experimental data with the error bars corresponding to the experimental standard deviations.

Similarly, for Yld2004, the inclusion of the plane strain, arc and shear data decreases the overall objective function error versus the conventional calibration to only uniaxial tensile and equal-biaxial data. The error in the equal-biaxial stress and R-value tends to increase as more experimental data is included in the calibration since the Yld2004 function is not flexible enough to completely capture all stress states. Table 42 shows large errors in the predicted uniaxial tensile stress and R-value if experimental data along only the RD, DD and TD is used in the calibration. Even though the equal-biaxial data is omitted from the calibration, Calibration 10 is selected as the Yld2004 master yield surface since it better models the plane strain and shear constitutive responses shown in Figure 99. It should be noted that the conventional calibration offers a particularly poor prediction of the plane strain response because the assumed exponent of 8 is too high for the AA6xxx-T81 alloy.

Table 42: Error between each calibration scheme and the conventional calibration for Yld2004 and AA6xxx-T81. Green highlighted cells indicate decreased error compared to the conventional scheme while red highlighted cells indicate a higher error compared to the conventional scheme. The additional data consistently decreased the error under plane strain tension and shear, with the best overall calibration obtained by omitting the equal-biaxial data from the calibration. All calibrations adopt the unweighted approach.

#	Description	σ_{UT}	R_{UT}	σ_{PST}	σ_b	R_b	σ_{Sh}	Overall
1	Conventional	0	0	0	0	0	0	0
2	Cal 1 + PST	4.1E-05	-4.8E-05	-6.8E-05	-2.7E-05	-2.0E-06	-3.1E-05	-1.3E-04
3	Cal 1 + PST + Arcs	5.7E-05	6.6E-04	-3.1E-04	6.3E-04	3.7E-06	-7.5E-04	2.9E-04
4	All Data *(m = 8)*	4.3E-05	2.1E-03	-5.1E-04	2.0E-04	-1.4E-06	-6.2E-04	1.2E-03
5	All Data along RD/TD/DD + TTS + EB (*m = 8)*	5.9E-05	3.4E-03	-2.9E-04	4.8E-05	-2.0E-06	-3.1E-04	2.9E-03
6	All Data along RD/TD/DD + TTS (*m = 8)* – No EB	4.3E-05	4.3E-03	-6.3E-04	2.5E-04	2.2E-04	-6.1E-04	3.6E-03
7	All Data (Variable Exponent)	2.5E-06	8.3E-04	-3.7E-04	4.5E-05	-2.0E-06	-4.6E-04	5.0E-05
8	All Data along RD/TD/DD + TTS + EB (Variable Exp)	3.8E-05	3.5E-03	-4.5E-04	3.2E-05	-1.3E-07	-6.1E-04	2.5E-03
9	All Data along RD/TD/DD + TTS (Variable Exp) – No EB	2.4E-04	5.9E-03	-7.8E-04	3.7E-03	1.0E-02	-8.1E-04	1.8E-02
10	No EB (Variable Exponent)	-2.5E-05	8.3E-05	-6.4E-04	2.0E-04	1.1E-04	-7.7E-04	-1.0E-03

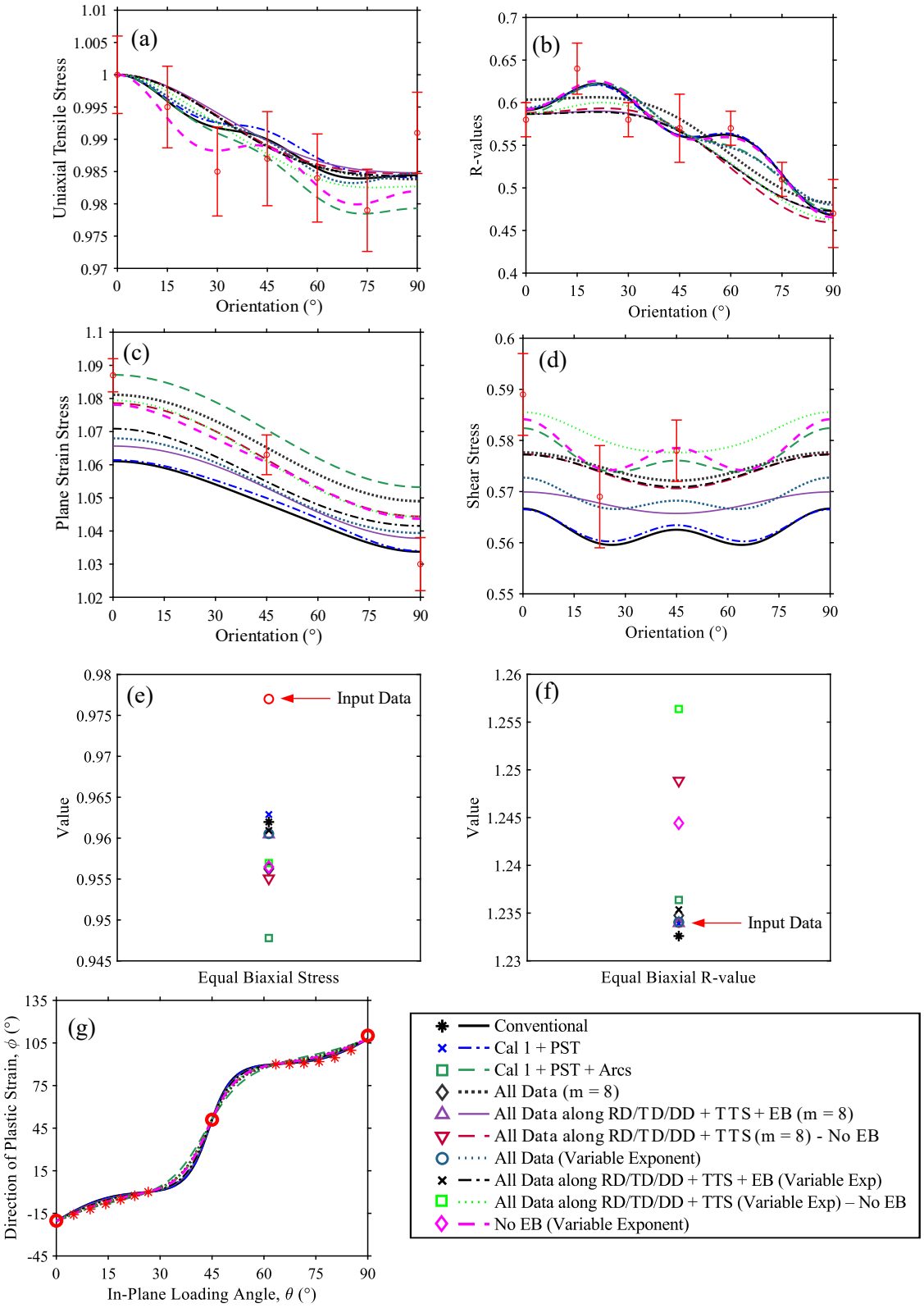

Figure 99: (a, c, d, e) Normalized stresses, (b, f) R-values and (g) plastic strain directions for the unweighted Yld2004 calibrations fit to the experimental data for AA6xxx-T81. Red circles and asterisks represent the available experimental data with the error bars corresponding to the experimental standard deviations.

7.3.3 Selection of Master Yield Criteria for AA6xxx-T81

Due to the relatively mild anisotropy of AA6xxx-T81, both Yld2004, shown in Figure 100(a), and Yld2000, shown in Figure 100(b), offer comparable predictions under plane stress loading. The corresponding parameters are shown in Table 43 and Table 44 for Yld2000 and Yld2004, respectively. Under 3-D loading, the Yld2004 model perfectly predicts the through-thickness shear stress of $\sigma^{TTS} = 0.5$.

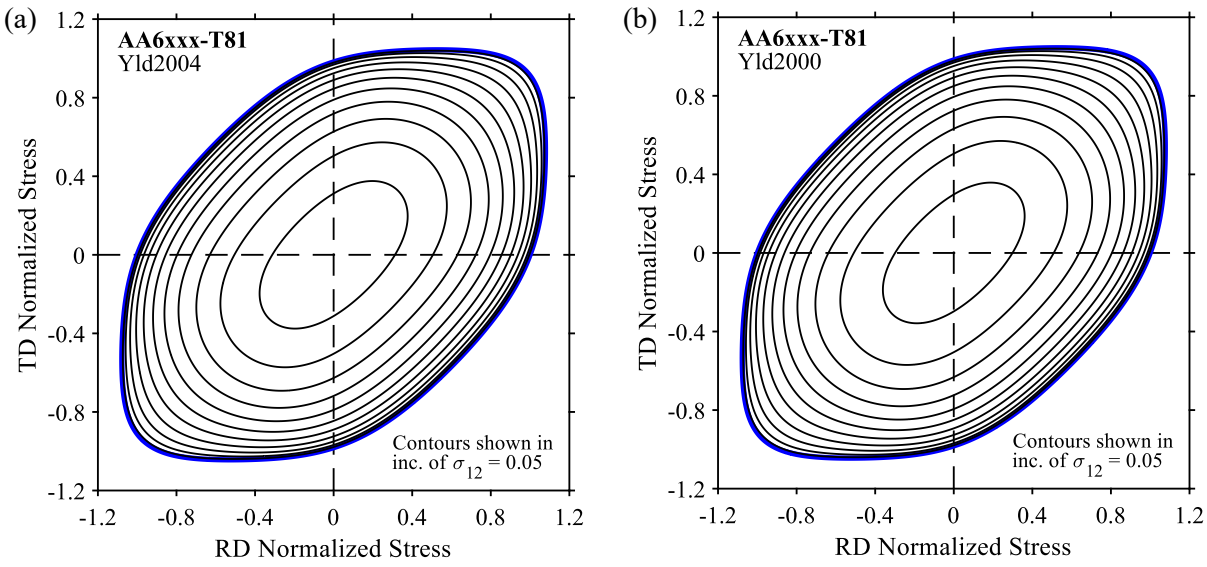

Figure 100: Calibrated (a) Yld2004 and (b) Yld2000 yield surfaces represented in plane stress $\sigma_{11} - \sigma_{22} - \sigma_{12}$ space for AA6xxx-T81.

Table 43: Coefficients of the selected Yld2000 master yield surface for AA6xxx-T81.

Material	m	α_1	α_2	α_3	α_4	α_5	α_6	α_7	α_8
AA6xxx-T81	6.4502	0.9571	0.9462	1.0524	1.0637	1.0310	1.0129	0.9639	1.0615

Table 44: Coefficients of the selected Yld2004 master yield surface for AA6xxx-T81.

Material	m	C'_{12}	C'_{13}	C'_{21}	C'_{23}	C'_{31}	C'_{32}	C'_{44}	C'_{55}
AA6xxx-T81	6.3623	1.3561	0.9821	0.9924	0.9145	1.2298	0.4953	1.1788	1.0237
cont'd	C'_{66}	C''_{12}	C''_{13}	C''_{21}	C''_{23}	C''_{31}	C''_{32}	C''_{44}	C''_{55}	C''_{66}
AA6xxx-T81	1.0237	0.1587	0.5191	0.7370	0.6441	1.2434	1.4586	0.7344	1.1972	1.1972

Yld2004 approaches the predictions of the Vegter criterion, particularly for the uniaxial R-values as evidenced by Figure 101(b). The extremes of the plane strain tensile yield stress variation, shown in Figure 101(c), cannot be captured by Yld2000 or Yld2004. While all three criteria accurately predict the direction of the plastic strains along the uniaxial to plane strain arc along RD, only the Vegter criterion accurately models the TD response seen in Figure 101(f).

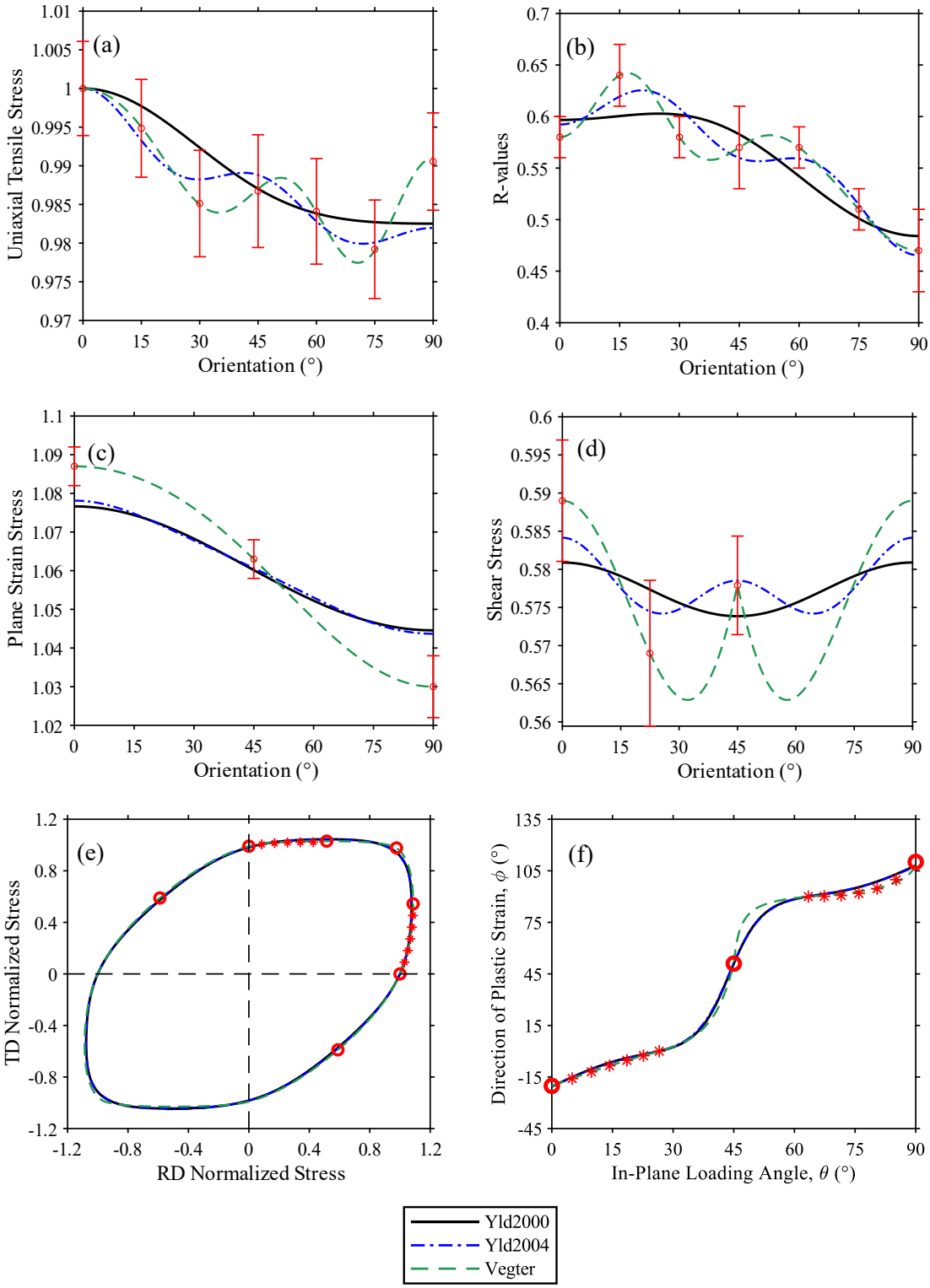

Figure 101: Yld2000, Yld2004 and Vegter master yield surfaces calibrated for AA6xxx-T81 comparing (a, c, d) predicted and experimental stresses, (b) R-values, (f) plastic strain directions and (e) the overall plane stress surface. The predicted equal-biaxial yield stresses are $\sigma_b = 0.957$ and $\sigma_b = 0.959$ for Yld2004 and Yld2000, respectively. The predicted equal-biaxial R-values are $R_b = 1.244$ and $R_b = 1.235$ for Yld2004 and Yld2000, respectively.

7.4 Calibration of a Master Yield Surface for AA6xxx-T4

In contrast to the AA6xxx-T81 aluminum, the AA6xxx-T4 alloy shows more anisotropy, with a higher plane strain yield strength along the rolling direction than along the diagonal and transverse directions. The alloy also shows substantial directional variability in the uniaxial tensile strength and R-value. The anisotropic response is reasonably captured by Yld2000 and Yld2004 when employing a stress-biased calibration approach that includes all data and a variable exponent. For two-dimensional finite-element simulations, the Vegter criterion offers the optimal calibration.

7.4.1 Impact of Weighting Approach for AA6xxx-T4

Table 45 compares the error in the stress-biased calibrations against the corresponding calibrations obtained using an unweighted approach. Biasing the Yld2000 calibration to the stresses consistently improves the prediction in plane strain, at the expense of the fit to the equal-biaxial and uniaxial tensile R-values. Overall, the unweighted approach results in a better overall calibration that captures both the stress and strain-based data.

Table 45: Error between the stress-biased and unweighted Yld2000 calibrations for AA6xxx-T4. Green highlighted cells indicate decreased error compared to the unweighted approach while red highlighted cells indicate a higher error compared to the unweighted approach. The stress-biased approach generally results in greater overall error than the unweighted approach.

#	Description	σ_{UT}	R_{UT}	σ_{PST}	σ_b	R_b	σ_{Sh}	Overall
1	Conventional	5.4E-04	2.0E-03	-2.7E-04	-1.6E-05	2.6E-04	-1.4E-04	2.4E-03
2	Cal 1 + PST	-3.6E-05	1.3E-03	-5.1E-05	-4.4E-07	2.4E-04	-1.2E-05	1.4E-03
3	Cal 1 + PST + Arcs	-9.7E-05	-1.4E-03	-7.1E-05	1.7E-07	2.0E-03	1.4E-05	4.7E-04
4	Cal 1 + PST + Arcs + Shear	7.1E-05	1.7E-03	-5.2E-05	1.6E-07	-2.3E-05	-2.7E-05	1.7E-03
5	All Data (m = 8)	-1.2E-04	-1.1E-04	-1.2E-04	-5.8E-07	2.9E-03	1.4E-06	2.6E-03
6	No EB (m = 8)	-2.6E-04	8.4E-04	-2.7E-04	2.1E-08	2.0E-02	2.5E-05	2.0E-02
7	All Data (Variable Exponent)	-5.2E-04	-5.4E-05	-6.0E-04	6.0E-05	1.0E-03	-5.6E-05	-1.6E-04
8	No EB (Variable Exponent)	-4.0E-05	1.5E-03	-3.7E-04	-3.3E-06	2.5E-02	-2.9E-05	2.6E-02

Table 46 illustrates that, for Yld2004, the unweighted calibration is preferred in 90% of the calibration schemes. A weight of $w_R = 0.1$ is not sufficient to capture the extreme variability in the uniaxial R-values. However, the stress-biased approach is selected because it provides the best calibration in the plane strain loading condition (Calibration 7), which is a focus of this thesis.

Table 46: Error between the stress-biased and unweighted Yld2004 calibrations for AA6xxx-T4. Green highlighted cells indicate decreased error compared to the unweighted approach while red highlighted cells indicate a higher error compared to the unweighted approach. The stress-biased approach generally results in greater error than the unweighted approach.

#	Description	σ_{UT}	R_{UT}	σ_{PST}	σ_b	R_b	σ_{Sh}	Overall
1	Conventional	7.2E-06	3.2E-04	1.1E-03	-4.3E-06	9.0E-05	1.2E-03	2.7E-03
2	Cal 1 + PST	1.5E-05	1.7E-03	-9.1E-05	-3.7E-05	7.9E-04	3.7E-05	2.4E-03
3	Cal 1 + PST + Arcs	1.2E-04	3.0E-03	-4.6E-04	-9.7E-05	2.0E-03	2.3E-05	4.5E-03
4	All Data *(m = 8)*	-9.1E-06	2.5E-03	-3.7E-04	8.8E-07	2.4E-03	-2.3E-05	4.5E-03
5	All Data along RD/TD/DD + TTS + EB *(m = 8)*	-2.0E-05	9.1E-04	-2.9E-04	-9.8E-06	2.3E-03	5.1E-06	2.9E-03
6	All Data along RD/TD/DD + TTS *(m = 8)* – No EB	-2.1E-04	-2.2E-03	-2.1E-04	3.8E-07	2.0E-02	-3.4E-05	1.7E-02
7	All Data (Variable Exponent)	1.4E-05	3.8E-03	-8.3E-04	-3.4E-05	-3.0E-05	-1.3E-04	2.8E-03
8	All Data along RD/TD/DD + TTS + EB (Variable Exponent)	-5.7E-05	-1.9E-03	1.7E-05	1.5E-05	1.7E-05	4.9E-06	-1.9E-03
9	All Data along RD/TD/DD + TTS (Variable Exponent) – No EB	-5.4E-05	8.3E-04	-3.9E-05	-3.6E-03	3.1E-01	1.9E-05	3.1E-01
10	No EB (Variable Exponent)	8.4E-06	3.9E-03	-2.0E-04	-3.5E-04	3.7E-02	-1.1E-04	4.1E-02

7.4.2 Impact of Calibration Scheme for AA6xxx-T4

The addition of plane strain and arc data, which are ordinarily omitted in a conventional calibration, improves the accuracy of the Yld2000 model. Including all data and calibrating the exponent as an additional parameter, offers the best overall prediction in Table 47. The overall error for Calibration 7 – the selected Yld2000 master yield surface – is 53% lower than the conventional Calibration 1. Figure 102(c) demonstrates the anchoring effect of the equal-biaxial point. If the equal-biaxial data is omitted, as in the case of Calibrations 6 and 8, the Yld2000 model is better able to predict the experimental plane strain yield strengths, at the expense of large errors in the equal-biaxial R-value and stress, seen in Figure 102(e, f, g).

Table 47: Error between each calibration scheme and the conventional calibration for Yld2000 and AA6xxx-T4. Green highlighted cells indicate decreased error compared to the conventional scheme while red highlighted cells indicate a higher error compared to the conventional scheme. The additional data consistently decreased the error under uniaxial tension and plane strain tension, with the best calibration obtained by adopting a variable exponent and including all data. All calibrations adopt the unweighted approach.

#	Description	σ_{UT}	R_{UT}	σ_{PST}	σ_b	R_b	σ_{Sh}	Overall
1	Conventional	0	0	0	0	0	0	0
2	Cal 1 + PST	1.3E-05	-6.8E-04	-1.8E-05	1.3E-07	3.6E-07	-1.6E-06	-6.9E-04
3	Cal 1 + PST + Arcs	-1.9E-04	-4.2E-03	-1.2E-04	1.6E-07	1.8E-03	3.5E-05	-2.6E-03
4	Cal 1 + PST + Arcs + Shear	-2.1E-05	-6.9E-04	-1.1E-04	1.4E-07	-2.4E-04	-1.0E-05	-1.1E-03
5	All Data *(m = 8)*	-2.8E-04	-6.4E-03	-2.5E-04	-2.2E-08	3.6E-03	7.3E-05	-3.2E-03
6	No EB *(m = 8)*	-5.3E-04	-5.7E-03	-4.7E-04	-2.0E-09	2.2E-02	1.1E-04	1.6E-02
7	All Data (Variable Exponent)	-6.7E-04	-6.4E-03	-7.0E-04	6.2E-05	7.7E-04	3.5E-05	-6.9E-03
8	No EB (Variable Exponent)	-6.6E-04	-5.1E-03	-1.1E-03	9.1E-05	2.8E-02	5.2E-05	2.2E-02

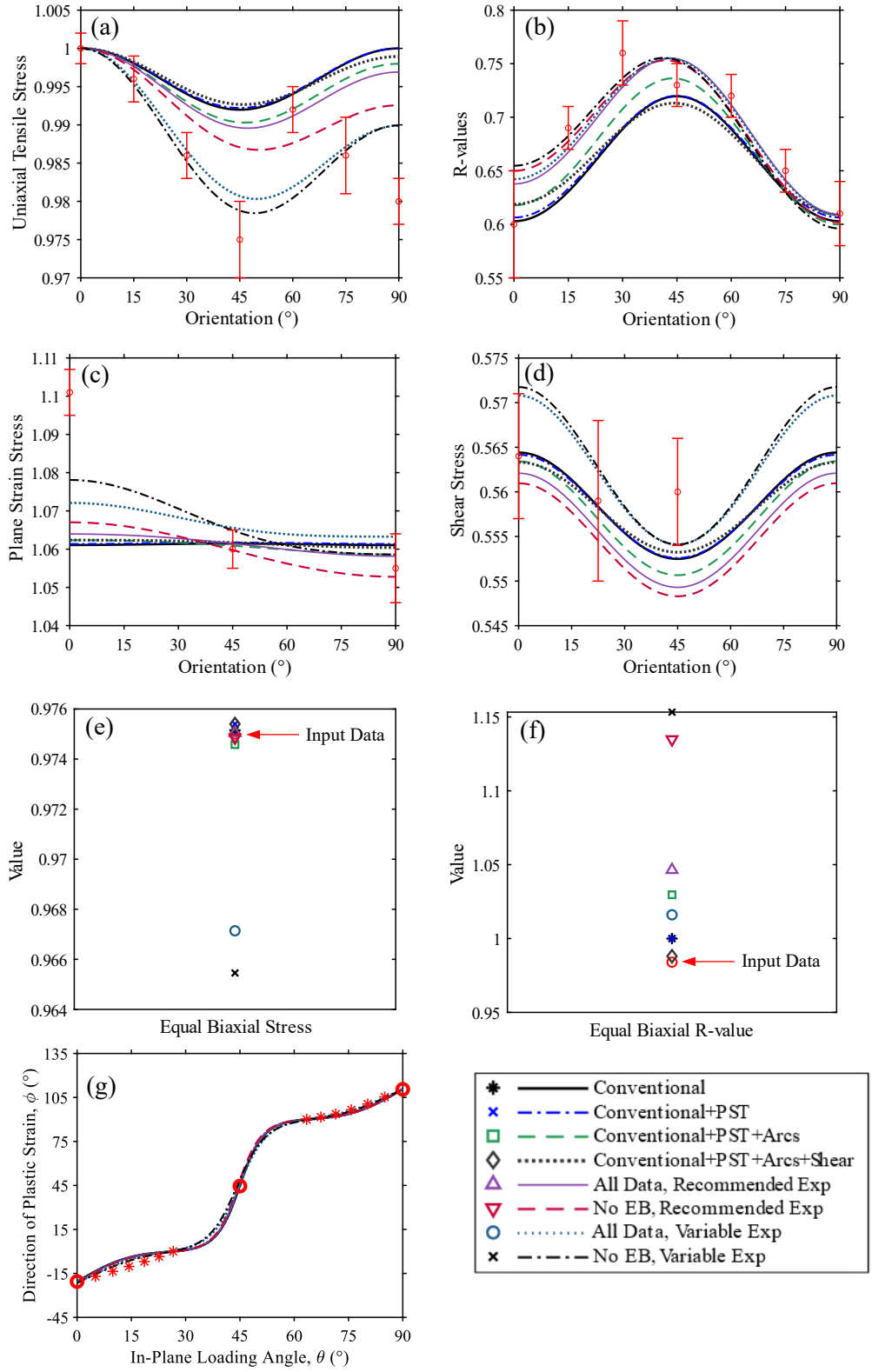

Figure 102: (a, c, d, e) Normalized stresses, (b, f) R-values and (g) plastic strain directions for the stress-biased Yld2000 calibrations fit to the experimental data for AA6xxx-T4. Red circles and asterisks represent the available experimental data with the error bars corresponding to the experimental standard deviations.

Similarly, the Yld2004 master yield surface was selected as Calibration 7 with a variable exponent and all the experimental data included in the calibration. Including the shear and plane strain data, as shown in Table 48, improves the predictions under these loading conditions by upwards of 64% versus the conventional approach.

Table 48: Error between each calibration scheme and the conventional calibration for Yld2004 and AA6xxx-T4. Green highlighted cells indicate decreased error compared to the conventional scheme while red highlighted cells indicate a higher error compared to the conventional scheme. The additional data consistently decreased the error under shear and plane strain tension, with the best overall calibration obtained by adopting a variable exponent and including all data in the calibrations. All calibrations adopt the stress-biased weighting approach.

#	Description	σ_{UT}	R_{UT}	σ_{PST}	σ_b	R_b	σ_{Sh}	Overall
1	Conventional	0	0	0	0	0	0	0
2	Cal 1 + PST	2.0E-05	1.3E-03	-4.6E-03	3.9E-05	7.1E-04	-5.8E-03	-8.3E-03
3	Cal 1 + PST + Arcs	8.2E-05	2.7E-03	-5.1E-03	6.6E-05	1.9E-03	-5.8E-03	-6.1E-03
4	All Data *(m = 8)*	-6.1E-05	2.2E-03	-5.0E-03	1.5E-04	2.4E-03	-5.9E-03	-6.2E-03
5	All Data along RD/TD/DD + TTS + EB (*m = 8)*	-1.9E-05	9.0E-03	-5.1E-03	1.0E-04	2.2E-03	-5.8E-03	3.8E-04
6	All Data along RD/TD/DD + TTS (*m = 8)* – No EB	4.8E-05	1.0E-02	-5.5E-03	4.0E-04	6.3E-02	-5.9E-03	6.2E-02
7	All Data (Variable Exponent)	-3.9E-05	3.5E-03	-5.5E-03	8.8E-05	-8.1E-05	-6.0E-03	-8.0E-03
8	All Data along RD/TD/DD + TTS + EB (Variable Exp)	-8.6E-06	6.7E-03	-5.5E-03	8.5E-05	-7.5E-05	-6.0E-03	-4.7E-03
9	All Data along RD/TD/DD + TTS (Variable Exp) – No EB	3.6E-05	7.7E-03	-5.5E-03	3.4E-04	3.2E-01	-6.0E-03	3.2E-01
10	No EB (Variable Exponent)	-4.4E-05	3.7E-03	-5.5E-03	5.8E-05	7.7E-02	-5.9E-03	6.9E-02

The Yld2004 model, while more flexible than Yld2000, cannot perfectly capture the anisotropic constitutive response of the AA6xxx-T4 under all loading conditions. Figure 103(c, d) illustrates how the plane strain and shear yield stresses are overpredicted in the conventional calibration, and better – albeit imperfectly – predicted when included in Calibrations 2-10. Including only tensile data along the RD, TD and DD in the calibration, and allowing for a variable exponent, provides the necessary flexibility to accurately predict the anisotropy in the plane strain yield strength. Unfortunately, this approach leads to a poor prediction of the uniaxial tensile stress and R-value shown in Figure 103(a, b).

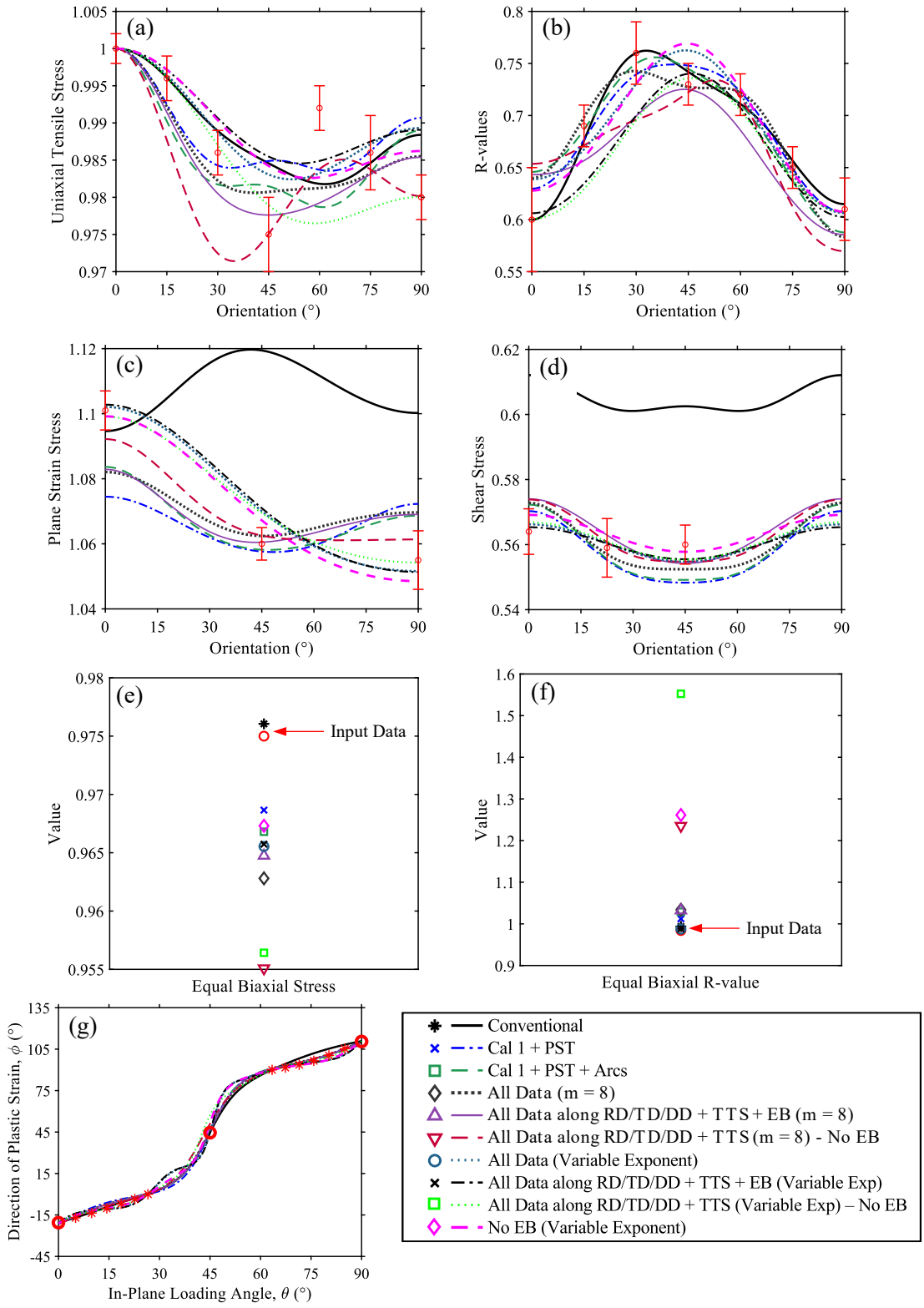

Figure 103: (a, c, d, e) Normalized stresses, (b, f) R-values and (g) plastic strain directions for the unweighted Yld2004 calibrations fit to the experimental data for AA6xxx-T4. Red circles and asterisks represent the available experimental data with the error bars corresponding to the experimental standard deviations.

7.4.3 Selection of Master Yield Criteria for AA6xxx-T4

Both Yld2004, shown in Figure 104(a), and Yld2000, shown in Figure 104(b), offer comparable predictions of the in-plane yielding behavior. However, Yld2004 has more flexibility to capture the directional dependent plane strain response than Yld2000. The corresponding parameters are shown in Table 49 and Table 50 for Yld2000 and Yld2004, respectively. Note that the Yld2004 out-of-plane parameters $C'_{55}, C'_{66}, C''_{55}$ and C''_{66} are set equal to unity since no through-thickness shear tests were performed for this alloy.

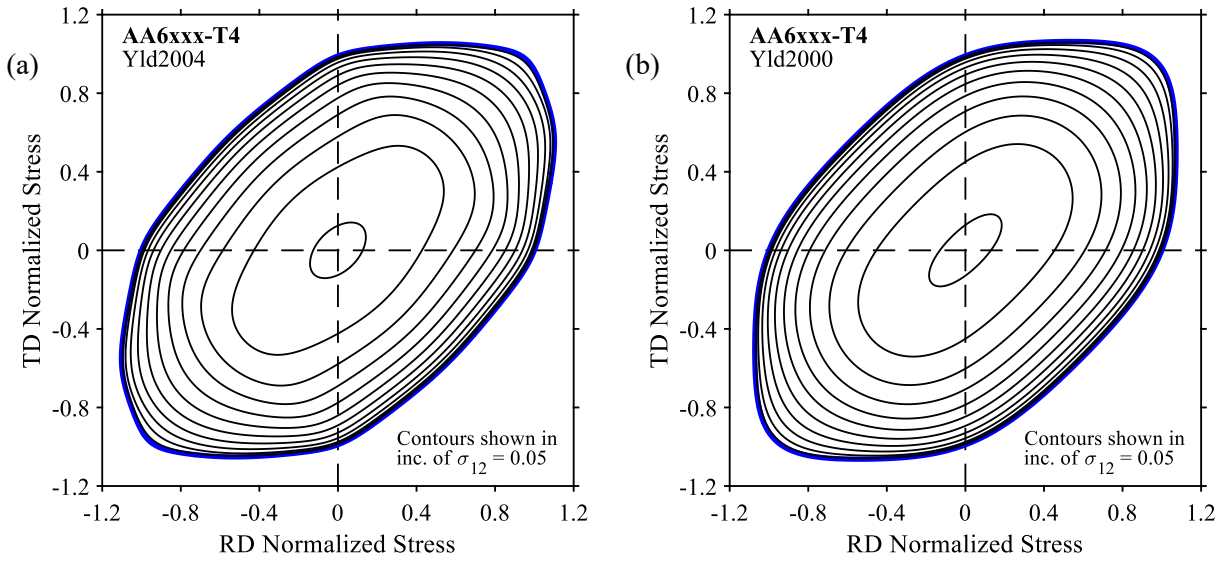

Figure 104: Calibrated (a) Yld2004 and (b) Yld2000 yield surfaces represented in plane stress $\sigma_{11} - \sigma_{22} - \sigma_{12}$ space for AA6xxx-T4.

Table 49: Coefficients of the selected Yld2000 master yield surface for AA6xxx-T4.

Material	m	α_1	α_2	α_3	α_4	α_5	α_6	α_7	α_8
AA6xxx-T4	6.7671	0.9616	0.9707	1.0256	1.0397	1.0312	1.0366	0.9959	1.0473

Table 50: Coefficients of the selected Yld2004 master yield surface for AA6xxx-T4.

Material	m	C'_{12}	C'_{13}	C'_{21}	C'_{23}	C'_{31}	C'_{32}	C'_{44}	C'_{55}
AA6xxx-T4	26.3222	0.6630	1.1896	0.5511	1.1032	0.8073	0.8179	0.6303	1
cont'd	C'_{66}	C''_{12}	C''_{13}	C''_{21}	C''_{23}	C''_{31}	C''_{32}	C''_{44}	C''_{55}	C''_{66}
AA6xxx-T4	1	1.2518	1.0678	1.1592	1.1430	0.6593	0.8400	1.2202	1	1

Figure 105 compares the master Yld2000 and Yld2004 calibrations with the Vegter criterion. The predicted plane strain yield stresses are similar for both the Yld2004 and Vegter criteria. The sharp increase in the uniaxial tensile yield stress at 60° from RD cannot be predicted by either Yld2000 or Yld2004.

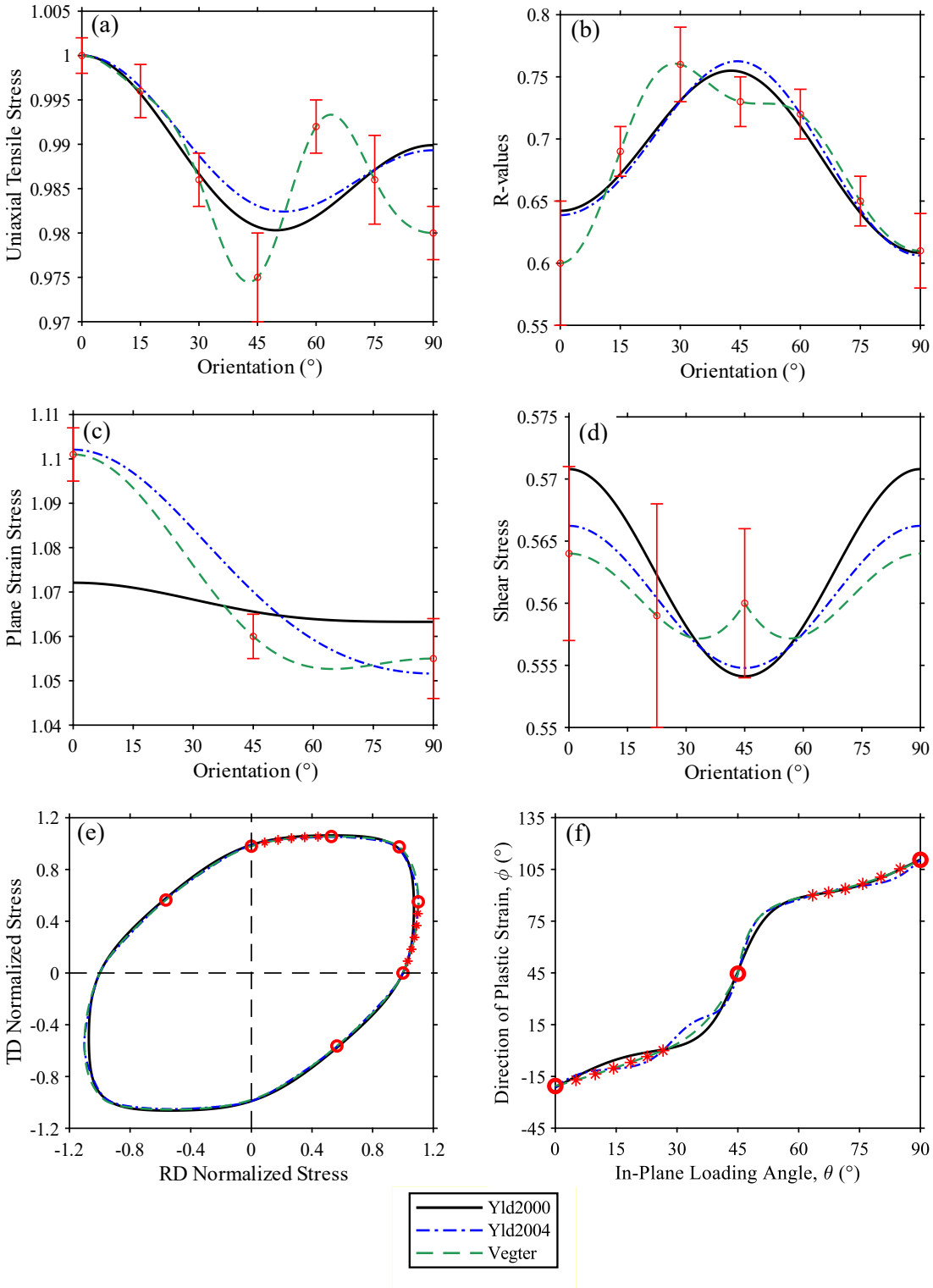

Figure 105: Yld2000, Yld2004 and Vegter master yield surfaces calibrated for AA6xxx-T4 comparing (a, c, d) predicted and experimental stresses, (b) R-values, (f) plastic strain directions and (e) the overall plane stress surface. The predicted equal-biaxial yield stresses are $\sigma_b = 0.966$ and $\sigma_b = 0.967$ for Yld2004 and Yld2000, respectively. The predicted equal-biaxial R-value is $R_b = 0.988$ and $R_b = 1.016$ for Yld2004 and Yld2000, respectively.

7.5 Summary of Master Yield Surface Calibration

Yld2000, Yld2004 and Vegter master yield surfaces were calibrated for each of the four materials studied in this thesis. Ten Yld2004 calibration schemes and eight Yl2000 calibration schemes were analyzed by successively adding additional data to the conventional calibration that used only uniaxial tensile and equal-biaxial data. For each material, the calibration schemes were compared using a consistent set of weighting parameters selected as the optimum of: $w_\sigma = w_R = w_N = 1$ (unweighted), $w_\sigma = 0.9$ and $w_R = w_N = 0.1$ (stress-biased), $w_\sigma = 0.9/n$ and $w_R = w_N = 0.1/n$ (normalized stress-biased) and $w_i = 1/s_i^2$ (inverse variance). The additional parameters afforded by the Yld2004 function provide greater calibration flexibility not available to the Yld2000 function, and closer agreement to the Vegter criterion in plane stress loading.

The addition of the plane strain yield strength and five arc points along the uniaxial-to-plane strain arc improved the model accuracy in the plane strain loading condition. Without knowledge of the plane strain tensile strength from experimental tests, the predicted value is controlled by the assumed exponent of the yield function. Addition of the plane strain yield strength alone decreased the squared error in plane strain tension by up to 82% (as in the case of the stress-biased calibration of Yld2004 for AA6xxx-T4) compared to the conventional calibration and holding the weighting method constant. Improving the accuracy of the yield surface in plane strain tension translates to an improved prediction of the onset of necking. Consequently, sheet metal forming processes may be optimized to avoid early failure and maximize the utility of the selected material.

Optimal calibrations were achieved by including all the available shear, plane strain tensile and uniaxial tensile data in the calibration while also adopting a variable yield exponent, calibrated to the experimental data as an additional parameter. Selected Yld2004 exponents of 26.3 for AA6xxx-T4, 6.36 for AA6xxx-T81, 38.53 for AA5182 and 19.34 for DP1180 challenge the conventional wisdom that exponents of $m = 8$ and $m = 6$ are most appropriate for FCC and BCC materials, respectively. The use of the recommended exponent limits the flexibility of the Yld2004 function, particularly affecting the curvature in the uniaxial to equal-biaxial tensile domain.

Although commonly omitted due to a lack of experimental data, calibrating the through-thickness shear stress is important for accurate solid element simulations. The experimentally determined through-thickness shear stress was included in the master yield surface calibration for DP1180 and AA6xxx-T81. Shear parameters of $C'_{55} = C'_{66} = -0.5355$ and $C''_{55} = C''_{66} = 1$ perfectly described the through thickness shear stress of $\sigma_{TTS} = 0.675$ for DP1180 while parameters of $C'_{55} = C'_{66} = 1.0237$ and $C''_{55} = C''_{66} = 1.1972$

corresponded to the shear stress ratio of $\sigma_{TTS} = 0.5$ for AA6xxx-T81 at the variable exponents noted previously.

Despite the addition of the plane strain tensile point and constraint, it is not recommended to down select the experimental data in other sheet and loading orientations to minimize the extent of the experimental testing. Omitting the uniaxial tensile stress and R-value at 15, 30, 60 and 75 degrees caused oscillations in the respective predicted responses for DP1180 and AA5182. Similarly omitting the equal biaxial stress and R-value leads to poor predictions of the respective response, particularly for AA5182 where the R-value is highly sensitive to the curvature along the plane strain tensile to equal-biaxial tensile arc due to the Tresca-like shape. Poor prediction of the equal-biaxial R-value under a reduced experimental testing regime is in line with the findings of Aretz *et al.* (2007). All available experimental data should be included for the most accurate master yield surface calibration.

In each case, the Vegter criterion provided the optimal plane stress calibration to the available experimental data. Each of the uniaxial tensile, plane strain tensile, shear and equal-biaxial stresses are defined exactly in the model as a Bezier curve hinge point while the equal-biaxial and uniaxial tensile R-values control the Bezier normal vector orientations. Using the plane strain constraint to fix the location of the plane strain tensile point resolves a fundamental issue with the original Vegter criterion, in which the location was unknown and allowed to occur anywhere on the uniaxial to equal-biaxial tensile arc. Furthermore, the generalized plane strain constraints at shear and plane strain tension are straightforward to enforce by controlling the direction of the Bezier normal vectors at the respective hinge points.

Chapter 8 Evaluation of Master Yield Surfaces

A calibrated master yield surface is critical to the accurate simulation of test coupons and components. This chapter evaluates the master yield surfaces calibrated in Chapter 7 in both plane strain tension and through-thickness shear. In Section 8.1, notch tests of Geometry B are simulated and compared to the corresponding experimental results along the limiting direction of each of the four materials tested in this thesis. In Section 8.2, a through-thickness shear test of the AA6xxx-T81 alloy is simulated and compared to the experimental load-displacement and stress-strain responses.

8.1 Evaluation in Plane Strain Tension

Post-necking simulations of the experimental tests conducted with Geometry B are ideal for evaluation of the master yield surfaces calibrated in Chapter 7. The magnitude and profile of the stress/strain distribution along the gauge width is sufficiently different than that of the Geometry A notch used for calibration, such that the simulated response will only be accurate if the plane strain yield strength and curvature of the UT-PST arc are correctly defined. Poor prediction of the response of a different geometry could indicate that the calibrated plane strain yield strength is somehow biased towards the choice of Geometry A used in this analysis, rather than an independent material parameter. Furthermore, like a uniaxial tension test, strain localization through the thickness causes a shift toward plane strain tension along much of the gauge region during necking. Assuming that the hardening curve is well calibrated to large strains, any error in the predicted stress and strain response will be due to a poorly calibrated yield surface. Therefore, notch Geometry B is employed for evaluation, as it was not used in the calibration of the plane strain yield strength or development of the master yield functions.

The hardening curves for the materials analyzed in this thesis were calibrated to large strains using mini shear tests. The post-processing of the shear tests was completed by Dr. Butcher and Dr. Abedini in each available direction, including the calculation of the converted shear response for AA6xxx-T4 and AA6xxx-T81. The author performed the shear conversion for DP1180 and AA5182 using the provided data. The flow stress obtained from the converted shear tests is dependent on the sheet orientation, since rotation of the shear band during plastic deformation activates a select range of the material's anisotropy. For example, a shear test conducted along the 45° direction may activate grains along the 45°-50° directions (assuming an arbitrary rotation of 5°). Therefore, the flow stress in the reference direction is bounded between the upper and lower converted shear stress curves, with the correct response being the one that promotes the best agreement between the simulated and experimental results holding the yield surface parameters constant.

For the three aluminum materials, the adjusted spline hardening model of Dr. Butcher, shown by Eq. (1.13), was employed and iteratively adjusted using the exponential decay function in Eq. (1.15) until good agreement was obtained with the post-uniform response of the notch specimens. The final hardening curves for each material are shown in Figure 106, where the solid line indicates data obtained from a standard uniaxial tension test up to necking. The selected values are $a = 0.7$ for AA5182, $a = 5$ for AA6xxx-T4 and $a = 0.4$ for AA6xxx-T81.

The hardening curve for the DP1180 steel was input in a tabular format (closely approximated using $a = 0.3$ and $b = 0$) and corrected for shear test geometry bias as part of ongoing research into shear test geometries. As explained by Narayanan *et al.* (2021), the accuracy of the equivalent stress predicted from mini shear specimens, and need for a correction factor, is dependent on the hardening rate of the material. The DP1180 has an approximately constant hardening exponent of $n = 0.06$ whereas the three aluminum materials have non-linear hardening exponents approaching $n = 0.2$ to 0.3 around uniform elongation. A 4-5% error in the predicted equivalent stress is apparent for materials with low hardening rates, such as the DP1180 steel used in this study, compared to an error of only approximately 1% for high or medium hardening materials like the three tested aluminums. Therefore, only the DP1180 shear curve required correction whereas the flow curve could be fit directly to the range of the converted shear responses for the AA6xxx-T81, AA6xxx-T4 and AA5182 materials.

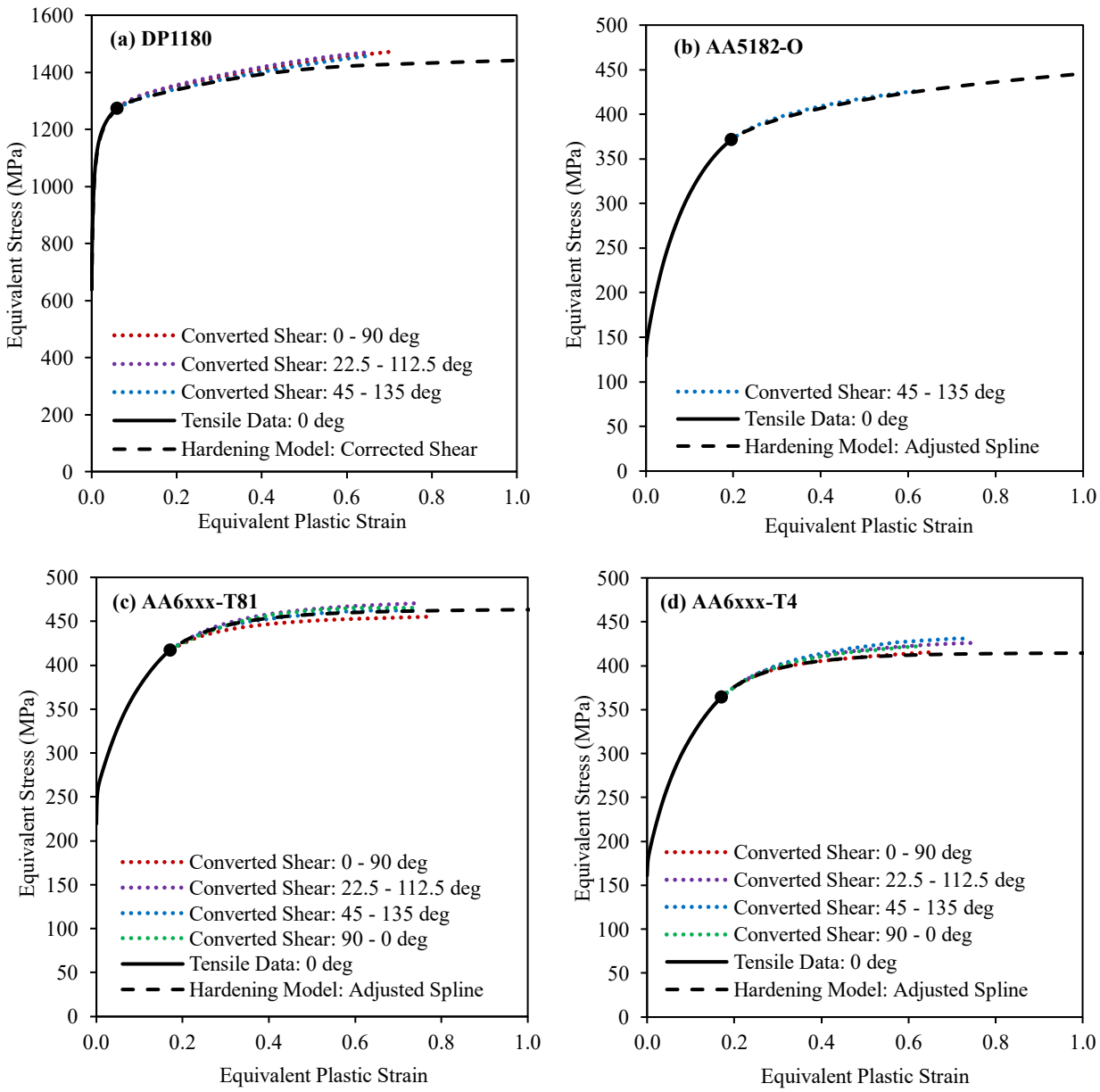

Figure 106: Spline hardening curves iteratively adjusted using an exponential decay function to provide good agreement between the post-necking regions of the simulated and experimental plane strain notch tests while also falling within the range of converted shear responses. The selected large-strain hardening models are shown for (a) DP1180, (b) AA5182, (c) AA6xxx-T81 and (d) AA6xxx-T4.

As discussed by Dunand and Mohr (2010), simulation of the post-necking response of a material requires not only solid elements and a 3-D yield function, but also a convergence study to determine the mesh size required to capture the through-thickness localization. Adopting the DP1180 material model for the convergence study, the 1 mm thick Geometry B notch specimen was modelled with 250, 100, 50 and 25 μm size elements in the gauge region corresponding to 2, 5, 10 and 20 elements through the half-thickness of the specimen, respectively. One-eighth symmetry was used to decrease the computational time, with

zero-normal displacement at each symmetry plane and a prescribed velocity of v = 0.005 mm/s at the nodes corresponding to the upper grip. The four meshes are shown in Figure 107.

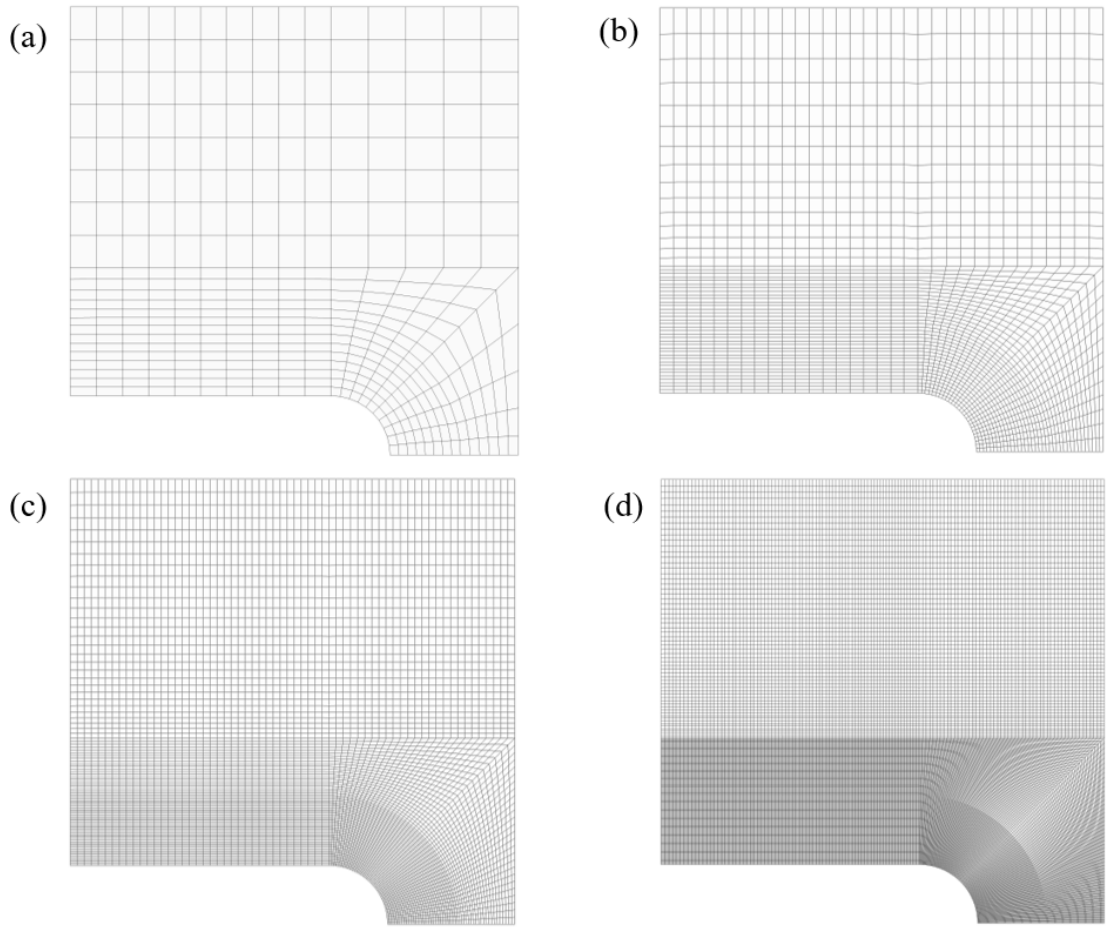

Figure 107: Eighth symmetry models of the Geometry B plane strain notch specimen used to assess convergence. The characteristic dimension of the elements in the gauge region are (a) 250 μm, (b) 100 μm, (c) 50 μm and (d) 25 μm. The size of the elements in the through-thickness direction is the same as the in-plane dimensions in the gauge regions.

As illustrated in Figure 108, convergence occurs at a 50 μm mesh size in exact agreement with the conclusions of Dunand and Mohr (2010). The error between the 50 μm and 25 μm mesh results at fracture are 0.7% for the stress and 3.7% for the major strain. In contrast, the error between the 100 μm and 50 μm results at fracture are 2.4% for the stress and 13.8% for the strain. Based on this convergence study, the 50 μm mesh is also selected for analysis of the other three materials, assuming similar behavior.

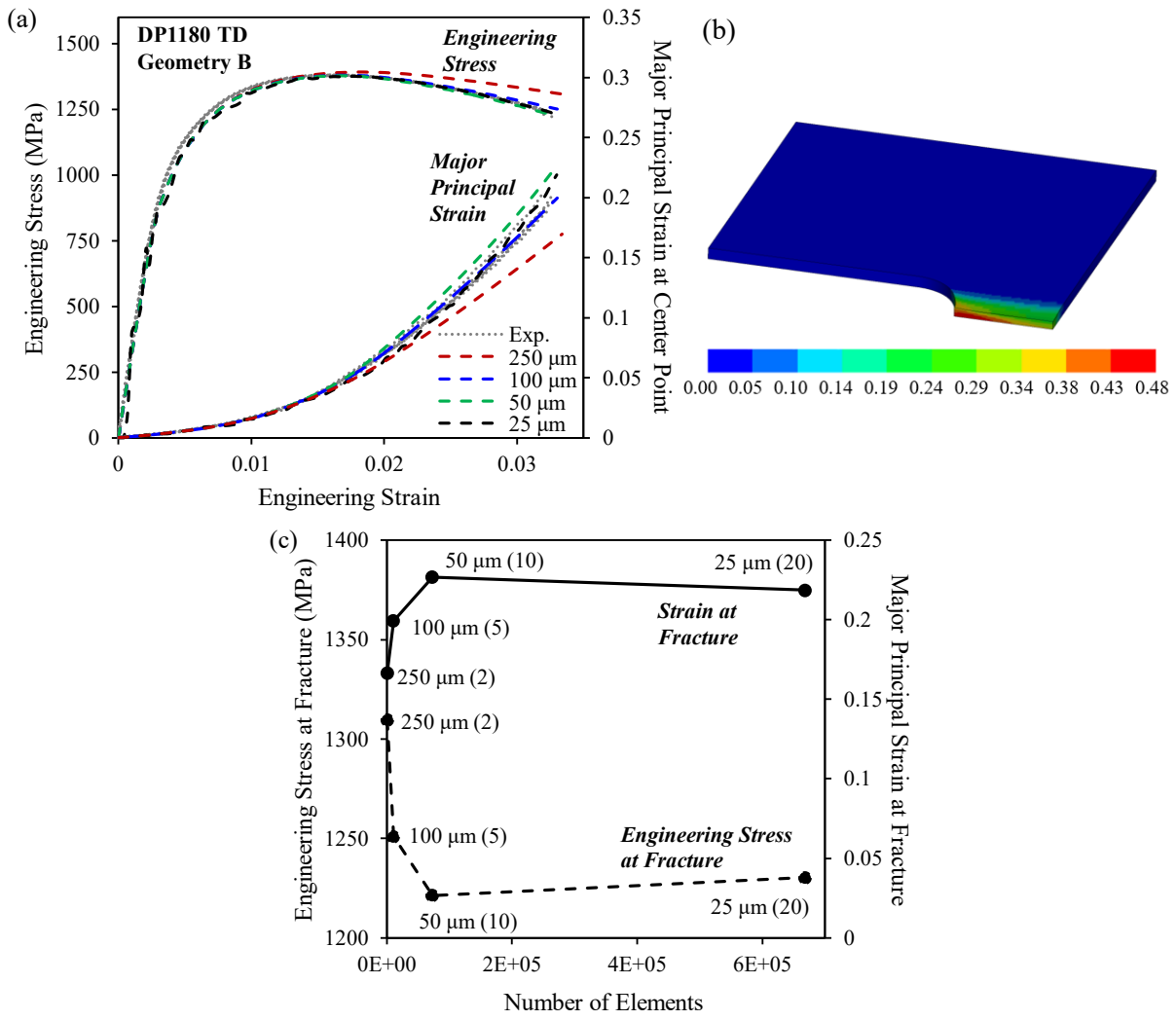

Figure 108: (a) Stress and strain responses obtained from the models using 250 µm, 100 µm, 50 µm and 25 µm element sizes compared to the experimental results, (b) FE contour plot of major strain at an engineering strain of 0.032 for the 50 µm mesh model and (c) convergence of engineering fracture stress and fracture strain as a function of the number of elements.

Both the stress and strain responses are in excellent agreement with the experimental data for DP1180. The error in the stress is just 0.5% at fracture and the error in the strain is 11.6%. The larger error in the strain may be due to the difference in resolution between the DIC measurements, with a VSGL of 0.5 mm, and the FE prediction with an element size of 50 µm (0.05 mm). Decreasing the measurement gauge length better captures the strain localization, as has been noted by other researchers including Khameneh *et al.* (2021) for shear tests. In contrast, maintaining a comparable length scale, as in the case of the 100 µm (0.1 mm) FE mesh and the DIC data with a VSGL of 0.5 mm, decreases the strain error to less than 1.2%. The ability of the Yld2004 model to capture the hardening response to fracture of an alternate notch geometry demonstrates the accuracy of the plane strain yield strength and the overall calibration.

The simulated stress-strain response for AA5182 shown in Figure 109(a) is within the variation of the experimental data up to the point of fracture. The excellent agreement between the simulated and experimental curves suggests that the master yield surface calibrated in Section 7.2 is a suitable model of the material. The accurate prediction of the evolution of the major principal strain at the center of the gauge region further confirms that the plane strain yield strength is correctly calibrated and associated flow is a suitable choice.

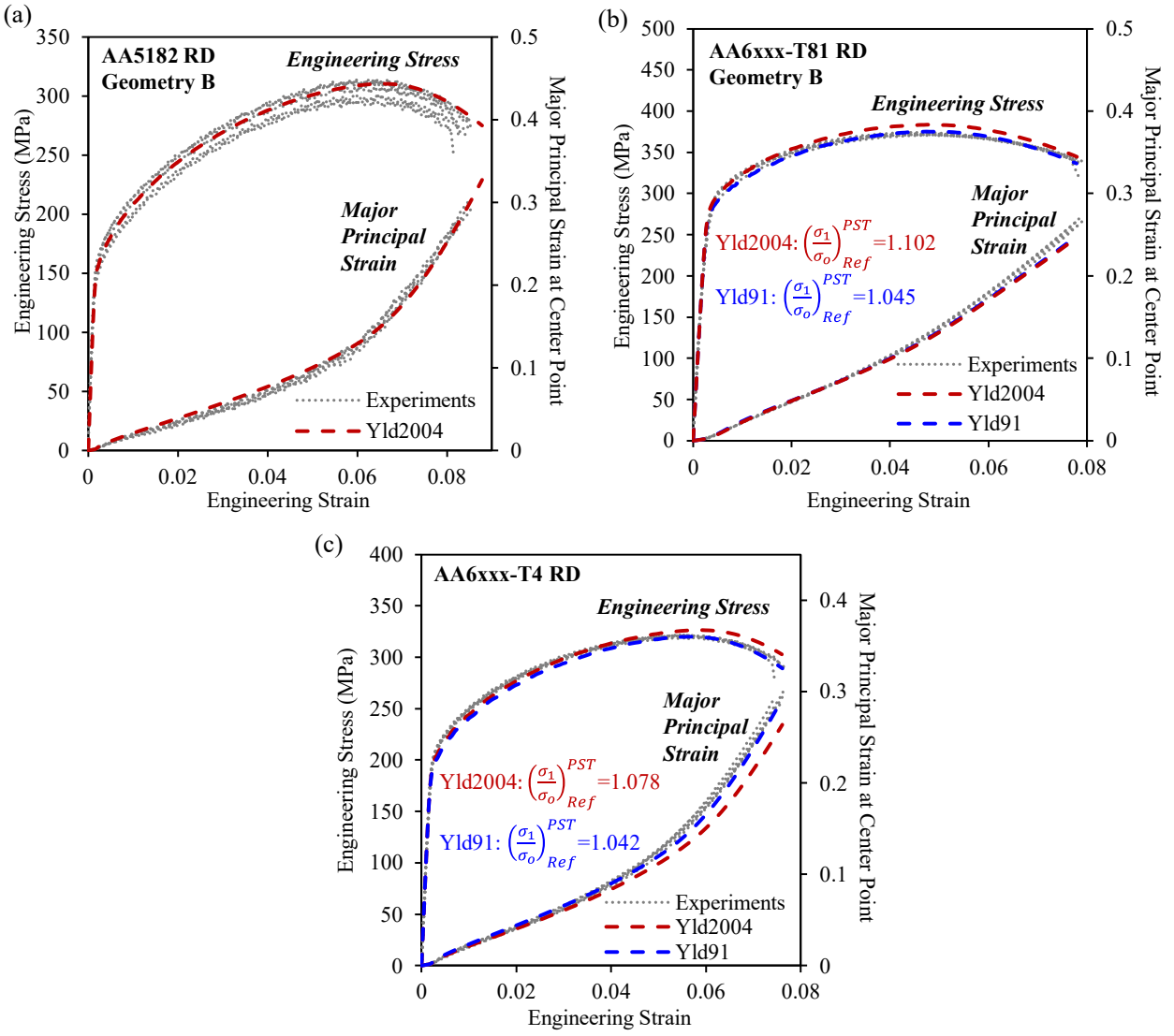

Figure 109: Comparison between FE predicted and experimental stress-strain responses for plane strain notch tests of (a) AA5182, (b) AA6xxx-T81 and (c) AA6xxx-T4 using Geometry B. The Yld2004 master yield surface, calibrated in Chapter 7, was used in the prediction of the engineering stress and major principal strain at the center point. For AA6xxx-T4 and AA6xxx-T81, the HF85-PSC conversion of Yld91 was used to estimate the plane strain yield strength that promotes the best agreement with the experimental data in the post necking region, due to the overprediction of the Yld2004 master yield surfaces.

For AA6xxx-T81, shown in Figure 109(b), and AA6xxx-T4, shown in Figure 109(c), the simulated and experimental responses are in excellent agreement up to peak load but diverge at larger strains possibly due to the complex plastic behavior of AA6xxx alloys. While differential hardening was negligible up to a plastic work of 40 MJ/m^3, it may be more pronounced at higher values of plastic work expected during post-uniform localization. Similarly, non-associated flow may be activated at large strains but negligible in the small range of strain studied in Chapter 4. Non-associated flow would be more important to capture in an FE model than the integration methodology since the strains and strain directions must be predicted in the FE model but are already known exactly from DIC in the integration methodology. The presence of differential hardening and/or non-associated flow in the large strain region could be a source of the small disagreement between the simulated and experimental responses.

An additional explanation for the difference in the simulated and experimental large strain responses of the AA6xxx alloys could be the presence of so-called GP-zones, or fine-grained participates formed during aging that serve as another obstacle to dislocation movement. As explained by Kuwabara *et al.* (2017) in a related study into the differential hardening and anisotropy of AA6xxx alloys, the contribution of GP-zones is not completely captured in phenomenological yield functions or continuum based finite element models. The small disagreement in Figure 109(b) and Figure 109(c) may be due to the inability of the Yld2004 function or the finite-element method to resolve this complex microstructural hardening behavior. Consider in contrast the non-age-hardenable AA5182-O shown in Figure 109(a); the simulated and experimental stress-strain responses are in excellent agreement over the entire range of deformation up to fracture.

By adopting the solid-element implementation of HF85-PSC by Narayanan *et al.* (2022), inverse analysis may be used to refine the plane strain tensile yield strength in the large strain region. The AA6xxx-T81 plane strain yield strength from inverse analysis is 1.045, 5.2% lower than the value of 1.102 calibrated using the notch integration methodology. For AA6xxx-T4, a plane strain yield strength of 1.042 is required to achieve good agreement with the large strain experimental response, whereas a value of 1.078 was calibrated using the notch integration methodology (3.3% higher). When analyzing materials with complex plastic behavior, the notch integration methodology provides an “initial guess” for further refinement by inverse analysis if additional accuracy is required.

8.2 Evaluation in Through-Thickness Shear

A finite-element model of the AA6xxx-T81 through-thickness shear test was generated to validate the Yld2004 master yield surface in a state of through-thickness shear. Despite also calibrating the DP1180 yield surface in through-thickness shear, the model was left unvalidated because the low fracture strains and experimental variability were not conducive to finite element modelling. The same AA6xxx-T81 model

of Section 6.2 was employed, selecting Type -2 elements, and employing the large strain hardening curve of Section 8.0. To activate the through-thickness direction, the x-axis was aligned with the RD (loading direction), y-axis with the TD and z-axis with the ND. A clamping force of 3 kN was applied to each of the rigid plates, consistent with the 6 kN applied in the experimental tests adjusting for half-symmetry.

The model showed relatively poor agreement with the experimental shear stress-strain curves displayed in Figure 110. Good agreement was observed in the elastic regime, up to and including the shear yield stress. However, a higher shear strain was realized in the simulations than in the experiments for a given displacement, possibly because of differing predictions of transverse strain gradients, gauge region rotation and localized thinning of the specimen near the notch root. Testing different specimen widths, notch profiles and eccentricities is recommended to determine the source of the error and finalize the optimum specimen geometry for experimental and numerical analysis.

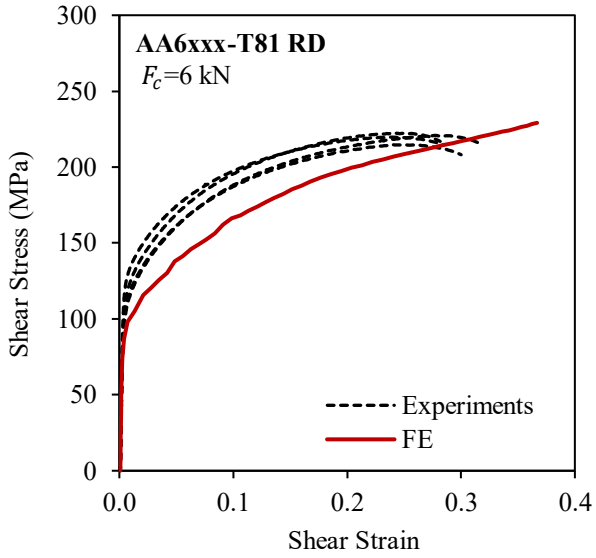

Figure 110: Comparison of simulated and experimental shear stress-strain for through-thickness shear tests of AA6xxx-T81 with the loading direction orientated parallel with the rolling direction. The load was corrected for friction using a coefficient of $\mu = 0.08$ before calculating the average shear stress acting over the gauge area.

Despite errors in the prediction of the shear stress, excellent agreement was obtained between the simulated and experimental load-displacement curves, seen in Figure 111(a), and the theoretical simple shear strain path in the center of the gauge region, seen in Figure 111(b). Since the load-displacement response is obtained with a 6 mm extensometer (tracking two nodes outside the gauge region) and the load cell measurement at the upper grip, it is less sensitive to localized gauge region rotation compared to the average shear stress responses. Therefore, agreement of the experimental and simulated load-displacement responses suggests correct calibration of the out-of-plane parameters of the Yld2004 master yield surface based on the overall global material response.

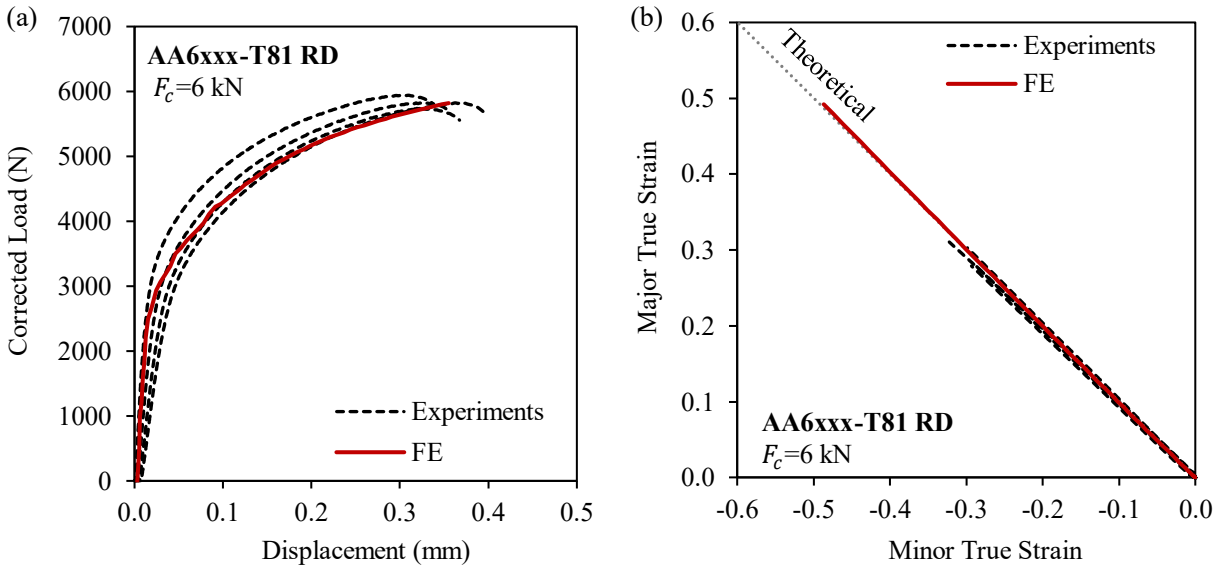

Figure 111: (a) Comparison of simulated and experimental load-displacement response and (b) strain path of the center element in the gauge region for through-thickness shear tests of AA6xxx-T81 with the loading direction orientated parallel with the rolling direction. The load was corrected for friction using a coefficient of $\mu = 0.08$.

8.3 Summary of Master Yield Surface Evaluation

The results of Chapter 8 attest to the effectiveness of the notch integration methodology used to determine the plane strain tensile strength. The simulated post-uniform hardening response was within the experimental variation of the experimental tests completed on a different notch geometry (so-called Geometry B) for DP1180 and AA5182. Inverse analysis of the FE model parameters suggested a plane strain yield strength of within just 5% of the experimentally calibrated value for AA6xxx-T81 and 3% of the experimentally calibrated value for AA6xxx-T4. The discrepancy between the integrated and inverse-analyzed plane strain yield strengths is likely due to differential hardening which could only be calibrated to 40 MJ/m^3 and not to the higher level of plastic work activated by the Geometry B specimen up to fracture. Other sources of error could include the activation of non-associated flow at large strains or the presence of GP-zones within the material that could not be well-captured by the phenomenological, continuum-based approach adopted in the analysis.

The through-thickness shear analysis was also well-modelled for AA6xxx-T81 using the calibrated Yld2004 master yield surface applied in a solid-element FE model of the through-thickness shear test. The model predicted a load-displacement response within the bounds of the experimental data and a simple shear response in the center of the gauge region. Despite differences in the shear stress-strain response, the

correct calibration of the Yld2004 through-thickness shear stress directly from experimental data – and not from virtual experiments or crystal plasticity – is a novel contribution to the study of sheet metal formability.

Chapter 9 Conclusions

Experimental characterization of sheet materials in states of plane strain tension and through-thickness shear is fundamental to the development of accurate material models for forming and impact processes in the automotive industry. Inaccurate – or incomplete – characterization hinders the adoption of advanced high strength steels and aluminums, which while necessary for light weighting, are challenging to model due to anisotropy. Though often neglected in yield function calibration, plane strain tension defines the formability limit of a material due to its intrinsic relationship with necking. Meanwhile bending operations, for instance at draw beads or folds in crumple zones, promote through-thickness shear in the sheet material. Despite the relevance of these loading conditions to modern forming challenges, experimental methods to determine constitutive properties have been either entirely lacking, as in the case of through-thickness shear, or plagued by inaccuracies in the empirical or inverse-analysis based techniques, as in the case of plane strain tension.

By adopting a proposed integration methodology, the constitutive response along the yield surface arc between uniaxial and plane strain tension was extracted from plane strain notch tests without empirical methods or isotropic correction factors. The so-called HF85-PSC yield function, developed from Hosford's 1985 yield function combined with the plane strain constraints of Butcher and Abedini (2019), provided the theoretical framework needed to optimize and calibrate the exponent of the yield surface arc. Relaxing the optimization constraints extended the model to non-associated flow and differential hardening.

Twenty-two FCC and BCC materials, characterized by Kuwabara and collaborators using biaxial cruciform tests, were reviewed to assess the suitability of both the plane strain constraints and the HF85-PSC yield function. According to the plane strain constraint, at a stress ratio of $\sigma_2/\sigma_1 = 0.5$ the strain ratio N_2/N_1 and strain-based Lode parameter v_L should both equal zero. In close adherence with the plane strain constraint, the experimental cruciform data indicated an absolute average strain ratio of 0.024±0.017 and Lode parameter of 0.037±0.026 across the 22 materials. For 17 of the materials, where the data was available, the stress and strain angle ϕ predicted by the HF85-PSC function were compared to the experimental cruciform data at the intermediate arc point of $\sigma_2/\sigma_1 = 0.25$. The average error in the predicted stress was just 1.2% with a 2.53° average deviation in the strain angle. Significant experimental evidence points to the applicability of the plane strain constraint, HF85-PSC yield function and consequently the novel integration methodology proposed in this work. At the very least, the common practice of allowing the plane strain location to drift in anisotropic yield function calibration appears unwise considering the experimental evidence that its location remains close to the theoretical value for pressure-independent plasticity.

Four different automotive materials were used to demonstrate the ability of the proposed integration methodology to determine the exponent of the uniaxial to plane strain arcs and corresponding plane strain yield strength. Experimental tests were performed along the rolling (RD), diagonal (DD) and transverse (TD) directions. In the case of isotropic hardening and associated flow, normalized plane strain yield strengths of 0.960-1.045, 1.099-1.163, 1.023-1.087 and 1.055-1.101 were determined for AA5182-O, DP1180, AA6xxx-T81 and AA6xxx-T4, respectively. Applying the non-associated model to the DD and TD responses of AA5182 indicated a Tresca-type yield surface and a lower exponent HF85-PSC plastic potential exponent of between 3-6. By allowing the HF85-PSC yield function exponent to evolve as a function of plastic deformation, mild differential hardening behavior was captured for the DP1180, AA6xxx-T4 and AA6xxx-T81 alloys. Testing the calibrated models in LS-DYNA illustrated good agreement with the experimental stress-strain and local strain responses.

A through-thickness shear test was developed and applied to the constitutive characterization of DP1180 and AA6xxx-T81. Two notches were cut through the thickness of the sheets, using wire electrical discharge machining (EDM), to promote a state of simple shear in the gauge region of the specimen. A clamping fixture was used to decrease gauge region rotation and bending. Strains were measured on the edge of the sheet with two-dimensional microscopic digital image correlation and an airbrush-generated microscale speckle pattern. The shear stress response was corrected for friction, after determining the Coulomb coefficient by comparing clamped and unclamped tensile data under analogous experimental conditions as the shear tests. Low fracture strains of just 0.05 for DP1180 and 0.3 for AA6xxx-T81 were attributed to wire EDM related defects and the sample width. However, for constitutive purposes the results were considered reasonable and the normalized through-thickness shear stresses were identified as 0.50 and 0.68 for the AA6xxx-T81 and DP1180, respectively.

The plane strain yield strengths, five points along each uniaxial to plane strain tension arc, and the through-thickness shear yield strength were included in Yld2000 and Yld2004 master yield surface calibrations. Holding the weighting method constant, the addition of the experimental data points decreased the error in the predicted stresses, R-values and plastic strain directions compared to a conventional calibration without plane strain or through-thickness shear data. For all four materials, the best calibrations were obtained by setting the yield function exponent as a free parameter, rather than selecting the recommended value of 6 or 8 for a BCC or FCC material, respectively.

The flexible Vegter criterion was used as a benchmark to envision how close the calibrated Yld2000 and Yld2004 master yield surfaces come to what would be considered a “perfect” calibration that fully captures all available experimental data points, while accurately interpolating the material response in the untested loading conditions. The addition of the plane strain constraint resolves the uncertainty of the plane strain

tension “hinge point” location in the original Vegter criterion. With the constraint applied, the Vegter criterion almost perfectly predicts the intermediate stresses and plastic strain directions along the arc between uniaxial and plane strain tension. The experimentally obtained plane strain yield strength, uniaxial tensile yield strength and R-value, shear yield strength, and equal-biaxial tensile yield strength and R-value are perfectly predicted since each act as a hinge point in the Bezier curve interpolation scheme. For each material, neither the Yld2000 nor Yld2004 calibrations could replicate the accuracy of the Vegter criterion for plane stress loading.

The Yld2000 and Yld2004 master yield surfaces were evaluated in the tensile quadrant by simulating the post-necking response of a different notch geometry until fracture in LS-DYNA. The smaller Geometry B was simulated along the limiting direction of each material. The stress and strain responses are different than the so-called Geometry A, adapted from Vegter and van den Boogaard (2006) and used for the calibration of the plane strain yield strength. The eighth symmetry, fully integrated solid element, explicit time integration simulations employed hardening curves calibrated to large strains using shear tests. The DP1180 material was used for an initial convergence study to determine that a 50 μm mesh size, with a minimum of 10 elements through the half-thickness, was needed to capture the post-necking localization. For each material, the predicted strain response in the center of the gauge region and global stress-strain response were in good agreement with the experimental data. A maximum error of just 5% between the experimental and modelled stress-strain curve was observed for the AA6xxx-T4 alloy.

To assess the validity of the AA6xxx-T81 master yield surface in through-thickness shear, the through-thickness shear tests were simulated in LS-DYNA, using the coefficient of friction obtained from the strip friction tests. Although a master yield surface was calibrated for DP1180 under this loading condition, the AA6xxx-T81 tests were better suited for finite element modelling due to a higher fracture strain and greater experimental repeatability. The excellent agreement of the AA6xxx-T81 simulated and experimental load-displacement responses suggests accurate calibration of the master yield surface in through-thickness shear and more broadly demonstrate the suitability of the proposed experimental characterization method. The simulated shear stress-strain response showed poor agreement with the experimental results, driven by greater shear strain in the model than in the experiments. More work is required to assess the influence of transverse strain gradients, localized thinning at the notches and notch eccentricity on the analysis.

Overall, the work in this thesis has highlighted two novel experimental methodologies to better characterize the response of anisotropic sheet materials under states of generalized plane strain, namely plane strain tension and through-thickness shear. Inclusion of the experimentally determined yield strengths in the calibration of master yield surfaces consistently improved the model predictions compared to the conventional approach predominant in the literature. Extensive finite element simulations validated the

models and explored the sensitivity of the proposed methodologies to experimental variables such as friction and geometry. Improved constitutive characterization in plane strain tension and through-thickness shear may improve component level forming and impact models, hastening the adoption of the advanced sheet materials necessary for automotive light weighting and emission reduction.

Chapter 10 Recommendations

Specific recommendations for future work include:

Chapter 3-5: Plane Strain Characterization Methodology

1. The plane strain notch integration methodology is best applied to specimens with a large aspect ratio (width/thickness > ~10) such as the geometry of Vegter and van den Boogaard (2006). Correction factors can be used for alternate geometries and should be further investigated.
2. Further evaluate the influence of the PLC effect on the integration accuracy. The AA5182 models in TD and DD showed the worst agreement with the experimental results, possibly due to the strong PLC effect along these orientations.
3. Further evaluate reasons for the peaks in the DP1180 strain distribution along the gauge width of Geometry A, including strain rate sensitivity. In the FE analysis, the magnitude of the predicted peaks was only on the order of 50% of the experimentally observed response. If DP1180 shows strain rate sensitivity, higher work hardening at the notches would result in a larger magnitude of strain along the gauge region more consistent with the experimental observations.
4. Further evaluate differential hardening. On one hand, errors in the hardening curve model could generate an illusion of differential hardening, when in fact none exists. On the other hand, differential hardening may exist but be poorly described by the sigmoid distribution selected in this analysis.

Chapter 6: Constitutive Characterization in Through-Thickness Shear

1. Optimize the through-thickness shear geometry. Implementing eccentricity may decrease rotation (Peirs *et al.*, 2012). Decreasing the sample width may delay fracture. A convergence study using 5 mm, 10 mm, and 25 mm wide samples would likely assist in determining the ideal width to maximize fracture strains.
2. Generate a specification for the wire EDM parameters and machining tolerances to minimize the size of the heat affected zone, especially for thinner sheet specimens where the shear gauge length is small.
3. Consider through-thickness shear tests in multiple orientations, rather than just along the rolling direction, to fully define the through-thickness anisotropy.
4. Incorporate a load cell at the lower grip of the test frame to quantify friction in through-thickness shear tests without additional testing. Assuming quasi-static loading, the difference between the

load cell readings at the top and bottom grips must equal the total frictional force, applied on both sides of the sample.

5. Study the impact of VSGL, element size and gauge length on the experimental and/or FE simulated strain measurements, as applicable.
6. Perform virtual experiments and/or a combined numerical-experimental analysis to correlate the force-displacement to the shear stress response in the center of the gauge region and define an appropriate procedure for direct experimental extraction.

Chapter 7: Calibration of Advanced Anisotropic Yield Functions Under States of Generalized Plane Strain

1. Use the Vegter criterion for materials where the Yld2000 criterion cannot accurately model the stress and strain response. All experimental data points and theoretical constraints are captured since they are programmed into the model as hinge points. The plane strain constraint resolves a fundamental issue in the original Vegter formulation where the location of the plane strain hinge point was unknown.
2. Calibrate the yield function exponent as a free parameter rather than assume the recommended values of $m = 6$ and $m = 8$ for BCC and FCC materials, respectively.

References

Abedini, A., Butcher, C., Nemcko, M.J., Kurukuri, S. and Worswick, M.J. (2017) Constitutive characterization of a rare-earth magnesium alloy sheet (ZEK100-O) in shear loading: studies of anisotropy and rate sensitivity, *Int J Mech Sci*, vol. 128-129, pp. 54-69.

Abedini, A., Butcher, C., Rahmaan, T. and Worswick, M.J. (2018) Evaluation and Calibration of Anisotropic Yield Criteria in Shear Loading: Constraints to Eliminate Numerical Artefacts, *Int J Solids Struct*, vol. 151, pp. 118-134.

Abedini, A., Butcher, C. and Worswick, M.J. (2018) Experimental fracture characterization of an anisotropic magnesium alloy sheet in proportional and non-proportional loading conditions, *Int J Solids Struct*, vol. 144-145, pp. 1-19.

Abedini, A., Noder, J., Kohar, C.P. and Butcher, C. (2020) Accounting for Shear Anisotropy and Material Frame Rotation on the Constitutive Characterization of Automotive Alloys using Simple Shear Tests, *Mech Mater*, vol. 148.

Abspoel, M., Scholting, M., Lansbergen, M., An, Y. and Vegter, H. (2017) A new method for predicting advanced yield criteria input parameters from mechanical properties, *J Mater Process Tech*, vol. 248, pp. 161-177.

Aksenov, S.A., Kliber, J., Puzino, Y.A. and Bober, S.A. (2015) Processing of plane strain compression test results for investigation of AISI-304 stainless steel constitutive behavior, *Journal of Chemical Technology and Metallurgy*, vol. 50, pp. 644-650.

Andar, M., Kuwabara, T., Yonemura, S. and Uenishi, A. (2010) Elastic-plastic and inelastic characteristics of high strength steel sheets under biaxial loading and unloading, *ISIJ Int*, vol. 50, no. 4, pp. 613-619.

An, Y.G., Vegter, H. and Elliott, L. (2004) A novel and simple method for the measurement of plane strain work hardening, *J Mater Process Technol*, vol. 155-156, pp. 1616-1622.

Aretz, H. and Barlat, F. (2014) Influence of Contact Friction on the Experimental Determination of the Balanced Biaxial Strain-Ratio Using the Disc Compression Test, *Key Eng Mater*, pp. 611-612.

Aretz, H., Hopperstad, O. and Lademo, O. (2007) Yield function calibration for orthotropic sheet metals based on uniaxial and plane strain tensile tests, *J Mater Process Technol*, vol. 186, no. 1-3, pp. 221-235.

Arooj, S., Shah, M., Sadiq, S., Jaffery, S. and Khushnood, S. (2014) Effect of Current in the EDM Machining of Aluminum 6061 T6 and its Effect on the Surphace Morphology, *Arab J Sci Eng*, vol. 39, pp. 4187-4199.

Azam, M., Jahanzaib, M., Abbasi, J., Abbas, M., Wasim, A. and Hussain, S. (2016) Parametric analysis of recast layer formation in wire-cut EDM of HSLA steel, *Int J Adv Manuf Technol*, vol. 87, pp. 713-722.

Bae, G.H. and Huh, H. (2011) Tension/compression test of auto-body steel sheets with the variation of the pre-strain and the strain rate, *WIT Transactions on Engineering Sciences*, vol. 72, pp. 213-225.

Bai, Y. and Wierzbicki, T. (2008) A new model of metal plasticity and fracture with pressure and lode dependence, *Int J Plast*, vol. 24, pp. 1071-1096.

Balakrishnan, V. (1999) *Measurement on in-plane Bauschinger effect in metal sheet [Master's Thesis]*, Columbus: The Ohio State University.

Banabic, D. (2010) *Sheet Metal Forming Processes: Constitutive Modelling and Numerical Simulation*, Heidelberg: Springer-Verlag.

Banabic, D., Aretz, H., Comsa, D.S. and Paraianu, L. (2005) An improved analytical description of orthotropy in metallic sheets, *Int J Plast*, vol. 21, pp. 493-512.

Banabic, D., Barlat, F., Cazacu, O. and Kuwabara, T. (2020) Advances in anisotropy of plastic behaviour and formability of sheet metals, *Int J Mater Form*, vol. 13, pp. 749-787.

Baral, M., Hama, T., Knudsen, E. and Korkolis, Y.P. (2018) Plastic deformation of commercially-pure titanium: experiments and modelling, *Int J Plast*, vol. 105, pp. 164-194.

Barlat, F., Aretz, H., Yoon, J.W.K.M.E., Brem, J.C. and Dick, R.E. (2005) Linear transformation-based anisotropic yield functions, *Int J Plast*, vol. 21, pp. 1009-1039.

Barlat, F., Brem, J.C., Yoon, J.W., Chung, K., Dick, R.E., Lege, D.J., Pourboghrat, F., Choi, S.-H. and Chu, E. (2003) Plane stress yield function for aluminum alloy sheets—part 1: theory, *Int J Plast*, vol. 19, no. 9, pp. 1297-1319.

Barlat, F., Kuwabara, T. and Korkolis, Y. (2018) 'Anisotropic plasticity and application to plane stress', in Altenbach, H. and Ochsner, A. (ed.) *Encyclopedia of Continuum Mechanics*, Heidelberg: Springer-Verlag GmbH Germany.

Barlat, F., Kuwabara, T. and Korkolis, Y.P. (2018) 'Anisotropic plasticity and application to plane stress', in Altenbach, H. and Ochsner, A. (ed.) *Encyclopedia of Continuum Mechanics*, Heidelberg: Springer-Verlag GmbH.

Barlat, F., Lege, D.J. and Brem, J.C. (1991) A six-component yield function for anisotropic materials, *Int J Plast*, vol. 7, no. 7, pp. 693-712.

Berstad, T., Lademo, O.-G. and Pederson, K. (2004) Formability Modeling with LS-DYNA, *8th International LS-DYNA Users Conference*, pp. 53-64.

Billur, E. and Altan, T. (2013) Three generations of advanced high-strength steels for automotive applications, Part 1, *Stamping Journal*, pp. 16-17.

Blaber, J. *Pattern Application*, [Online], Available: http://www.ncorr.com/index.php/pattern-application [4 December 2020].

Boger, R.K., Wagoner, R.H., Barlat, F., Lee, M.G. and Chung, K. (2005) Continuous, large strain, tension/compression testing of sheet material, *Int J Plast*, vol. 21, no. 12, pp. 2319-2343.

Bridgman, P.W. (1952) *Studies in Large Plastic Flow*, New York: McGraw-Hill.

Brosius, A., Kusters, N. and Lenzen, M. (2018) New method for stress determination based on digital image correlation data, *CIRP Annals*, vol. 67, no. 1, pp. 269-272.

Butcher, C. and Abedini, A. (2017) Shear confusion: Identification of the appropriate equivalent strain in simple shear using the logarithmic strain measure, *Int J Mech Sci*, vol. 134, December, pp. 273-283.

Butcher, C. and Abedini, A. (2019) On anisotropic plasticity models using linear transformations on the deviatoric stress: physical constraints on plastic flow in generalized plane strain, *Int J Mech Sci*, vol. 161-162, p. 105044.

Byrne, E. and Simonsen, M. (2016) *Subset, step size and strain filter selection*, [Online], Available: https://www.correlatedsolutions.com/support/index.php?/Knowledgebase/Article/View/10/0/subset-step-size-and-strain-filter-selection [6 March 2020].

Cai, Z., Diao, K., Wu, X. and Wan, M. (2016) Constitutive modeling of evolving plasticity in high strength, *Int J Mech Sci*, vol. 107, pp. 43-57.

Cai, Z.Y., Meng, B., Wan, M., Wu, X.D. and Fu, M.W. (2020) A modified yield function for modeling of the evolving yielding behavior and micro-mechanism in biaxial deformation of sheet metals, *Int J Plast*, vol. 129, p. 102707.

Chen, Z., Gandhi, U., Lee, J. and Wagoner, R.H. (2016) Variation and consistency of Young's modulus in steel, *J Mater Process Technol*, vol. 227, pp. 227-243.

Choung, J.M. and Cho, S.R. (2008) Study on true stress correction from tensile tests, *J Mech Sci Technol*, vol. 22, pp. 1039-1051.

Coppieters, S., Hakoyama, T., Eyckens, P., Nakano, H., Van Bael, A., Debruyne, D. and Kuwabara, T. (2019) On the synergy between physical and virtual sheet metal testing: calibration of anisotropic yield functions using a microstructure-based plasticity model, *Int J Mater Form*, vol. 12, pp. 741-759.

Correlated Solutions *Strain Calculation in Vic-3D*, [Online], Available: http://www.correlatedsolutions.com/supportcontent/strain.pdf [6 October 2020].

Correlated Solutions *Vic-3D Software Manual - Version 8.4*, [Online], Available: http://www.correlatedsolutions.com/supportcontent/VIC-3D-8-Manual.pdf [2 April 2021].

Cui, Z., Guo-hui, Z. and Mao, W.-m. (2013) Effect of Crystallographic Texture on Anistoropy of Yield Strength in X100 Pipeline Steel, *Journal of Iron and Steel Research, International*, vol. 20, no. 8, pp. 66-71.

Cvitanic, V., Vlak, F. and Lozina, Z. (2008) A finite element formulation based on non-associated plasticity for sheet metal forming, *Int J Plast*, vol. 24, pp. 646-687.

Danas, K. and Castaneda, P. (2012) Influence of the Lode parameter and the stress triaxiality on the failure of elasto-plastic porous materials, *Int J Solids Struct*, vol. 49, pp. 1325-1342.

Davies, G. (2012) *Materials for Automobile Bodies*, Amsterdam: Elsevier.

Dick, C.P. and Korkolis, Y.P. (2015) Anisotropy of thin-walled tubes by a new method of combined tension and shear loading, *Int J Plast*, vol. 71, pp. 87-112.

Dong, Y., Kakisawa, H. and Kagawa, Y. (2015) Development of microscale pattern for digital image correlation up to 1400 °C, *Optics and Lasers in Engineering*, vol. 68, pp. 7-15.

Dunand, M. and Mohr, D. (2010) Hybrid experimental–numerical analysis of basic ductile fracture experiments for sheet metals, *Int J Solids Struct*, vol. 47, no. 9, pp. 1130-1143.

Engler, O. and Hirsch, J. (2007) Polycrystal-plasticity simulation of six and eight ears in deep-drawn aluminum cups, *Mater. Sci. Eng., A* , vol. 452-453, April, pp. 640-651.

Esmaeilpour, R., Kim, H., Park, T., Pourboghrat, F., Xu, Z., Mohammed, B. and Abu-Farha, F. (2018) Calibration of Barlat Yld2004-18P yield function using CPFEM and 3D RVE for the simulation of single point incremental forming (SPIF) of 7075-O aluminum sheet, *Int J Mech Sci*, vol. 145, pp. 24-41.

Eyckens, P., Van Bael, A. and Van Houtte, P. (2009) Marciniak-Kuczynski type modelling of the effect of Through-Thickness Shear on the forming limits of sheet metal, *Int J Solids Struct*, vol. 25, pp. 2249-2268.

Fatemi, A. and Dariani, B. (2016) The effect of normal and through thickness shear stresses on the formability of isotropic sheet metals, *Journal of the Brazilian Society of Mechanical Sciences and Engineering*, vol. 38, October, pp. 119-131.

Flores, P., Tuninetti, V., Gilles, G., Gonry, P., Duchene, L. and Habraken, A.M. (2010) Accurate stress computation in plane strain tensile tests for sheet metal using experimental data, *J Mater Process Technol*, vol. 210, pp. 1772-1779.

Froes, F.H. (1994) Advanced metals for aerospace and automotive use, *Mater Sci Eng, A*, vol. 184, no. 2, pp. 119-133.

Geng, L., Shen, Y. and Wagoner, R.H. (2002) Anisotropic hardening equations derived from reverse-bend testing, *Int J Plast*, vol. 18, pp. 743-767.

Grytten, F., Holmedal, B., Hopperstad, O.S. and Borvik, T. (2008) Evaluation of identification methods for Yld2004-18p, *Int J Solids Struct*, vol. 24, pp. 2248-2277.

Gu, B., He, J., Shuhui, L. and Zhongqin, L. (2020) Anisotropic fracture modeling of sheet metals: From in-plane to out-of-plane, *Int J Solids Struct*, vol. 182-183, pp. 112-140.

Ha, J., Baral, M. and Korkolis, Y. (2018) Plastic anisotropy and ductile fracture of bake-hardened AA6013 aluminum sheet, *Int J Solids Struct*, vol. 155, pp. 23-139.

Hartmann, C., Weiss, H., Lechner, P., Vol, W., Neumayer, S., Fitschen, J. and Steidl, G. (2021) Measurement of strain, strain rate and crack evolution in shear cutting, *J Mater Process Technol*, vol. 288.

Herrmann, J., Suttner, S. and Merklein, M. (2017) Experimental investigation and numerical modeling of the bond shear strength of multi-layered 6000 series aluminum alloys, *Procedia Engineering*, vol. 183, pp. 283-290.

Hill, R. (1948) A theory of the yielding and plastic flow of anisotropic metals, *Proceedings of the Royal Society of London, Series A*, vol. 193, pp. 281-297.

Hill, R. (1950) A theory of the plastic bulging of a metal diaphragm by lateral pressure, *The London, Edinburgh, and Dublin Philosophical Magazine and Journal of Science*, vol. 41, no. 322, pp. 1133-1142.

Hill, R. (1950) *Mathematical Theory of Plasticity*, Oxford: Oxford University Press.

Hill, R. (1979) Theoretical plasticity of textured aggregates, *Mathematical Proceedings of the Cambridge Philosophical Society*, vol. 85, pp. 179-191.

Hill, R. and J.W., H. (1992) Differential Hardening in Sheet Metal Under Biaxial Loading: A Theoretical Framework, *J Appl Mech*, vol. 59, pp. 1-9.

Holmberg, J., Wretland, A., Berglund, J. and Beno, T. (2018) Surface integrity after post processing of EDM processed Inconel 718 shaft, *Int J Adv Manuf Technol*, vol. 95, pp. 2325-2337.

Hora, P., Tong, L. and Berisha, B. (2013) Modified maximum force criterion, a model for the theoretical prediction of forming limit curves, *Int J Mater Form*, vol. 6, pp. 267-279.

Hosford, W.F. (1972) A generalized isotropic yield criterion, *Int J Mech Sci*, vol. 39, pp. 607-609.

Hosford, W.F. (1979) 'On yield loci of anisotropic cubic metals', Dearborn, Michigan.

Hosford, W.F. (1985) Comments on anisotropic yield criteria, *Int J Mech Sci*, vol. 7-8, pp. 423-427.

Hosford, W.F. (2013) *Fundamentals of Engineering Plasticity*, New York: Cambridge University Press.

Hou, Y., Min, J., Guo, N., Lin, J., Carsley, J., Stoughton, T., Traphoner, H., Clausmeyer, T. and Tekkaya, A.E. (2019) Investigation of evolving yield surfaces of dual-phase steels (In Press), *J Mater Process Tech*.

Hou, Y., Min, J., Lin, J., Carsley, J. and Stoughton, T. (2018) Cruciform specimen design for large plastic strain during biaxial tensile testing, *IOP Conference Series: Journal of Physics*, vol. 1063, p. 012160.

Hwang, Y.-M. and Chen, C.-C. (2020) Investigation of Effects of Strip Metals and Relative Sliding Speeds on Friction Coefficients by Reversible Strip Draw Tests, *Metals*, vol. 10, p. 1369.

International Organization for Standardization (2014) *ISO16842: Metallic materials - sheet and strip - biaxial tensile testing method using a cruciform test piece*.

Joo, G., Huh, H. and Choi, M. (2016) Tension/compression hardening behaviors of auto-body steel sheets at intermediate strain rates, *Int J Mech Sci*, vol. 108-109, pp. 174-187.

Kalpakjian, S. and Schmid, S. (2008) *Manufacturing Processes for Engineering Materials*, 5th edition, Jurong, Singapore: Pearson Prentice Hall.

Karafillis, A.P. and Boyce, M.C. (1993) A general anisotropic yield criterion using bounds and a transformation weighting tensor, *J Mech Phys Solids*, vol. 41, no. 12, pp. 1859-1886.

Kato, H., Tottori, Y. and Sasaki, K. (2014) Four-point bending test of determining the stress-strain curves asymmetric between tension and compression, *Exp Mech*, vol. 54, p. 489492.

Kawaguchi, J., Kuwabara, T. and Sakurai, T. (2015) Formulation of the differential hardening of 5000 series aluminum alloy sheet for enhancing the predictive accuracy of sheet metal forming simulations, *Journal of The Japan Institute of Light Metals*, vol. 65, no. 11, pp. 554-560.

Kelly, P. *Lecture Notes: An Introduction to Solid Mechanics*, [Online], Available: https://pkel015.connect.amazon.auckland.ac.nz/SolidMechanicsBooks/Part_II/index.html [26 March 2022].

Khalfallah, A., Alves, J., Oliveira, M. and Menezes, L. (2015) Influence of the characteristics of the experimental data set used to identify anisotropy parameters, *Simul Modell Pract Theory*, vol. 53, pp. 15-44.

Khameneh, F., Abedini, A. and Butcher, C. (2021) Lengthscale effects in optical strain measurement for fracture characterization in simple shear, *Int J Fracture*, vol. 232, pp. 153-180.

Klocke, F., Hensgen, L., Klink, A. and Schwedt, A. (2016) Structure and Composition of the White Layer in the Wire-EDM Process, *Procedia CIRP*, vol. 42, pp. 673-678.

Kramer, S., Reu, P., Turner, D. and Bonk, S. (2016) 'A Speckle Patterning Study for Laboratory-Scale DIC Experiments', Conference Proceedings of the Society for Experimental Mechanics Series, Philadelphia, 33-35.

Kupke, A. (2017) *Effect of the microstructure on the unloading characteristics of DP steel [PhD Thesis]*, Victoria, Australia: Deakin University.

Kuwabara, T. (2014) Multiaxial stress tests for metal sheets and tubes for accurate material modeling and forming simulations, *Acta Metall Slovaca*, vol. 14, pp. 428-437.

Kuwabara, T., Hashimot, K., Iizuka, E. and Yoon, J.W. (2011) Effect of anisotropic yield functions on the accuracy of hole expansion simulations, *J Mater Process Technol*, vol. 211, pp. 475-481.

Kuwabara, K. and Ichikawa, K. (2015) Hole expansion simulation considering the differential hardening of a sheet metal, *Rom J Tech Sci Appl Mech*, vol. 60, pp. 63-81.

Kuwabara, T., Kumano, Y., Ziegelheim, J. and Kurosaki, I. (2009) Tension–compression asymmetry of phosphor bronze for electronic parts and its effect on bending behavior, *Int J Plast*, vol. 25, no. 9, pp. 1759-1776.

Kuwabara, T. and Kurita, K. (2000) Measurement of plastic deformation characteristics of 6000-type sheet aluminum alloy under biaxial tension and verification of yield criteria (in Japanese), *Journal of Japan Institute of Light Metals*, vol. 50, pp. 2-6.

Kuwabara, T., Mori, T., Asana, M., Hakoyama, T. and Barlat, F. (2017) Material modeling of 6016-O and 6016-T4 aluminum alloy sheets and application to hole expansion forming simulation, *Int J Plast*, vol. 93, pp. 164-186.

Kuwabara, T., Mori, T., Asano, M., Hakoyama, T. and Barlat, F. (2017) Material modeling of 6016-O and 6016-T4 aluminum alloy sheets and application to hole expansion forming simulation, *Int J Plast*, vol. 93, pp. 164-186.

Kuwabara, T. and Nakajima, T. (2011) Material modeling of 980 MPa dual-phase steel sheet based on biaxial tensile test and in-plane stress reversal test, *J Solid Mech Mater Eng*, vol. 12, pp. 709-720.

Kuwabara, T. and Sugawara, F. (2013) Multiaxial tube expansion test method for measurement of sheet metal deformation, *Int J Plast*, vol. 45, pp. 103-118.

Kuwabara, T., Umemura, M., Yoshida, K., Kuroda, M., Hirano, S. and Kikuta, Y. (2006) Forming limit strains of 5000 series aluminum alloys with different magnesium contents (in Japanese), *Journal of Japan Institute of Light Metals*, vol. 56, no. 5, pp. 323-328.

Kuwabara, T., Van Bael, A. and Iizuka, E. (2002) Measurement and analysis of yield locus and work hardening characteristics of steel sheets with different r-values, *Acta Materialia*, vol. 50, pp. 3717-3729.

Lademo, O.-G., Hopperstad, O.S. and Langseth, M. (1999) An evaluation of yield criteria and flow rules for aluminium alloys, *Int J Plast*, vol. 15, no. 2, pp. 191-208.

Lee, J.-Y., Lee, K.-J., Lee, M.-G., Kuwabara, T. and Barlat, F. (2019) Numerical modeling of accurate prediction of strain localization in hole expanision of a steel sheet, *Int J Solids Struct*, vol. 156-157, pp. 107-118.

Lenzen, M. and Merklein, M. (2018) Improvement of Numerical Modelling Considering Plane Strain Material Characterization with an Elliptical Hydraulic Bulge Test, *J Manuf Mater Process*, vol. 2, no. 6.

Li, S., He, J., Gu, B., Zeng, D., Xia, C., Zhao, Y. and Lin, Z. (2018) Anisotropic fracture of advanced high strength steel sheets: Experiment and theory, *Int J Plast*, vol. 103, pp. 95-118.

Lode, W. (1926) Versuche über den Einfluß der mittleren Hauptspannung auf das Fließen der Metalle Eisen, Kupfer und Nickel, *Zeitschrift für Physik*, vol. 36, no. 11-12, November, pp. 913-939.

Logan, R.W. and Hosford, W.F. (1980) Upper-bound anisotropic yield locus calculations assuming -pencil glide, *Int J Mech Sci*, vol. 22, no. 7, pp. 419-430.

Lou, Y. and Yoon, J.W. (2018) Anisotropic yield function based on stress invariants for BCC and FCC metals and its extension to ductile fracture criterion, *Int J Plast*, vol. 101, pp. 125-155.

Mahmudi, R. (1999) A novel technique for plane-strain tension testing of sheet metals, *J Mater Process Technol*, vol. 86, no. 1-3, pp. 237-244.

Marciniak, Z. and Kuczynski, K. (1967) Limit strains in the process of stretch-forming sheet metals, *Int J Mech Sci*, vol. 9, no. 9, pp. 609-620.

Marth, S., Haggblad, H., Oldenburg, M. and Ostlund, R. (2016) Post necking characterisation for sheet metal materials using full field measurement, *J Mater Process Technol*, vol. 238, pp. 315-324.

MathWorks *Find circles using circular Hough transform - MATLAB imfindcircles*, [Online], Available: https://www.mathworks.com/help/images/ref/imfindcircles.html [4 December 2020].

MathWorks *How GlobalSearch and MultiStart Work*, [Online], Available: https://www.mathworks.com/help/gads/how-globalsearch-and-multistart-work.html#bsds7nj-1 [20 March 2021].

Mativenga, P. (2018) 'Micromachining', in Chatti, S. and Tullio, T. (ed.) *CIRP Encyclopedia of Production Engineering*, Heidelberg: Springer.

Min, J., Stoughton, T.B., Carsley, J.E., Carlson, B., Lin, J. and Gao, X. (2017) Accurate characterization of biaxial stress-strain response of sheet metal from bulge testing, *Int J Plast*, vol. 94, pp. 192-213.

Min, J., Stoughton, T.B., Carsley, J.E. and Lin, J. (2016) Compensation for process-dependent effects in the determination of localized necking limits, *Int J Mech Sci*, vol. 117, pp. 115-134.

MIT (2008) On the Road in 2035: Reducing Transportation's Petroleum Consumption and GHG Emissions.

Mulder, H., Eyckens, P. and van den Boogaard, T. (2015) 'Differential Hardening in IF Steel: Experimental Results and a Crystal Plasticity Based Model', Advanced Constitutive Models in Sheet Metal Forming, Zurich, 115-120.

Nagano, C., Kuwabara, T., Shimada, Y. and Kawamura, R. (2018) Measurement of differential hardening under biaxial stress of pure titanium sheet, *IOP Conf. Ser.: Mater. Sci. Eng.*, vol. 418.

Narayanan, A., Abedini, A., Weinschenk, A., Worswick, M.J. and Butcher, C. (2021) Evaluation of Simple Shear Test Geometries for Constitutive Characterization using Virtual Experiments, *IOP Conf. Ser.: Mater. Sci. Eng.*, vol. 1157, p. 012066.

Narayanan, A., Bourque, C., Fast-Irvine, C., Abedini, A., Anderson, D. and Butcher, C. (2022) 'Identification of the Plane Strain Yield Strength of Anisotropic Sheet Metals using Inverse Analysis of Notch Tests (Unpublished Research)', WCX SAE World Congress Experience.

Noder, J. (2017) *Characterization and Simulation of Warm Forming of 6xxx and 7xxx Series Aluminum Alloys [Master's Thesis]*, Waterloo: University of Waterloo.

Noder, J. and Butcher, C. (2019) A comparative investigation into the influence of the constitutive model on the prediction of in-plane formability for Nakazima and Marciniak tests, *Int J Mech Sci*, vol. 163, p. 105138.

Oak Ridge National Laboratory (2017) *Transportation Energy Data Book*, 36th edition, Oak Ridge, Tennessee: Oak Ridge National Laboratory.

Omer, K., Butcher, C. and Worswick, M. (2020) Characterization and application of a constitutive model for two 7000-series aluminum alloys subjected to hot forming, *Int J Mech Sci*, vol. 165, p. 105218.

Peirs, J., Verleysen, P. and Degrieck, J. (2012) Novel Technique for Static and Dynamic Shear Testing of Ti6Al4V Sheet, *Exp Mech*, vol. 52, pp. 729-741.

Plunkett, B., Lebensohn, R.A., Cazacu, O. and Barlat, F. (2006) Anisotropic yield function of hexagonal materials taking into account texture development and anisotropic hardening, *Acta Materialia*, vol. 54, pp. 4159-4169.

Pucik, T., Brannon, R.M. and Burghardt, J. (2015) Nonuniqueness and instability of classical formulations of nonassociated plasticity, I: case study, *J Mech Mater Struct*, vol. 10, no. 2, March, pp. 123-148.

Rahmaan, T. (2015) *Low to High Strain Rate Characterization of DP600, TRIP780, AA5182-O [Master's Thesis]*, Waterloo: University of Waterloo.

Rahmaan, T., Abedini, A., Butcher, C., Pathak, N. and Worswick, M. (2017) Investigation into the shear stress, localization and fracture behaviour of DP600 and AA5182-O sheet metal alloys under elevated strain rates, *Int J Impact Eng*, vol. 108, pp. 303-321.

Rossi, M., Broggiato, G.B. and Papalini, S. (2008) Application of digital image correlation to the study of planar anisotropy of sheet metals at large strains, *Meccanica*, vol. 43, pp. 185-199.

Rossi, M., Lattanzi, A. and Barlat, F. (2018) A general linear method to evaluate the hardening behaviour of metals at large strain with full-field measurements, *Strain*, vol. 54, p. e12265.

Rudnicki, J.W.i. and Rice, J.R. (1975) Conditions for the localization of deformation in pressure-sensitive dilatant materials, *J Mech Phys Solids*, vol. 23, pp. 371-394.

Sandler, I.S. and Rubin, D. (1987) 'The consequences of non-associated plasticity in dynamic problems', in Desai, C. (ed.) *Constitutive laws for engineering materials*, Tucson, AZ: Elsevier.

Scheider, I., Brocks, W. and Cornec, A. (2004) Procedure for the determination of true stress-strain curves from tensile tests with rectangular cross section experiments, *J Eng Mater Technol*, vol. 126, no. 1, pp. 70-76.

Selvarajou, B., Kondori, B., Benzerga, A.A. and Joshi, S.P. (2016) On plastic flow in notched hexagonal close packed single crystals, *J Mech Phys Solids*, vol. 94, pp. 73-97.

Simões, V., Coër, J., Laurent, H., Oliveira, M., Alves, J., Manach, P. and Menezes, L. (2013) 'Influence of the yield criteria in the numerical simulation of an AA5745-O cylindrical cup', Bilbao, Spain.

Stoughton, T. (2002) A non-associated flow rule for sheet metal forming, *Int J Plast*, vol. 18, no. 5-6, pp. 687-714.

Stoughton, T. and Yoon, J.W. (2008) On the existence of indeterminate solutions to the equations of motion under non-associated flow, *Int J Plast*, vol. 24, no. 4, April, pp. 583-613.

Stoughton, T. and Yoon, J.W. (2009) Anisotropic hardening and non-associated flow in proportional loading of sheet metals, *Int J Plast*, vol. 25, no. 9, pp. 1777-1817.

Straka, L., Corny, I. and Pitel, J. (2016) Properties evaluation of thin microhardened surface layer of tool steel after wire EDM, *Metals*, vol. 6, no. 95.

Suh, Y.S., Saunders, F.I. and Wagoner, R.H. (1996) Anisotropic yield functions with plastic-strain-induced anisotropy, *Int J Plast*, vol. 12, no. 3, pp. 417-438.

Sun, L. and Wagoner, R.H. (2013) Proportional and non-proportional hardening behavior of dual-phase steels, *Int J Plast*, vol. 45, pp. 174-187.

Swift, H.W. (1952) Plastic instability under plane stress, *J Mech Phys Solids*, vol. 1, no. 1, pp. 1-18.

Tamai, Y. and Manabe, K. (2013) Effects of contact pressure, sliding velocity and sliding length Effects of contact pressure, sliding velocity and sliding length, *Journal of the JSTP*, vol. 629, pp. 537-541.

Taylor-Hobson (n.d) *Surtronic 3+ Operating Instructions*.

Tian, H., Brownell, B., Baral, M. and Korkolis, Y.P. (2016) Earing in cup-drawing of anisotropic Al-602-T4 sheets, *Int J Mater Form*, vol. 71, pp. 87-112.

Uddeholm (2007) *EDM of Tool Steel*, Hagfors, Sweden: Uddeholm, Available: https://www.uddeholm.com/files/edm-english.pdf.

van den Boogaard, T., Havinga, J., Belin, A. and Barlat, F. (2015) Parameter reduction for the Yld2004-18p yield criterion, *Int J Mater Form*, vol. 9, pp. 175-178.

van Liempt, P. and Sietsma, J. (2016) A physically based yield criterion 1. Determination of the yield stress based on analysis of pre-yield dislocation behaviour, *Materials Science & Engineering A*, vol. 662, pp. 80-87.

Vegter, H. and van den Boogaard, A.H. (2006) A plane stress yield function for anisotropic sheet material by interpolation between biaxial stress states, *Int J Plast*, vol. 22, pp. 557-580.

Wagoner, R.H. (1980) Measurement and analysis of plane-strain work hardening, *Metall Trans A*, vol. 11A, pp. 165-175.

Wang, K. and Wierzbicki, T. (2015) Experimental and numerical study on the plane-strain blanking process on an AHSS shet, *Int J Fract*, vol. 194, no. 1, pp. 19-36.

Yamanaka, A. and Kuwabara, T. (2015) Material modeling and forming simulation of 5182 aluminum alloy sheet using numerical biaxial tensile test based on homogenized crystal plasticity finite element method (in Japanese), *Journal of Japan Institute of Light Metals*, vol. 65, no. 11, pp. 561-567.

Yanaga, D., Kuwabara, T., Uema, N. and Asano, M. (2012) Material modeling of 6000 series aluminum alloy sheets with different density cube textures and effect on the accuracy of finite element simulation, *Int J Solids Struct*, vol. 49, no. 25, pp. 3465-3488.

Yanaga, D., Takizawa, H. and Kuwabara, T. (2013) Material modeling of 6016-O and 6016-T4 aluminum alloy sheets and application to hole expansion forming simulation, *Journal of the Japan Society for Technology of Plasticity*, vol. 55, no. 636, pp. 55-61.

Yanaga, D., Takizawa, H. and Kuwabara, T. (2014) Formulation of differential work hardening of 6000 series aluminum alloy sheet and application to finite element analysis, *Journal of the Japan Society for Technology of Plastic*, vol. 55, no. 36, pp. 55-61.

Yin, Q., Zillmann, B., Suttner, S., Gerstein, G., Biasutti, M., Tekkaya, A., Wagner, M., Merklein, M., Schaper, M., Halle, T. and Brosius, A. (2014) An experimental and numerical investigation of different shear test configurations for sheet metal characterization, *Int J Solids Struct*, vol. 51, pp. 1066-1074.

Yoon, J.W., Barlat, F., Dick, R.E. and Karabin, M.E. (2006) Prediction of six or eight ears in a drawn cup based on a new anisotropic yield function, *Int J Plast*, vol. 22, pp. 174-193.

Yu, T.X. and Zhang, L.C. (1996) *Plastic bending: theory and applications*, Singapore: World Scientific.

Zhang, H., Diehl, M., Roters, F. and Raabe, D. (2016) A virtual laboratory using high resolution crystal plasticity simulations to determine the initial yield surface for sheet metal forming operations, *Int J Solids Struct*, vol. 80, pp. 111-138.

Zhang, K.S., Hauge, M., Odegard, J. and Thaulow, C. (1999) Determining material true stress-strain curve from tensile specimens with rectangular cross section, *Int J Solids Struct*, vol. 36, pp. 3497-3516.

Zheng, K., Politis, D., Wang, L. and Lin, J. (2018) A review on forming techniques for manufacturing lightweight complex—shaped aluminium panel components, *Int J Lightweight Mater Manuf*, vol. 1, no. 2, pp. 55-80.